UNIVERSITY OF CALIFORNIA, MERCED

Computational Studies of Metal Oxide Hydrolysis and Improved Maximum Overlap Methods

A dissertation submitted in partial satisfaction of the
requirements for the degree
Doctor of Philosophy

in

Theoretical Chemistry

by

Ali Abou Taka

Committee in charge:

Professor Christine Isborn, Chair
Professor Hrant Hratchian, Advisor
Professor Liang Shi
Professor Aurora Pribram-Jones
Professor Chih-Chun Chien

2021

The dissertation of Ali Abou Taka is approved, and it is acceptable in quality and form for publication on microfilm and electronically:

(Professor Hrant Hratchian, Advisor)

(Professor Liang Shi)

(Professor Aurora Pribram-Jones)

(Professor Chih-Chun Chien)

(Professor Christine Isborn, Chair)

University of California, Merced

2021

DEDICATION

To my family.

To my partner.

To my friends.

To refugees worldwide.

Stay resilient and don't give up on your dreams.

EPIGRAPH

There is no wealth like knowledge,
and no poverty like ignorance.
—Imam Ali Ibn Abi Talib (pbuh)

TABLE OF CONTENTS

LIST OF FIGURES

LIST OF TABLES

ACKNOWLEDGEMENTS

I would like to start by acknowledging my advisor and mentor, Prof. Hrant Hratchian, for his guidance and patience throughout my doctoral degree. I appreciate every piece of advice you gave me.

I would like to express my gratitude to my committee members Prof. Christine Isborn, Prof. Liang Shi, and Prof. Chih-Chun Chien, for all the guidance and feedback I received throughout my doctoral journey. I would also like to express my profound gratefulness to Prof. Aurora Pribram-Jones for her help and motivation for the past couple years.

I would like to thank my family for their enormous support.

Finally, I would like to take a moment to appreciate my personal journey. I am grateful that I was fortunate enough and tenacious enough to overcome the challenges that lead me to this accomplishments. I appreciate my resilience which allowed me to defy the low expectations and obtain a doctoral degree.

VITA

2013	B. S. in Chemistry , Lebanese American University
2014-2016	Graduate Teaching Assistant, American University of Beirut
2016	M. S. in Chemistry, American University of Beirut
2016-2020	Graduate Teaching Assistant, University of California, Merced
2020-2021	Graduate Student Researcher, University of California, Merced
2021	Ph. D. in Chemistry, University of California, Merced

PUBLICATIONS

Abou Taka, A., Corzo, H. H., Pribram-Jones, A., Hratchian, H.P. "Good Vibrations: Calculating Excited State Frequencies Using Ground State Self-Consistent Field Models", *Submitted to The Journal of Chemical Theory and Computation* (2021)

Abou Taka, A., Lu. S.-Y., Zuehlsdorff, T., Gowland, D., Corzo, H., Pribram-Jones, A., Shi, L., Hratchian, H.P., Isborn, C. "Comparison of Linear Response Theory, Projected Initial Maximum Overlap Method, and Molecular Dynamics Based Vibronic Spectra: The Case of Methylene Blue", *Submitted to The Journal of Chemical Theory and Computation* (2021)

Corzo, H. H., **Abou Taka, A.**, Pribram-Jones, A., Hratchian, H.P. "Using Projection Operators with Maximum Overlap Methods to Simplify Challenging Self-Consistent Field Optimization", *Accepted at The Journal of Computational Chemistry* (2021)

Mason, J. L.; Harb, H.; **Abou Taka, A.**; McMahon, A.; Huizenga, C. D.; Corzo, H. H.; Hratchian, H.P. and Jarrold, C.C , "New Photoelectron-Valence Electron Interactions Evident in the Photoelectron Spectrum of Gd_2O^-", *The Journal of Physical Chemistry A* 125, 45, 9892–9903 (2021)

Mason, J. L.; Harb, H.; **Abou Taka, A.**; McMahon, A.; Huizenga, C. D.; Corzo, H. H.; Hratchian, H.P. and Jarrold, C.C , "Photoelectron spectra of $Gd_2O_2^-$ and non-monotonic photon-energy dependent variations in populations of close-lying neutral states", *The Journal of Physical Chemistry A* 125, 3, 857–866 (2021)

Abou Taka, A.; Babin, M.; Sheng, X.; DeVine, J.A.; Neumark, D.M. and Hratchian, H.P, "Unveiling the coexistence of structural isomers in the hydrolysis of ZrO_2: A combined computational and photoelectron spectroscopy study", *The Journal of Chemical Physics*, 153(24), 244308 (2020)

Devine, J.A.; **Abou Taka, A.**; Babin, M.C.; Weichman, M.L.; Hratchian, H.P. and Neumark, D.M., "High–resolution photoelectron spectroscopy of $TiO_3H_2^-$: Probing the TiO_2^- + H_2O dissociative adduct", *The Journal of Chemical Physics*, 148, 222810 (2018)

ABSTRACT OF THE DISSERTATION

Computational Studies of Metal Oxide Hydrolysis and Improved Maximum Overlap Methods

by

Ali Abou Taka
Doctor of Philosophy in Theoretical Chemistry
University of California Merced, 2021
Professor Christine Isborn, Chair

This dissertation has two main objectives. The first objective of this dissertation is to emphasize the importance of synergistic interactions between experimentalists and theorists. Such work can lead to a holistic understanding of chemical processes yielding an understanding whose whole is greater than the sum of its parts. Chapters two and three describe new insights on hydrolysis reactions at TiO_2 and ZrO_2 done in close collaboration with experimental colleagues. Studies of such metal oxides are motivated by the critical role they play in chemical catalysis and a multitude of other high-impact applications. As discussed in these two chapters, the rich spectroscopic data attained by experimentalists studying these systems can only be interpreted after engaging theoretical simulation. Interestingly, such calculations often stretch the capabilities of readily available computational models and often motivate new methodological and theoretical advancements to explore excited state computational methods.

Motivated by the titanium and zirconium studies, the second part of this dissertation evaluates a new tool for locating excited states at a ground state computational cost, which has been termed the Projection-based Maximum Overlap Method (PMOM) and Projection-based Initial Maximum Overlap Method (PIMOM). Chapter four introduces the PMOM and PIMOM methods and provides an initial demonstration of their applicability to various classes of excited electronic

states. Chapter five extends the use of the model to the evaluation of excited state molecular properties, such as optimizing excited state minimum energy structures, evaluating adiabatic excitation energies, and calculating vibrational frequencies. Chapter six presents a case where PMOM and PIMOM successfully lead to simulations of the spectrum of methylene blue, while simulations using popular time-dependent density functional theory models seemingly fail to locate a spin-pure state. Chapter seven highlights the usage of PIMOM to explore exotic electronic excited states in Lanthanides. Specifically, this chapter discusses the photoelectron spectra of Gd_2O^-.

The final chapter reviews the results of the dissertation. Examining the outcomes of that work, the final chapter also outlines potential new directions motivated by the reported research.

Chapter 1

Introduction

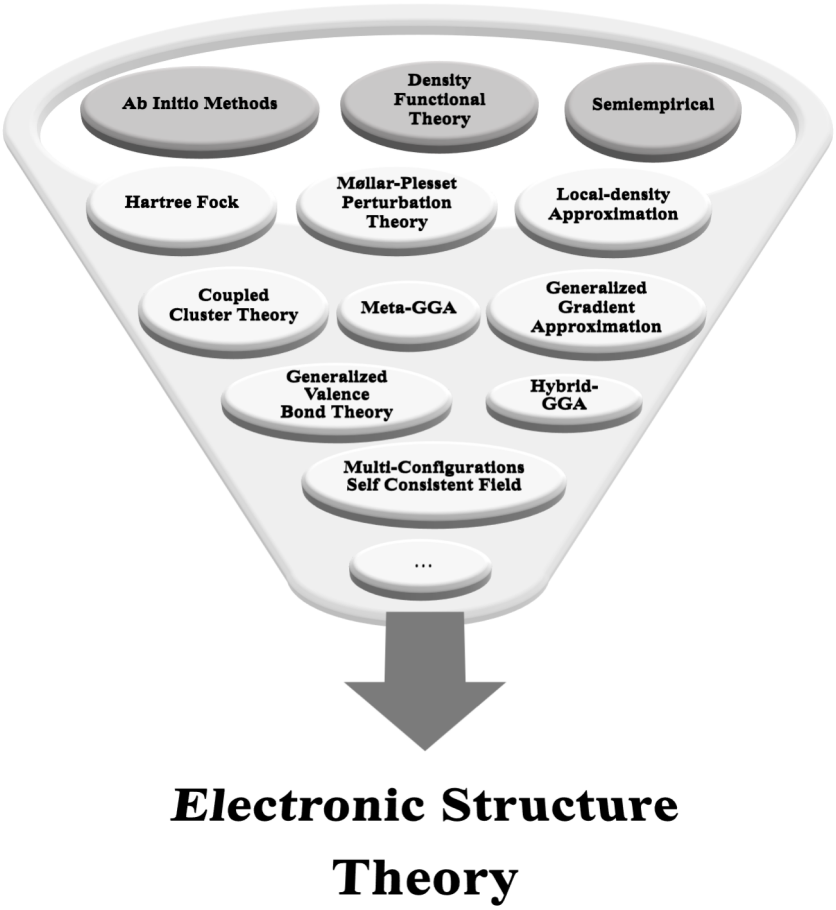

Figure 1.1: Some of the electronic structure methods that contribute to the evolvement of the electronic structure field

1.1 The Schrödinger Equation

In atoms and molecules, the description of the motion of electrons plays and important role in the understanding of their electronic structure. Exploring the electronic structure and the properties of many-electron systems can be done by means of the famous Schrödinger equation (SE), Eq. 1.1,

$$\hat{\mathrm{H}}\Psi = \mathrm{E}\Psi, \tag{1.1}$$

where $\hat{\mathrm{H}}$ is the Hamiltonian of the system, E is the energy of the system, and Ψ is the many-electron wave function. Theoretical chemists approach the above equation in two different manners, in a time-dependent and time-independent fashion. In the time-dependent fashion, the Schrödinger equation is reformulated as

$$i\hbar\frac{\partial\Psi(x,t)}{\partial t} = -\frac{\hbar^2}{2m}\frac{\partial^2\Psi}{\partial x^2} + V(x,t)\Psi(x,t), \tag{1.2}$$

where i is the imaginary unit, $\hbar$ is Planck's constant divided by 2π, and V is the potential operator. This equation demonstrates how $\Psi(x,t)$ evolves with spatial and time variation. In other words, the solutions of Eq. 1.3, the time–dependent Schrödinger equation (TDSE), describe the dynamical behaviour of the quantum mechanical system whose characteristic wave function reads

$$\Psi(x,t) = \Psi(x)e^{-iEt/\hbar}. \tag{1.3}$$

On the other hand, derivation of the time–independent Schrödinger equation (TISE) begins by assuming the separability of the space and time coordinates. By using the trial solution, Eq. 1.3, and taking the appropriate derivatives substituted in Eq. 1.2, gives:

$$E\Psi(x)e^{-iEt/\hbar} = -\frac{\hbar^2}{2m}\frac{\partial^2\Psi(x)}{\partial x^2}e^{-iEt/\hbar} + V(x)\Psi(x)e^{-iEt/\hbar}. \tag{1.4}$$

After canceling the factor exp[-iEt/$\hbar$] from both sides, the TISE reads

$$-\frac{\hbar^2}{2m}\frac{\partial^2\Psi(x)}{\partial x^2} + V(x)\Psi(x) = E\Psi(x). \tag{1.5}$$

The wave function Ψ is not an observable quantity and represent the probability amplitude of the quantum system. The square of this probability amplitude,

ψ^2, defines the probability density of finding the electrons in space. Although the wave function does not have a direct physical observable, it needs to meet some requirements to be a so-called well-behaved valid wave function. These requirements are defined as follow: i) The wave function needs to be quadratically integrable, i.e. the integral over all space of $|\psi^2|$ is finite. ii) The wave function needs to be single-valued; this is important since it does not make sense to have more than one solution for the probability of finding a particle at a certain point. iii) The wave function and its derivatives need to be continuous with no discontinuity in all regions.

1.2 Approximated Methods

Solving the TISE is usually only possible for a limited number of systems. Thus, for many systems one can only construct approximated solutions for the TISE. In what follows, two main approximations are discussed. The first approximation is related to the Variational Method, which allows to approximate the lowest ground and excited state energies. The second is the Born–Oppenheimer Approximation (BOA) [6], which assumes that the wave functions of an atomic nuclei and their electrons can be treated separately since the nucleus is much heavier than the electrons.

1.2.1 Variational Theorem

When it comes to solving the Schrödinger equation, the variational method presents an important procedure to approximate the solutions of the eigenvalue problem. The variational principle states that given a normalized wave function, $\left|\tilde{\Phi}\right\rangle$, that satisfies the appropriate boundary conditions, the expectation value for the Hamiltonian is an upper bound to the exact ground state energy,

$$\left\langle \tilde{\Phi} \right| \hat{\mathrm{H}} \left| \tilde{\Phi} \right\rangle \geq \mathrm{E}_{\mathrm{exact}}. \tag{1.6}$$

Equation 1.6 may be proven by expanding a trial wave function $\left|\tilde{\Phi}\right\rangle$, as a linear combination of real orthonormal basis functions,

$$\left|\tilde{\Phi}\right\rangle = \sum_i c_i \left|\phi_i\right\rangle . \tag{1.7}$$

Substituting Eq. 1.7 in Eq. 1.6, gives

$$\begin{aligned}
\left\langle\tilde{\Phi}\right| \hat{\mathrm{H}} \left|\tilde{\Phi}\right\rangle &= \sum_{ij} c_i c_j \left\langle\phi_i\right| \hat{\mathrm{H}} \left|\phi_{\mathrm{j}}\right\rangle \\
&= \sum_{ij} c_i c_j \mathcal{E}_j \left\langle\phi_i \mid \phi_j\right\rangle \\
&= \sum_{ij} c_i c_j \mathcal{E}_j \delta_{ij} \\
&= \sum_i |c_i|^2 \mathcal{E}_i
\end{aligned} \tag{1.8}$$

Since E_{exact} is the lowest-energy eigenvalue, $\mathcal{E}_j \geq E_{exact}$. Multiplying both sides by the non-negative $\sum_i |c_i|^2$ yields

$$\sum_i |c_i|^2 \mathcal{E}_i \geq \sum_i |c_i|^2 E_{exact}. \tag{1.9}$$

Since we are starting with orthonormal wave functions, $\langle\Phi \mid \Phi\rangle = 1$,

$$\begin{aligned}
1 &= \left\langle\tilde{\Phi} \,\middle|\, \tilde{\Phi}\right\rangle \\
&= \sum_{ij} c_i c_j \left\langle\phi_i \mid \phi_j\right\rangle \\
&= \sum_{ij} c_i c_j \delta_{ij} \\
&= \sum_i |c_i|^2
\end{aligned} \tag{1.10}$$

Therefore, $\mathcal{E}_i \geq E_{exact}$, proving that the variational solution is an upper bound solution of the exact ground state energy.

1.2.1.1 Linear Variational Problem

As stated above, the variational approximation presents an efficient approach for solving the TISE. Minimizing the energy can't be done by solving

$$\frac{\partial}{\partial c_k}\left\langle \tilde{\Phi} \left| \hat{\mathrm{H}} \right| \tilde{\Phi} \right\rangle = 0 \qquad k = 1, 2, ..., N \tag{1.11}$$

because the N parameters are not independent. However, this problem can be solved by introducing a Langrangian multiplier which yields

$$\begin{aligned} \mathcal{L}(c_1, ...c_N, E) &= \left\langle \tilde{\Phi} \left| \hat{\mathrm{H}} \right| \tilde{\Phi} \right\rangle - E\left(\left\langle \tilde{\Phi} \mid \tilde{\Phi} \right\rangle - 1 \right) \\ &= \sum_{ij} c_i c_j H_{ij} - E\left(\sum_i c_i^2 - 1 \right) \end{aligned} \tag{1.12}$$

With a normalized wave function, the added constraint to the expectation value of the Hamiltonian evaluates to zero based on Eq. 1.10. Then, the variational problem can be solved by

$$\frac{\partial \mathcal{L}}{\partial c_k} = \sum_j c_j H_{kj} + \sum_i c_i H_{ik} - 2Ec_k = 0 \tag{1.13}$$

since $\hat{\mathrm{H}}$ is a Hermitian and symmetric operator, i.e. $H_{ij} = H_{ji}$, Eq. 1.13 can be reorganized as the standard eigenvalue problem, in a matrix form,

$$\mathbf{Hc} = E\mathbf{c}. \tag{1.14}$$

1.2.2 The Born–Oppenheimer Approximation

Born and Oppenheimer suggested the concept of the "clamped nuclei" in 1927.[6] This concept was proposed based on the fact that the nucleus is much heavier than the electron, by 1838 times to be accurate. As a consequence of this fact, Born and Oppenheimer suggested the expression of the wave function, ψ_{Total}, as a product between the electronic wave function, $\psi_{electronic}$, and the nuclear wave function, $\psi_{nuclear}$. This separation further enables the separation of the Hamiltonian operator into electronic and nuclear terms. The full Hamiltonian operator is expressed as:

$$\hat{\mathrm{H}}(\mathbf{r},\mathbf{R}) = \mathcal{T}_{\mathrm{e}}(\mathbf{r}) + \mathcal{T}_{\mathcal{N}}(\mathbf{R}) + \mathcal{V}_{\mathrm{ee}}(\mathbf{r}) + \mathcal{V}_{\mathcal{N}\mathcal{N}}(\mathbf{R}) + \mathcal{V}_{\mathrm{e}\mathcal{N}}(\mathbf{r},\mathbf{R}) \tag{1.15}$$

where **r** denotes the electronic coordinates and **R** denotes the nuclear coordinates. $\mathcal{T}_e$ and $\mathcal{T}_\mathcal{N}$ are the electronic and kinetic operators. $\mathcal{V}_{ee}$ and $\mathcal{V}_{\mathcal{N}\mathcal{N}}$ are the electron-electron and nuclear-nuclear repulsion potentials while $\mathcal{V}_{e\mathcal{N}}$ is the electron-nuclear attraction potential. The electron-nuclear attraction potential, $\mathcal{V}_{e\mathcal{N}}$, is neglected based on the BOA and replaced by an indirect dependence on the coordinates of the nuclei. Thus enabling the separation of the wave function:

$$\Psi_T(\mathbf{r},\mathbf{R}) = \Psi_e(\mathbf{r};\mathbf{R})\Psi_N(\mathbf{R}) \tag{1.16}$$

As it is shown in Eq. 1.16 above, the electronic wave function depends parametrically on the nuclear coordinates. This form of dependence comes from the fact that the electrons move much faster than the nuclei; thus the geometry of the nucleus is assumed to be fixed. This enables solving the TISE for the electronic term first, where the electronic Hamiltonian is now written as:

$$\hat{\mathrm{H}}_\mathrm{e}(\mathbf{r};\mathbf{R}) = \mathcal{T}_\mathrm{e}(\mathbf{r}) + \mathcal{V}_\mathrm{ee}(\mathbf{r}) + \mathcal{V}_{\mathrm{e}\mathcal{N}}(\mathbf{r};\mathbf{R}) + \mathcal{V}_{\mathcal{N}\mathcal{N}}(\mathbf{R}) \tag{1.17}$$

We can see in Eq. 1.17, that the nuclear repulsion potential is just a constant added to the electronic Hamiltonian. After solving the electronic part of the TISE,

$$\hat{\mathrm{H}}_\mathrm{e}(\mathbf{r};\mathbf{R})\Psi_\mathrm{e}(\mathbf{r};\mathbf{R}) = \mathrm{E}_\mathrm{e}\Psi_\mathrm{e}(\mathbf{r};\mathbf{R}) \tag{1.18}$$

the nuclear part,

$$\hat{\mathrm{H}}_\mathrm{N}(\mathbf{R})\Psi_\mathcal{N}(\mathbf{R}) = \mathrm{E}\Psi_\mathcal{N}(\mathbf{R}), \tag{1.19}$$

is solved. Where the nuclear Hamiltonian, $\hat{\mathrm{H}}_\mathrm{N}$,

$$\hat{\mathrm{H}}_\mathrm{N}(\mathbf{R}) = \mathcal{T}_\mathcal{N}(\mathbf{R}) + \mathrm{E}_\mathrm{e}(\mathbf{R}) \tag{1.20}$$

include the nuclear kinetic term and the total electronic energy, which is usually referred as the potential energy surface (PES) of the system. Solving Eq. 1.19 will provide the total energy of the system that includes the electronic, vibrational, rotational, and translational energies.

1.3 Slater Determinants

The simplest way to approximate the wave function of a many-particle system is to take the product of the individual orthogonal wave functions.

$$\Psi(\mathbf{x}_1, \mathbf{x}_2, ..., \mathbf{x}_N) = \mathcal{X}_1(\mathbf{x}_1)\mathcal{X}_2(\mathbf{x}_2)...\mathcal{X}_N(\mathbf{x}_N). \tag{1.21}$$

This representation is known as the Hartree product.[7] Clearly, this approach offers a simple way for breaking down the complexity of the wave function by treating the electrons as independent particles, i.e. a mean field approach. Although this approach is appealing, it fails to satisfy the Pauli exclusion principle.[8] This comes down to the necessity of having an anti-symmetric wave function defined as:

$$\Psi(\mathbf{x}_1, \mathbf{x}_2) = -\Psi(\mathbf{x}_2, \mathbf{x}_1). \tag{1.22}$$

This hurdle can be overcome by taking a linear combination of both Hartree products such that

$$\Psi(\mathbf{x}_1, \mathbf{x}_2) = \frac{1}{\sqrt{2}} \begin{vmatrix} \mathcal{X}_1(\mathbf{x}_1) & \mathcal{X}_2(\mathbf{x}_1) \\ \mathcal{X}_1(\mathbf{x}_2) & \mathcal{X}_2(\mathbf{x}_2) \end{vmatrix}. \tag{1.23}$$

The generalization of the above equation was proposed by Slater in 1929.[9] Taking into account the anti-symmetric nature of the many-electron wave function, the Slater determinant is written as

$$\Psi(\mathbf{x}_1, \mathbf{x}_2, ..., \mathbf{x}_N) = \frac{1}{\sqrt{N!}} \begin{vmatrix} \mathcal{X}_1(\mathbf{x}_1) & \mathcal{X}_2(\mathbf{x}_1) & ... & \mathcal{X}_N(\mathbf{x}_1) \\ \mathcal{X}_1(\mathbf{x}_2) & \mathcal{X}_2(\mathbf{x}_2) & ... & \mathcal{X}_N(\mathbf{x}_2) \\ \vdots & \vdots & \ddots & \vdots \\ \mathcal{X}_1(\mathbf{x}_N) & \mathcal{X}_2(\mathbf{x}_N) & ... & \mathcal{X}_N(\mathbf{x}_N) \end{vmatrix}, \tag{1.24}$$

which is often written in a compact way as

$$\Psi(\mathbf{x}_1, \mathbf{x}_2, ..., \mathbf{x}_N \equiv |\mathcal{X}_1, \mathcal{X}_2, ..., \mathcal{X}_N\rangle \equiv |1, 2, ..., N\rangle\,, \tag{1.25}$$

where the normalization constant is omitted and implied by noting the number N. It can be shown that the Slater determinant obeys the the anti-symmetry requirement since exchanging two rows, which is equivalent to exchanging two electrons, would change the sign of the determinant, and consequently the sign the wave function.

1.4 Orbitals and Basis Sets

In section 1.2.1, we expanded the wave function in Eq. 1.7 as a linear combination of basis functions. In principle the wave function is a mathematical function that describes the behaviour of electrons in the quantum system. Electrons are mainly described by two characteristics, their spatial distribution and their spin nature. The spatial distribution is given by the probability of finding the electron in a small volume, defined as, $|\psi(\mathbf{r})|^2$. This brings us to define the spatial orbital, $\psi(\mathbf{r})$, which is a function of the position vector $\mathbf{r}$. The spatial molecular orbitals, since we are mainly interested in molecules, are usually assumed to be orthogonal, i.e.

$$\langle \psi_i(\mathbf{r}) \mid \psi_j(\mathbf{r}) \rangle = \delta_{ij}. \tag{1.26}$$

By assuming a complete set of the spatial orbitals $\{\psi_i\}$, we can expand an arbitrary function, $f(\mathbf{r})$, as

$$f(\mathbf{r}) = \sum_{i}^{\infty} c_i \psi_i(\mathbf{r}) \tag{1.27}$$

where c_i are constant coefficients. Eq. 1.27 can not be applied in practice, since we can not work with infinite set. Instead, the summation is terminated at a certain number, K, such that the finite set spans a region that is enough to accurately describe electrons in the orbitals, for which we can say that this finite set is exact in the subspace spanned.

The second component for accurate description of the electron is their spin nature, i.e., spin up, α, and spin down, β. Now combining these two characteristics, we introduce the wave function, $\mathcal{X}(\mathbf{x})$, that contains both the space and spin coordinates. Since there are two options for the spin orbital, α or β, the wave function is now defined as

$$\mathcal{X}(\mathbf{x}) = \begin{cases} \psi(\mathbf{r})\alpha(\omega) \\ \psi(\mathbf{r})\beta(\omega) \end{cases} . \tag{1.28}$$

The molecular wave function is further decomposed into a linear combination of atomic orbitals (LCAO).

$$\psi_i(\mathbf{r}) = \sum_{\mu}^{N} C_{\mu i} \phi_\mu(\mathbf{r}) \tag{1.29}$$

This brings us to the concept of the basis set that is used in quantum computational chemistry. Two types of basis functions are commonly used in electronic structure calculations: Slater Type Orbital (STO) and Gaussian Type Orbital (GTO). Slater proposed the usage of exponential functions as atomic basis functions in 1930,[10]

$$\chi_{\zeta,n,l,m}(r,\theta,\phi) = NY_{l,m}(\theta,\phi)r^{n-1}e^{-\zeta r}, \tag{1.30}$$

where N is a normalization constant and $Y_{l,m}(\theta,\phi)$ are spherical harmonic functions. The exponential part of these functions is based on Hydrogen-like orbitals; thus, there are not radial nodes inherited in this representation. This drawback can be overcome but taking a linear combination of STOs. However, this will increase the computational cost to a point where it becomes limited to small systems.
In 1950, S.F Boys, proposed the usage of GTOs. GTOs brought speed and feasibility for carrying out large molecular systems and can be written in polar or cartesian coordinates, [11, 12]

$$\chi_{\zeta,n,l,m}(r,\theta,\phi) = NY_{l,m}(\theta,\phi)r^{2n-2-l}e^{-\zeta r^2} \tag{1.31}$$

$$\chi_{\zeta,l_x,ly,l_z}(x,y,z) = Nx^{l_x}y^{l_y}z^{l_z}e^{-\zeta(x^2,y^2,z^2)}, \tag{1.32}$$

where the sum of l_x, l_y, and l_z determines the type of the orbital. For example a sum of $l_x + l_y + l_z = 2$ resembles a d-orbital.
Although GTOs are much computationally faster to compute, they suffer from two major challenges.[13] First, at the nucleus, GTOs do not have the cusp that STOs show, but it rather they have a zero slope. Second, GTOs fall off too fast far from the nucleus and lacks the tail-behaviour that STOs have.
Minimizing and overcoming these challenges is done by taking a linear combination of a GTOs, primitive functions, each with a different values of ζ to give a contracted Gaussian function.[14]

$$g_c = \sum c_i g_p \tag{1.33}$$

where g_c is a contracted Gaussian, g_p is a primitive Gaussian, and c_i is a contraction coefficient.

Basis set equations taking the form of STO-nG (where n is the number of GTOs combined) are considered to be minimal basis sets. Although basis sets with $n = 2 - 6$ have been derived, it has been found that $n = 3$ (STO-3G) gives reliable results, considering the minimal basis sets as adding more primitive Gaussian Type Orbital (PGTO)s add a very little improvement.[15]

Bigger basis sets, beyond the STO-nG family, is needed to accurately describe molecular systems and obtain reliable results. The most popular families of basis sets are the so-called Pople basis sets and the Dunning basis sets.[16, 17, 18, 19, 20, 21]

The Pople basis set are known for being of split-valence nature and generally of the form k-nlmG.[16, 17] Where k represents the number of sp-type inner shell PGTOs. nlm indicate the how many functions are the valence electrons split into, nl for double zeta split, and nlm for triple zeta split, and how many PGTOs are used in primitive GTOs. For example, 6-31G means there are 6 PGTOs allocated for core electrons, the inner part of the valence electrons is a contraction of 3 PGTOs, and the outer valence is represented by one PGTO. Whereas a 6-311G basis set is an example of a triple zeta split valence basis set, where the valence electrons are split into three functions, Three GTOs for contracted valence orbitals, and two sizes of GTO for extended valence orbitals. Pople's basis sets also can be increased by adding polarization (+) and diffuse functions (*) to better describe some systems such as anions, excited states, and charge transfer states. In polarization, additional functions are added to describe polarization of the electron density of the atom in molecules to add flexibility to the basis set. While adding diffuse functions is done by adding Gaussian basis functions with a small exponents that will extra flexibility to the tail portion of atomic orbitals.

On the other hand, Dunning correlation-consistent basis set are denoted by cc-pVXZ (where X= D, T, Q, 5, 6, 7). These bases set were designed to recover correlation energy.[18, 19, 20, 21] Dunning's basis sets converge smoothly toward the complete (infinite) basis set limit. Polarization functions are included in the definition, (p), and diffuse functions can be added by using the prefix "aug". For example, aug-cc-pVTZ indicate a polarized valence triple zeta basis set augmented

with diffuse functions.

In general, care must be taken when choosing which basis set is suitable for the system under investigation. For example, anions, excited states, and Rydberg states may need polarized and diffuse functions to have a better description of the orbitals and reliable results. Thus, one should consider how much time it would take to run the molecule and use the basis set that represents the best compromise between computational efficiency and level of accuracy.

1.5 Ground State Methods

Majority of the quantum chemical problems are addressed in the frame of ground state calculations. The ground state of a quantum mechanical system is defined as the lowest energy-state. Locating such state, or states if they are degenerate, is done by efficiently solving the TISE within specific approximations. Depending on the system and the computer resources available for the calculation , one can choose from a range of different computational approaches that lies within single or multi-reference, wave function or density based methods.

1.5.1 Hartree-Fock Theory

The Hartree–Fock (HF) approximation is a central approximation in quantum chemistry. It is a single reference method, i.e the wave function is approximated by a single Slater determinant of N spin-orbitals, Eq. 1.25. The HF approximation makes use of the variational principle to minimize the electronic energy such that

$$\begin{aligned} E_0 &= \langle \Psi_0 \left| \mathcal{H} \right| \Psi_0 \rangle \\ &= \sum_i \langle i \left| h \right| i \rangle + \frac{1}{2} \sum_{ij} \langle ij \mid\mid ij \rangle \\ &= \sum_i \langle i \left| h \right| i \rangle + \frac{1}{2} \sum_{ij} \Big[\langle ij \mid ij \rangle - \langle ij \mid ji \rangle \Big] \end{aligned} , \tag{1.34}$$

where $\sum_{ij} \left[\langle ij \mid ij \rangle \right]$ is the coulomb term and $\sum_{ij} \langle ij \mid ji \rangle$ is the exchange integral that arises from the anitisymmetric nature of the single determinant. It is important to mention that, unlike the coulomb term, the exchange term has no classical

analogous. The coulomb operator is defined as

$$\mathcal{J}_i(1)(\mathcal{X}_\rangle(1) = \left[\int dx_2\ \mathcal{X}_j^*(2) r_{12}^{-1} \mathcal{X}_j(2)\right] \mathcal{X}_i(1)\big] = \langle ij \mid ij\rangle\,, \tag{1.35}$$

and the exchange operator is defined as

$$\mathcal{K}_i(1)(\mathcal{X}_\rangle(1) = \left[\int dx_2\ \mathcal{X}_j^*(2) r_{12}^{-1} \mathcal{X}_i(2)\right] \mathcal{X}_j(1) = \langle ij \mid ji\rangle\,. \tag{1.36}$$

The HF energy is minimized using a Langranian multiplier by imposing a constraint that the spin orbitals remain orthonormal,

$$\mathcal{L}[\mathcal{X}_i] = E_0[\mathcal{X}_i] - \sum_{ij} \epsilon_{ij}[\langle i \mid j\rangle - \delta_{ij}]. \tag{1.37}$$

Taking the first variation of the Langrangian, $\delta\mathcal{L}$, and after some mechanical derivations, we get

$$\begin{aligned}\delta\mathcal{L}[\mathcal{X}_i] &= \sum_i \langle \delta i| \left[\left(h + \sum_j \mathcal{J}_i - \mathcal{K}_j\right)|i\rangle - \sum_j \epsilon_{ij}\,|j\rangle\right] + \text{complex conjugate.} \\ &= 0\end{aligned} \tag{1.38}$$

With the arbitrary variation, δi, the quantity in square brackets must be zero. Thus, giving

$$\left[h + \sum_j \mathcal{J}_j - \mathcal{K}_j\right]|i\rangle = \sum_j \epsilon_{ij}\,|j\rangle\,, \tag{1.39}$$

where the Fock operator, f is defined by the quantity in brackets. Thus, the so-called HF potential may be defined as

$$\mathcal{V}^{HF}(x_i) = \sum_j \mathcal{J}_j(x_i) - \mathcal{K}_j(x_i). \tag{1.40}$$

The HF potential represent the average field experienced by the i-th electron due to the presence of the remaining electrons.

The result of Eq. 1.39 is not quite the eigenvalue problem that we are interested in solving. However, a simple reformation of Eq. 1.39 can be done using a unitary transformation. A new set of spin orbitals, $\mathcal{X}_i^{'}$, is defined by a unitary transformation,

$$\mathcal{X}_i^{'} = \sum_j \mathcal{X}_j U_{ji} \tag{1.41}$$

and a new set of the matrix $\epsilon^{'}$ is also defined as

$$\epsilon^{'}{}_{ij} = \sum_{lk} U^{*}_{li} \epsilon_{ij} U_{jk} \tag{1.42}$$

using Eqs. 1.41 and 1.42, we define the canonical eigenvalue HF equation

$$f^{'} \left| i^{'} \right\rangle = \epsilon^{'} \left| i^{'} \right\rangle \tag{1.43}$$

It is important to mention that the Fock operator is invariant to the unitary transformation of the spin-orbitals.

1.5.1.1 Restricted Closed-Shell Hartree-Fock

We discussed in the previous section the formal derivation of the HF equations. In 1951, Roothan and Hall transformed the HF equation into a more computationally feasible form.[22, 23] For a closed-shell system, they assumed a spin restricted formalism, which means that α and β are constrained to have the same spatial orbital.

Since the spatial and the spin components of the wave functions are orthonormal, we can integrate out the spin coordinates defining the closed-shell restricted HF equations

$$f(r_1)\psi_i(r_1) = \epsilon_i \psi_i(r_1) \qquad i = 1, 2, ..., N/2. \tag{1.44}$$

The closed-shell Fock operator has the form,

$$f(r_1) = h(r_1) + \sum_{i}^{N/2} 2J_i(r_1) - K_i(r_1). \tag{1.45}$$

The contribution of Roothaan was showing that the spatial MO, ψ_i, can be expanded as a linear combination of atomic orbitals

$$|\psi_i\rangle = \sum_{\mu} C_{\mu i} |\phi_\mu\rangle \,, \tag{1.46}$$

using Eq. 1.46, the HF equations can be rewritten as

$$f \sum_{\nu} C_{\nu i} |\phi_\nu\rangle = \epsilon_i \sum_{\nu} C_{\nu i} |\phi_\nu\rangle \,. \tag{1.47}$$

Left multiplying of Eq. 1.47 by $\langle\phi_\mu|$ yields

$$\langle\phi_\mu| f \sum_\nu C_{\nu i} |\phi_\nu\rangle = \epsilon_i \sum_\nu C_{\nu i} \langle\phi_\mu \mid \phi_\nu\rangle . \tag{1.48}$$

Defining the Fock matrix element, $F_{\mu\nu}$, and the overlap matrix element, $S_{\mu\nu}$, Eq. 1.48 can be rewritten as

$$\sum_\nu F_{\mu\nu} C_{\nu i} = \epsilon_i \sum_\nu C_{\nu i} S_{\mu\nu}, \tag{1.49}$$

and more compactly, the Roothaan equations in a matrix form is

$$\mathbf{FC} = \mathbf{SC}\epsilon. \tag{1.50}$$

1.5.1.2 Unrestricted Hartree-Fock

Since no all systems are closed-shell, we need a more generalized form that can accommodate open-shell system. Thus, the spin-orbitals are no longer spatially constrained,

$$\mathcal{X}_\rangle(\mathbf{x}) = \begin{cases} \phi_i^\alpha(\mathbf{r})\alpha(w) \\ \phi_i^\beta(\mathbf{r})\beta(w). \end{cases} \tag{1.51}$$

Since α and β spin functions can't be exchanged, after integrating out spin, the Fock operators are defined as

$$f^\alpha(r_1) = h(r_1) + \sum_i^{N^\alpha} \left[J_i^\alpha(r_1) - K_i^\alpha(r_1)\right] + \sum_i^{N^\beta} J_i^\beta(r_1) \tag{1.52}$$

for the α electrons and

$$f^\beta(r_1) = h(r_1) + \sum_i^{N^\beta} \left[J_i^\beta(r_1) - K_i^\beta(r_1)\right] + \sum_i^{N^\alpha} J_i^\alpha(r_1) \tag{1.53}$$

for the β electrons. Using a similar mechanical derivations outlined in the previous section, we can define the two matrix equations for the α and β orbitals,

$$\mathbf{F}^\alpha\mathbf{C}^\alpha = \mathbf{SC}^\alpha\epsilon^\alpha \tag{1.54}$$

$$\mathbf{F}^\beta\mathbf{C}^\beta = \mathbf{SC}^\beta\epsilon^\beta. \tag{1.55}$$

The above two equations define the unrestricted HF equations which are also known by the Pople-Nesbet HF equations.[24]

Key Remarks Beside dealing with open-shell systems, UHF, unlike RHF, is known to capture the correct behaviour of bond breaking dissociation limit. Since the α and β molecular orbitals (MOs) are not spatially constrained. Thus, as the bond is stretched, the spatial degeneracy is broken and the electrons can localize into the molecular fragments.

This correction obtained through utilizing UHF comes with the price of the so-called spin contamination. Once the MOs spatial symmetry is broken, the wave function is no longer spin pure giving rise to the well-known Löwdin's *symmetry dilemma*. In other words, we know the exact solution (lowest energy solution) will have certain symmetries, but if we include these symmetries in our approximated variational Hamiltonian, we can only raise the energy and not lower it. Thus, one may use UHF broken symmetry solutions for the sake of lowering the energy towards the exact energy.

The amount of spin contamination is measured by the expectation value of the S^2 operator, $\langle S^2 \rangle$. For a spin pure systems, $\langle S^2 \rangle$ is defined as

$$\left\langle S^2 \right\rangle = S_z(S_z + 1), \tag{1.56}$$

where $S_z = \frac{n_\alpha - n_\beta}{2}$. For example, $\langle S^2 \rangle$ for a singlet would be 0, $\langle S^2 \rangle = 0$ $(0+1)$, and $\langle S^2 \rangle$ for a doublet would be 0.75, $\langle S^2 \rangle = 0.5$ $(0.5 + 1)$. A spin contaminated state will always have a $\langle S^2 \rangle$ value larger than the spin pure value, which is attributed to the contamination of higher spin states, such as triplets and quintets contaminants in singlet spin states.

On the other hand, the UHF $\langle S^2 \rangle$ is defined as

$$\left\langle S^2 \right\rangle = S_z(S_z + 1) + n_\beta - \sum_{i\bar{j}}^{n_{occ}} (S_{i\bar{j}})^2, \tag{1.57}$$

where n_β is the number of beta electrons, and the last term is the $\alpha - \beta$ overlap. In the case of RHF calculation, i.e, for spin pure state, the overlap will evaluate to n_β; thus $\langle S^2 \rangle$ evaluates to $S_z(S_z + 1)$.

1.5.2 Post HF Methods

The Hartree-Fock method is known to capture 99% of the exact energy. However, that last 1% is still important for quantitatively describing interesting chemistry. This 1% is attributed to correlation energy.[25]

$$E_{\text{corr}} = E_{\text{exact}} - E_{\text{RHF}} \tag{1.58}$$

There are two types of correlation energies. The first type is the Coulomb correlation energy. This energy describes the interaction between the spatial position of electrons due to their Coulomb repulsion, which is important in describing some systems. The other type is the Fermi correlation, which prohibits two electrons of the same spin to be present at the same space and time. This is inherited in the definition of the Slater determinant. Thus, the correlation energy presented in Eq. 1.58 is solely coming from the Coulomb correlation energy.
Accounting for some of the correlation energy is usually done by employing post Hartree-Fock methods, such as, but not limited to, nth–order Møller–Plesset perturbation theory (MPn), Coupled Cluster (CC), and Configuration Interaction (CI).

1.5.2.1 Configuration Interaction

The HF method is a single-determinant mean field aproximation. This means that only one reference determinant and average electron potential is used to compute the electronic energy. Imagine now that the wave function is defined by one Slater determinant expanded to generate multiple determinants by permuting electrons to the virtual space. This expansions will generate the different configurations needed to correctly characterize and recover the electronic correlation of the system under study. This procedure for recovering the electronic correlation is known as Configuration Interaction. The CI expansion is variational, and if the expansion is complete and a large enough basis set is used, then the Full Configuration Interaction (FCI) energy is defined. The FCI energy is defined as the exact energy which fully includes all non-relativistic correlation energy effects. Obviously, this result is amazing, but unfortunately, FCI is impractical for more than half

dozen of electrons. Therefore, the CI expansion is usually truncated after some order of orbital permutation or "excitation". For example, if only single electron permutations or excitations are considered, the configuration interaction singles (CIS) is defined, whereas if single and double permutations are considered then, the configuration interaction singles and doubles (CISD) is defined. This process can continue until all the N permutations in M orbitals are considered, CISDT, CISDTQ, ..., CISDTQ-N. Thus, in its cluster form the FCI [25] expansion may be written as

$$\Psi^{FCI} = D_0 c_0 \quad + \sum_i \sum_a D_i^a c_i^a + \sum_{i<j} \sum_{a<b} D_{ij}^{ab} c_{ij}^{ab} \tag{1.59}$$

$$+ \sum_{i<j<k} \sum_{a<b<c} D_{ijk}^{abc} c_{ijk}^{abc} + \cdots , \tag{1.60}$$

where the indices i, j, k denote occupied spin-orbitals or Dirac bi-spinors, whereas the a, b, c indices represent the corresponding unoccupied (virtual) one-electron functions, and $D_{ijk\ldots}^{abc\cdots}$ represent the Slater determinants. The finite CI expansion consisting on the formation of all possible Slater determinants for the one-electron functions to form, in a variational manner, the so-called FCI expansion coefficients, $c_{ijk\ldots}^{abc\ldots}$. As we see in Eq. 1.59, for this determinant expansion the cost increases factorially. To be accurate, we have 2K spin orbitals, where K is the number of spatial orbitals. The number of electrons is N which leave us with 2K - N virtual orbitals. If we have n-tuple excitations, then the total number of configurations will be

$$\binom{N}{n}\binom{2K-N}{n}, \tag{1.61}$$

which restricts the application of Full CI only for small to medium systems with limited number of basis functions. Thus, truncation of the wave function is needed to capture some of the correlation energy and still afford the calculation. The two most famous truncated CI are singly-excited states (CIS) and singly and doubly-excited states (CISD).

Although the truncated CI approach provide a way to recover correlation energy, it is not size consistent, i.e., the energy of a system (AB) should be equal to the

sum of the energy A + B at non-interacting distance.[26] Another violation is the size-extensivity requirement for which the energy should scale linearly with the number of electrons.[27, 28] This last however, may be less important for the FCI approximation than for other approximations since in FCI the size-extensivity requirement can be over come by the variational upper bound error sensibility analysis[29, 30].

1.5.2.2 Coupled Cluster

Coupled Cluster theory was introduced in the late 1960s by Čižek and Paldus. [31, 32, 33] It has been known to be one of the most reliable and computationally affordable methods to approximate FCI correlated solutions. The main idea in CC theory is the ground state wave function, $|\psi_0\rangle$, is given by an *exponential* ansatz

$$|\psi_{CC}\rangle = e^{\hat{T}} |\psi_0\rangle , \tag{1.62}$$

where $e^{\hat{T}}$ is expanded as

$$e^{\hat{T}} = 1 + \hat{T} + \frac{\hat{T}^2}{2!} + \frac{\hat{T}^3}{3!} + ... + \frac{\hat{T}^N}{N!}, \tag{1.63}$$

and $\hat{T}$ is the excitation operator and it can be written as a linear combination of single, double, triple, etc excitations, up to N-fold excitations for an N electron system

$$\hat{T} = \hat{T}_1 + \hat{T}_2 + \hat{T}_3 + ... + \hat{T}_N, \tag{1.64}$$

where

$$\hat{T}_1 |\Phi_0\rangle = \sum_{i}^{occ} \sum_{a}^{virt} t_i^a \phi_i^a, \tag{1.65}$$

and

$$\hat{T}_2 |\Phi_0\rangle = \sum_{i>j}^{occ} \sum_{a>b}^{virt} t_{ij}^{ab} \phi_{ij}^{ab}. \tag{1.66}$$

The coefficients, t_i^a, t_{ij}^{ab}, ..., of the determinants are called amplitudes.
The orders of the excitations in Eq. 1.63 can be rearranged and written as

$$e^{\hat{T}} = 1 + \hat{T}_1 + \left(\hat{T}_2 + \frac{1}{2}\hat{T}_1^2\right) + \left(\hat{T}_3 + \hat{T}_1\hat{T}_2 + \frac{1}{6}\hat{T}_1^3\right) + ..., \tag{1.67}$$

it can be seen in Eq. 1.67 that there is one way to form single excitations, but there are two ways for the doubles; a pure double excitation, $\hat{T}_2$, or by two successive single excitations, $\hat{T}_1\hat{T}_1$, where the second term is referred to disconnected doubles and disconnected excitations. Thus recovering the size-extensivity property that is lost in truncated CI. CC is usually also truncated as in CI, for which the CCSD refers to CC with single and double excitations.[34] Also another famous truncated CC is CCSDT, where it also includes triple excitations.[35] Including the full triple excitations increases the computational from N^6 in CCSD to N^8 and can be prohibitive in many systems. An approximation can be enforced to include the triple excitations in a perturbative fashion leading to the rise CCSD(T) that showed high accuracy in calculating a variety of molecular properties.[36, 37, 38]

1.5.2.3 Møller–Plesset Perturbation Theory

Perturbation theory comes in hand as a solution to recover electron correlation. There are different orders of perturbations, for which MP2 is the most commonly used and will be discussed here.[39] The Hamiltonian in now defined as the HF Hamiltonian (H_0) plus some perturbation in the form of a fluctuation potential,

$$H = H_0 + \lambda V, \tag{1.68}$$

where λ is a dimensionless parameter. Expanding the Energy and the wave function as a function of λ,

$$E = E^{(0)} + \lambda^1 E^{(1)} + \lambda^2 E^{(2)} + ... \tag{1.69}$$

and

$$\Psi = \Psi_0 + \lambda^1 \Psi^{(1)} + \lambda^2 \Psi^{(2)} + ... \,. \tag{1.70}$$

After doing some Algebra, we get that $E^{(0)}$ reads

$$E^{(0)} = \langle \Psi_0 \, | H_0 | \, \Psi_0 \rangle \,. \tag{1.71}$$

Which is the energy obtained from the Fock operator. To get the HF energy, we add the first perturbed energy, $E^{(1)}$, that is defined as

$$E^{(1)} = \langle \Psi_0 \, | V | \, \Psi_0 \rangle \,. \tag{1.72}$$

Thus the HF energy is

$$E_0 = E^{(0)} + E^{(1)} \tag{1.73}$$

Adding the higher terms of E will basically start accounting for the correlation energy.

$$E_{corr} = E^{(2)} + E^{(3)} + E^{(3)} + ... \ . \tag{1.74}$$

The first term in Eq. 1.74 is the MP2 correlation energy. The total MP2 energy is given by

$$E_{MP2} = E_{HF} - \frac{1}{4} \sum_{ab}^{N_{virt}} \sum_{ij}^{N_{occ}} \frac{|\langle ab| |ij\rangle|^2}{\epsilon_a + \epsilon_b - \epsilon_i - \epsilon_j}. \tag{1.75}$$

1.5.3 Density-Based Methods

It is fair to say that Density Functional Theory (DFT) is by far the most widely used electronic structure method to study different chemical systems. Not until 1990s, when DFT started emerging into quantum-chemical applications after paving its way in solid-state physics in 1970s. The strength of DFT is in its auspicious cost-accuracy ratio compared with more expensive correlated methods such as post-HF methods such as CCSD and MP2.

1.5.3.1 The Hohenburg-Kohn Theorems

In principle, the external potential, i.e. the positions of the nuclei, determines the properties of the system. The question that is raised here is, is this also true for the density?

To answer that, Hohenburg and Kohn came up with two theorems that prove that the density is enough to determine the ground state properties of the system.[40]

The first theorem states that *the external potential is a unique functional of the electron density in the ground state, and therefore the total energy is also a functional of the ground state electron density.* A consequence of the first Hohenberg-Kohn theorem is that all properties of a system are determined from only the ground state electron density,

$$E[\rho(\mathbf{r})] = \int \rho(\mathbf{r}) v_{ext}(\mathbf{r}) d\mathbf{r} + F[\rho(\mathbf{r})], \tag{1.76}$$

where $v_{ext}(\mathbf{r})$ is the external potential and $F[\rho(\mathbf{r})]$ is an unknown universal functional of the electron density $\rho(\mathbf{r})$ only.

The second theorem states that the ground state energy of the system obtained by the functional will give the lowest energy if and only if the input density is the true ground-state density. In other words, it establishes the variational theorem. That's said, for a given trial electron density, ρ_t, the energy obtained using the trial density will result in an upper bound of the true energy, $E[\rho] \geq E_0$.

The two theorems give rise to the fundamental statement of DFT

$$\delta\Big[E[\rho] - \mu\big(\int \rho(\mathbf{r})d\mathbf{r} - N\big)\Big] = 0. \tag{1.77}$$

Eq. 1.77 illustrastes that the ground state energy of a many-electron system can be obtained by minimising the energy functional, Eq. 1.76, subject to the constraint that the number of electrons, N, is conserved.

1.5.3.2 The Kohn-Sham Method

In Kohn-Sham (KS) DFT formulation, the system is studied based on mapping the fully interacting system onto an auxiliary non-interacting system that yields the exact ground state density represented by a single Slater determinant. [41, 42]

The density of the system is defined as

$$\rho(\mathbf{r}) = \sum_{i}^{N_{occ}} |\phi_i^2|. \tag{1.78}$$

The KS Fock operator, $\hat{f}_{KS}$, can be defined by the sum of an effective one-electron potential and the kinetic energy of the non-interacting system,

$$\hat{f}_{KS} = \hat{T}_s + \hat{V}, \tag{1.79}$$

where the kinetic operator, $\hat{T}_s$, is similar to the HF kinetic term. The local potential, $\hat{V}$, can be decomposed into three terms as follow:

$$\hat{V} = \hat{J} + \hat{V}_{XC} - \hat{V}_{Ne}, \tag{1.80}$$

where $\hat{J}$ and $\hat{V}_{Ne}$ are the regular Coulomb operator and the nuclear-electron attraction operator. $\hat{V}_{XC}$ is the exchange-correlation potential defined as

$$\hat{V}_{XC} = \frac{\partial E_{XC}[\rho(\mathbf{r})]}{\partial \rho(\mathbf{r})}, \tag{1.81}$$

where E_{XC} is the exchange-correlation energy which can be expanded as

$$E_{XC}[\rho] = T[\rho] - T_s[\rho] + V_{ee}[\rho] - J[\rho]. \tag{1.82}$$

This added energy corrects the kinetic energy due to the interacting nature of the electrons in the system as well as it accounts for the electron-electron repulsion. The exchange-correlation energy ensures the exactness of DFT.[42] However, until this day, there is no exact form for this term, rather different approximations that have shown a great success.

The KS Fock operator in Eq. 1.79 can be used to formulate the DFT problem in a similar fashion to the HF one. Thus the eigensystem will have the form

$$\left[\hat{T}_s + \hat{V}\right]\psi_i(\mathbf{r}) = \epsilon_i \psi_i(\mathbf{r}). \tag{1.83}$$

1.5.3.3 Exchange-Correlation Functionals Flavors

As mentioned in the previous section, the exchange-correlation function is unknown. Different functionals are proposed in the literature to tackle this problem and several approximations are formulated. There are five principal classes of functionals that have been proposed. The first and oldest functional is the local density approximation (LDA). This functional is based on the local electron density and was proposed by Hohenberg and Kohn in their original DFT work.[41] LDA has shown to work well for solid state calculations, however its success does not apply to chemical and molecular problems. An extension of the LDA was also proposed by Perdew and co-workers and is called the generalised gradient approximation (GGA). [43] In GGA, the electron density and its gradient are considered in evaluating exchange-correlation functional. A further improvement to GGA is the inclusion of the kinetic energy density which involves derivatives of the occupied Kohn-Sham orbitals. This funstional is referred to as meta-GGA.[44, 45]

A different class of functional was proposed by ti83 in 1992, ti83's functionals are often referred to as hybrid functionals that linearly combine GGA and exact HF exchange.[46] Finally, we have the double-hybrid functionals that combine an MP2-like correlation with exact HF exchange with to a DFT calculation.

1.6 Excited State Methods

We have discussed in the previous chapter the main methods used to study molecular system at the ground state level. However, interesting chemistry also happens at the excited state level, making it really important to develop methods that are well suited to address these kind of problems. Unlike the small set of methods mainly used in conducting ground state calculations, a wide range of various excited state methods are established in the literature. In what follow, I will be discussing a couple of excited state methods that are grouped into two categories, single-reference methods and multi-reference methods.

1.6.1 Single-Reference Methods

There are a large number of single-reference approaches floating in the literature such as configuration-interaction singles (CIS),[47] CIS with doubles (CISD),[34] time dependent Density Functional Theory (TD-DFT), [48, 49] Equation-of-Motion Coupled Cluster (EOM-CC),[50, 51] Symmetry-Adapted Cluster-Configuration Interaction (SAC-CI), [52] Linear Response Coupled Cluster (LR-CC),[53] Constrained DFT,[54] many-body Green's functions methods,[55] and more.
Before going into the details of single-reference methods, let us point out the difference between the two terms single-reference and single-determinant. The Single-reference framework refers to a method that is based on a reference state approximated by a single determinant. Such definition includes methods such as CIS and TD-DFT, where the excited states in these methods are formed as single determinants.

1.6.1.1 Configuration-interaction Singles

The simplest CI approach can be achieved by truncating the expansion at single excitations to get the so-called CIS. In the CIS approach we use orbitals of the Hartree-Fock wave function to generate all singly excited final configuration using only one determinant. A linear combination of the singly excited determinants will form the CIS wave function,

$$\Psi_{CIS} = c_0\Phi_0 + \sum_{ia} c_i^a \Phi_i^a, \tag{1.84}$$

where singly substituted determinants are constructed by replacing an occupied orbital in the ground state (i, j, k,...) with a virtual orbital in the ground state (a, b, c,..). The coefficients, c_i^a, are determined by diagonalizing the Hamiltonian matrix in the basis of the ground state determinant, Ψ_0 and the singly excited determinant, Ψ_1. Thus leading to the following matrix eigenvalue problem:

$$\begin{pmatrix} \langle \Psi_0 \left| H \right| \Psi_0 \rangle & \langle \Psi_0 \left| H \right| \Psi_i^a \rangle \\ \langle \Psi_i^a \left| H \right| \Psi_0 \rangle & \langle \Psi_i^a \left| H \right| \Psi_i^a \rangle \end{pmatrix} \begin{pmatrix} c_0 \\ c_i^a \end{pmatrix} = \mathcal{E}_0 \begin{pmatrix} c_0 \\ c_i^a \end{pmatrix}. \tag{1.85}$$

According to the Brillouin's theorem, singly excited determinants, Ψ_i^a, do not interact directly with a reference HF determinant,Ψ_0. Thus, the mixing of the two states, the off-diagonal element, do not contribute to the energy. Thus,

$$\langle \Psi_0 \left| H \right| \Psi_i^a \rangle = 0. \tag{1.86}$$

The excitation energy is simply the difference between HF ground state energy and CIS excited state energies.

The CIS method has some appealing features. It is relatively fast compared to other methods, that is as $\mathcal{O}(N^4)$ with a prefactor that can impose computational challenges with large systems. Also, CIS is a variational method, so the energy obtained through CIS represents an upper bound of the true energy. Finally, since CIS allow positive and negative combination of α and β excitations from one doubly occupied orbital, CIS can obtain spin pure singlets and triplet states for closed-shell systems.

On the other hand, CIS has some major disadvantages such as the overestimation of excitation energies by 0.5 - 2 eV.[56, 57] This can be attributed to the fact that the wave function demands doubly and higher excited determinants to have a better flexibility and description within the canonical HF orbitals. Also this error can be attributed to the absence of electron correlation within the CIS method. Moreover, CIS violates the Thomas-Reiche-Kuhn dipole sum rule, which requires the sum of transition dipole moments to be equal to the number of electrons.[58]. Furthermore, due to the nature of the CIS formalism, CIS is incapable of describing double excitations.

1.6.1.2 TD-DFT

TD-DFT is an extension of DFT which is used to investigate properties of systems in the presence of time-dependent potentials, such as electric or magnetic fields. In 1984, Runge and Gross provided a formal foundation for TD-DFT.[59] In their work, they presented a defined mapping between the time-dependent external potential of a system and its time-dependent density. Within the same framework used in ground state DFT, the Kohn-Sham approach is applied to the TDSE. Thus yielding the time-dependent Kohn-Sham equations

$$\left(-\frac{1}{2}\nabla^2 + v_s(\mathbf{r},t)\right)\psi(\mathbf{r},t) = i\frac{\partial\psi(\mathbf{r},t)}{\partial t}, \tag{1.87}$$

where the potential v_s is defined as

$$v_s(\mathbf{r},t) = v_{ext}(\mathbf{r},t) + \int \frac{\rho(\mathbf{r}',t)}{|\mathbf{r}-\mathbf{r}'|}d\mathbf{r}' + \frac{\partial E_{XC}[\rho(\mathbf{r}',t)]}{\partial\rho(\mathbf{r}',t)}. \tag{1.88}$$

Similar to the conventional counterpart, the exchange correlation effects are included in the third term of Eq. 1.88. The exchange correlation term is still unknown and is approximated in practice. The adiabatic local density approximation (ALDA) is the first approximation generally made, in which the originally non-local (in time) time-dependent xc kernel is replaced with a time-independent local. This approximation is based on the assumption that the density varies only slowly with time, consequently allowing the use of a standard local ground-state xc potential in the TDDFT framework. In other words, the ground state functionals, like B3LYP and others, are also used in TDDFT calculations.

Another approximations are reported in the literature, such as the Tamm-Dancoff approximation (TDA), which can reduce the cost by a factor of two when hybrid functionals are used.[60, 61, 62] TDA has also shown to significantly improve the excitation energies for triplet states, amending issues associated with triplet instabilities of the reference wave functions.[63] The resolution-of-the-identity (RI) techniques applied to density approximation may reduce their computational cost by a factor of 3-8 depending on the system. [64, 65] Thus extending the pool of system size for which TD-DFT can be achieved, by adding a marginal error owing to the cancellation of error in the total energies obtained for ground and excited states.

TD-DFT is being used today in a vast range of applications to various types systems in chemistry, solid-state physics, materials science, and biology.[49, 66, 66, 67, 68, 69, 70, 71, 72] Overall, TD-DFT has shown a great success with excitation energies that tend to have few tenths of an eV in error. These successful outcomes depend significantly on the system and type of excitation considered. For example, TD-DFT is known to give large errors with extended π-systems[73, 74] and charge-transfer (CT) states.[75, 76]. Failures in TD-DFT stem from the inability of the xc-functionals to correctly describe the 1/r asymptotic behavior, which instead falls rapidly.[77] Also the available xc-functionals are built to evaluate ground state properties. Thus it is expected to see some limitations when applying ground state functionals to calculate excited state properties.

To over come some limitations encountered with CIS and TD-DFT, other expensive and more accurate methods such as LR-CC$_n$, EOM-CC, SAC-CI can be used. These methods offer an alternative way to compute excited state energies yet a much higher cost. Thus limiting the usage of such methods to small and medium size molecular systems.

1.6.2 Multi-Reference Methods

In the previous section, single reference methods, which vary in computational cost, are discussed. Even with expensive methods such as EOM-CC and CC$_n$, which are known for their high accuracy, in many cases, these methods still depend on

the quality of the ground state reference. Basically, without a good configuration as reference these approaches may end up showing erroneous results specially for strong correlated and open-shell systems away from the equilibrium geometry. Thus, in many cases it is necessary the formulation of a multi-configurational initial reference.

1.6.2.1 Multi-Configuration Self-Consistent Field

Studying systems near bond breaking or systems with di-radical character may require a method with a multi-determinantal initial reference. As one might guess, instead of using one reference, one must generate multiple determinants that may be used to describe the different configuration in the initial reference. Ideally generating all the different configurations will yield the exact solution which corresponds to do doing FCI. However this is limited to small-medium size systems.
In most of the cases, important chemistry happens within the valence orbitals while the core orbitals are dormant. Thus, one can divide the orbitals into two spaces, active and inactive spaces. From the active space, which consists of occupied and unoccupied orbitals, all different configurations will be formed. This method, the Complete Active Space Self-Consistent Field (CASSCF), was developed by Roos and coworkers in 1980. [78, 79] However, selecting the active space is tricky and not straightforward. There is not a well-defined systematic way for structuring the active space, but rather with some trial and error and chemical intuition.
This method is usually noted by [n,m]-CASSCF, where n is the number of electrons in the active space and m is the number of active orbitals. In a CASSCF calculation the chosen set of active orbitals will construct the working space from all configurations with corresponding orbital given space. Keeping in mind that CASSCF is FCI within the active space, the space can get large and computational unfeasible quickly.
For such reason, the Restricted Active Space (RAS) provides an alternative to CAS and allowing the calculation to have a bigger space. RASSCF was introduced by Olsen and coworkers in 1988.[80] Here, the restricted active subspace is divided into three subsets I, II, and III, requiring a minimal number of occupied spin

orbitals in space I while space III requires a maximal number. The number of electrons in space II is unrestricted and is treated similarly to the active space in CAS calculations. Although RAS provides a way to work with larger active sapce, it adds another layer of complexity to the already complex CASSCF. Now the user has to choose subspaces RAS1, RAS2, and RAS, which, again, are not well-defined.

Assuming the active space is well-chosen and the calculation is computational feasible, another setback is the lack of dynamic correlation. CAS methods are known for the ability to account for static correlation. However, to have a "near-exact" wave function dynamic correlation should be included; thus when an orbital window that does not include all the orbital of the system is selected, another method to obtain dynamical correlation is required to be applied on the obtained CAS wave function. Andersson and coworkers proposed the use second-order perturbation theory on the obtained wave function.[81, 82] The reference obtained with CAS is a zeroth order wave function and thus CASPT2 calculation gives a second order estimate of the difference between the CASSCF and the full CI energy. The quality of the final answer of CASPT2 depends largely on how big and reliable the active space is. It is often necessary to modify the active space and the selection of roots in the CASSCF calculation until the desired result is obtained.

Chapter 2

Interpreting the High-Resolution Photoelectron Spectrum of $TiO_3H_2^-$: Probing the TiO_2^-+H_2O Dissociative Adduct

Slow electron velocity-map imaging spectroscopy of cryogenically cooled $TiO_3H_2^-$ anions is used to probe the simplest titania/water reaction, $TiO_2^{0/-}$ + H_2O. The resultant spectra show vibrationally resolved structure assigned to detachment from the cis-dihydroxide $TiO_3H_2^-$ geometry based on density functional theory calculations, demonstrating that for the reaction of the anionic TiO_2^- monomer with a single water molecule, the dissociative adduct is energetically preferred over a molecularly adsorbed geometry. Thiswork represents a significant improvement in resolution over previous measurements, yielding an electron affinity of 1.2529(4) eV as well as several vibrational frequencies for neutral $TiO(OH)_2$.

2.1 Introduction

Titania (TiO_2) is an inexpensive, extensively studied, and environmentally benign semiconducting material with widespread applications in photovoltaics,[83, 84, 85,

86] pollution management, [83] chemical sensing,[87, 88] and heterogeneous catalysis. [89, 90, 91] The landmark discovery of photosensitization of water on a TiO_2 electrode [92] sparked a decades-long pursuit to harness the photocatalytic properties of TiO_2 as a practical means of solar-powered hydrogen fuel production.[93, 94] However, the success of this endeavor has been limited in part by a lack of the mechanistic understanding necessary to design better catalysts. [95] Here, we present high-resolution photoelectron spectra of the $TiO_3H_2^-$anion accompanied by theoretical analysis, in order to probe the nature of the interaction between $TiO_2^-$and a single water molecule.

The most natural starting point for understanding water oxidation by TiO_2 is a consideration of how water adheres to bulk titania surfaces, an active and complex area of research.[96, 97, 98] The extent to which water dissociates on a TiO_2 surface is known to be dependent on surface structure,[99] with varying propensities for dissociative versus molecular adsorption for different crystal phases and planes [100, 101, 102, 103, 104, 105] as well as a dependence on the extent of surface coverage by water.[106, 107] While dissociation tends to play a minor role in water adsorption on stoichiometric TiO_2 surfaces, it is found to be strongly preferred at point defects such as steps,[108] edges,[109, 110] and in particular, oxygen vacancies.[111, 112, 113, 114, 115, 116, 117] Thus, the conceptual key to understanding the surface chemistry of water on titania from a molecular level is the chemistry that occurs at these defect sites.

It is challenging to design a bulk experiment that is uniquely sensitive to the chemistry occurring at a specific surface defect. Defect sites typically make up a small fraction of total surface area and are difficult to reproducibly generate. Gas phase metal oxide clusters have been shown to be useful model systems for gaining mechanistic insight into complex catalytic processes, as these species show structural motifs such as dangling moieties and undercoordinated atoms that mimic the geometries at common defect sites.[118, 119, 120, 121, 122] The control afforded by gas-phase experiments provides the ability to systematically manipulate reactivity-related factors such as particle size, charge, and stoichiometry. Fast-flow laser ablation ion sources allow the production of both bare and reacted clusters,[123]

enabling the characterization of reactants, products, and potentially intermediates or transition states of model catalytic reactions using gas-phase spectroscopic techniques. [124, 125] These species have the added benefit of being computationally tractable, enabling experimentalists and theorists to develop a clear, molecular-scale understanding of catalytic reaction mechanisms which is difficult to obtain from bulk experiments alone.

The experimental spectroscopic characterization of bare $(TiO_2)_n$ clusters constitutes a growing body of work,[126, 127, 110] including contributions from our laboratory.[128, 129] Less work has been done to probe species formed from the reaction of small $(TiO_2)_n$ clusters with a discrete number of water molecules, which can either adsorb molecularly or dissociatively as on the bulk surface. The hydration of cationic TiO^+ by up to 60 water molecules has been studied by mass spectrometry, though this measurement does not provide insight into the structure of the resultant clusters.[91] These solvated cations have been structurally characterized using infrared action spectroscopy by Zheng and co-workers,[92] who have also performed anion photoelectron spectroscopy (PES) on the anionic $(TiO_2^-)(H_2O)_{0–7}$ clusters.[93] In both cases, their spectra indicated dissociative adsorption of water to form hydroxide species. Weichman and co-workers [94] have recently used infrared action spectroscopy to systematically characterize the anionic $(TiO_2)_n^-$ $(D_2O)_m$ clusters for n = 2–4 and m = 1–3, finding that the dissociative geometries are preferred for these clusters as well.

A number of groups have used theoretical treatments— most commonly density functional theory (DFT) – to assess the extent to which H_2O molecules dissociate on small $(TiO_2)_n$ clusters. [95, 96, 97] The most comprehensive work in this area has been carried out by Dixon and co-workers,[97, 99] who used a hybrid genetic algorithm to determine the lowest-energy structures for $(TiO_2)_n(H_2O)$m (n = 1–4, m= 1–2n) clusters.[100] Geometry optimizations and single point calculations were carried out using both DFT and coupled cluster methods, yielding similar results for all model chemistries used. For the simplest stoichiometric TiO_2/water reaction, TiO_2 + H_2O, they found that the di-hydroxyl $TiO(OH)_2$ structure, in which the water is split, is preferred over molecular adsorption ($TiO_2 \cdot H_2O$) by

over 40 kcal mol^{-1}. Of the two dissociatively adsorbed structures reported, the planar C_{2v} *cis*-hydroxyl isomer was found to be more stable than the C_s *trans*-OH isomer, though the energy difference was less than 3 kcal mol^{-1}.

The only experimental work on this system comes from the aforementioned anion PES study by Zheng and coworkers, [93] who reported the photodetachment spectrum for $TiO_3H_2^-$ formed by a laser ablation reactor source. This spectrum showed a single broad electronic band spanning ∼1 eV in electron binding energy (eBE), reflecting extended unresolved vibrational progressions. From this spectrum, they estimated an electron affinity (EA) of 1.15 ± 0.8 eV and a vertical detachment energy (VDE) of 1.51 ± 0.08 eV. By comparison to their photoelectron spectrum of bare TiO_2^- and DFT calculations, the anion geometry was assigned to the $TiO(OH)_2^-$ dissociative adduct. Other than the general assignment based on the position of the detachment feature, little information regarding the structure of the $TiO_3H_2^{-/0}$ species can be gleaned from this work.

Slow electron velocity-map imaging of cryogenically cooled anions (cryo-SEVI) is a high-resolution variation of traditional anion PES which provides vibrationally resolved detachment spectra reflecting the geometric and vibronic structure of the anion and neutral. Previously, we have used cryo-SEVI to characterize the unreacted TiO_2^- monomer;[128] here, we probe the $TiO_3H_2^-$ species, corresponding to a single TiO_2^- reacted with one water molecule. These spectra represent a significant improvement in resolution compared to the work of Zheng and co-workers, showing an extensive vibrational structure with typical peak widths of 10 cm^{-1} full-width at half-maximum (fwhm). With the assistance of DFT calculations, we assign the anion structure to the dissociative di-hydroxide $TiO(OH)_2^-$ isomer identified as the lowest energy neutral geometry by Dixon and co-workers. Several vibrational frequencies for the neutral $TiO(OH)_2$ species are extracted, as well as its EA. A comparison to the unreacted TiO_2^- cryo-SEVI spectra elucidates the energetic effect of charge on the $TiO_2^{-/0}$ + H2O reaction, highlighting the utility of small metal oxide clusters as tools for understanding catalytic reactions.

2.2 Computational Details

Possible minimum-energy structures for both anionic and neutral TiO_2 + H_2O were explored using a variety of DFT-based model chemistries. The preliminary results suggested meaningful differences between model chemistries. Therefore, initial benchmarking calculations were carried out to compare six DFT-based model chemistries with the results of coupled-cluster singles and doubles (CCSD) calculations, [34, 130] as summarized in Sec. A.1 in appendix A. Based on comparisons of these CCSD results to DFT predicted energetic ordering of candidate anion and neutral minimum energy structures as well as vertical and adiabatic detachment energies (ADEs) (Tables A.1 and A.1 in appendix A), the exchange and Yang-Parr-Lee correlation functionals (B3LYP) were employed with the Def2TZVP basis set,[131, 132, 133, 134, 135] and this model chemistry has been employed for the calculations described below.

Both doublet and quartet states were considered for anion candidates; singlet (closed-shell and open-shell) and triplet states were considered for the neutral candidates. For all identified structures, doublet anions are more stable than quartet species and the closed-shell singlet state was found to be more stable than the open-shell singlet or triplet state. Excited state calculations were carried out using the same model chemistry within the time-dependent DFT (TDDFT) formalism.[49, 136, 137] Analysis of these excited state calculations was facilitated by Martin's Natural Transition Orbital (NTO) model.[138]

All calculations were carried out using a local development version of the Gaussian suite of electronic structure programs.[139] Converged Kohn-Sham determinants were tested for stability.[140] Molecular geometries were optimized using standard methods[141] and the reported potential energy minima were verified using analytical second-derivative calculations. Franck-Condon (FC) spectra were simulated using the implementation by Bloino, Barone, and co-workers.[142, 142] Care was taken to determine appropriate scaling factors for the DFT force constants calculated for the lowest-energy neutral state (Table A.2) such that simulated FC progressions aligned well with the experimental spectra.

To describe the nature of the detached electron we have employed the Natural Ion-

ization Orbital (NIO) model of Thompson, Harb, and Hratchian.[110] The NIO model provides a compact orbital representation of ionization processes by utilizing one-particle difference densities. Natural orbital analysis involving this difference density yields a simplified interpretation of electronic detachment processes. The NIO model has recently been shown to provide a convenient means to distinguish between one-electron transitions and those where the one-electron process is accompanied by excitation of a second electron into the virtual orbital space.[97] The current system is Koopmans-like, evidenced by the strong resemblance between the NIO and the canonical highest-occupied molecular orbital (HOMO)of the **1-1a** anion (Fig. A.1), and thus the detachment transitions considered here are one-electron transitions that can be equivalently described by considering the NIO or the anion HOMO. As such, the method of Liu and Ning [143] was applied to the HOMO of the lowestenergy anion to calculate the eKE-dependent PAD expected for the removal of an electron from this orbital; the results are shown as the solid lines in Fig. 2.2.

2.3 Results and Discussion

2.3.1 Experimental Results

The cryo-SEVI spectrum for detachment from $TiO_3H_2^-$ is shown in Fig. 2.1. In this figure, the blue trace corresponds to an overview scan taken with a relatively high detachment energy and the black traces are higher resolution SEVI scans taken with variable photon energies. The overview spectrum spans 10 000-13 500 cm¹ in eBE and exhibits considerable vibrational structure, revealing increasing spectral congestion as the eBE increases. Due to this increased complexity, our analysis will be focused on the first ∼2000 cm¹ of structure. In this region, the high-resolution scans reveal a number of transitions (A1-11 and B1-11) with typical peak widths of ∼10 cm¹ fwhm, corresponding to detachment to different vibronic levels of the neutral TiO3H2 species. The sharp onset of structure at peak A1 gives an EA of 1.2529(4) eV for TiO_3H_2. The remainder of the spectrum is dominated by a ∼675 cm¹ progression (A1-3-7-11), modulated by several weaker patterns. Peak

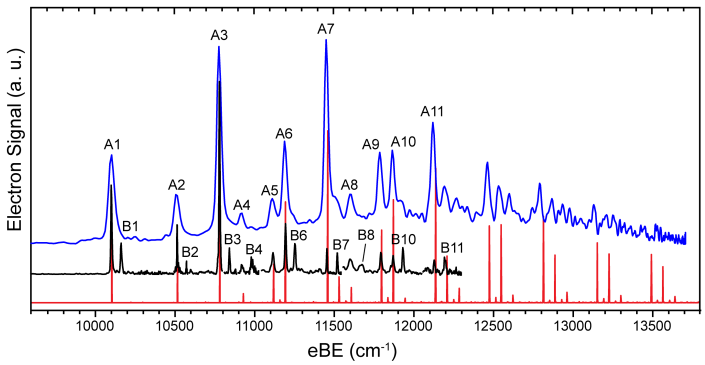

Figure 2.1: Cryo-SEVI spectrum of $TiO_3H_2^-$. The blue trace is an overview spectrum taken with a photon energy of 13721 cm^{-1}, and the black traces are high-resolution scans taken at variable photon energies. Black traces are scaled to match relative peak intensities observed in the overview as much as possible. The red stick spectrum shows the Franck-Condon simulation for detachment from the **1-1a** C_{2v} *cis*-OH $TiO(OH)_2^-$ geometry using scaled neutral frequencies.

positions, widths, and shifts from the origin are summarized in Table I.

The EA provided by cryo-SEVI is larger than the value of 1.15(8) eV reported by Zheng and co-workers.[93] This discrepancy is understandable given the lower resolution of their spectrum and the experimental conditions used to obtain it. In that work, individual transitions in the extended Franck- Condon progressions blend together to form a broad structureless feature, and the lack of a clear onset complicates the extraction of the EA. Additionally, the ions probed in the previous work were not cooled prior to detachment, and given the relatively high temperatures typical of ions produced by laser ablation,[144] the resultant spectra likely contain contributions from hot bands that can occur lower the apparent electron binding energy relative to the true EA. Hot bands are effectively eliminated in the cryo-SEVI experiment, where ions are cooled to ∼10 K prior to detachment.[145]

Measurement of the PADs of features labeled in Fig. 2.1 reveals that all transitions fall into one of two groups with distinct angular distributions. These two groups are represented in Fig. 2.2a, which plots the anisotropy parameter (β) versus eKE for peaks A1-3 and B1-3. Features A1-3 show positive values of β, whereas features B1-3 show isotropic ($\beta \sim 0$) angular distributions. The remainder of fea-

tures in Fig. 2.1 shows PADs that are qualitatively similar to one of these two groups, and are labeled accordingly, where peaks labeled A correspond to parallel ($\beta > 0$) detachment transitions and peaks labeled B have isotropic ($\beta \sim 0$) PADs. These anisotropy parameters are summarized qualitatively in Table I. Each B-series transition lies ∼60 cm^{-1} above a peak in the A1-11 series, and has been numbered accordingly.

These two groups also showdistinctly different dependencies of the photodetachment cross section on eKE. Far from threshold, the A1-11 series dominates the spectrum, as can be seen in the overview spectrum in Fig. 2.1. As the photon energy is lowered, transitions in the B1-11 series become more apparent, resulting from the relative attenuation of the A1-11 peaks. This trend is illustrated in Fig. 2.2b, where peaks A1 and B1 are shown for several photon energies and the intensities are normalized to the peak intensity of B1. The relative scaling of detachment cross sections for low-eKE detachment is given by the Wigner threshold law

$$\sigma \propto (\mathrm{eKE})^{l+1/2}, \tag{2.1}$$

where σ is the detachment cross section and l is the angular momentum of the detached electron. According to this law, a sharper decrease in detachment signal as the photon energy is lowered reflects higher l detachment channels; it can therefore be inferred that transitions A1-11 correspond to higher l detachment than transitions B1-11.

2.3.2 Structural Assignment of $TiO_3H_2^-$

Figure 2.3 shows optimized minimum-energy structures located on the anionic and neutral TiO_3H_2 potential energy surfaces, as well as zero-point corrected energies. Cartesian coordinates for these structures are provided in Secs. A.2 and A.3. In agreement with previous work by Dixon and co-workers,[100] the C_{2v} dissociative structure(**1-1a′**) is found to be the lowest-energy neutral geometry; likewise, the **1-1a** geometry is the lowest-energy anion isomer. Two additional minimum-energy structures, **1-1b** and **1-1e**, were found on the anion potential energy surface to lie

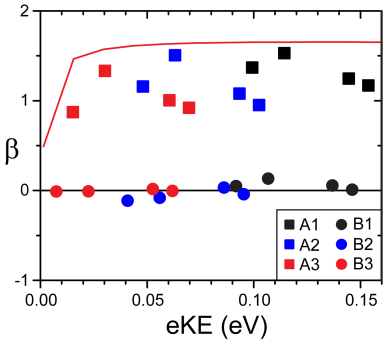

(a)

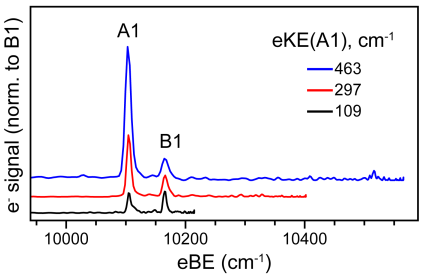

(b)

Figure 2.2: (a) Anisotropy parameters of peaks A1-3 and B1-3 extracted from VMI images obtained at multiple photon energies. The solid line shows the calculated anisotropy parameter expected for detachment from the **1-1a** anion HOMO found by DFT. (b) Detachment spectra of $TiO_3H_2^-$ at several photon energies.Photon energies used are 10568 (blue), 10297 (red), and 10215 cm^{-1} (black).

0.08 and 0.19 eV above **1-1a**, respectively, and differ from this isomer by rotation of the hydroxide groups. A local minimum corresponding to the *trans*-OH **1-1b′** geometry was discovered at an energy of 0.11 eV above the neutral **1-1a′** structure, in reasonable agreement with the relative energy reported by Dixon. No neutral minimum corresponding to the **1-1e** isomer was identified. The lowest-energy molecularly adsorbed TiO_3H_2 adduct reported by Dixon was also identified as a local minimum for both anion (**1-1c**) and neutral (**1-1c′**), though these structures lie 2.34 and 3.13 eV above the anion and neutral global minima, respectively.

Given the relative energies of the anion geometries shown in Fig. 2.3, the most likely structures contributing to the cryo-SEVI spectrum of $TiO_3H_2^-$ correspond to the dissociative geometries **1-1a** and **1-1b**. The assignment of a dissociatively adsorbed anion geometry is consistent with the assessment of Zheng and co-workers.**52** Predicted adiabatic detachment energies (ADEs) for **1-1a** and **1-1b** are 1.23 and 1.26 eV, respectively, both in good agreement with the experimental electron affinity (1.25 eV). In both cases, NIO analysis clearly indicates that the detached electron resides in the anion HOMO, which strongly resembles the Ti dz2 orbital, Fig. 2.4 . Analysis of the NIO for either **1-1a** or **1-1b** gives an orbital

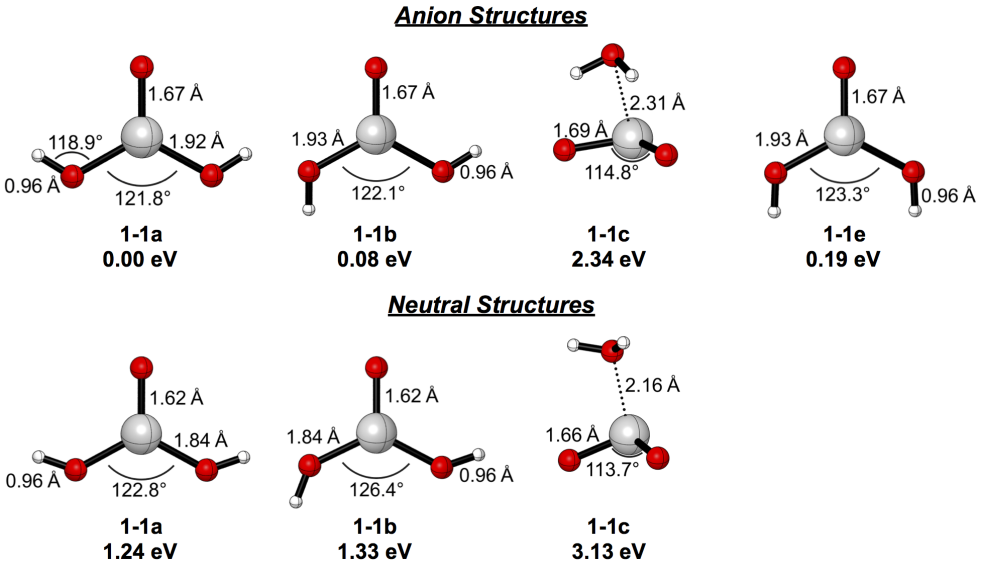

Figure 2.3: Optimized geometries of anionic and neutral TiO_3H_2 found with B3LYP/Def2TZVP. Energies are provided relative to the **1-1a** geometry of the anion and include zero-point corrections. Geometric parameters are also provided.

angular momentum of L = 2, such that detachment from either of these orbitals would be expected to primarily yield outgoing p- ($l = 1$) and f-wave ($l = 3$) electrons. This high-l detachment is consistent with the observed attenuation of the signal near threshold for peaks A1-11.

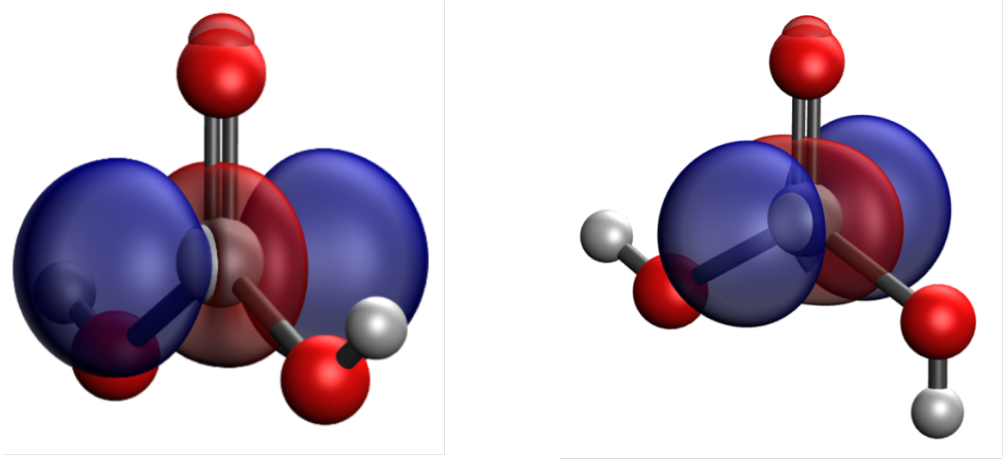

(a) (b)

Figure 2.4: NIO describing the electron detachment from the 1-1a (a) and 1-1b (b) anion to the ground electronic state of the corresponding neutral species.

Additionally, the eKE-dependence of the anisotropy parameter calculated98 for detachment from the **1-1a** HOMO (Fig. 2.2a, solid lines) is in good agreement with the measured β values for peaks A1-11, showing positive values in the eKE region of interest. Given the similarity between the **1-1a** and **1-1b** NIOs, detachment from the **1-1b** isomer is expected to have a similar PAD. The agreement between experiment and theory further supports the conclusion that the global minimum of the $TiO_3H_2^-$ anion takes the dissociative $TiO(OH)_2^-$ dihydroxide geometry and that detachment from one of these isomers to the ground state of the corresponding neutral accounts for the most intense structure (A1-11).

To determine definitively which of these species is responsible for the experimentally observed detachment transitions, we consider the Franck-Condon profiles for detachment from both isomers, as the FC profile is highly sensitive to the anion and neutral geometries. Of these two isomeric candidates, the FC profile for detachment from the $\tilde{X}^2A_1$ state of the **1-1a** anion provides better agreement with experiment than detachment from the $\tilde{X}^2A'$ **1-1b** anion. The calculation in Fig.2.1 using scaled frequencies is shown in red in Fig. 2.1 and reproduces the dominant vibrational structure observed in the experimental spectrum. In particular, the first several intense features (A1-3) are reproduced in the FC simulation for **1-1a**, whereas the **1-1b** simulation shows extra structure between A1 and A3. Thus, we assign the **1-1a** *cis*-OH geometry as the lowest-energy isomer of $TiO_3H_2^-$, and the observed spectral features reflect the vibronic structure of the corresponding **1-1a′** neutral.

2.3.3 Vibrational assignments

The agreement between the simulated and experimental spectra in Fig. 2.1 enables straightforward asswignment of the major structure (A1-11) as $\tilde{X}^1A_1 \leftarrow \tilde{X}^2A_1$ detachment transitions terminating in totally symmetric vibrational levels of the neutral ground state (Table I). The less intense B1-11 series of peaks are not fully described by this FC simulation, and the previously described PADs indicate that these transitions do not have the same electronic character as A1-11. As such, we will first address the vibrational assignments of A1-11.

The dominant progression (A1-3-7-11) is assigned to the ν_3 vibrational mode, which corresponds to a symmetric Ti–OH stretching motion (Fig. A.1). The shift of peak A3 from the vibrational origin (A1) gives a frequency of 678(5) cm^{-1} for this mode. There is also significant participation of the ν_4 totally symmetric OH wagging mode in the spectrum (A2, A6, A10), as well as some activity in the ν_2 terminal Ti=O stretch (A5, A9). The shifts of peaks A5 and A2 give neutral vibrational frequencies of 1016(8) and 413(3) cm^{-1} for ν_2 and ν_4, respectively. Table II summarizes the energetic quantities for neutral TiO(OH)2 extracted from experiment and compares them to the **1-1a′** B3LYP/Def2TZVP results, showing reasonably good agreement for these totally symmetric modes.

The Franck-Condon activity of different normal modes can be rationalized by considering the geometrical changes that occur upon photodetachment, which are summarized for the B3LYP/Def2TZVP **1-1a** $\tilde{X}^2A_1$ anion and **1-1a′** $\tilde{X}^1A_1$ neutral equilibrium geometries in Table A.4. The most significant change is a 13.6° increase in the H−O−Ti bond angle, which results in the FC activity of the ν_4 OH-wagging mode. The involvement of the titanium-oxygen stretching modes ν_2 and ν_3 is a reflection of the change in bond lengths upon photodetachment for both the terminal Ti=O bond as well as the hydroxide Ti=O bonds. The hydroxide and terminal Ti−O bonds of the B3LYP geometries decrease by 0.08 and 0.05 Å, respectively, corresponding to modest 3%–4% decreases in these bond lengths. These constitute the second– and third-largest fractional changes upon detachment for the five geometrical parameters summarized in Table A.4.

While the above considerations fully assign peaks A1-11, the differing PADsand threshold behavior of peaks B1-11 indicate that these transitions have different electronic character, ruling out assignment to Franck-Condon allowed transitions within the $\tilde{X}^1A_1 \leftarrow \tilde{X}^2A_1$ electronic band including vibrational hot bands. These transitions are also unlikely to correspond to detachment from an excited anion state, as a TDDFT calculation for the anion (Table A.5) does not reveal an excited state with sufficiently low excitation energy to be populated in the cold trap, where ions typically have temperatures on the order of 10 K. It is possible that peaks B1-11 arise from detachment to a separate electronic state of neutral $TiO(OH)_2$,

and that the two groups of features correspond to overlapping electronic bands with the A1-B1 spacing providing the electronic term energy. However, this would require a neutral state with a term energy of around 60 cm^{-1}, and the present theoretical results do not provide evidence for such a state, with the lowest-energy neutral excited state of **1-1a′** lying 3.86 eV above the closed-shell singlet (Table A.5).

Another possible assignment for peaks B1-11 is detachment from a different $TiO_3H_2^-$ geometry. In the current theoretical framework, the **1-1b** *trans*-OH $TiO(OH)_2^-$ dissociative adduct is expected to be only 0.08 eV higher than the *cis*-OH (**1-1a**) isomer. Given this low relative energy as well as its structural similarity to the global minimum, this geometry could interconvert with the slightly more stable **1-1a** geometry in the ion trap, resulting in contributions from multiple isomers in the cryo-SEVI spectrum. However, the barrier for conversion of the **1-1a** isomer to the **1-1b** geometry is estimated to be ∼1300 cm^{-1} from constrained optimization and single point calculations, indicating that such interconversion is highly unlikely in the cold environment of the ion trap. Additionally, as discussed above, the NIOs for the **1-1a** and **1-1b** isomers are quite similar, Fig. 2.4, with both orbitals dominated by Ti d_{z^2} character. Thus, if detachment features from the **1-1b** geometry were observed, the transitions would not have PADs that deviate so significantly from the *cis*-OH detachment transitions, ruling out assignment of peaks B1-11as detachment from the **1-1b** anion. A similar argument can be made to rule out detachment from the **1-1e** isomer, which also differs from **1-1a** only by rotation of the hydroxyl groups.

Given the above considerations, and the observation that each of the B1-11 features lies ∼60 cm^{-1} above a transition in the A1-11 series, we conclude that these features correspond to detachment transitions terminating in $\tilde{X}^1A_1$ vibrational levels with odd quanta of excitation along a low frequency non-totally symmetric mode. These FC-forbidden transitions obtain their oscillator strength and PADs through Herzberg-Teller (HT) coupling to an excited neutral electronic state.101 The most likely vibrational assignment for peaks B1-11 involves the b_1-symmetric ν_8 mode, which corresponds to the umbrella-like motion of the Ti atom through the plane

of the three oxygen atoms and has the lowest calculated frequency (Table A.3) for the **1-1a′** neutral. Each Bi transition in the B1-11 series is thus assigned as terminating in the state corresponding to the A_i transition, plus a single quantum of excitation along ν_8. With this assignment, the position of peak B1 relative to A1 gives a vibrational frequency of 60(4) cm^{-1} for the ν_8 umbrella mode of neutral $TiO(OH)_2$.

We now consider the symmetry requirements for the excited electronic state which gives rise to transitions B1-11 through Herzberg-Teller coupling. Consider a vibronic state $|a\rangle$ whose electronic and vibrational symmetries are Γ^a_{elec} and Γ^a_{vib}, respectively. This state can undergo HT-coupling with another vibronic state, $|b\rangle$, with symmetries Γ^b_{elec} and Γ^b_{vib}, provided

$$\Gamma^a_{elec} \otimes \Gamma^a_{vib} \otimes \Gamma^b_{elec} \otimes \Gamma^b_{vib} \supset \Gamma_{TS}, \tag{2.2}$$

where Γ_{TS} is the totally symmetric representation within the relevant molecular point group. If state b is FC-allowed for detachment from the anion in question (i.e., $\langle b \mid \Psi_{anion} \rangle$), detachment to state a will reflect the b-state electronic character, which will be observable in the PAD and threshold behavior.

In the current case, the observed HT-coupled levels correspond to states with odd quanta of excitation along the b1-symmetric ν_8 mode ($\Gamma^a_{vib} = b_1$) within the vibrational manifold of the ground neutral electronic state ($\Gamma^a_{elec} = A_1$).Within the C2v point group, these levels are Franck-Condon forbidden, and so can only be observed if they mix with some vibronic level b that is not FC-forbidden, i.e., $\Gamma^b_{vib} = a_1$. Thus, the observed features must arise from HT-coupling with a B1-symmetric electronic excited state. The lowest such singlet state identified from TDDFT (Table A.5) is the relatively high-lying $\tilde{C}^1A_1$ excited state, residing 4.45 eV above neutral $\tilde{X}^1A_1$ **1-1a′**. Using the NTO model, we determined that this state would involve detachment from an orbital with angular momentum L = 1, resulting in outgoing *s*- ($l = 0$) and *d*-wave ($l = 2$) electrons, in contrast to the *p*- and *f*-wave detachment expected from the **1-1a** NIO. Thus, the assignment of peaks B1-11 as arising from Herzberg-Teller coupling to this $^1B_1$ state is consistent with the observed relative attenuation of A1-11 versus B1-11 as photon energy is

lowered.

2.3.4 Charge effects on the $TiO_2 + H_2O$ reaction

The cryo-SEVI spectrum of unreacted TiO_2^- has been previously reported, giving an electron affinity of 1.5892(5) eV for the singlet ground state of TiO_2.**48** The electron affinity of the $TiO(OH)_2$ dissociative adduct is lower by roughly 0.3 eV, and this difference provides insight into the energetic effects of charge on the dissociation of H2O by TiO_2. The lower electron affinity for the reacted species implies that the neutral TiO_2 + H_2O → $TiO(OH)_2$ reaction is more exothermic than the anionic counterpart—that is, reaction with water to form the dissociative $TiO(OH)_2$ adduct stabilizes neutral TiO_2 more than it does the anion. As a consequence, it can be inferred that neutral TiO_2, where the titanium center has a +4 oxidation state, is more reactive towards water than anionic TiO_2^- where the Ti oxidation state is +3. The energies shown in Fig. 2.3 indicate that the molecularly adsorbed **1-1c′** geometry has an even lower EA (0.79 eV) than the dissociative structures. Given that all the geometries in Fig. 2.3 involve binding interactions between the water oxygen and Ti, this charge effect likely derives from donation of electron density from the incoming water molecule to the metal center, which in turn is favored by a higher titanium oxidation state.

The enhanced reactivity towards water of neutral TiO_2 echoes the electrochemical mechanism of water splitting in photoelectrochemical cells (PECs) where titania is used as a photoanode.14 In these systems, the generally understood mechanism is initiated by photoexcitation of titania, resulting in the formation of an electron-hole pair. The electron is then transferred to the cathode, typically a metal, leaving behind a hole in the valence band of TiO_2. These holes participate in the oxidation half-reaction,

$$H_2O \rightarrow \frac{1}{2}O_2 + 2H^+ + 2e^-, \tag{2.3}$$

while the electrons at the cathode participate in the reduction half-reaction,

$$2H^+ + 2e^- \rightarrow H_2, \tag{2.4}$$

Within this mechanistic picture, the photosensitization of water by TiO_2 is a consequence of the ability of TiO_2 to donate a hole (or, equivalently, accept an electron). Direct parallels between the chemistry occurring in such PECs and the gasphase $TiO_2^{-/0}$reaction considered here are difficult to make, due to the fundamental differences in the electronic structures for these two systems and the increased complexity associated with the condensed phase. However, it is interesting to note that the reactivity of TiO_2 with water in the gas phase reflects, to some extent, the bulk electrochemical behavior—namely, the energetics of the TiO_2/water reaction are directly related to the oxidation state of the Ti center, with a more positively charged metal atom resulting in a more energetically favorable interaction with water.

2.4 Conclusion

Vibrationally-resolved photoelectron spectra of the $TiO_3H_2^-$ anion are obtained using slow electron velocity map imaging of cryogenically cooled anions, yielding spectra that reflect the vibronic structure of neutral TiO_3H_2. These results provide a significant improvement in resolution over prior work on this system, clearly resolving the onset of the structure at the adiabatic detachment energy. A Franck-Condon simulation for detachment from the C_{2v} **1-1a** $TiO(OH)_2^-$ *cis*-hydroxide geometry captures the dominant vibrational structure observed experimentally, enabling the assignment of this geometry as the lowest-energy anion isomer in agreement with density functional theory calculations. In addition to transitions reproduced in the FC simulations, a series of features resulting from Herzberg-Teller coupling to an excited neutral electronic state is identified in the cryo-SEVI spectrum, evidenced by noticeable differences in the angular and energy dependence of the photodetachment cross sections.

The comparison of the current spectral results to the previously reported cryo-SEVI spectrum of unreacted TiO_2 provides insight into the reactivity of $TiO_2^{-/0}$ towards water. The lowered electron affinity of TiO3H2 relative to TiO_2 indicates that neutral TiO2 is stabilized to a greater extent than anionic TiO_2^- by reaction with

water, suggesting that the reaction of TiO_2 with water is impeded by excess negative charges. This conclusion is consistent with the existing electrochemical understanding of photocatalytic water splitting by TiO_2 in photoelectrochemical cells, where the sensitization of water arises from the ability of TiO_2 to accept electron density. This chapter highlights the relevance of gas-phase studies of metal oxide cluster reactions to bulk catalytic reactions, as well as the utility of cryo-SEVI as a structural probe for such systems.

Chapter 3

Unveiling the Coexistence of Cis and Trans Isomers in the Hydrolysis of ZrO_2 to Explain the Observed Photoelectron Spectrum of ZrO_2H_3

High-resolution anion photoelectron spectroscopy of the $ZrO_3H_2^-$ and $ZrO_3D_2^-$ anions and complementary electronic structure calculations are used to investigate the reaction between zirconium dioxide and a single water molecule, ${ZrO_2}^{0/-} + H_2O$. Experimental spectra of $ZrO_3H_2^-$ and $ZrO_3D_2^-$ were obtained using slow photoelectron velocity-map imaging of cryogenically cooled anions, revealing the presence of two dissociative adduct conformers and yielding insight into the vibronic structure of the corresponding neutral species. Franck–Condon simulations for both the cis- and trans-dihydroxide structures are required to fully reproduce the experimental spectrum. Additionally, it was found that water-splitting is stabilized more by ZrO_2 than TiO_2, suggesting Zr-based catalysts are more reactive toward hydrolysis.

3.1 Introduction

Zirconium dioxide (ZrO_2) is an extensively studied material with widespread applications in medicine,[146, 147, 148] gas-cleaning technology,[149] ceramics,[150, 151] corrosion-resistant materials [152, 153, 154], and heterogeneous catalysis [155]. As in the case of titania (TiO_2), photosensitization of water on a ZrO_2 electrode has inspired the development of ZrO_2 based technologies to exploit its photocatalytic properties for solar–powered hydrogen fuel cells [156, 157, 158, 159, 160]. Despite significant effort, these technologies are not yet viable, in part due to the limited mechanistic knowledge needed for further development.[161] Specifically, a more complete understanding of the interaction between ZrO_2 and water is required to develop these devices. Here, we present high-resolution photoelectron spectra of the $ZrO_3H_2^-$ anion in tandem with electronic structure calculations, providing insight into the simplest reaction of $ZrO_2^{0/-}$ with water.

There is a vast body of work on the surface chemistry of metal oxides aimed at understanding water oxidation,[162, 163, 164, 165, 166, 167, 168, 169] with a considerable number of studies specifically probing the ZrO_2 surface.[170, 171, 172, 173, 174] From this body of work, it has become clear that defect sites play a critical role in the catalytic process,[108, 175, 176, 177, 178, 179] thus investigating the interaction of water molecules at these sites is crucial for gaining insights into the water splitting mechanism. Such studies are challenging, however, owing to the difficulty of synthesizing and probing molecular-scale structures embedded with low density on bulk surfaces.[180, 181, 182, 183, 184, 185, 186, 187, 188] Overcoming the hurdles of generating and controlling defect sites can be bypassed by preparing and studying gas–phase metal oxide clusters, as these species show structural motifs that mimic the geometries of common defect sites.[189, 190, 121] Further, the relatively small size of these systems makes them computationally tractable, enabling experimentalists and theorists to determine their electronic structure, geometries, and catalytic reaction mechanisms - a task not viable from bulk studies alone.[191, 192, 193, 194, 195] There has been substantial progress made in understanding the structure and reactivity of small metal oxide clusters, [196, 197, 198, 199, 200, 201] including several studies on the interaction between

titanium dioxide clusters and water molecules.[181, 202, 203, 204]

Of particular relevance is the work of Zheng and co-workers, who performed anion photoelectron spectroscopy (PES) on the anionic $(TiO_2)(H_2O)_{0–7}$ clusters and inferred that dissociative adsorption of water occurs to form a hydroxide species.[202] We recently reinvestigated the $(TiO_2^-)(H_2O)$ system using slow electron velocity-map imaging of cryogenically cooled anions (cryo-SEVI), a high-resolution form of anion PES, coupled with detailed computational simulations.[205] That work shows evidence that the dissociative adduct, *cis*-dihydroxide $TiO(OH)_2^-$, is a planar C_{2v} structure that is energetically favored over a molecularly adsorbed complex and other lower-symmetry dissociative species.

Though still a Group IV metal oxide, ZrO_2 has been studied less extensively than titania. [123, 206, 207, 208, 209, 210, 211] Within the bulk framework, Sayama et al.[161] initiated significant interest in the field with the discovery of the photocatalytic decomposition of water on pure ZrO_2 powder following UV irradiation. Later, it was shown that adding a carbonate-based salt such as $NaHCO_3$ or Na_2CO_3 to an aqueous ZrO_2 suspension increased the gas evolution rate in the photocatalytic decomposition of water.[212] The interaction of water with bulk zirconia surfaces has been characterized and investigated by X-ray powder diffraction, high-resolution transmission electron microscopy, X-ray photoelectron spectroscopy, calorimetry, and Fourier-transform infrared spectroscopy (FTIR),[213, 214, 215, 216] along with periodic density functional theory (DFT) calculations.[217, 218, 219, 220] Notably, the FTIR investigation by Holmes and coworkers[216] of water sorption on ZrO_2 found bands corresponding to chemisorbed OH groups, suggesting that water bound to the surface of ZrO_2 forms a $OZr(OH)_2$– like structure.

Bare $(ZrO_2)_n^{0/-}$ clusters have been extensively studied using PES,[221, 222, 223] matrix-IR spectroscopy,[224] Fourier-transform microwave spectroscopy,[225] laser-induced fluorescence,[226] resonant multi-photon ionization,[226] dispersed fluorescence,[226] and computational methods.[227, 224, 221, 228, 229, 230] Despite this growing body of work, there is no experimental data on the reactions of these clusters with a water molecule, though computational studies by Dixon et al.[231] on the

$(ZrO_2)_n$ + H_2O (n=1-4) reaction find these clusters are capable of splitting water. That work shows the dissociative adduct to be more stable than the molecularly adsorbed species by roughly 200 kJ/mol, at both the DFT and coupled cluster levels of theory, in agreement with experimental observations on bulk zirconia.[220] Further, the optimized geometries of the dissociative adduct were found to adopt only a *cis*-hydroxide geometry in contrast with computational results for the $TiO_2^{0/-}$ + H_2O dissociative adducts, where both *cis* and *trans* isomers were identified.[205, 232]

Here, we present a combined computational and experimental investigation of $ZrO_3H_2^-$ and $ZrO_3D_2^-$, thereby probing fundamental aspects of the $ZrO_2^{0/-}$ + H_2O gas-phase reaction. The dense and highly resolved vibrational structure seen in the cryo-SEVI spectra is only reproduced if detachment from both low-lying isomers of the $ZrO(OH)_2^{0/-}$ system, the *cis*-dihydroxide and *trans*-dihydroxide dissociative adducts, are considered. Additionally, the electron affinity of the neutral *cis*-dihydroxide structure and adiabatic electron affinity (ADE) of the anionic *trans*-dihydroxide are reported along with vibrational frequencies of both neutral structures. Further, agreement between experiment and theory facilitates not only the structural determination of these clusters, but also provides insight into the differences between the hydrolysis reactions of TiO_2 and ZrO_2.

3.2 Computational Details

A variety of DFT-based model chemistries were used to identify possible minimum energy structures along the anionic and neutral ZrO_2 + H_2O surface. Initial benchmark work was carried out by comparing six different functionals (B3LYP, B3PW91, M06, M06L, PBE1PBE and ωB97XD) and two basis sets (def2tzvp and the Stuttgart/Cologne ECP28MHF (SC)) resulting in 12 different model chemistries.[233, 133, 234, 235, 236, 237, 134, 238, 239, 240, 241, 242] Tables S1-S6 summarize the results obtained from these benchmark calculations. Preliminary results suggested meaningful differences in normal mode frequencies and vertical excitation energies. After a detailed inspection of these results and comparison with the experimental

data presented here, we determined that the ωB97XD/SC model chemistry best reproduces the observed relative experimental energies and vibrational frequencies. A number of electronic states for the anion and neutral species were investigated. For the anion, doublet and quartet spin states were considered, while singlet and triplet states were included for the neutral. All model chemistries predicted lowest spin states (neutral singlet and anion doublet) to be energetically most stable. Excited-state calculations were carried out using the same model chemistry within the (linear response) time–dependent DFT (TDDFT) formalism.[49, 136, 137]
All calculations were carried out using a local development version of the GAUSSIAN suite of electronic structure programs.[243] Stability was tested on all converged Kohn–Sham determinants.[244, 245] Standard methods were used for optimizing molecular geometries,[246] and the nature of located stationary points were verified using analytical second–derivative calculations.[247, 248] Franck–Condon (FC) spectra were generated using the implementation by Bloino, Barone, and co–workers.[249, 250] Simulated PES spectra, including FC progressions, were adjusted to align with the experimental spectra after shifting DFT force constants of the neutral state. Full details, including scaling factors and shifting parameters, are provided in appendix B. Characterization of electron detachment was facilitated by the Natural Ionization Orbital (NIO) model.[251] The NIO model provides the Dyson orbital for a ΔSCF treatment of electron detachment and, within the sudden approximation, provides insight to electron relaxation accompanying electron detachment. The NIO model has been successfully employed in a number of recent studies involving similar systems.[252, 251, 205]

3.3 Results and Discussion

3.3.1 Experimental Results

Cryo-SEVI spectra of $ZrO_3H_2^-$ and $ZrO_3D_2^-$ are shown in Figs. 3.1 and 3.2, respectively. In both figures, overview spectra, taken with relatively high photon energies, are displayed in blue atop composite high-resolution scans in black taken with various photon energies. While the overview spectrum displays structure for

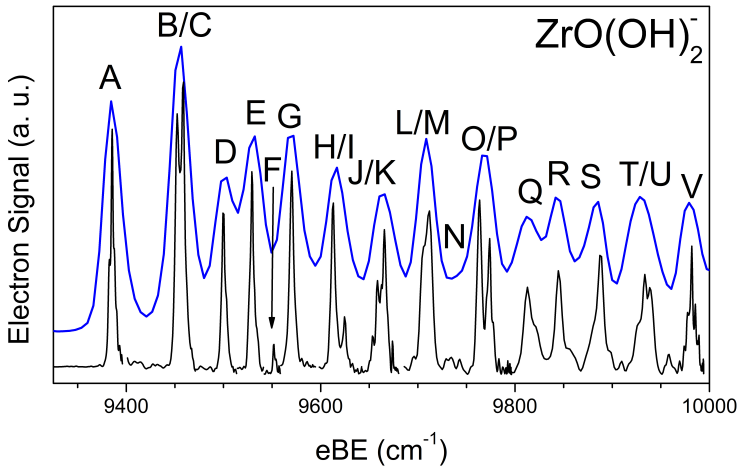

Figure 3.1: Cryo-SEVI spectra of ZrO_3H_2. The overview spectrum (blue, $h\nu$ = 10,747 cm^{-1}) is vertically offset from the high-resolution traces (black, variable photon energies).

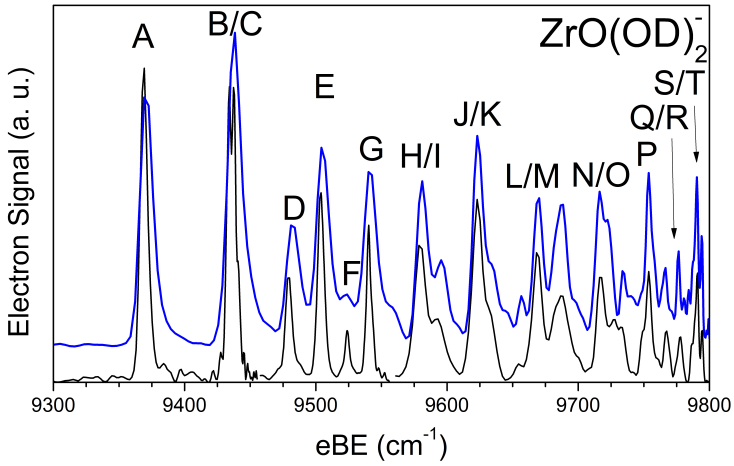

Figure 3.2: Cryo-SEVI spectra of ZrO_3D_2. The overview spectrum (blue, $h\nu$ = 9,802 cm^{-1}) is vertically offset from the high-resolution traces (black, variable photon energies).

eBEs up to ∼10,750 cm^{-1}, high resolution scans were collected only out to ∼10,000 cm^{-1}. see appendix B for the full overview spectrum. These high-resolution traces highlight structure covering eBEs from 9,300 to 10,000 cm^{-1}, revealing a number of transitions (A-V and A-T in ZrO_3H_2 and ZrO_3D_2, respectively) that correspond to detachment to different vibrational levels of the neutral ZrO_3H_2 and ZrO_3D_2 species. Peaks as narrow as 4 cm^{-1} fwhm are reported, owing to strong photoelectron signal at low eKEs where resolution is highest. It should be noted that ions with $m/z = 140$ were chosen despite the possible contribution from $^{92}ZrO_3^-$ as well as the target $^{90}ZrO_3H_2^-$ species; the electron affinity of ZrO_3 has not been experimentally determined, but is calculated to be 3.06 eV, substantially higher than the photon energies employed in this work (<1.35 eV), and thus should not contribute to the reported spectra.

The sharp onset of structure at peak A, the vibrational origin, allows for determination of the EAs for ZrO_3H_2 and ZrO_3D_2 as 1.1636(5) and 1.1616(7) eV, respectively. Beyond peak A, we observe a prominent doublet of peaks (B/C) residing just above 9,400 cm^{-1} in both spectra, split by ∼5 cm^{-1}. A similar doublet is observed near 9,800 cm^{-1} in both spectra (peaks O/P in the spectrum of ZrO_3H_2 and S/T in ZrO_3D_2). Owing to the doublet structure, assignment by inspection is not straightforward, as discussed below.

Experimentally determined parameters are reported in Tables 3.1 and 3.2 for ZrO_3H_2 and ZrO_3D_2, respectively, while peak positions, widths, and assignments are listed in Tables 3.3 and 3.4. Measured PADs of peaks A, B, C, and D are shown in Fig. 3.3. All PADs reported display a similar trend - features have an anisotropy parameter, β, near zero at low eKE that becomes increasingly positive as the eKE rises.

3.3.2 Calculations

The structures found in our previous work[205] on the $TiO_2^{0/-}$+H_2O reaction were used as starting points for minimum energy structure searches. Figure 3.4 shows the minimum energy structures found on the anionic and neutral ZrO_3H_2 potential energy surfaces, along with corresponding zero–point corrected energies relative

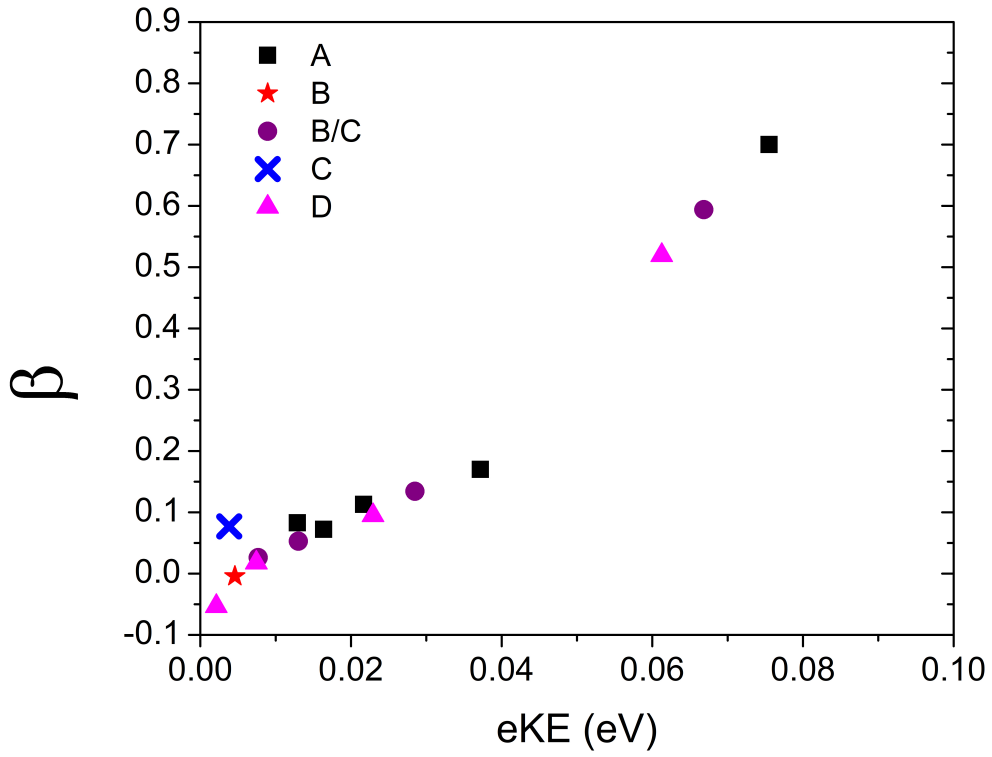

Figure 3.3: Photoelectron angular distributions for peaks A, B, C, and D of ZrO_3H_2

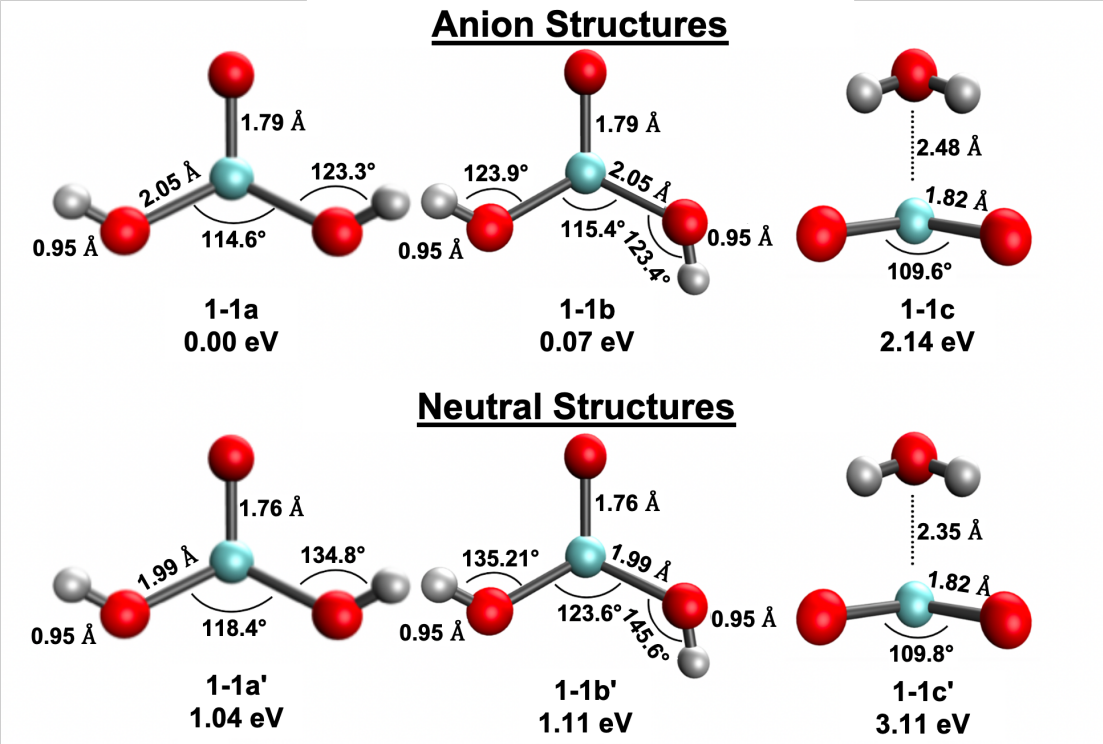

Figure 3.4: Optimized geometries of anionic and neutral ZrO_3H_2 found with ωB97XD/SC. Energies are provided relative to the **1-1a** geometry of the anion and include zero-point corrections. Geometric parameters are also provided.

to **1-1a**. Cartesian coordinates for these optimized structures are provided in appendix B. In agreement with previously reported work by Dixon and co-workers [231] and similar to our previous report on $TiO(OH)_2$,[205] a dissociative adduct (**1-1a′**) with a *cis*-OH geometry was found to be the lowest energy neutral structure. Similarly, the **1-1a** geometry was found to be the lowest energy anion structure. Two other structures were identified for both neutral and anion states, labeled **1-1b** (*trans*–OH) and **1-1c** (molecularly adsorbed). Structure **1-1b** differs from **1-1a** by rotation of one hydroxide ligand and lies only 0.07 eV above the global minimum. Thus the two structures, **1-1a** and **1-1b**, are conformers related by OH bond rotation with a barrier in the anion of 0.016 eV. The neutral *trans*-hydroxide **1-1b′** lies at 0.07 eV above neutral **1-1a′**, while the lowest energy neutral molecularly adsorbed species is 3.11 eV above the anion minimum while it's anion is 2.14 eV above the minimum of the anionic *cis* structure. Interestingly, unlike $TiO_3H_2^{0/-}$, the $ZrO_3H_2^{0/-}$ dissociative adducts are found to have non-planar optimized structures. Given its high relative energy with respect to the dissociative adducts, the molecularly adsorbed adduct **1-1c** was excluded from further consideration. The calculated adiabatic detachment energies (ADEs) for **1-1a** and **1-1b**, 1.04 eV and 1.11 eV respectively, are both in good agreement with the experimental value of 1.1636(5) eV, determined by the position of peak A. NIO analysis for both **1-1a** and **1-1b** shows the detached electron originates in the anion HOMO, which is localized on Zr and strongly resembles a metal d_{z^2} orbital (Fig. 3.5). The similarity of the NIO results suggests that both structures should have similar photodetachment cross-sections and angular distributions.

3.4 Analysis

3.4.1 Assignment of spectra

To examine the possible contributions of the two candidate structures and whether one or both of them are responsible for the observed experimental detachment transitions, we considered FC simulations for electron detachment from both isomers, shown as red sticks for **1-1a** and blue sticks for **1-1b** in Fig. 3.6 and 3.7,

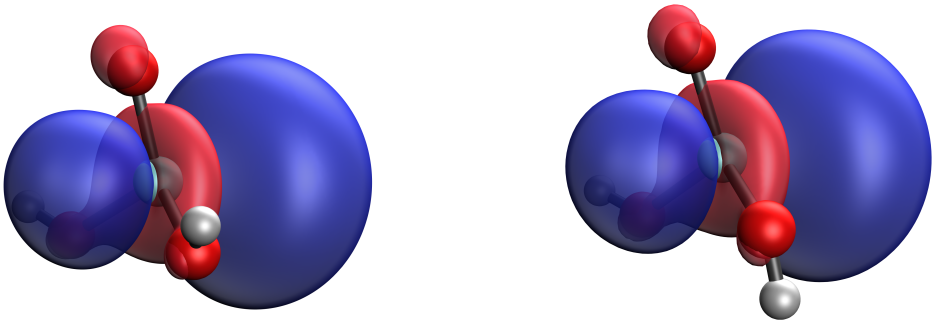

(a) (b)

Figure 3.5: NIO describing the electron detachment from the anion of **1-1a** (a) and **1-1b** (b) to corresponding ground electronic state of the neutral species.

using experimental frequencies when available. Simulated spectra using unscaled frequencies are shown in Fig.3.8. Each isomer has distinct FC progressions; that corresponding to **1-1a** shows a short progression in the out-of-plane bending mode, ν_{12} (ω_{12a} = 73 cm^{-1}), while that of **1-1b** shows an extended progression for the same mode (ω_{12b} = 67 cm^{-1}), owing to a greater change in the dihedral angle between **1-1b** and **1-1b′** than in the **1-1a** manifold as outlined in Tables S7 and S8. Further, FC-simulations for the **1-1b** manifold show considerably more structure due to activity along the ν_{10} and ν_{11} O-H wagging modes (ω_{10b} = 167 cm^{-1}, ω_{11b} = 115 cm^{-1}) that serve as the isomerization coordinate to the **1-1a′** structure.
As shown in Fig. 3.6, simulation of detachment from **1-1a** only replicates features A, B, P, Q, and V of the cryo-SEVI spectrum of ZrO_3H_2, failing to capture the majority of the observed structure. Conversely, simulations for the **1-1b** isomer capture the majority of the spectral structure, but fail to replicate the doublets B/C and O/P observed in the high-resolution traces. A composite of both simulations replicates the observed experimental spectrum well, including the doublet structure of peaks B/C and O/P, suggesting the presence of both isomers in the experiment. In addition to enabling identification of the anion isomers, the well-resolved vibrational structure in the spectra allows us to determine vibrational frequencies of the neutral **1-1a′** and **1-1b′** isomers of $ZrO(OH)_2$ and $ZrO(OD)_2$, as reported in Tables 1 and 2, respectively. Remarkably, we are able to distinguish features arising from transitions along the ν_{12} modes of the **1-1a′** and **1-1b′** isomers, despite their fre-

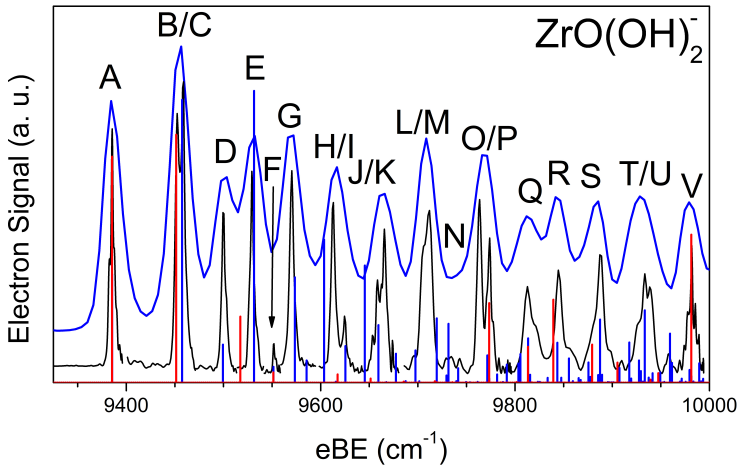

Figure 3.6: Cryo-SEVI spectra of $ZrO_3H_2^-$ overlaid with Franck-Condon stick spectra for the **1-1a** (red) and **1-1b** (blue) isomers.

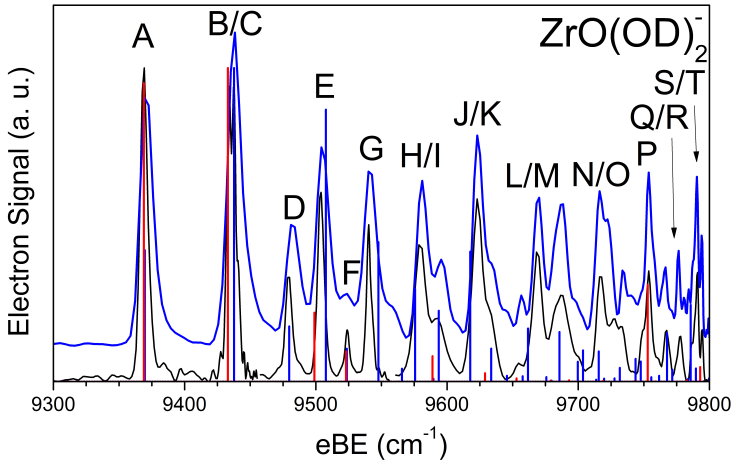

Figure 3.7: Cryo-SEVI spectra of $ZrO_3D_2^-$ overlaid with Franck-Condon stick spectra for the **1-1a** (red) and **1-1b** (blue) isomers.

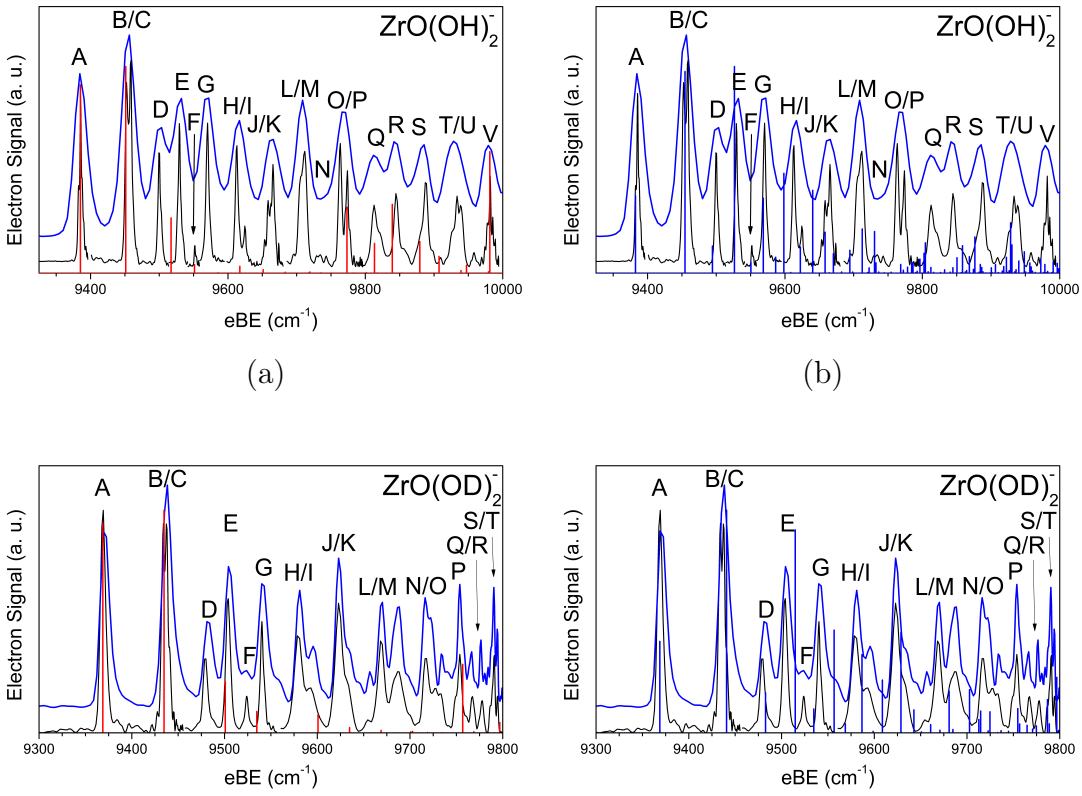

Figure 3.8: Cryo-SEVI spectrum of ZrO_3H_2 (top row) and ZrO_3D_2 (bottom row) with Franck-Condon simulations for detachment from the **1-1a** and **1-1b** anion structures using neutral frequencies that have not been scaled.

quencies differing by only 6 cm^{-1}. One dominant pattern in the spectrum (peaks C, E, and H in both $ZrO(OH)_2$ and $ZrO(OD)_2$) corresponds to a progression of the ν_{12} out-of-plane bend of the **1-1b′** isomer with a vibrational frequency of 73(3) cm^{-1} (69(3) cm^{-1} in $ZrO(OD)_2$). Further, agreement between experimental and computational results allows for assignment of peaks D, F, and N to the vibrational fundamentals of the ν_{11}, ν_{10}, and ν_8 modes of the **1-1b′** isomer, allowing for the determination of their vibrational frequencies as 115(3), 167(2), and 358(3) cm^{-1} (110(4), 155(3), and 347(5) cm^{-1} in $ZrO(OD)_2$).

Table 3.1: Summary of electronic and vibrational energies for neutral $ZrO(OH)_2$ extracted from the cryo-SEVI experiment compared to the (unscaled) results from ωB97XD/SC calculations.

	1-1a′		**1-1b′**	
	Exp	Theor	Exp	Theor
ADE (eV)	1.1636(5)	1.04	1.1636(5)	1.04
ν_5 (cm^{-1})	597(2)	622.8		
ν_6 (cm^{-1})	429(6)	513.7		
ν_8 (cm^{-1})			358(3)	416.8
ν_9 (cm^{-1})	388(4)	428.8		
ν_{10} (cm^{-1})			167(2)	191.0
ν_{11} (cm^{-1})	167(2)	170.3	115(3)	141.0
ν_{12} (cm^{-1})	67(3)	87.6	73(3)	75.0

A similar treatment can be applied for the detachment transition to **1-1a′**. Features B, F, P, Q, and V correspond to transitions involving one quanta along the ν_{12}, ν_{11}, ν_9, ν_6, and ν_5 normal coordinates, allowing for determination of their vibrational frequencies as 67(3), 167(2), 388(4), 429(6), and 597(2) cm^{-1} in $ZrO(OH)_2$. The same vibrational modes are observed in the deuterated spectra, with the exception of the ν_5 mode owing to the truncation of this spectra before its appearance, appearing as features B, F, P, and T with vibrational frequencies of 65(3), 155(3), 384(5), and 425(3) cm^{-1}. The remaining structure in both spectra corresponds

Table 3.2: Summary of electronic and vibrational energies for neutral $ZrO(OD)_2$ extracted from the cryo-SEVI experiment compared to the (unscaled) results from ωB97XD/SC calculations.

	1-1a′		**1-1b′**	
	Exp	Theor	Exp	Theor
ADE (eV)	1.1616(7)	1.04	1.1616(7)	1.04
ν_6 (cm^{-1})	425(3)	395.2		
ν_8 (cm^{-1})			347(5)	316.4
ν_9 (cm^{-1})	384(5)	323.8		
ν_{10} (cm^{-1})			155(3)	181.1
ν_{11} (cm^{-1})	155(3)	159.9	110(4)	117.3
ν_{12} (cm^{-1})	65(3)	82.4	69(3)	70.9

to transitions with excitation along multiple vibrational modes; details of these assignments can be found in Tables 3.3 and 3.4 for $ZrO(OH)_2$ and $ZrO(OD)_2$, respectively. Given that the **1-1b** simulations reproduce most of the spectral features observed, one needs to consider if it is possible to interpret the spectrum with this isomer alone. Previous cryo-SEVI studies have uncovered myriad non-Born Oppenheimer behavior in small molecules that fail to be reproduced by FC simulations, most notably vibronic coupling.[253, 254, 255, 256] The signatures of this phenomenon in cryo-SEVI are well established, arising due to borrowed electronic character from an excited state.[205, 254, 256, 257, 258, 259, 260] Among these signatures are differing photoelectron angular distributions between transitions that are allowed only through vibronic coupling and those that are FC-allowed.

In the present work, doublet splittings of peaks B and P are notably absent from the **1-1b** simulations. For peak B to correspond to a vibronic coupling induced transition, as opposed to a Franck-Condon allowed transition within the **1-1a** band of transitions as listed in Table 1, would require a non-totally-symmetric vibrational frequency on the order of 70 cm^{-1} in the **1-1b′** isomer. No calculated frequency is within a factor of 2 of this value; indeed, the best candidate is the ν_{11} mode (ω_{11} =

141 cm^{-1}) corresponding with the transition that produces peak D. Further, the PADs of features B/C do not differ from one another, as shown in Fig. S10. The similar PADs for detachment from both isomers are in agreement with our NIO analyses that suggest the detached electron resides in a similar orbital for **1-1a** and **1-1b**, resulting in outgoing electrons with similar partial wave composition. As the measured PADs reflect the angular momentum of the detached electron, they are tied to the electronic character of each photodetachment transition and are thus expected not to differ between detachment from **1-1a** or **1-1b**.

An alternative option is that peaks B and P could report on transitions from or to excited anionic or neutral states. The calculated values of the lowest anion and neutral excited electronic states, 1.5 and 4.5 eV above their respective ground states, render them inaccessible as the cryogenic nature of the cryo-SEVI experiment produces ions with electronic temperatures on the order of 10K (0.86 meV)[261, 262, 253] and the photon energies employed in this experiment are $<$ 1.35 eV.

As much of the structure in the **1-1b** FC simulation originates from the ν_{12} umbrella-mode, an alternative possibility for the origin of the doublet structure of peaks B/C and O/P is inversion doubling. Such a process occurs when a vibrational mode distorts a molecule such that it breaks planar symmetry, leading to a double-well potential surface splitting the vibrational levels supported by such a surface, most famously occurring in the umbrella mode of ammonia.[263] If such a double-well surface is capable of supporting both a left and right wavefunction on the anionic potential and both sides of the well are populated, this will give rise to a doublet of transitions following photodetachment.[264, 265] Our calculations indicate that the inversion barrier for the **1-1b** isomer is 1.64 eV, owing to the large dihedral angle of this structure. Considering the high barrier, we expect for contributions from tunneling splitting to be too small to observe. The structure observed in the cryo-SEVI spectra presented is thus most reasonably assigned to photodetchment from two different anion isomers, each resulting in a neutral isomer of similar molecular symmetry and overall structure.

The observation of multiple structural isomers in a cryo-SEVI experiment has

been observed previously in the cryo-SEVI spectra of $Ti_2O_4^-$ and $Zr_2O_4^-$.[222] In that work, the spectra were assigned to detachment from anionic structural isomers with relative energetics (6.7 kJ/mol and 10.5 kJ/mol, respectively) that are comparable to those reported in the present study (7.5 kJ/mol).[222] The assignment to two different isomers of $Ti_2O_4^-$ and $Zr_2O_4^-$ was suggested and supported by FC progressions with dichotomous PADs and notably different onsets resulting from unique adiabatic detachment energies for each isomer. As the structures observed here are conformers related by a bond rotation, it is unsurprising that neither the PADs or ADEs differ substantially in the present work, suggesting the **1-1a** and **1-1b** isomers have ADEs lying within our experimental resolution (2 cm^{-1}). This result is consistent with the calculated energetics that show the energy difference between the *cis* and *trans* conformers are virtually identical in the anion and neutral.

3.4.2 Comparison to $TiO(OH)_2$

The presence of two low-lying anion isomers of the $ZrO_2 + H_2O$ dissociative adduct is in contrast with our previous findings for the Ti-containing analogue of this system, in which we observe detachment solely from the **1-1a** isomer.[205] In that work, the cryo-SEVI spectrum is relatively sparse, displaying less structure in the first 2,000 cm^{-1} than is observed in the 800 cm^{-1} of spectral structure presented here and shows no signs of contribution from the **1-1b** isomer. Given that the experimental conditions to generate both species differ only by the identity of the metal target used to generate clusters of interest, the observation of two isomers in the present study is particularly interesting.

Our calculations show that the energetics of both Ti- and Zr- containing **1-1a** and **1-1b** anions are nearly identical with the **1-1a** structure more stable than **1-1b** by 0.08 and 0.07 eV in the Ti- and Zr- systems, respectively. Further, the calculated barriers to interconversion between the *cis*-**1-1a** and *trans*-**1-1b** structures are similar for these two systems. Here, we calculate the *cis*-to-*trans* barrier for $TiO(OH)_2^-$ to be 803 cm^{-1} (0.100 eV) while the *trans*-to-*cis* barrier is 159 cm^{-1} (0.020 eV). For $ZrO(OH)_2^-$, these barriers are calculated as 737 cm^{-1} (0.091 eV) and

Table 3.3: Peak positions, shifts from peak A, and assignments for the detachment transitions in the cryo-SEVI spectrum of $ZrO(OH)_2^-$. Uncertainties in peak positions correspond to one standard deviation obtained from a Gaussian fit to the corresponding feature in the high-resolution scan.

Peak	**eBE**	**Shift**	**Assignment**	
			1-1a′	**1-1b′**
A	9385(4)	0	0_0^0	0_0^0
B	9452(4)	67	12_0^1	
C	9458(4)	73		12_0^1
D	9500(4)	115		11_0^1
E	9529(4)	144		12_0^2
F	9552(2)	167	11_0^1	10_0^1
G	9570(4)	185		$11_0^1 12_0^1$
H	9613(4)	228		12_0^3
I	9624(2)	239		$10_0^1 12_0^1$
J	9659(6)	274		$9_0^1 12_0^1$
K	9666(4)	281		12_0^4
L	9705(6)	320		$10_0^1 12_0^2$
M	9712(6)	327		$11_0^1 12_0^3$
N	9743(4)	358		8_0^1
O	9763(4)	378		
P	9773(4)	388	9_0^1	$10_0^1 12_0^3$
Q	9814(12)	429	6_0^1	$8_0^1 12_0^1$
R	9844(6)	459	$9_0^1 12_0^1$	$10_0^1 11_0^1 12_0^1$
S	9887(8)	502	$6_0^1 12_0^1$	$11_0^3 12_0^2$
T	9933(3)	548		$10_0^1 11_0^2 12_0^2$
U	9939(4)	554		
V	9982(1)	597	5_0^1	$7_0^1 11_0^1 12_0^1$

Table 3.4: Peak positions, shifts from peak A, and assignments for the detachment transitions in the cryo-SEVI spectrum of $ZrO(OD)_2^-$. Uncertainties in peak positions correspond to one standard deviation obtained from a Gaussian fit to the corresponding feature in the high-resolution scan.

Peak	**eBE**	**Shift**	**Assignment**	
			1-1a′	**1-1b′**
A	9369(6)	0	0_0^0	0_0^0
B	9434(3)	65	12_1^0	
C	9438(3)	69		12_1^0
D	9479(5)	110		11_1^0
E	9504(5)	135		12_2^0
F	9524(3)	155	11_1^0	10_1^0
G	9540(4)	171		$11_0^1 12_0^1$
H	9579(8)	210		12_3^0
I	9593(11)	224	$11_0^1 12_0^1$	$10_0^1 12_0^1$
J	9623(8)	254		$11_0^1 12_0^2$
K	9634(7)	265		$9_0^1 12_0^1$
L	9669(7)	300		$10_0^1 12_0^2$
M	9686(12)	317		$11_0^1 12_0^3$
N	9716(7)	347		8_1^0
O	9729(16)	360		$10_0^1 12_0^3$
P	9753(7)	384	9_1^0	
Q	9767(4)	398		$11_0^3 12_1^0$
R	9778(3)	409		
S	9790(3)	421		$8_0^1 12_1^0$
T	9794(1)	425	6_1^0	

130 cm^{-1} (0.016 eV), respectively, suggesting one might expect similar populations of conformers in each experiment.

Given the similarity in the geometries, energetics, and barriers of these clusters, it is likely that the observation of both the **1-1a** and **1-1b** species in $ZrO(OH)_2^-$ but not $TiO(OH)_2^-$ results from disparate ion temperatures in these two systems. Such a disparity could result from the method by which these clusters are generated – laser ablation of a metal target generates a hot plasma that condenses to form the clusters of interest. It is well established that the cluster condensation process results in significant heating,[266] as the binding energy of each additional atom is deposited into the cluster. Given that such growth events can occur late in the clustering channel and the bond enthalpy of Zr-O exceeds that of Ti-O by nearly 100 kJ/mol,[267] it is likely these two systems will have differing thermal populations prior to entering the cryogenic trap, with $ZrO(OH)_2^-$ hotter than $TiO(OH)_2^-$. The increased temperature will enhance the population of higher lying isomers relative to the global minimum structure and such a distribution is likely to be mirrored in the trap, as buffer gas cooling is known to favor kinetic trapping.[268, 269] Such a result would agree with previous cryo-SEVI studies of clusters, where we find trapping of ions in low-lying local minima.[222, 270, 271]

It should also be noted that in the case of TiO_3H_2, the appearance of the umbrella mode (ν_{12} here, ν_8 in TiO_3H_2) was ascribed to vibronic coupling,[205] while no such non-Born-Oppenheimer process is observed here, despite similar energetics for the states involved. In that work, the Ti-containing analogue was determined to be a planar C_{2v} structure in both its neutral and anionic forms, resulting in an FC-forbidden umbrella mode, as the out-of-plane motion of this vibrational mode breaks the C_{2v} symmetry of the molecule. Conversely, the Zr-containing systems presently observed are non-planar C_s structures with dihedral angles ranging from 20°-30° whose molecular symmetry is not perturbed by the umbrella mode. While this motion can only be observed through vibronic coupling in the Ti-system, such a mode is readily accessible for ZrO_3H_2 without violating the Born-Oppenheimer approximation.

3.5 Reactivity of MO_2 with H_2O

The cryo-SEVI spectrum of unreacted ZrO_2^- has been previously reported, giving an electron affinity of 1.6397(5) eV for the singlet ground state of ZrO_2.[223] The electron affinity of the $ZrO(OH)_2$ dissociative adducts reported here are lower by nearly 0.5 eV, suggesting the neutral $ZrO_2 + H_2O \rightarrow ZrO(OH)_2$ reaction is more exothermic than its anionic counterpart. The reaction with water to form the dissociative $ZrO(OH)_2$ adduct stabilizes neutral ZrO_2 more than it does the anion, implying that the neutral, which has a zirconium center with a +4 oxidation state, is more reactive toward water than anionic ZrO_2 where Zr has an oxidation state of +3. A similar trend in electron affinities was seen for TiO_2 and $TiO(OH)_2$. Taken together, these results suggest that this charge effect likely derives from donation of electron density from the incoming water molecule to the metal center, favoring a higher oxidation state.[205]

Notably, the measured difference in EA for the Ti–containing system was roughly 0.3 eV, suggesting that the addition of water to the Zr-based system stabilizes ZrO_2 relative to its anion a full 0.2 eV (19.2 kJ/mol) more than the Ti–based system. In turn, this implies an increased reactivity of the ZrO_2 moiety compared to TiO_2. As single site catalyst studies have found high photocatalytic activity attributed to the increased reactivity of single TiO_2 structures anchored onto porous surfaces,[272, 273] the results presented here show promise for the development of Zr-based analogues with increased efficiency. While it is difficult to make a direct comparison between the chemistry occurring at the bulk surface and the gas-phase $ZrO_2^{0/-}$ reaction, the trends reported here do reflect the electrochemical behavior of the bulk,[273] especially with respect to a higher oxidation state resulting in a more energetically favorable interaction with water.

3.6 Conclusion

A joint DFT and high–resolution photoelectron study has been used to investigate the hydrolysis of $ZrO_2^{0/-}$. Experimental spectra of $ZrO_3H_2^-$ are reported using slow electron velocity map imaging of cryogenically cooled anions, revealing the presence

of two dissociative adduct conformers and yielding insights into the vibronic structure and energetics of the corresponding neutral species. The high resolution afforded by this technique reveals a dense vibrational manifold dissimilar to the well–separated peaks obtained in the cryo-SEVI study of the titanium analogue.[205] Franck-Condon simulations for both the cis– (**1-1a**) and *trans*–dihydroxide (**1-1b**) structures are required to fully reproduce the complicated cryo-SEVI spectra, representing the first report of the *trans*–hydroxide (**1-1b**) structure of the ZrO_3H_2 system. The appearance of these two isomers is attributed to differing cluster temperatures prior to reaction with H_2O or D_2O, resulting in an enhancement of the population of structure **1-1b** in $ZrO_3H_2^-$. Further, the greater stabilization of water-splitting by ZrO_2 than TiO_2 suggests higher reactivity for Zr-based catalysts, offering new insights into the development of single-site catalysts for H_2 production.

Chapter 4

Modeling Excited–Sates with PIMOM

As we do these fruitful collaboration, what we have not mentioned yet, is the process that involves doing the necessary simulations. There are couple challenges that we face when doing such calculations, one of them is locating the excited state. Sometimes, getting such a state can be important but also tricky. Particularly in the case of the Titanium, locating the excited state was important to explain the experimental spectra. This motivated the work that I will discuss here. These challenges drove researching ways to locate exotic states efficiently. Having an efficient model is crucial to evaluate the second derivatives to simulate the desired spectra. Evaluating the second derivatives is currently available within the linear response models but they get computationally expensive and prohibitive with large systems. Given the mentioned considerations we have investigated the usage of ground state based methodologies to model excited states.

4.1 Introduction

After discussing some advantages and disadvantages of single- and multi-reference methods, we are going to discuss another single-reference approximation. Recalling some of the failures in widely used single-reference methods, TD-DFT and CIS, such as the inability to describe double excitations [274], inaccurately de-

scribing charge-transfer and Rydberg states[75, 76], as well as, the overestimation of excitation energies with CIS.[56, 57] This leads us to explore another single-reference methodology to explore excited states, specifically Δ-self–consistent–field (Δ-SCF).

In this chapter, we present several Δ-SCF-based methods, highlight their pros and cons, and then introduce an affordable computational algorithm termed the projection initial maximum overlap method (PIMOM). After presenting the PI-MOM method, the metric N_{virt} is outlined to assess the behavior of the proposed method. we examine the performance of PIMOM with single excitations, double excitations, and one-electron ionizations for different molecular systems.

4.1.1 Overview on Δ-SCF Methods

Single–configuration SCF approximations are essential for determining the ground state energies of atoms and molecules. The HF method is the simplest of the SCF approximations, and the fundamental scheme for finding the best possible one–electron wave–functions to use in approximating the exact wave–function of multi–electron systems. In computational quantum chemistry, these one–electron wave–functions represent the primary reference for correlated models such as coupled–cluster theory,[275, 276, 277, 28] multi–configurational SCF models,[275, 278, 279, 280, 281] Møller–Plesset perturbation models,[275, 28, 282] etc. The one–electron scheme presented in the HF SCF definition may be improved in the KS formulation of DFT. The DFT approach may correct the HF results by incorporating some of the missing electron–electron interactions and the Coulomb repulsion terms missing in HF. Because of its reduced computational cost, density functional SCF techniques have significantly impacted the avenues for which ground state energies are computed in quantum chemistry and other related fields.

HF and DFT procedures follow a linear variational method, which causes SCF energies to be an upper bound to the exact energy of a system. Thus, the lowest ground state energy that can be computed using the HF SCF method will be the most accurate energy for the many–body system approximated as solutions of many one–electron problems. In many computational implementation and algorithms

for the HF and KS methods, the SCF formulation has at its core, the Aufbau principle.[283, 284, 285] However, the applications of the SCF procedures within an Aufbau principle scheme have been mainly limited to investigation of ground state problems, whereas SCF procedures within a non–Aufbau scheme have been shown to provide access to different electronic states. This suggest that non–Aufbau SCF approximations may be used to explore chemical properties of molecular systems within different states, including electronic excited and ionized states.[286, 287, 283, 288]

Efficient and reliable methods for studying excited electronic states and exotic ground state problems are essential for the application of electronic structure theory to frontier problems in chemistry. In the last few decades, computational chemistry has seen extraordinary advances in ground state and excited state methodologies.[289, 290, 291, 292, 293] In particular, ground state KS DFT and linear response TD-DFT have become the workhorses of modern computational chemistry. Despite these advancements, practitioners still often experience significant challenges with both ground and excited state calculations. In many cases, the desired electronic structure can be quite challenging to locate as part of standard SCF optimizations, if not entirely elusive. Without a reliable methodology or metric to guide these choices, such studies often rely on equal parts of science and art by the practitioner.

For cases where TD-DFT approximations fail to correctly describe molecular systems, excited state approximations based on SCF solutions offer an alternative approach. Different excited states may be approximated by independent SCF solutions. This approach for computing excited state energies is often referred as the Δ-SCF approximation. Excited state energies may be provided by differences in the total energies of two different SCF solutions. This scheme for describing excited states, known as Δ-SCF, provides excitation energies that account for orbital relaxation corrections.

In the last decade, a plethora of different approaches for the Δ-SCF procedure have been proposed in the literature, from which the maximum overlap method (MOM) has been the most explored approach. [294, 275, 295] MOM and its prede-

cessor, the initial maximum overlap method (IMOM), have shown great success in converging solutions corresponding to different electronic excited states. In these methodologies, the orbital population in the SCF procedure is dictated by the overlap between the occupied orbitals on successive SCF iterations instead of the Aufbau principle.

maximum overlap method (MOM)-based approaches have been applied to core-level excitation energies, valence excitations, and excited state geometries.[294, 275, 295] Despite these successes, such techniques can be sensitive to the SCF optimization algorithm and to the given MO guess; thus, the desired non-Aufbau solution can be challenging to obtain. Responding to this observation, multiple groups have proposed alternative algorithms for driving SCF searches to non-Aufbau solutions. Two recent algorithms are the squared–gradient minimization[296] and the state–targeted energy projection.[286]

In the hait2020excited approach, the saddle-point optimization is switched into a proper minimization by optimizing the square of the orbital gradient rather than the energy Lagrangian. This approach may avoid variational collapse in the SCF procedure; however, the method is 2-3× more computationally expensive than the traditional SCF algorithm and may converge to solutions that do not correspond to stationary points in SCF space. The second recent alternative, carter2020state, is closely related to the Big Shift method proposed by Zernert and co-workers in 1982.[297] carter2020state and Big Shift schemes decrease occupied–virtual rotations during SCF iterations by introducing a modified level shift to guide the MO optimization toward a target solution.

A primary attraction of MOMs is the simplicity of the approach. Indeed, most MOMs essentially integrate into SCF programs and used with existing SCF gradient, hessian, and property codes. Nevertheless, there are important and recognized limitations and challenges with MOMs. Whereas recent literature has thoroughly demonstrated the successful use of such models,[298, 296, 294, 275, 295] a challenge that remains is the documented dependence of SCF success on the definition of the modified Aufbau metric (*vide infra*).[299, 300, 301, 302, 297, 303, 304, 305, 296]

In this Chapter, we present a projector-based method that can be added to the

MOM family of methods. We examine the use of MOM and initial maximum overlap method (IMOM) approaches with a non-Aufbau metric based on a projection operator describing a target density in the basis of the current MOs at each SCF iteration. The formulation of the projection maximum overlap method (PMOM) and PIMOM presented in this work provides a simple, yet highly effective, alternative to previous metrics, as well as a useful relationship to population analysis. Based on this formulation, we provide a convenient diagnostic metric, N_{virt}, describing the agreement between target and actual states. The remainder of this chapter describes the PMOM/PIMOM approach, demonstrates the performance of the methods, and illustrates the use of the N_{virt} diagnostic metric.

4.2 PIMOM

4.2.1 Theory

As mentioned above, using MOM-like approaches to drive SCF solvers toward a solution resembling a target electronic structure has been demonstrated in the literature for some time.[306, 307, 297, 302, 300, 308, 309, 310, 311, 312, 294, 275, 295, 313, 314] In this section, we describe our construction of a projection-based framework and a proposed metric for quantitatively assessing the relationship between target and current electronic structure (either specific iterations during the SCF procedure or the converged SCF result). For the remainder of this section, indices employ Pople's convention.[315] Specifically, Greek letters are used to denote atomic orbitals (AOs) and Roman letters denote MOs. MO indices $i, j, k, \ldots$ denote occupied MOs; $a, b, c, \ldots$ denote virtual MOs; and $p, q, r, \ldots$ denote all (both occupied and virtual) MOs. In what follows, the MO coefficients for the target and current electronic structures are given by matrices $\mathbf{C}^{\text{target}}$ and $\mathbf{C}$; the AO overlap matrix is given by matrix $\mathbf{S}$.

This report focuses on the recent MOM implementations by Gill and co-workers, which can be categorized into two general variants.[294, 275, 295] The first category uses the occupied molecular orbitals generated in each SCF cycle as the target state for the next SCF cycle – referred to as MOM. The second approach uses the initial

guess, often prepared by a user from a previous calculation, as a pinned target state for all SCF cycles – referred to as IMOM. In both cases, the SCF procedure is carried out using a modified Aufbau principle where a measure of overlap, or agreement, of each MO with the target state is used in lieu of the canonical MO Fock operator eigenvalues.

The modified Aufbau rule used in MOM schemes can be defined according to an ordered list of metrics, $\{s_p\}$. In general, this list aims to quantify the overlap of each current MO with the occupied MO sub-space of the target state. A variety of $\{s_p\}$ definitions have appeared in the literature. Three such definitions include giving $\{s_p\}$ as the sum of target–occupied–MO/current–MO overlap elements,[313, 295]

$$s_p = \sum_i \left\langle i^{\text{target}} \mid p \right\rangle = \sum_{\mu\nu} \sum_{i^{\text{target}}} C_{\mu i}^{\text{target}} S_{\mu\nu} C_{\nu p}, \tag{4.1}$$

as the square root of the previous sum,[275]

$$s_p = \left(\sum_i \left\langle i^{\text{target}} \mid p \right\rangle \right)^{1/2} = \left(\sum_{\mu\nu} \sum_{i^{\text{target}}} C_{\mu i}^{\text{target}} S_{\mu\nu} C_{\nu p} \right)^{1/2}, \tag{4.2}$$

and as the square-root of the sum of squared target occupied MO/current MO overlap integrals,[294]

$$s_p = \left(\sum_i \left| \left\langle i^{\text{target}} \mid p \right\rangle \right|^2 \right)^{1/2} = \left[\sum_{\mu\nu} \sum_{i^{\text{target}}} \left(C_{\mu i}^{\text{target}} S_{\mu\nu} C_{\nu p} \right)^2 \right]^{1/2}. \tag{4.3}$$

An alternative construction for the modified Aufbau metric, s_p, may be derived using a projection operator. We refer to this approach as PMOM (or PIMOM when the target is the initial determinant). The PMOM/PIMOM scheme begins by defining the target system's density operator, $\mathscr{P}^{\text{target}}$, which projects a ket onto the occupied MO space of the target system:

$$\mathscr{P}^{\text{target}} = \sum_i \left| i^{\text{target}} \right\rangle \left\langle i^{\text{target}} \right|. \tag{4.4}$$

This projection operator can be represented in the basis of the current MOs at each SCF cycle as

$$P_{pq}^{\text{target}} = \left\langle p \left| \mathscr{P}^{\text{target}} \right| q \right\rangle = \sum_i \left\langle p \mid i^{\text{target}} \right\rangle \left\langle i^{\text{target}} \mid q \right\rangle. \tag{4.5}$$

Note that both occupied and virtual current-cycle SCF MOs are necessary to provide a complete basis. When the SCF procedure is carried out in the AO basis, Eq. (4.5) is given by

$$P_{pq}^{\text{target}} = \sum_{i} \sum_{\mu\nu} \sum_{\lambda\sigma} C_{\mu p} S_{\mu\lambda} C_{\lambda i}^{\text{target}} C_{\sigma i}^{\text{target}} S_{\sigma\nu} C_{\nu q}, \tag{4.6}$$

where $\mathbf{C}$, $\mathbf{C}^{\text{target}}$, and $\mathbf{S}$ are the current set of MO coefficients, target system MO coefficients, and the AO overlap matrix respectively.

Given that the MO basis is orthonormal, P_{pq}^{target} can be used to give the target density's gross Mulliken populations partitioned into the current MO basis. With this in mind, the PMOM and PIMOM models define the modified Aufbau metric, s_p, as

$$s_p = \sum_{q} P_{pq}^{\text{target}}. \tag{4.7}$$

In cases where the current set of occupied MOs results in the same electron density as the target system,

$$n_{el} = \sum_{i} s_i, \tag{4.8}$$

where n_{el} is the number of electrons. This observation suggests a simple metric for quantifying agreement between the current and target electron densities. Specifically, we define N_{virt} as the projection of the current virtual MOs onto the target system's occupied MOs,

$$N_{virt} = n_{el} - \sum_{i} s_i = \sum_{a} s_a, \tag{4.9}$$

where N_{virt} is in units of electrons. We note the conceptual similarity of our N_{virt} metric with the excitation number described by Gill and coworkers and promotion number by Head-Gordon et al.[316, 294, 317] In all cases, these different metrics use changes in electron density (in units of electrons) to describe differences between wave functions (or determinants).

Figure 4.1 shows a flowchart demonstrating a standard MOM algorithm. As shown,the algorithm starts with an initial guess that is typically provided by the user and often models a desired electronic excited state. This initial guess provides the atomic overlap and the molecular coefficients that are used to define the

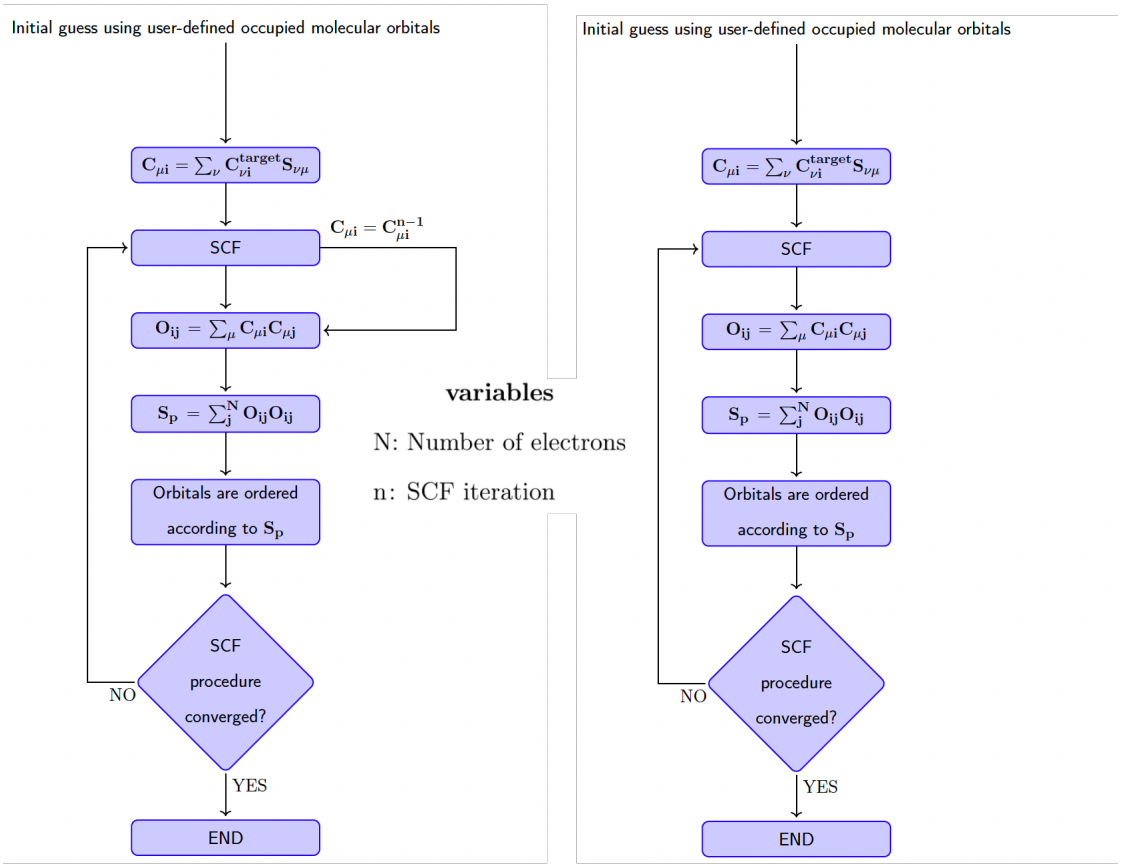

Figure 4.1: Standard PMOM(left)/PIMOM(right) SCF algorithm flowcharts.

projector that is used in each SCF iteration. After the projection of the current SCF state the orbitals are re-arranged and the convergence of the SCF is tested; the process repeats until convergence is met.

4.2.2 Numerical Tests

The MOM, IMOM, PMOM, and PIMOM methods have been implemented in a local development version of the GAUSSIAN suite of electronic structure programs.[318] To demonstrate and validate PMOM and PIMOM, this section considers representative sets of singly excited states, double excited states, and ionized states. Converged electronic structures were characterized by visualization of occupied MOs and using a modified form of the natural ionization orbital (NIO) program by Hratchian and coworkers.[319, 320, 321] Further assessment was carried out by calculation of Δ-SCF results. Initial guess MOs were selected based on the

ground-state, HF-optimized reference. Excited state guesses were generated by obeying the excited state orbital-symmetry, i.e. a pair of the converged ground state orbitals were permuted to yield the correct symmetry of the desired excited state. In cases where molecular symmetry descriptors were not available, natural orbitals were used to define the initial guess reference for the PIMOM method.
The sub-sections below consider different categories of benchmark systems, as discussed above. The performance for each of the MOM, IMOM, PMOM, and PIMOM approaches was evaluated using the number of SCF iterations needed to converge to the desired electronic structure; calculations were considered failed if convergence was not achieved within 500 SCF iterations. A letter "f" is used below to indicate a calculation that converged to an incorrect state or failed to converge within 500 iterations. Calculations that incorrectly converged to the ground state solution were characterized as a variational collapse result and are recorded below as "v.c."

4.2.2.1 Single excitations

A set of representative molecules for the calculation of single exited states, shown in Fig. 4.2, were selected from the literature.[322, 299] All computations were carried out using the Hartree–Fock and B3LYP methods in combination with the Karlsruhe basis set Def2-TZVP (see Table 4.1). When the various tested SCF driver techniques successfully led to convergence to the desired electronic state, the resulting Δ-SCF excitation energies were in good agreement with reference values (see appendix C). MOM failed to access any of the desired states in this test set. IMOM also failed to locate the desired electronic structure in most cases, though IMOM did converge to the correct structure for the $\pi \rightarrow 3s$ tetrafluoroethene excited state at the HF level. PMOM was able to access the desired states for all molecules except nitrobenzene at the HF level, where the calculation exhibited variational collapse to the ground state solution.
PIMOM, on the other hand, successfully led to SCF solutions corresponding to all desired states with both model chemistries. Though IMOM, PMOM, and PIMOM are all able to converge to the same excited state for many of the included test

molecules, the number of SCF iterations needed to converge in each case varied. For instance, IMOM required more iterations to converge than PMOM and PIMOM in the case of the tetrafluoroethene molecule, whereas for nitrobenzene the iterations needed using PIMOM were significantly fewer than needed with PMOM calculations.

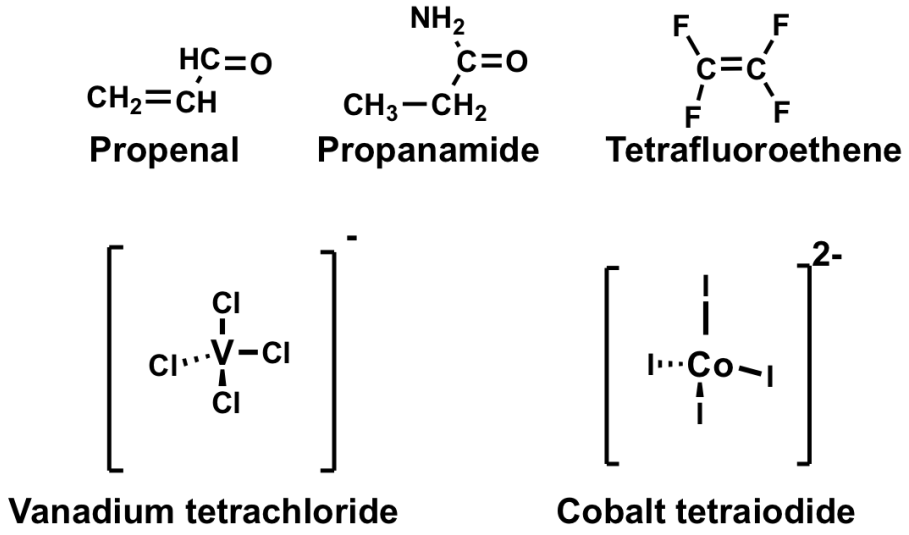

Figure 4.2: Representative set of molecules for singly excited states

The N_{virt} value, Eq. 4.9, is an additional metric to evaluate converged states and is reported for all cases studied in Table 4.2. In the case of the MOM and IMOM methods, the value of N_{virt} is larger than one. Larger N_{virt} values represent multiple-electron deviations from the user-defined target electronic structure. In the case of the converged states with PMOM and PIMOM, the values of N_{virt} are small, which support the notion that the projection-based methods perform well at driving the SCF program to the desired target electronic structure. Fractional N_{virt} values in these cases may be interpreted as the result of orbital relaxation as our target electronic structures were defined by an occupied-virtual permutation of the ground state MO structure. As shown in Table 4.1, PMOM has a v.c. result for nitrobenzene ground state. In this case, $N_{virt} = 1$ indicating that the user-provided target single electron excitation and ground state differ by one occupied-to-virtual transition. For the included vanadium and cobalt complexes,

Molecule	Model Chemistry	Transition	MOM	IMOM	PMOM	PIMOM
Propenal	B3LYP/Def2TZVP	$n \rightarrow \pi^*$	f	f	15	15
	HF/Def2TZVP	$n \rightarrow \pi^*$	f	f	18	18
Propanamide	B3LYP/Def2TZVP	$n \rightarrow \pi^*$	f	f	19	19
	HF/Def2TZVP	$n \rightarrow \pi^*$	f	f	32	31
Tetrafluoroethene	B3LYP/Def2TZVP	$\pi \rightarrow 3s$	f	f	11	11
	HF/Def2TZVP	$\pi \rightarrow 3s$	f	18	16	16
Nitrobenzene	B3LYP/Def2TZVP	$\pi \rightarrow \pi^*$	f	f	29	21
	HF/Def2TZVP	$\pi \rightarrow \pi^*$	f	f	v.c	44
Vanadium tetrachloride	B3LYP/LANL2DZ	$^4T_2$	f	f	19	19
	HF/LANL2DZ	$^4T_2$	f	f	13	13
Cobalt tetraiodide	B3LYP/LANL2DZ	$^4T_2$	f	f	13	13
	HF/LANL2DZ	$^4T_2$	f	f	16	16

Table 4.1: Number of SCF iterations required to converge to the targeted singly excited state. The failure of the SCF procedure to converge to either the target or any solution is indicated with the letter "f," whereas variational collapse is indicated by "v.c."

the $^4T_2$ state has previously only been accessible via the guided SCF method.[299] The current work demonstrates that PMOM and PIMOM were able to reproduce the same results.

Figures 4.3 and 4.4 show the progress of the SCF procedure for the case of the $\pi \rightarrow \pi^*$ excitation of nitrobenzene. Energy as function of SCF cycle number is shown in Fig. 4.3; the metric N_{virt} as function of the SCF cycle number is presented in Fig. 4.4. As shown in Fig. 4.3(a), MOM and IMOM present a high degree of energy oscillations after a few SCF iterations (5 iterations) and the SCF energy in these cases eventually diverges from the desired final state energy. This is also reflected in the value of N_{virt}. In both MOM and IMOM calculations, N_{virt} presents iterations with quite large values. These two observations suggest that MOM and IMOM, in the current implementation and using the simple initial guess wave functions employed here, can drift far from the desired solution.

Figures 4.3 and 4.4 also show results for PMOM and PIMOM calculations. The behavior of PMOM leads to variational collapse to the ground state with a N_{virt}

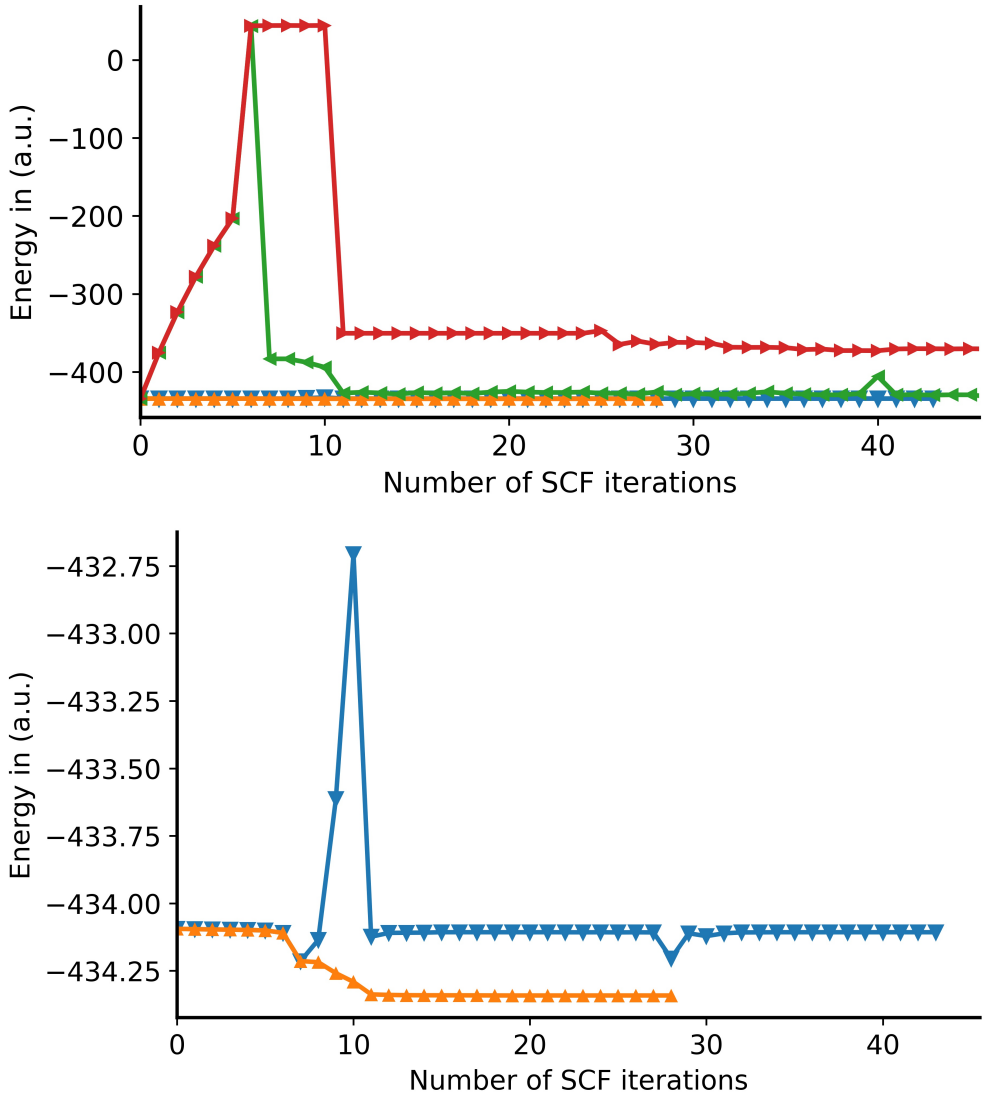

Figure 4.3: Energy convergence to SCF solutions for the excited state of nitrobenzene with MOM (red traces), IMOM (green traces), PMOM (orange traces), and PIMOM (blue traces). Plot (a) shows the results of all the approaches while (b) shows PMOM and PIMOM only. The first 45 cycles are shown. MOM and IMOM did not converge after 500 cycles, PMOM collapsed to the ground state after 27 cycles, and PIMOM converged after 44 cycles.

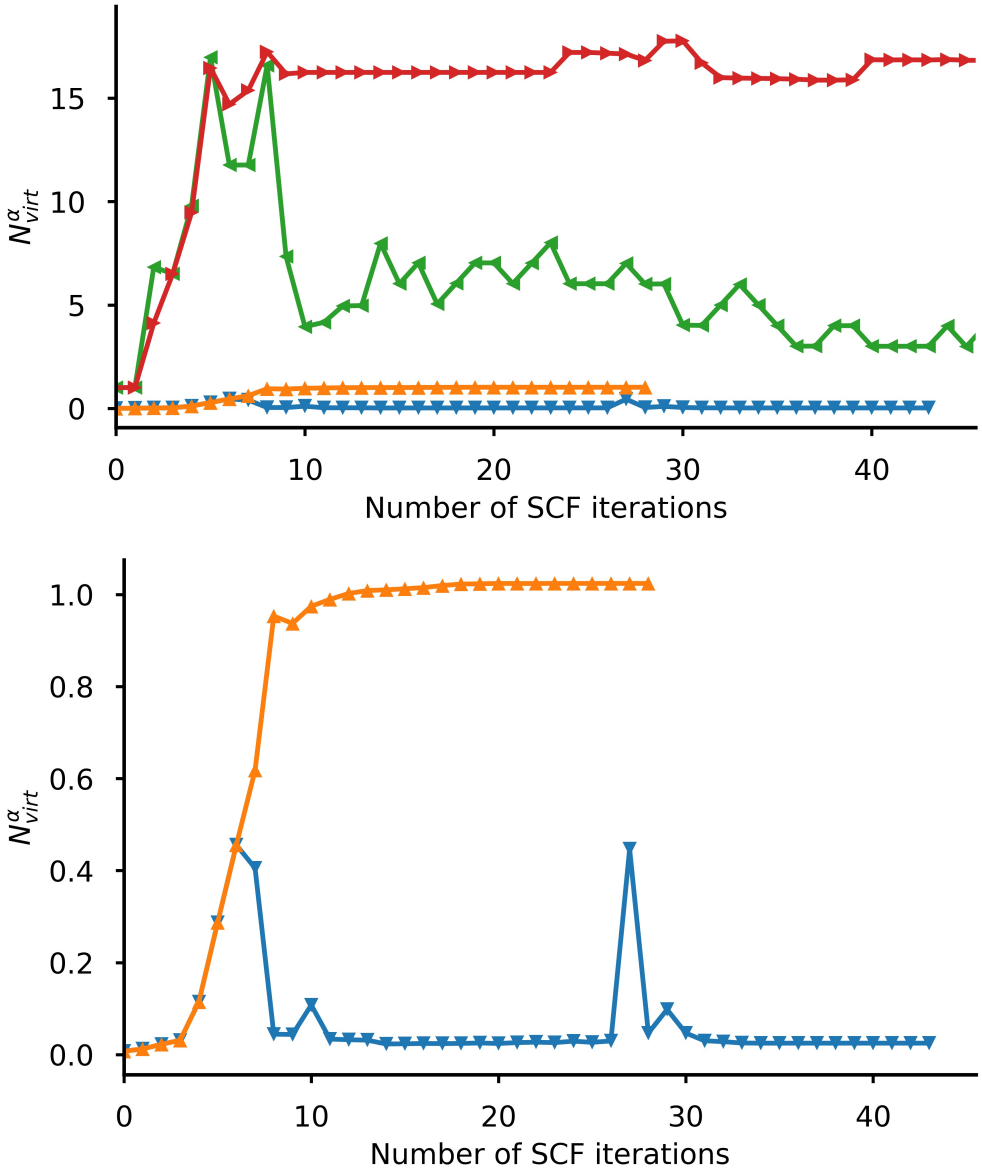

Figure 4.4: N^{α}_{virt} metric at each SCF iteration for the excited state of nitrobenzene with MOM (red traces), IMOM (green traces), PMOM (orange traces), and PIMOM (blue traces). Plot (a) shows the results of all the approaches while (b) shows PMOM and PIMOM only. The first 45 cycles are shown. MOM and IMOM did not converge after 500 cycles, PMOM collapsed to the ground state after 27 cycles, and PIMOM converged after 44 cycles.

Molecule	Model Chemistry	MOM	IMOM	PMOM	PIMOM
Propenal	B3LYP/Def2TZVP	3.1 | 4.2	3.1 | 8.1	0.1 | 0.1	0.1 | 0.1
	HF/Def2TZVP	4.0 | 6.3	5.1 | 6.1	0.4 | 0.1	0.4 | 0.0
Propanamide	B3LYP/Def2TZVP	6.0 | 1.1	10.5 | 11.1	0.0 | 0.0	0.0 | 0.0
	HF/Def2TZVP	2.8 | 7.1	6.7 | 9.1	0.6 | 0.1	0.6 | 0.1
Tetrachloroethane	B3LYP/Def2TZVP	1.0 | 1.0	2.0 | 1.0	0.0 | 0.0	0.0 | 0.0
	HF/Def2TZVP	7.1 | 7.2	0.0 | 0.0	0.0 | 0.0	0.0 | 0.0
Nitrobenzene	B3LYP/Def2TZVP	6.0 | 4.1	1.0 | 4.0	0.0 | 0.0	0.0 | 0.0
	HF/Def2TZVP	17.5 | 15.7	6.0 | 5.0	1.0 | 0.1	0.0 | 0.0
Vanadium tetrachloride	B3LYP/Def2TZVP	7.8 | 6.8	8.4 | 6.3	0.2 | 0.0	0.2 | 0.0
	HF/Def2TZVP	7.5 | 7.5	8.2 | 7.0	0.6 | 0.1	0.6 | 0.1
Cobalt tetraiodide	B3LYP/Def2TZVP	11.0 | 7.6	11.9 | 11.8	0.0 | 0.3	0.0 | 0.3
	HF/Def2TZVP	7.1 | 6.7	11.0 | 9.1	0.0 | 0.6	0.0 | 0.6

Table 4.2: Values of the N_{virt} metric for singly excited states. Values corresponding to the α and β spin–orbital spaces are separated by a vertical pipe.

value of 1.0. This value corresponds to the one electron difference between the desired excited state and converged ground state SCF solutions. Again, the N_{virt} metric provides a useful tool for assesing the behavior of such Δ-SCF methods. On the other hand, PIMOM shows steady convergence to the correct excited state solution. As expected, N_{virt} for the final PIMOM converged wave function is nearly zero.

4.2.2.2 Double excitations

Figure 4.5 shows a set of arene examples included to study the use of the tested schemes on double-excitation states. This set has been used in earlier work reporting IMOM.[294] We also include the $1\sigma_g^2 \rightarrow 1\sigma_u^2$ excitation in H_2 using the augmented mcc-pV8Z plus additional $2f2g$ diffuse functions. In all cases, we were able to reproduce previously reported energy values. Table 4.3 reports our results for the arene molecules. The MOM was only able to access one of the targeted states, whereas IMOM was unable to converge to any of the targets. PMOM and PIMOM required the same number of iterations to converge to the same energy values for all states. The values of N_{virt} for this set of molecules, shown in Table 4.4, are again consistent with our interpretation of N_{virt}. For the converged states, the value of N_{virt} is smaller than 1 and corresponds to orbital relaxation in

the excited state.

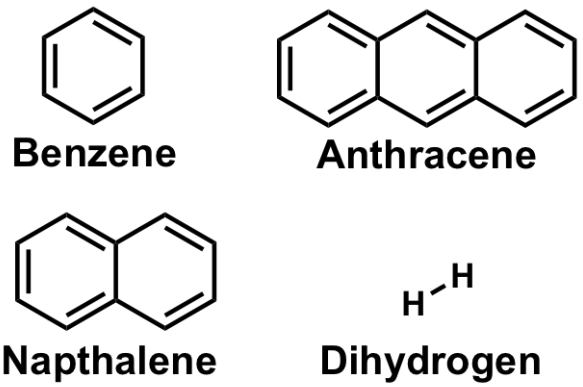

Figure 4.5: Representative set of molecules for doubly excited states

Molecule	Model Chemistry	State	MOM	IMOM	PMOM	PIMOM
Benzene	BLYP/6-311G*	$5\ ^1A_g$	f	f	9	9
	HF/6-311G*	$5\ ^1A_g$	f	f	10	10
Napthalene	BLYP/6-311G*	$4\ ^1A_g$	9	f	9	9
	HF/6-311G*	$4\ ^1A_g$	f	f	11	11
Anthracene	BLYP/6-311G*	$2\ ^1A_g$	f	f	12	12
	HF/6-311G*	$2\ ^1A_g$	f	f	14	14

Table 4.3: Number of SCF iterations required to converge to the doubly excited target state. The failure of the SCF procedure to converge to either the target or any solution is indicated with the letter "f".

4.2.2.3 Ionizations

Ionized states were evaluated by computing the ionization energy corresponding to electron detachment from orbitals other than that of the HOMO of the initial state. Results for a representative set of molecules are presented in Table 4.5, showing only PMOM and PIMOM successfully accessed all ionized states and did so within the same number of SCF iterations. MOM and IMOM only converged to the desired ionized state for formaldehyde. In that particular case, the number

Molecule	Model Chemistry	MOM	IMOM	PMOM	PIMOM
Benzene	BLYP/6-311G*	4.1	3.3	0.0	0.0
	HF/6-311G*	3.3	4.1	0.0	0.0
Naphthalene	BLYP/6-311G*	0.0	10.5	0.0	0.0
	HF/6-311G*	10.1	15.9	0.0	0.0
Anthracene	BLYP/6-311G*	8.4	14.0	0.0	0.0
	HF/6-311G*	14.8	16.0	0.1	0.1

Table 4.4: Values of the N_{virt} metric for the computed doubly excited states.

of SCF iterations was the same as those for PMOM and PIMOM. As in previous cases, the N_{virt} values for the converged states have values less than 1 (Table 4.6). The ionization energies computed for the converged states are in good agreement with literature values.[323]

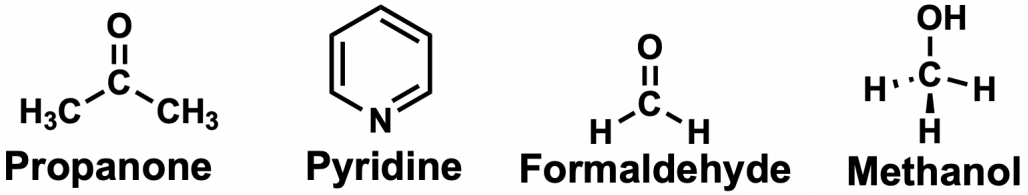

Figure 4.6: Representative set of molecules for ionized states

4.2.3 Conclusions

This work described and assessed the PMOM and PIMOM projection-based pair of maximum-overlap-methods. For the systems examined here, PIMOM is a particularly robust member of the maximum-overlap-method family. In particular, this work has demonstrated that the PIMOM can converge to intended electronic structure solutions using relatively simple user-provided initial guess reference as a target wave function. Specifically, this report used permutations of ground state occupied/virtual MO pairs as initial and target wave functions.

As shown above, the PMOM and PIMOM both perform quite well. Indeed, for the cases included here, PMOM and PIMOM are the most consistent and efficient of the MOMs considered. In most cases, PMOM and PIMOM require the same

Molecule	Model Chemistry	State	MOM	IMOM	PMOM	PIMOM
Propanone	B3LYP/6-311G(d,p)	$2b_1$	f	f	13	13
	HF/6-311G(d,p)	$2b_1$	f	f	16	16
Methanol	B3LYP/6-311G(d,p)	$7a'$	f	f	12	12
	Hf/6-311G(d,p)	$7a'$	f	f	18	18
Pyridine	B3LYP/6-311G(d,p)	$9b_2$	f	f	14	14
	Hf/6-311G(d,p)	$9b_2$	f	f	21	21
formaldehyde	B3LYP/6-311G(d,p)	$1b_1$	10	10	10	10
	HF/6-311G(d,p)	$1b_1$	13	13	13	13

Table 4.5: Number of SCF iterations required to converge to the correct ionized state. The failure of the SCF procedure to converge to either the target or any solution is indicated with the letter "f."

number of iterations to converge. At first glance, this may suggest no apparent advantage from using PIMOM versus PMOM. However, in cases such as nitrobenzene, PMOM exhibits variational collapse and results in optimization to the ground state, which is consistent with previous literature showing that the *initial* guess wave function is generally a better target choice for maximum-overlap-methods than the evolving wave function from the previous SCF cycle.[294]

The presented N_{virt} metric provides a simple and conceptually convenient measure of agreement between the desired target and the current or final SCF results during a calculation employing a maximum-overlap method. In successful calculations, N_{virt} values were close to zero. For the cases in which a maximum-overlap scheme failed to converge to the desired solution, the N_{virt} values comparing a target SCF solution and final result were greater than 1. And in cases where the final SCF solution resulted from variational collapse, N_{virt} is roughly equal to the number of intended excited electrons. We envision using N_{virt} during a maximum-overlap-method based calculation to identify problematic SCF optimizations early in the iterative process. One could envision incorporating such a metric with tools meant to stabilize the optimization process, such as the recently reported carter2020state technique.[286]

Although PIMOM has been shown to be a reliable method for converging chal-

Molecule	Model Chemistry	MOM	IMOM	PMOM	PIMOM
Propanone	B3LYP/6-311G(d,p)	4.1 | 3.1	2.1 | 3.1	0.0 | 0.1	0.0 | 0.1
	HF/6-311G(d,p)	2.8 | 7.1	6.7 | 6.0	0.6 | 0.1	0.6 | 0.1
Methanol	B3LYP/6-311G(d,p)	1.1 | 3.0	2.0 | 2.0	0.0 | 0.1	0.0 | 0.1
	HF/6-311G(d,p)	1.0 | 2.4	1.0 | 1.3	0.0 | 0.6	0.0 | 0.6
Pyridine	B3LYP/6-311G(d,p)	8.7 | 7.3	6.1 | 5.4	0.0 | 0.0	0.0 | 0.0
	HF/6-311G(d,p)	6.5 | 6.8	11.0 | 7.3	0.1 | 0.2	0.1 | 0.2
formaldehyde	B3LYP/6-311G(d,p)	0.0 | 0.0	0.0 | 0.0	0.0 | 0.0	0.0 | 0.0
	HF/6-311G(d,p)	0.0 | 0.1	0.0 | 0.1	0.0 | 0.1	0.0 | 0.1

Table 4.6: Values of the N_{virt} metric for the different ionized excited states computed. Values corresponding to the α and β spin–orbital spaces are separated by a vertical pipe.

lenging SCF solutions, questions remain regarding the resemblance of converged PIMOM SCF solutions and molecular electronic states and about limitations when describing wave functions that may be properly multi-determinantal in nature. The presented PIMOM formulation employs a simple form for the projector operator. In some cases, the $\mathscr{P}^{\text{target}}$ operator may not be compactly representable for a system's Hilbert space. In these cases, one may find degenerate sub-spaces corresponding to a single eigenvalue of the operator containing multiple (perhaps infinite) $|i\rangle\langle i|$-like terms[324, 325, 326, 327, 328]. For such cases, two-argument projector operators may be more prudent for the formulation of the PIMOM algorithm. Work exploring such questions is underway.

Chapter 5

Good Vibrations: Calculating Excited State Molecular Properties Using PIMOM

After developing and testing PIMOM to locate excited states, the next step is to test the applicability of PIMOM to optimize excited state structures and evaluate molecular properties. In this chapter, I will present and analyse the results obtained by using PIMOM to optimized and evaluate excited state for a representative data set.

5.1 Introduction

The interest in electronic excited states arises from their importance in fields as varied as photochemistry, analytical chemistry, materials science, and biology.[329, 330, 331, 332, 333, 334, 335, 336, 337, 338, 339] Insights into photochemical and photophysical processes are often reliant on information about excited–state potential energy surfaces, such as their effects on geometry changes upon excitation.[340, 341] Based on vibrational modes' dependence on molecular geometries may generate different vibrations, induce forbidden transitions, or facilitate non–adiabatic coupling.[342, 343] Advancements in experimental techniques involving exited–state molecules demand accurate and efficient computational routes to excited–

state geometries and electronic structure of molecules.

Variational computational chemistry methods based on Slater determinants built of spin–orbitals provide a foundation for defining and computing SCF, configuration–interaction, and other types of wavefunctions. These methods and those based on probability densities constrained by Slater determinant requirements produce reasonable approximations for molecular excited–states and the description of some of their properties.[9, 344, 345] In particular, computational methods based on the HF and KS equations have proven effective in calculating binding energies, excitation energies, and corresponding transition probabilities. More precise descriptions of excited states may be obtained by multiconfigurational methods,[346, 82, 347] where, in addition to the ground–state Slater determinant, determinants constructed via swaps of occupied with virtual orbitals are included in the SCF. In multiconfigurational methods, Slater determinants are weighted by expansion coefficients obtained variationally by diagonalizing the Hamiltonian matrix.[348] These expansion coefficients and the spin–orbitals are further optimized in the SCF, which makes addressing large systems prohibitively expensive computationally.

In the Hartree–Fock theory framework, an alternative for dealing with strongly correlated molecular systems is provided by the couple cluster (CC) method, which is intended as a more efficient procedure to approximate the full configuration–interaction wavefunction. In general, the accuracy of CC computational methods depends on the truncation level in the CC expansion, the larger the expansion the more accurate the result. However, larger CC expansions come with higher computational costs, limiting CC methods to a smaller set of applications. On the other hand, the Kohn–Sham framework offers a density–based approach framed as TD-DFT.[49, 136, 137, 349] In TD-DFT, the complicated many–body time-dependent Schrödinger equation is reformulated by a set of time–dependent single–particle equations whose orbitals yield the same time–dependent density. Although the TD-DFT equations may be formally exact, their computational implementation requires an approximation for the unknown XC potential. These DFT approximations have proven to be effective in many cases, and in fact, TD-DFT has achieved massive success in different areas.[350, 351, 352, 353, 354, 355, 356, 357, 358, 359,

360, 361, 362, 363, 364, 365]

Among the methods based on the cluster expansion of Slater determinants, the so-called CI single approximation (Configuration Interaction Singles (CIS)) where only single orbital substitutions are generated, and TD-DFT may be the only candidates for addressing large molecular systems. Although these methods provide, in many cases, enough information for the characterization of excited–state systems, they both suffer from limitations. CIS neglects important contributions to electron correlation and, since only single substitutions are considered, CIS cannot describe doubly excited states.[56] On the other hand, the available TD-DFT approximations give substantial errors for excited states of molecules with extended π–systems,[73, 74] and cannot accurately describe double excitations or charge–transfer (CT) states.[75, 366, 367] Despite inherited errors in the chosen method, vertical excitation energies (VEEs), which are computationally feasible, lack the accuracy needed for experimental observables. For example, comparing VEEs to experimental absorption maxima is plausible and appropriate if and only if three specific requirements are met: 1) the geometry of the molecule does not change upon excitation (i.e., the Franck-Condon approximation), 2) the transition probability is maximized at the ground state minimum, and 3) the absorption maxima are independent of vibronic and rotational effects. According to Herzberg, these conditions are usually not satisfied even in simple cases, such as transitions in CS_2 or HCN.[368, 369] This difficulty is compounded by the computational expense of optimizing excited–states, calculating adiabatic detachment energies, and acquiring properties, such as frequencies and dipole moments.

One way to describe excited–states and obtain orbital relaxed excited determinant is through Δ-SCF methods. In the past decade, Gill and coworkers reintroduce the idea of SCF calculations for excited–states using the maximum overlap method (MOM), which was further upgraded to the initial maximum overlap method (IMOM).[295, 370] This concept has been used to explore different electronic and structural properties in molecules. [370, 295, 306, 307, 300, 308, 309, 310, 311, 296, 286] In such methodologies, standard ground–state SCF algorithms are used in IMOM to find a stationary point in the SCF space that maximizes

the overlap with the occupied orbital space defined by an initial guess set of occupied one–electron (molecular) orbitals. However, these low–cost approaches often suffer from a number of challenges, including convergence difficulties and variational collapse. In the previous chapter, the projected initial molecular overlap method (PIMOM), an interpretive tool based on MOM and IMOM, were shown to provide new insights helpful in overcoming some of the challenges of the previous algorithms and providing better chemical and physical understanding for the maximum overlap models.[371]

Although Δ-SCF methods provide a computationally feasible approach, they result in broken–symmetry (BS) solutions. The BS determinant often shows a mixture of different spin–pure configurations and results in the so–called spin contaminated state. Errors corresponding with these solutions may results in a significant change in the energies, demanding a way to remedy those errors. Correcting spin contaminated states may be done using spin–projection methods. Among other methods, the approximate projection (AP) technique, which was proposed by Yamaguchi and co–workers, [372] has been successfully used in correcting spin–contamination errors.[373, 374, 375, 376, 377]

In this chapter, the competence of the PIMOM framework for geometry optimization and frequency calculation of excited–states molecules is explored. An overview of the method and computational details are given. Assessing the method and exploring the effect of approximate spin–purification procedure are also explored. Final remarks and conclusions are given at the end of the chapter.

5.2 Computational Methods

5.2.1 Initial Projected Maximum Overlap Method

Standard self–consistent–field eigenstates solutions are achieved by iteratively solving the following equation,

$$\mathbf{FC} = \mathbf{SC}\varepsilon \tag{5.1}$$

where $\mathbf{F}$ is the Fock or Kohn–Sham matrix, which depends on molecular orbital (MO) coefficients matrix,$\mathbf{C}$. $\mathbf{S}$ is the overlap matrix in the atomic orbital basis,

and ε is the orbital energy vector. The conventional way of solving this eigenvalue problem is by diagonalizing $\mathbf{F}$, obtaining a new set of MOs and filling the lowest MOs using the Aufbau principle until convergence. Reasonable approximations for SCF excited–state solutions may be produced by imposing additional control over the spin–orbitals through symmetry restrictions, overlap matching, inclusion of additional constraints on Lagrangian functions or other means.[378, 312, 379, 380, 381] Fulfillment of stationary conditions, usually of the Brillouin type[382, 383] is the usual criterion for self–consistency, but in some cases this standard cannot be applied.[384, 158] A practical strategy for accessing excited–states solutions may be incorporated in the Δ-SCF methods, where instead of the Aufbau principle, Δ-SCF methods use a projector operator that dictates the orbitals' ordering, as one finds in conventional MOM-based approaches. The Δ-SCF method's algorithm begins by defining the target system's density projector, $\mathscr{P}^{\text{target}}$,

$$\mathscr{P}^{\text{target}} = \sum_{i}^{N} \left|\varphi_i^{\text{target}}\right\rangle \left\langle\varphi_i^{\text{target}}\right|. \tag{5.2}$$

In the MO basis of the current SCF cycle, Eq. (5.2) reads

$$P_{pq}^{\text{target}} = \langle p \left|\mathscr{P}\right| q\rangle = \sum_{i} \left\langle p \;\middle|\; i^{\text{target}}\right\rangle \left\langle i^{\text{target}} \;\middle|\; q\right\rangle, \tag{5.3}$$

where the same AO basis set is required for the target and current SCF state. Thus, Eq. (5.3) may be rewritten as

$$P_{pq}^{\text{target}} = \sum_{i} \sum_{\mu\nu} \sum_{\lambda\sigma} C_{\mu p} \langle \mu \mid \lambda \rangle C_{\lambda i}^{\text{target}} C_{\sigma i}^{\text{target}} \langle \sigma \mid \nu \rangle C_{\nu q}, \tag{5.4}$$

where $\langle \mu \mid \nu \rangle$ are the AO overlap matrix elements, $S_{\mu\nu}$. In equation (5.4), the target density matrix in the AO basis may be expressed as $P_{\mu\nu}^{\text{target}} = \sum_i C_{\mu i}^{\text{target}} C_{\nu i}^{\text{target}}$. Thus, equation (5.4) may be written in matrix form as

$$\mathbf{P}_{(MO)}^{\text{target}} = \mathbf{C}^T \mathbf{S} \mathbf{P}^{\text{target}} \mathbf{S} \mathbf{C}, \tag{5.5}$$

where the subscript "MO" has been included to clearly indicate that the resultant density matrix is given in the current MO basis. Using this equation, the metric employed in the Δ-SCF method to order the MO orbitals is given by

$$s_p = P_{pp}. \tag{5.6}$$

In the Δ-SCF approach, different SCF excited–state solutions are accessed by generating s_p values using an initial vector state guess, similar to the IMOM procedure.[370] Δ-SCF methods add an additional constraint to the SCF procedure by anchoring the initial guess vector state and projecting it in the vector state of each SCF cycle. Since the projection is defined using an initial vector space, it is crucial that the initial guess resembles the desired excited state.

5.2.2 Approximate Projection Method

The effect of spin contamination on adiabatic excited states is investigated. For this purpose, the approximate projection (AP) model of Yamaguchi and co–workers[372] was employed. This model has been expanded to include first and second derivatives.[385, 386] In fact, several works have shown the effectiveness of this model and demonstrated the condition for which this model is suitable. [387, 376, 388, 377] To carry out AP calculations, two converged determinants are required: (1) a broken–symmetry state, i.e.,the contaminated state, and (2) a spin–pure high–spin state. Using those determinants, the AP energy expression is constructed as follows:

$$E_{AP} = \alpha E_{LS} + (1 - \alpha) E_{HS} \tag{5.7}$$

where

$$\alpha = \frac{\langle S^2_{HS} \rangle - S_{z,LS}(S_{z,LS} + 1)}{\langle S^2_{HS} \rangle - \langle S^2_{LS} \rangle} \tag{5.8}$$

Subscript low–spin (LS) refers to (broken–symmetry) low-spin state, and high–spin (HS) corresponds to (spin-pure) high-spin state.

5.2.3 Computational Details

In order to demonstrate the robustness and effectiveness of Δ-SCF methods for excited–state properties, the adiabatic energies and vibrational frequencies of a representative set of molecules were calculated. The results obtained with Δ-SCF methods were compared with results obtained with CIS, TD-DFT, and experimental data. All ground and excited–state structures were optimized using ti83's three–parameter hybrid functional with Lee–Yang–Parr correlation (B3LYP)[389]

and Hartree–Fock method,[390] with four different basis sets, two Pople basis sets, 6-311G and 6-311++G(d,p)[391, 392, 393, 394, 395] , and two Dunning basis sets, aug-cc-pVDZ and aug-cc-pVTZ.[396, 397, 398, 399, 400, 401, 402, 403] All the Δ-SCF results were obtained using an implementation of the PIMOM method for Δ-SCF in a local development version of Gaussian.[318] Molecular geometries for ground–state structures were optimized using standard methods,[246] and the reported potential energy minima were verified using analytical second–derivative calculations. The ground–state minimum structures were used as a starting point for the optimization using Δ-SCF methods, and those were also verified using analytical second–derivative calculations. Initial guesses for Δ-SCF methods were generated by permuting orbitals of the ground–state converged wavefunction resembling the desired excited–state. AP–Δ-SCF calculations and optimizations were carried out on the spin contaminated systems and verified using analytical second–derivative calculations. Excited–state calculations were also carried out using the same model chemistry within the time–dependent DFT (TD-DFT) formalism[49, 136, 137] and CIS to evaluate the performance of Δ-SCF methods.[47]

5.3 Results and Discussions

5.3.1 Data Set

Excited–state computation tools are expensive and somewhat limited compared to the ground–state toolbox, especially for polyatomic molecules. The purpose of this study is to investigate the modified SCF algorithm, PIMOM, to access different excited states, as well as describe their spectroscopic properties in specific, fundamental vibrational frequencies. This data set was chosen based on available experimental results from gas–phase spectroscopy and can be carried out using the two well–known, relatively feasible, CIS and TD-DFT methods.[4, 5, 404, 405, 406, 407, 408, 409, 410, 411] Furthermore, this data set was chosen to contain various diatomic and polyatomic molecules, in which the excited states have different character and spin multiplicity.

5.3.2 Adiabatic Excitation Energies

Table 5.1: Calculated adiabatic excitation energies (eV) using TD-DFT and Δ-DFT in comparison with the experiment.

		6–311G		6–311++G(d,p)	
Sys	**Exp.**	**TD-DFT**	**Δ-DFT**	**TD-DFT**	**Δ-DFT**
BH	2.87	2.75	1.67	2.74	1.69
BF	6.34	6.13	4.24	6.09	4.31
SiO	5.31	4.83	4.12	5.20	4.44
CO	8.07	7.51	6.21	7.95	6.60
N_2	8.59	7.92	6.97	8.50	7.53
ScO	2.04	1.35	1.77	2.00	1.72
BeH	2.48	2.58	2.37	2.56	2.35
AsF	3.19	2.95	2.96	2.87	2.87
NH	3.70	3.98	3.64	3.90	3.61
CrF	1.01	1.47	1.44	1.25	1.23
CuH	2.91	3.35	2.46	2.98	2.70
Li_2	1.74	1.93	1.09	1.93	1.07
Mg_2	3.23	3.45	2.32	3.26	2.26
PH_2	2.27	2.19	2.13	2.34	2.24
CH_2S	2.03	2.04	1.64	2.06	1.67
C_2H_2	5.23	4.92	4.64	4.70	4.38
$C_2H_2O_2$	2.72	2.21	1.93	2.42	2.12
HCP	4.31	3.91	3.74	3.86	3.60
HCN	6.48	6.02	5.70	5.95	5.59
C_3H_4O	3.21	2.98	2.64	3.15	2.78
CH_2O	3.49	3.36	2.79	3.59	3.01
CCl_2	2.14	-[1]	1.36	1.99	1.29
SiF_2	5.34	4.85	3.79	5.31	3.96
MAE		**0.33**	**0.78**	**0.18**	**0.70**
RMSE		**0.38**	**0.96**	**0.23**	**0.86**

Table 5.2: Calculated adiabatic excitation energies (eV) using CIS and Δ-HF in comparison with the experiment.

		6–311G		6–311++G(d,p)	
Sys	**Exp.**	**CIS**	**Δ-HF**	**CIS**	**Δ-HF**
BH	2.87	3.03	1.64	2.89	1.50
BF	6.34	6.49	4.39	6.54	4.51
SiO	5.31	5.23	2.90	6.09	3.74
CO	8.07	8.01	6.36	8.74	7.00
N_2	8.59	8.65	7.25	9.45	8.06
ScO	2.04	2.30	1.60	2.07	2.05
BeH	2.48	2.78	2.64	2.76	2.64
AsF	3.19	3.83	3.57	3.76	3.44
NH	3.70	4.05	3.79	4.18	3.84
CrF	1.01	1.15	0.98	0.99	0.60
CuH	2.91	3.97	1.70	3.93	1.42
Li_2	1.74	2.11	0.96	2.10	0.92
Mg_2	3.23	3.59	2.69	3.34	2.46
PH_2	2.27	2.33	2.20	2.68	2.38
CH_2S	2.03	1.99	0.58	2.71	0.90
C_2H_2	5.23	4.68	4.07	4.49	3.71
$C_2H_2O_2$	2.72	3.24	3.12	3.56	3.30
HCP	4.31	3.46	3.03	3.59	2.95
HCN	6.48	5.54	4.88	5.95	4.78
C_3H_4O	3.21	4.36	1.29	4.58	1.67
CH_2O	3.49	3.99	1.51	4.10	1.66
CCl_2	2.14	2.08	0.69	2.40	1.07
SiF_2	5.34	5.69	3.97	5.96	4.09
MAE		**0.39**	**1.08**	**0.53**	**0.98**
RMSE		**0.51**	**1.28**	**0.63**	**1.14**

Δ-SCF methods,[412, 413] especially the maximum overlap methods, have shown great success in accessing vertical excited–states.[370, 295, 316, 313, 414, 275] Adiabatic excitation energies, however, are much more complicated to calculate, since geometry and orbital optimization are required for their description. Table 5.1 shows the adiabatic excited state energies calculated using TD-DFT and Δ-B3LYP with the four basis sets considered. Δ-B3LYP yielded comparable results to TD-DFT, where TD performed better than Δ-B3LYP with average errors between 0.42 and 0.52 eV.

Upon increasing the basis set from 6–311G to 6–311++G(d,p), the mean absolute error (MAE) of the calculated adiabatic excitation energies of TD-DFT and Δ-B3LYP decreased by 0.17 eV and 0.08 eV, respectively. This improvement can be explained by the addition of polarization and diffuse functions, which provides a better qualitative description for electronic excited states.[415] A similar behavior is observed using Dunning's basis sets, for which the mean average error for both TD and Δ-SCF–based calculation decreased by 0.05 and 0.04 eV, respectively, upon increase of the basis set size. This improvement is smaller than the one observed with the Pople basis, which is not unexpected since the two Dunning's basis sets use a larger number of polarization and diffuse functions.

In the case of CIS, the MAE ranges between 0.41 and 0.55 eV, which is smaller than the MAE obtained using Δ-HF, 1.00–1.14 eV, as reported in Table 5.2. Upon adding diffuse and polarization functions, unlike TD-DFT, the excitation energy accuracy decreased, where the MAE obtained using 6–311G is smaller than the MAE of 6–311++G(d,p) by 0.14 eV. On the other hand, for Dunning's basis sets, a smaller difference is observed, 0.05 eV, favoring the bigger basis set. On the other hand, Δ-HF showed an increase in accuracy as the basis set is increased, where MAE decreased by 0.14 eV with the Pople basis and 0.12 eV with Dunning's basis sets.

Absolute errors in TD-DFT and Δ-B3LYP adiabatic excitation energies are noticeably smaller than those found with CIS and Δ-HF, which is expected due to the correlation effects included in DFT. The AEE obtained using Δ-SCF of the investigated systems here showed an underestimation, which can be attributed to

several factors, such as the over relaxation effect, strong correlation, and spin contamination. In general, the correct description of excited states requires a balanced treatment of orbital relaxation and correlation effects due to the sudden transition between the initial and final states, which is currently treated inadequately in Δ-SCF.

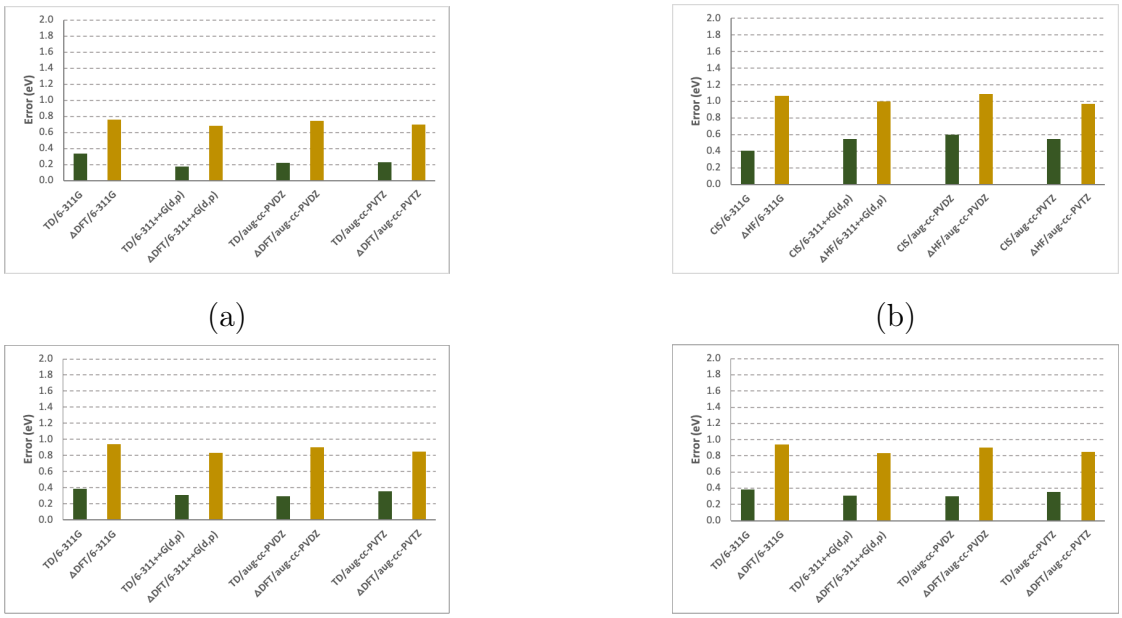

Figure 5.1: Errors in adiabatic excitation energies obtained using (a) Δ-DFT and TD-DFT and (b) Δ-HF and CIS with respect to experiment. RMSE of the adiabatic excitation energies obtained using (c) Δ-DFT and TD-DFT and (d) Δ-HF and CIS with respect to experiment are also reported.

5.3.3 Vibrational Analysis of the Excited States

The computed excited–state frequencies from all methods gave smaller relative errors than the relative errors of the adiabatic excitation energies. Table 5.4 shows the calculated vibrational frequencies using TD-DFT and Δ-B3LYP with the different basis sets considered. Unlike the computed excitation energies, the mean absolute errors obtained using Δ-B3LYP are less than those obtained using the TD-DFT methodologies by 11–28 cm^{-1}.

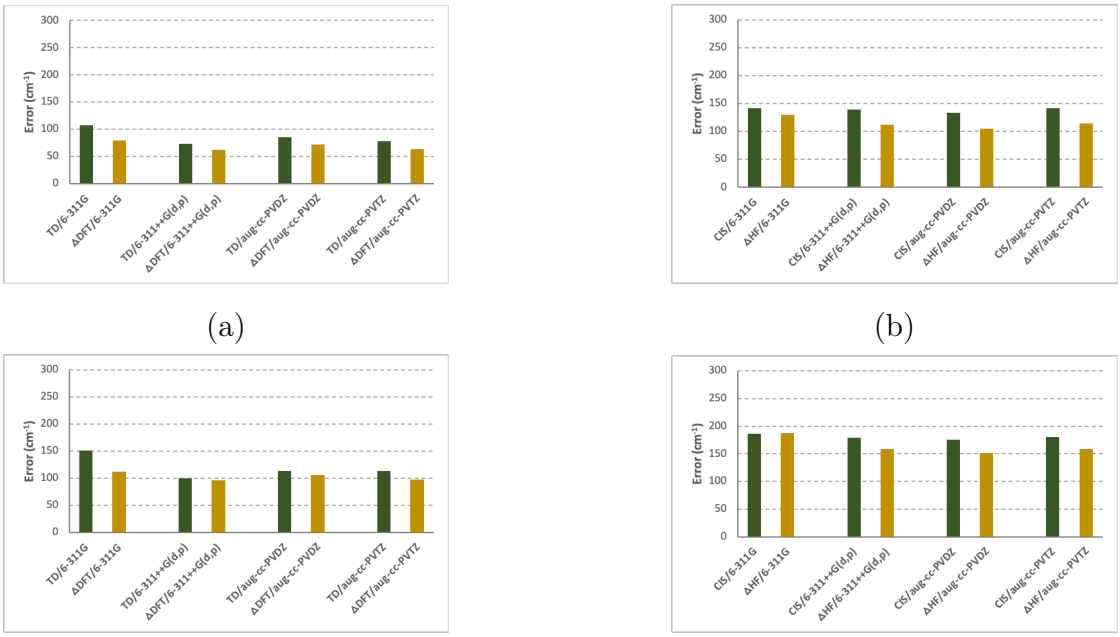

Figure 5.2: Mean absolute errors in vibrational frequencies obtained using (a) Δ-DFT and TD-DFT and (b) Δ-HF and CIS with respect to experiment. RMSE is also reported for (c) Δ-DFT and TD-DFT and (d) Δ-HF and CIS.

The effect of basis set is less significant in the accuracy of the calculated vibrational frequencies. In the case of the Pople basis set, the addition of diffuse and polarization functions lowered the MAE by 34 cm^{-1} and 17 cm^{-1} for TD and Δ-B3LYP , respectively. Dunning's basis set showed a similar behavior with an increase in accuracy of 8 cm^{-1} for both TD and Δ-B3LYP , respectively. Pople's basis set, 6–311++G(d,p), gave the lowest MAE of 62 cm^{-1} with Δ-B3LYP and 73 cm^{-1} with TD.

In general, Δ-B3LYP gave superior results to TD with all the basis sets considered, where variations in the basis set did not alter the overall performances of TD nor Δ-B3LYP. The lowest MAE was reported using 6–311++G(d,p); thus the discussion will be focused on this basis set. In cases such as the 1 $^1\Sigma_u^+$ state of Mg_2, the $\nu_2(a_1)$ mode of the 1^1B_1 of CCl_2, and the $\nu_4(a_1)$ mode of the 1 $^1A''$ state of CH_2O, Δ-B3LYP yielded remarkably more accurate vibrational frequencies than TD by 22% 36% and 14%, respectively. These results may be due to the incomplete TD-

DFT treatment of the correlation effects arising from non–valence and degenerate orbitals.[416] On the other hand, in the case of the 1 $^1\Sigma_u^+$ of Li_2 and the 1 $^1\Pi$ of CO, Δ-B3LYP gave higher error in the computed vibrational frequencies by 16% and 10%, respectively. The reason for these results may be the multi–configurational nature that is not captured as well as the overestimation of orbital relaxation in the Δ-B3LYP calculation.

Unsurprisingly, CIS and Δ-HF performed worse than TD-DFT and Δ-DFT. As shown in Table 5.5 the MAE of CIS ranges between 139 cm^{-1} and 142 cm^{-1}, higher than the MAE of TD, which ranges between 73 cm^{-1} and 107 cm^{-1}. These results may be attributed to the exchange–correlation effects in DFT and the fact that the ground state is well represented by a single KS–determinant. This gives DFT a clear advantage over the CIS and HF methods. Δ-HF displayed a MAE that ranges between 112 cm^{-1} and 139 cm^{-1}, significantly higher than the MAE obtained using DFT, which attained an uppermost MAE of 79 cm^{-1}.

Δ-HF performed similarly or better than CIS in all the cases considered in this data set. For example, for the $\nu_3(a')$ mode of the CH_2S 1 $^1A_2$ excited state, CIS resulted in a 30% error, much higher than the error resulting from Δ-HF, 9%. Also, CIS sustained large errors in describing the excited states of the carbonyl compounds, such as C_3H_8O, CH_2O, and $(CHO)_2$, unlike HF, where the errors were much less for most of the vibrational modes. These examples demonstrate well the advantages and disadvantages of describing excited states using CIS, TD or Δ-SCF. In most cases, Δ-SCF methods presented a similar or better accuracy in calculating the vibrational frequencies of the considered excited states.Detailed tables showing the behavior observed by the different models considered can be found in appendix D).

5.3.4 Spin Purification of Excited States

In many cases, the excited state obtained using Δ-SCF approach will be spin contaminated, motivating an exploration of spin purification methods. In particular, we will focus on the approximate projection model of Yamaguchi and co–workers[372] that has been extended via analytic gradients and second

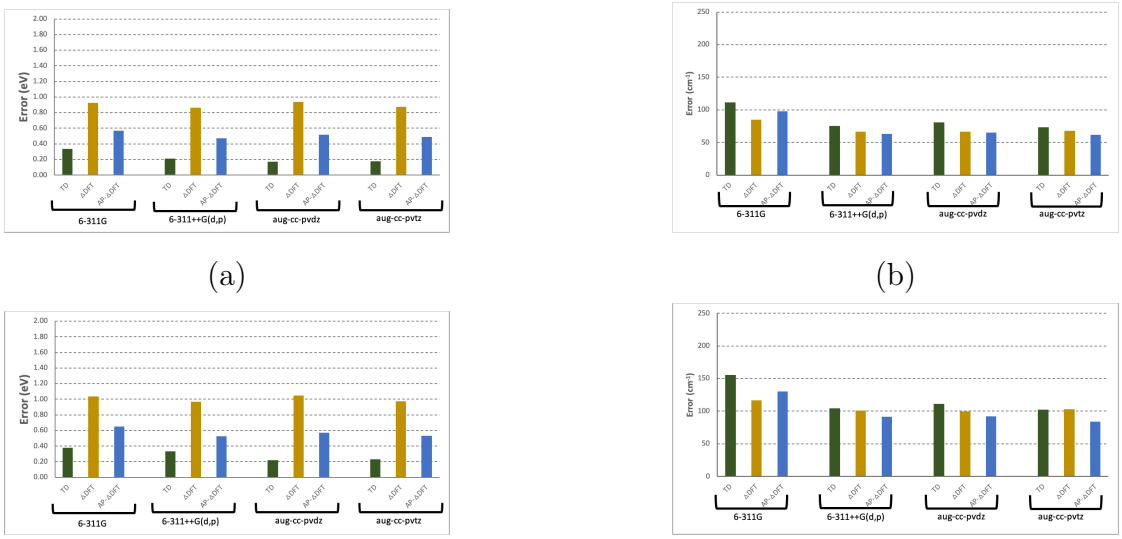

Figure 5.3: Mean absolute errors in Adiabatic Excited Energies and vibrational frequencies obtained using (a) & (b) Δ-DFT and TD-DFT. RMSE is also reported for the same models (c) & (d).

derivatives.[385, 386, 388, 387, 376, 377]

Using a contamination factor, $\alpha^* = 1 - \alpha$, excited states suffering from heavy spin contamination were identified and assessed for spin purification. The closer the value of α^* to zero, the less contaminated the solution. Thus, for systems with α^* close to zero, AP will have mild or no effect on calculated energies. Using a threshold of 5%, 17 systems were explored using the AP model. It is important to note that the conditions under which the AP model is expected to behave well include situations where the spin contaminated state has only one contaminant to be projected out of the higher spin state. With this in mind, we identified C_2H_2 and CO as systems inappropriate for this AP approach. Using HF with all the basis sets considered, the triplet state of C_2H_2 exhibited symmetry breaking, C_{2_h} to C_s, and the different symmetries of the low- and high-spin states caused difficulties in AP convergence. Before presenting AP's performance on the considered systems, it is important to note that CO, using HF/6–311G, was excluded since the triplet also showed high spin contamination. In what follows we discuss the effect of AP on the obtained excited states, and since the behavior was similar for all models,

we are discussing the results obtained using 6-311++G(d,p) basis. Full details obtained using the other model chemistries are provided in appendix D.

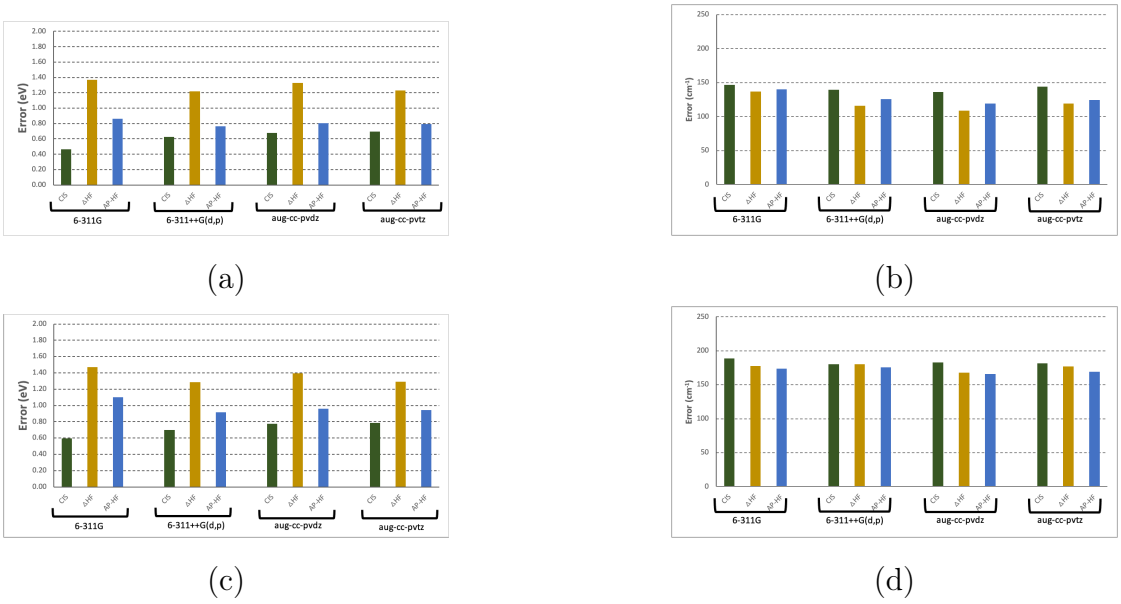

Figure 5.4: Mean absolute errors in Adiabatic Excited Energies and vibrational frequencies obtained using (a) & (b) Δ-SCF, and CIS. RMSE is also reported for the same models (c) & (d).

The effect of the AP model on energies was significant for all model chemistries considered, for which the MAE for Δ-SCF methods decreased by ∼0.4 eV for Δ-DFT and ∼0.5 eV for Δ-HF methods, as shown in Figs. 5.3 and 5.4. In cases such as BF and SiF_2 , AP–Δ-DFT reduced the error by 0.95 and 0.76 eV, respectively, using 6–311++G(d,p) basis. This highlights the efficacy of AP in treating multi–determinantal states. A similar behavior has been observed for the AP–Δ-HF method, where the error of BF and SiF_2 dropped by 1.63 and 0.67 eV, respectively. On the other hand, it is well known that Δ-SCF excitation energies for open–shell singlets, despite the spin contamination, are often unexpectedly accurate.[295, 370, 316] This is observed in the cases of CuH, where the error dropped from 0.21 eV to 0.09 eV, and CH_2S, where the error decreased by 0.08 eV to reach 0.28 eV.
This remarkable difference and improvement in the energetics upon spin purification using AP was not observed in the errors of the frequencies, as shown in Figs. 5.3 and 5.4. These results are expected and in agreement with a previous study that

Sys.	Exp.	TD	Δ-B3LYP	AP–Δ-B3LYP	CIS	Δ-HF	AP–Δ-HF
BH	**2.87**	2.74	1.69	2.30	2.89	1.50	2.68
BF	**6.34**	6.09	4.31	5.26	6.54	4.51	6.54
SiO	**5.31**	5.20	4.44	4.83	6.09	3.74	3.97
CO	**8.07**	7.95	6.60	7.37	8.74	7.00	8.63
N_2	**8.59**	8.50	7.53	8.03	9.45	8.06	8.83
CuH	**2.91**	2.98	2.70	3.00	3.93	1.42	1.93
Li_2	**1.74**	1.93	1.07	1.21	2.10	0.92	1.47
CCl_2	**2.14**	1.99	1.29	1.81	2.40	1.07	2.18
CH_2S	**2.03**	2.06	1.67	1.75	2.71	0.90	0.92
Mg_2	**3.23**	3.26	2.26	2.70	3.34	2.46	3.79
C_2H_2O	**2.72**	2.42	2.12	2.31	3.56	3.30	3.31
HCP	**4.31**	3.86	3.65	3.83	3.59	2.95	3.26
CH_2O	**3.49**	3.59	3.01	3.17	4.10	1.66	1.76
C_3H_4O	**3.21**	3.15	2.78	2.87	4.58	1.67	1.73
SiF_2	**5.34**	5.31	3.96	4.72	5.96	4.09	5.92
HCN	**6.48**	5.95	5.59	5.85	5.95	4.78	5.23
C_2H_2	**5.23**	4.70	4.38	4.61	4.49	3.71	-
MAE		**0.21**	**0.86**	**0.47**	**0.63**	**1.22**	**0.76**
RMSE		**0.38**	**0.97**	**0.52**	**0.77**	**1.39**	**0.96**

Table 5.3: Adiabatic excitation energies before and after approximate projection on systems with Spin contamination above 5%. 6-311++G(d,p) basis set was used.

suggest that this spin projection technique often does not result in large structural changes but can give meaningful changes in energy.[377] AP showed a slight improvement on the frequencies when diffuse and polarization functions are included in the basis sets, where the MAE decreased by ∼4 cm^{-1} and the RMSE decreased by ∼11 cm^{-1}. However, in the case of 6–311G, the MAE and RMSE increased by ∼12 cm^{-1}, yet, both Δ-DFT and AP–Δ-DFT perform better than TD-DFT (see Fig.5.3). This basis set dependence, especially in the presence of polarization functions, can be rationalized by the fact that for a good description of excited states, diffuse functions need to be considered for the correct electronic description of the excited state molecules. Furthermore, the proliferation of virtual orbitals in larger basis sets may lead in principle to a increase of the correlation energy and a better performance of the AP. On the other, the MAE of the frequencies obtained by AP–Δ-HF, was ∼4 cm^{-1} higher than the Δ-HF method, but the RMSE was ∼10 cm^{-1} better than Δ-HF method. This suggest that for extreme cases, where the error is high, AP–Δ-HF preformed better than Δ-HF. In brief, it is safe to say that AP–Δ-SCF is expected to perform comparably to Δ-SCF methods, yet some caution must be taken based on the system under investigation.

			6–311G		6–311++G(d,p)	
Sys	**State**	**Exp.**	**TD**	**Δ-DFT**	**TD**	**Δ-DFT**
BH	$1\ ^1\Pi$	2251	2259	2462	2363	2510
BF	$1\ ^1\Pi$	1265	1061	1157	1224	1262
SiO	$1\ ^1\Pi$	853	769	754	884	881
CO	$1\ ^1\Pi$	1518	1385	1531	1539	1693
N_2	$1\ ^1\Pi g$	1694	1622	1680	1737	1791
ScO	$1\ ^2\Pi$	876	921	880	838	899
BeH	$1\ ^2\Pi$	2089	2138	2097	2155	2112
AsF	$1\ ^3\Pi$	412	390	395	399	400
NH	$1\ ^3\Pi$	3231	2989	3101	3053	3180
CrF[a]	$2\ ^6\Pi$	629	598	624	576	625
CuH	$2\ ^1\Sigma^+$	1698	1138	1291	1650	1637
Li_2	$1\ ^1\Sigma_u^+$	255	256	200	261	208
Mg_2	$1\ ^1\Sigma_u^+$	191	116	188	156	191
PH_2	$1\ ^2A_1$	951	914	932	980	978
CH_2S[b]	$1\ ^1A_2$	799	811	742	801	782
		820	845	823	896	836
		1316	1393	1368	1372	1351
		3034	3140	3121	3127	3112
		3081	3275	3260	3240	3228
C_2H_2	$1\ ^1A_u$	1048	1108	1114	1092	1103
		1385	1398	1385	1433	1420
$C_2H_2O_2$[c]	$1\ ^1A_u$	233	260	255	251	243
		379	386	392	386	400
		509	533	531	519	516
		720	823	816	779	758
		735	828	818	780	772
		952	1028	1032	971	974
		1172	1259	1230	1197	1224
		1196	1302	1287	1239	1242
		1281	1412	1305	1528	1426
		1391	1481	1464	1572	1556
		2809	3032	3060	2966	3003
HCP	$1\ ^1A''$	567	714	705	694	716
		951	866	949	957	947
HCN	$1\ ^1A''$	941	1000	1004	983	985
		1496	1436	1417	1531	1509
C_3H_4O[d]	$1\ ^1A''$	250	254	241	261	240
		333	304	298	295	292
		488	518	507	504	498
		582	534	532	508	514
		644	738	663	709	625
		909	964	969	934	941
		1266	1114	1090	1094	108
		1133	1369	1298	1376	131
CH_2O[e]	$1\ ^1A''$	683	428	564	575	698
		899	930	924	891	894
		1177	1253	1142	1300	1247
		1321	1369	1361	1358	1301
		2851	3050	3020	2987	2954
		2968	3174	3140	3085	3048
CCl_2[f]	1^1B_1	303	-	262	192	300
		634	-	540	590	638
SiF_2[g]	$1\ ^1B_1$	342	192	218	233	242
		360	542	645	672	748
		598	554	755	768	861
MAE			**107**	**79**	**73**	**62**
RMSE			**151**	**112**	**100**	**96**

[a] Experimental data from Ref. 404
[b] Experimental data from Ref. 405
[c] Experimental data from Ref. 406
[d] Experimental data from Refs. 407 & 408
[e] Experimental data from Ref. 409
[f] Experimental data from Ref. 410
[g] Experimental data from Ref. 411

Table 5.4: Calculated harmonic vibrational frequencies in cm^{-1} using TD-DFT and Δ-DFT in comparison with experiment. Experimental results are taken from Ref. 4 for diatomic and from Ref. 5 for polyatomic molecules, unless otherwise stated.

			6–311G		6–311++G(d,p)	
Sys	**State**	**Exp.**	**CIS**	**Δ-HF**	**CIS**	**Δ-HF**
BH	$1\ ^1\Pi$	2251	2442	2441	2532	2511
BF	$1\ ^1\Pi$	1265	1169	1171	1316	1311
SiO	$1\ ^1\Pi$	853	738	722	905	807
CO	$1\ ^1\Pi$	1518	1410	745	1636	1706
N_2	$1\ ^1\Pi$g	1694	1774	1770	1919	1894
ScO	$1\ ^2\Pi$	876	923	808	977	923
BeH	$1\ ^2\Pi$	2089	2242	1950	2248	1986
AsF	$1\ ^3\Pi$	412	526	382	448	403
NH	$1\ ^3\Pi$	3231	3692	3329	3645	3425
CrF[e]	$2\ ^6\Pi$	629	625	613	615	618
CuH	$2\ ^1\Sigma^+$	1698	1734	1589	1810	1718
Li_2	$1\ ^1\Sigma_u^+$	255	273	235	272	245
Mg_2	$1\ ^1\Sigma_u^+$	191	254	184	157	197
PH_2	$1\ ^2A_1$	951	993	997	1058	1065
CH_2S[f]	$1\ ^1A_2$	799	811	725	862	827
		820	845	900	1068	894
		1316	1393	1473	1491	1491
		3034	3140	3267	3262	3256
		3081	3275	3417	3367	3382
C_2H_2	$1\ ^1A_u$	1048	1148	1168	1153	1176
		1385	1521	1478	1548	1508
$C_2H_2O_2$[g]	$1\ ^1A_u$	233	263	256	254	248
		379	440	434	439	431
		509	572	557	547	523
		720	871	893	834	823
		735	910	904	851	840
		952	1086	1067	1015	976
		1172	1389	1376	1301	1286
		1196	1394	1401	1326	1309
		1281	1577	1580	1703	1680
		1391	1730	1660	1813	1790
		2809	3250	3248	3172	3172
HCP	$1\ ^1A''$	567	509	755	593	625
		951	975	926	1045	1004
HCN	$1\ ^1A''$	941	975	759	976	917
		1496	1559	1579	1633	1555
C_3H_4O[h]	$1\ ^1A''$	250	182	247	164	251
		333	341	315	332	313
		488	541	540	519	535
		582	704	547	676	543
		644	508	660	427	641
		909	1118	996	1089	984
		1266	1611	1160	1535	1170
		1133	1321	1406	1260	1402
CH_2O[i]	$1\ ^1A''$	683	275	664	437	796
		899	1020	1077	948	1089
		1177	1457	1143	1386	1235
		1321	1592	1522	1632	1520
		2851	3228	3238	3132	3211
		2968	3346	3375	3219	3329
CCl_2[j]	1^1B_1	303	289	273	312	313
		634	560	540	678	671
SiF_2[k]	$1\ ^1B_1$	342	263	247	290	284
		360	728	704	831	836
		598	828	803	947	951
MAE			**142**	**139**	**139**	**112**
RMSE			**186**	**194**	**179**	**158**

[a] Experimental data from Ref. 404
[b] Experimental data from Ref. 405
[c] Experimental data from Ref. 406
[d] Experimental data from Refs. 407 & 408
[e] Experimental data from Ref. 409
[f] Experimental data from Ref. 410
[g] Experimental data from Ref. 411

Table 5.5: Calculated harmonic vibrational frequencies in cm^{-1} using CIS and Δ-HF in comparison with experiment. Experimental results are taken from Ref. 4 for diatomic and from Ref. 5 for polyatomic molecules, unless otherwise stated

5.4 Remarks and Conclusion

5.4.1 Generating Initial Guess

In MOM–based methods, starting with an initial guess that resembles the desired excited state is crucial to locating it. Previous considerations into the nature of the excited state and its symmetry are the quickest and easiest way to access the desired solution using PIMOM. An orbital permutation from the reference ground state to match the excited state in nature and symmetry suffices in most cases as an initial guess for the PIMOM framework. Nevertheless, in cases where multiple determinants are important for the description of the excited state, any of those are an option for generating the initial guess. For instance, consider the $1^1\Pi$ excited state of SiO. TD-DFT shows three configurations involved in representing this excitation, as follows: an amplitude of 0.17162 for the $11\alpha \rightarrow 13\alpha$ determinant, 0.67339 for the $11\alpha \rightarrow 12\alpha$ determinant, and -0.12437 for the $8\alpha \rightarrow 12\alpha$ determinant. Generating an initial guess by permuting either orbital 11α with orbital 12α or orbital 11α with orbital 13α , led to a $1^1\Pi$ excited states with a 4.44 eV excitation energy. However, permuting orbital 8α with orbital 12α let to a $1^1\Pi$ excited state located at 8.20 eV above the ground state. Clearly, either one of the first two permutations led to the correct state. However, in the last solution, though the symmetry of the state may be correct, the energy is off, thus not yielding the desired targeted state. Importantly, we note that using the Natural Transition Orbital (NTO) model to characterize the state, and using those orbitals as initial guess orbitals, led us to the correct state in all cases, including this one. We suggest the NTO model as an approach for generating initial states, particularly in instances where there is no clear one electron transition in the canonical molecular orbital basis.

5.4.2 Summary

In this chapter, I presented a Δ-SCF approach using the PIMOM framework to access adiabatic excited states and describe fundamental properties such as vibrational frequencies. Although TD-DFT and CIS provided a slightly better energetics

than PIMOM, the excited vibrational frequencies obtained with PIMOM were in better agreement with the experiment than either TD-DFT or CIS. The AP model improved the AEE for both DFT and HF and did not have a significant effect on the vibrational frequencies. Since SCF calculations are more affordable than other available excited–state methods, especially for exploring large systems, PIMOM presents a viable computational approach for modeling excited states molecular properties at ground–state computational cost. This work shows the significance of using the AP model to correct the adiabatic excitation energies with having minimal effect on the calculated frequencies. Given the results showed in this work, AP-Δ-SCF technique results in a comparable performance and lower computational cost to single reference excited state models such as, CIS and TD-DFT.

Chapter 6

Franck-Condon Spectra using TD vs PIMOM: The Case of Methylene Blue

Simulation of optical spectra is essential to molecular characterization and, in many cases, critical for interpreting experimental spectra. The most common method for simulating vibronic absorption spectra relies on the geometry optimization and computation of normal modes for ground and excited states. In this chapter, we show that utilization of such a procedure within an adiabatic linear response theory framework may lead to state mixings and a breakdown of the Born-Oppenheimer approximation, resulting in a poor description of absorption spectra. In contrast, computing excited states via a self-consistent field method in conjunction with a maximum overlap model produces states that are not subject to such mixings. We show that this latter method produces vibronic spectra much more aligned with vertical excitation procedures, such as those computed from a vertical gradient or molecular dynamics trajectory based approach.

6.1 Introduction

Excited states of chromophores play an important role in a wide variety of applications, including solar energy capture, photocatalysis, bioluminescence/fluores-

cence, and electro-optic materials.[417, 418, 419, 420, 421, 422] Predicting optical spectra and accurately characterizing excited state potential energy surfaces (PESs) affords a deeper understanding of these systems but requires accurate excited state methodologies. Even if an excited state method behaves well in regions of a vertical excitation, further challenges exist in modeling the PES near regions of a conical intersection as the Born-Oppenheimer approximation becomes less valid. In particular, adiabatic excited state methods that allow mixing of excited states can produce PESs that strongly deviate from harmonic curvature in regions of state crossings. Along an adiabatic surface that might mix excited states of different character, the nature of the state may change near regions of a conical intersection.

Due to its efficiency and relatively black box implementation, linear response theory in conjunction with time-dependent density functional theory (TDDFT) is the method of choice for most excited state calculations, including those needed for modeling optical spectroscopy.[423, 424, 425] Linear response theory avoids computation of a wave function by computing excitation energies and transition densities through the linear response formalism, defining all properties by the response of the energy or action functional.[426] Although many studies have demonstrated the ability of LR-TDDFT to accurately describe valence excited states with a single excitation character (see Ref. 427 and references therein), the adiabatic excited states of a system built from solving the TDDFT matrix equations derived from first-order time-dependent perturbation theory and linear response theory fail to accurately describe excited states with double excitation character, so may inadequately describe the PES for such states.[428, 429, 430, 431]

The Δ self-consistent field (ΔSCF) family of methods presents an alternative to linear response methods for computing excited states.[370, 295, 432, 433, 434, 296, 286] In contrast to linear response methods that mix excited states together to produce adiabatic surfaces, ΔSCF approaches solve for a single excited state of consistent character, and thus the excited state wave functions can be considered diabatic states. In recent years, P. Gill and coworkers rejuvenated the idea of converging SCF calculations for excited states using maximum overlap concepts.[295, 370]

Maximum overlap methodologies (MOM) use standard ground–state SCF algorithms modified to maximize the overlap between the molecular orbitals of the desired SCF reference and that computed in the current SCF iteration. In many instances, this procedure suffices to find stationary points in the SCF space that correspond to excited state solutions, which are often characterized as saddle points in SCF space. The projected initial maximum overlap method (PIMOM) has recently been shown to be a robust member of the family of MOM algorithms. In this variation of the MOM, the algorithm eases the convergence of excited SCF solutions by introducing a projector operator that not only preserves the target state of interest but facilitates the definition of excited state reference that is fundamental for the SCF solution.[371, 435]

The use of the ΔSCF approach comes with advantages and disadvantages that depend on the system's excited state of interest. One of the main advantages of ΔSCF approaches is that the computational expense of the simulation is no more than a regular ground state Hartree-Fock or DFT calculation. Also, these approaches produce a proper wave function; thus evaluating molecular properties of excited states is much more straightforward than in linear response theory as all ground state machinery can be used directly. The MOM family of methods is able to model challenging excited states, including double excitations.[294] On the other hand, ΔSCF approaches may suffer from variational collapse and have a strong dependency on the user-provided target guess. Another downside of using these types of approximations is that for a given state the SCF procedure can only generate state specific, non–orthogonal excited state solutions. Thus, a different calculation is needed for every electronic state of interest. Although PIMOM has shown its robustness in locating challenging electronic excited states, one challenge that is inherited in ΔSCF approximations is that excited state SCF solutions are often of broken–symmetry, i.e. spin contaminated. Spin contamination is an artificial mixing of different electronic spin-states as a consequence of permitting the spatial parts of α and β spin-orbitals to differ. However, errors associated with broken–symmetry solutions can be remedied using spin–projection methods.[373, 374, 375, 376, 377]

Vibronic spectra can be computed with a variety of methods. Perhaps the most popular method for larger molecules is to parametrize harmonic potentials by computing the Hessian and then using the frequencies and displacements from normal modes computed at the ground and excited state minima, which takes the form of a generalized Brownian oscillator model. Within this harmonic approximation to the PES, the nuclear wave functions are known, and overlaps can be calculated between ground and excited state wave functions to determine the intensity of vibronic transitions, yielding the exact Franck-Condon spectrum for the harmonic surfaces.[436] This Hessian based approach can easily accommodate Duschinsky effects or normal mode mixing upon electronic excitation.[437] The substantial computational cost associated with the excited state Hessian calculation is avoided with the vertical gradient approach, where the excited state gradient is computed at the ground state minimum and the normal modes and frequencies are assumed to be the same for the excited state as in the ground state.[438, 439, 440] This vertical gradient method may be particularly well-suited to computing spectra if the excited state minimum is close to a conical intersection, as adiabatic excited state methods may yield substantial changes in PES character in this region.[441, 442] In a study by Avila Ferrer and Santoro comparing vertical gradient and adiabatic Hessian approaches for the computation of vibronic spectra, the authors concluded that discrepancies in the vibronic spectra of these two methods are diagnostic for the failure of the harmonic approximation and/or a breakdown of the Born–Oppenheimer approximation due to geometry-dependent mixing of states.[443]

An alternative approach to the direct computation of wave function overlap is the use of energy gap time correlation functions within a cumulant expansion to the linear response function.[444] These energy gap time correlation functions can be constructed from a time-series of excitation energies computed for configurations along a molecular dynamics trajectory, usually obtained from ground state dynamics that sample the region of vertical excitation.[445, 446] Molecular dynamics trajectories generally treat the nuclei classically and thus produce classical correlation functions, but the necessary quantum correlation functions can be approximated with a quantum correction factor.[447, 448, 449, 450] Although the

cumulant expansion to the linear response function is formally exact, in practice it is generally truncated at second or third order. Truncation at second order is exact for a system with a Gaussian distribution of energy gap fluctuations, which occurs for displaced harmonic potentials of the same frequency. Changing the frequency or rotating the potentials may introduce nonlinear coupling that can be partially captured by the third order term, which also is able to incorporate some effects of anharmonic potentials.[445, 451] During a molecular dynamics trajectory, the system may sample configurations in anharmonic regions of the potential, thus absorption spectra computed from energy gap fluctuations can capture some features of anharmonic potentials.

We compare the above mentioned methods in modeling the excited states and linear absorption vibronic spectrum of the methylene blue chromophore in vacuum. A recent study by de Queiroz *et al.* of the $S_0 \rightarrow S_1$ Franck-Condon vibronic spectrum *in vacuo* obtained at the linear response TDDFT B3LYP/def2-SV(P) level of theory predicts a very large vibronic shoulder.[452] However, very recent work by some of the authors suggests that the LR-TD-B3LYP $S_0 \rightarrow S_1$ vibronic shoulder may be due to S_1/S_2 state mixing and a potential breakdown of the Born-Oppenheimer approximation.[453]

In this chapter, we investigate this state mixing possibility more thoroughly and also present the ability of PIMOM to approximate excited states and absorption spectra that are not subject to state mixing and thus find that PIMOM is more amenable than LR-TDDFT to the use of the excited state Hessian for predicting vibronic spectra. After giving a brief overview the theory of PIMOM and various methods for computing absorption spectra, we compare excited states computed with adiabatic LR-TDDFT and PIMOM for methylene blue. We then showcase the simulated vibronic spectra computed with the following approaches: adiabatic Hessian LR-TDDFT, vertical gradient LR-TDDFT, Hessian PIMOM, and a truncated cumulant expansion of the linear response function obtained from computed energy gaps along a molecular dynamics trajectory. Computation of the spectral density reveals which normal mode couples most strongly to the optical excitation and is responsible for the large vibronic shoulder predicted by adiabatic Hessian

LR-TD-B3LYP. Analysis of this normal mode shows that LR-TD-B3LYP predicts S_1/S_2 state mixing along this coordinate. In contrast, PIMOM predicts an S_1 PES of consistent character and produces a vibronic spectrum accordant with vertical gradient and molecular dynamics trajectory approaches.

6.2 Computational details

6.2.1 Geometry optimization, normal mode computation, and Franck-Condon vibronic spectral calculations

All ground and excited–state structures were optimized using hybrid B3LYP and the range-separated hybrid CAM-B3LYP functionals with the 6-31+G* Pople basis set,[391] with ground state Kohn-Sham determinants tested for stability.[140, 245] Excited–state calculations were carried out using the same model chemistry either within the LR formalism[424, 136, 137] or with the PIMOM ΔSCF method. Initial guesses for PIMOM ΔSCF states were generated by permutation of orbitals of the ground–state converged wave function to resemble the desired excited–state. HOMO–LUMO MOs we permuted to generate the S_1 initial guess while HOMO-1–LUMO MOs for S_2 state. Converged electronic excited states were verified by visualization of occupied MOs and using a modified form of the natural ionization orbitals (NIO) program by Hratchian and coworkers.[319, 320, 321] All ΔSCF results were obtained using an implementation of the PIMOM algorithm in a local development version of Gaussian.[318]

Molecular geometries for ground and excited–states were optimized using standard methods,[246] and the reported PES minima were verified using analytical second–derivative calculations.[247, 248] For methylene blue, the ground state S_0 optimized structure is of C_{2v} symmetry for both B3LYP and CAM-B3LYP. This C_{2v} symmetry is maintained for the S_1 minimum obtained for PIMOM/B3LYP, PIMOM/CAM-B3LYP, and LR-TDDFT/CAM-B3LYP. However, for the LR-TDDFT/B3LYP, the S_1 minimum is of C_s symmetry.

Hessian based vibronic spectra, under the harmonic approximation, were simulated

using the implementation by Bloino, Barone, and co-workers for both PIMOM and LR–TDDFT by computing the Hessian and displacements at the ground and excited state minima.[249] The vertical gradient Franck-Condon vibronic spectra for LR–TDDFT were also computed.[438, 439, 440]

6.3 Results and discussion

6.3.1 Comparison of PIMOM and LR-TDDFT excitation energies and difference densities

Before we analyze vibronic absorption spectra computed with different methods, it is worthwhile to examine the excitation energies computed with PIMOM and LR-TDDFT for the vertical excitation energies computed from the S_0 ground state optimized geometry and the from the S_1 excited state optimized geometry. At the S_0 minimum, the S_1 state is primarily HOMO $\rightarrow$ LUMO character, whereas the S_2 state is primarily HOMO-1 $\rightarrow$ LUMO. These MO occupations were used to find the corresponding PIMOM excited states and corresponding geometric and electronic state minima.

Optimized Geometry	**PIMOM** $\mathbf{E_{S_2}}$-$\mathbf{E_{S_1}}$ **(eV)**	**LR-TDDFT** $\mathbf{E_{S_2}}$-$\mathbf{E_{S_1}}$**(eV)**	$\mathbf{f_{S_1}/f_{S_2}}$
$\mathbf{S_0}$	0.54	0.13	0.810/0.001
$\mathbf{S_1^{LR\text{-}TDDFT}}$	0.44	0.29	0.382/0.350
$\mathbf{S_1^{PIMOM}}$	0.52	0.10	0.796/0.003

Table 6.1: B3LYP $S_2 - S_1$ electronic energy gaps in eV at S_0, $S_1^{\text{LR-TDDFT}}$, and $S_1^{\text{LR-TDDFT}}$ optimized geometries obtained using PIMOM and LR-TDDFT approaches. Oscillator strengths (f) of S_1 and S_2 are also reported for LR-TDDFT.

Table 6.1 shows the energy gaps between the S_1 and S_2 states computed with PIMOM and LR-TD-B3LYP for the S_0 minimum as well as for the excited state S_1 minimum for both methods. The energy gaps between these states are larger for PIMOM than for LR-TDDFT, with LR-TD-B3LYP having a fairly small energy

gap of 0.1-0.3 eV. Interestingly, for the LR-TD-B3LYP S_1 minimum, the energy gap decreases for PIMOM and increases for LR-TD-B3LYP. At this LR-TD-B3LYP S_1 optimized geometry, the oscillator strength f of both the $S_0 \rightarrow S_1$ and the $S_0 \rightarrow S_2$ changes substantially, with the bright S_1 transition losing oscillator strength and the dark S_2 transition gaining oscillator strength, with nearly equal values at this geometry, indicating substantial mixing of the S_1 and S_2 states at this point. This mixing is supported by the MO contributions, which at this geometry are a mixture of HOMO $\rightarrow$ LUMO and HOMO-1 $\rightarrow$ LUMO.

In contrast to LR-TD-B3LYP, LR-TD-CAM-B3LYP yields consistent S_1 and S_2 states for the geometries considered here, with similar S_1 to S_2 energy gaps and oscillator strengths for S_0 and both S_1 geometries, see Table 6.2. The LR-TD-CAM-B3LYP energy gap between S_1 and S_2 is also larger than that with LR-TD-B3LYP, suggesting less state mixing. However, PIMOM shows the opposite trend, with the S_1 to S_2 CAM-B3LYP gap being smaller than the B3LYP gap. For both functionals, the PIMOM S_1 to S_2 energy gap decreases by 0.02 eV going from the S_0 minimum to the PIMOM S_1 minimum, suggesting that PIMOM is more functional agnostic than LR-TDDFT, as it is not subject to the inconsistent treatment of excited states of different character or adiabatic state mixing effects.

Optimized Geometry	**PIMOM** $\mathbf{E_{S_2}}$-$\mathbf{E_{S_1}}$ **(eV)**	**LR-TDDFT** $\mathbf{E_{S_2}}$-$\mathbf{E_{S_1}}$**(eV)**	$\mathbf{f_{S_1}/f_{S_2}}$
$\mathbf{S_0}$	0.49	0.38	0.959/0.006
$\mathbf{S_1^{LR\text{-}TDDFT}}$	0.47	0.36	0.930/0.006
$\mathbf{S_1^{PIMOM}}$	0.47	0.34	0.931/0.006

Table 6.2: CAM-B3LYP $S_2 - S_1$ electronic energy gaps in eV at S_0, $S_1^{\text{LR-TDDFT}}$, and $S_1^{\text{LR-TDDFT}}$ optimized geometries obtained using PIMOM and LR-TDDFT approaches. Oscillator strengths of S_1 and S_2 are also reported for LR-TDDFT.

To further illustrate the behavioral difference between LR-TDDFT and PIMOM, the B3LYP electron density difference between the ground and S_1 excited state densities computed at the LR-TDDFT S_1, PIMOM S_1, and ground state optimized geometries are shown in Fig. 6.1. PIMOM produces a consistent density differ-

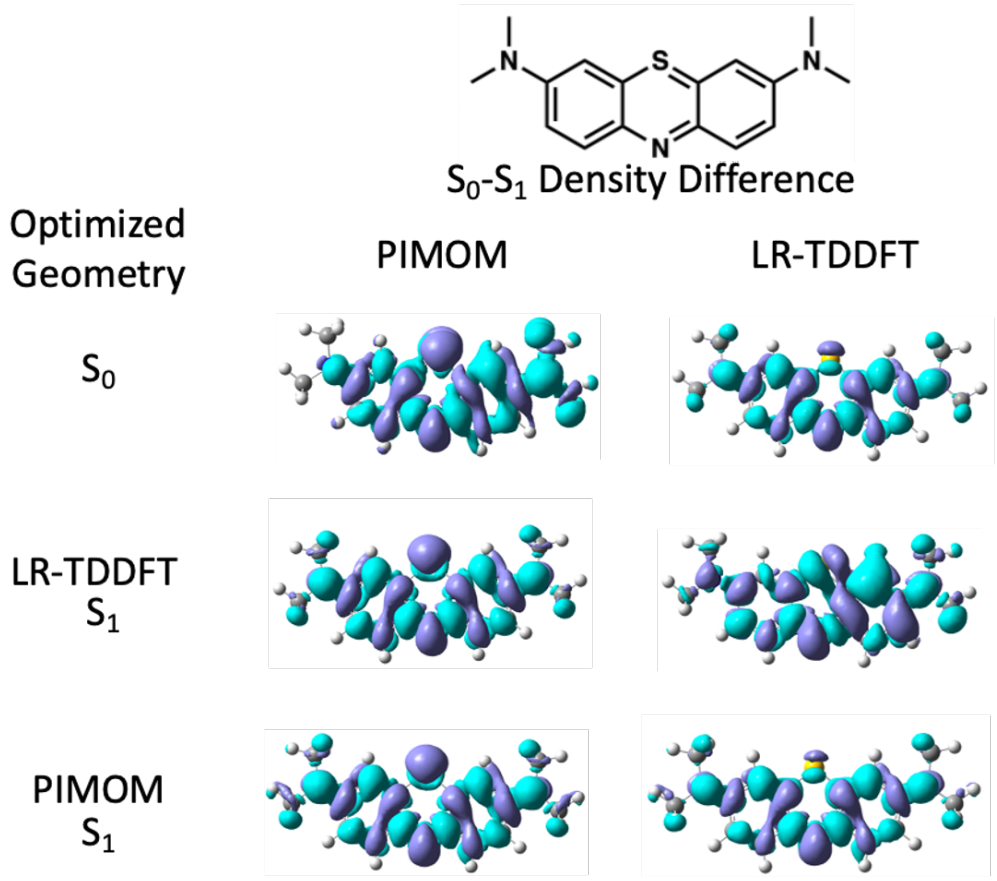

Figure 6.1: The structure of the methylene blue chromophore and the B3LYP density difference between the ground and S_1 excited state at the ground state S_0, LR-TDDFT S_1, and PIMOM S_1 optimized geometries.

ence for all three optimized geometries, indicating that the treatment of the S_1 state is consistent for all three geometries. The LR-TD-B3LYP density differences obtained at the ground state and the PIMOM optimized geometries are similar to the density differences predicted by PIMOM. In contrast, the LR-TD-B3LYP difference densities shows qualitatively different character for the LR-TD-B3LYP S_1 minimum, with notable symmetry breaking, demonstrating that PIMOM and LR-TDDFT produce S_1 states of substantially different character for this geometry. The CAM-B3LYP density differences (shown in appendix E) are in excellent agreement for both PIMOM and LR-TDDFT for all geometries. The CAM-B3LYP PIMOM density differences are very similar to the B3LYP PIMOM density differences, again showing that the PIMOM method is not as subject to the functional dependencies of the LR-TDDFT procedure.

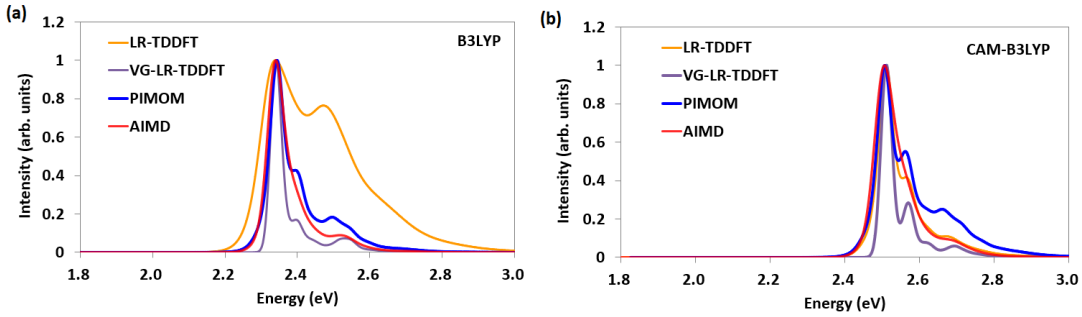

Figure 6.2: (a) B3LYP and (b) CAM-B3LYP $S_0 \rightarrow S_1$ vibronic spectra computed with: the adiabatic Hessian from linear response TDDFT (LR-TDDFT), the vertical gradient from LR-TDDFT (VG-LR-TDDFT), the Hessian from PIMOM, and LR-TDDFT energy gap time correlation function from the ground state AIMD trajectory (AIMD). Note that spectra are energetically aligned as mentioned in the main text.

6.3.2 Linear absorption spectra

The four spectral methods, which include adiabatic Hessian LR-TDDFT, vertical gradient LR-TDDFT, Hessian based PIMOM, and AIMD, are compared in Fig. 6.2 for B3LYP and CAM-B3LYP. The vibronic spectra for (PIMOM, AIMD) are shifted by (0.83 eV, -0.05 eV) for B3LYP and (0.76 eV, -0.03 eV) for CAM-

B3LYP, respectively, such that the 0-0 transitions coincide with those for LR-TDDFT, for better comparison of spectral shapes.

Each of the methods examined here employs different approximations. LR-TDDFT is an adiabatic, perturbative approach that does not properly describe states of double excitation character. Additionally, adiabatic Hessian and normal mode calculation at the LR-TDDFT excited state minimum may not be well-behaved if PESs mix together in this region. In such cases, a harmonic approximation may be insufficient to properly describe the adiabatic PES. In contrast, the vertical gradient approach avoids the computation of the excited state minimum and normal modes, instead computing only the excited state gradient at the optimized geometry of the ground state. Although this vertical gradient approach is often assumed to be more inaccurate than the full normal mode calculation at the S_1 excited state minimum, the vertical gradient approach may be better suited for modeling absorption spectra than the adiabatic Hessian approach if the S_1 minimum is near a surface crossing. Indeed, in Fig. 6.2a, we see significant differences in the spectra computed with the adiabatic Hessian LR-TD-B3LYP approach obtained with full geometry optimization and normal mode computation at the LR S_1 minimum compared to that obtained with the vertical gradient approach. Note that both of these LR methods use the same ground state normal modes. Thus, the only difference is the treatment of the S_1 excited state surface, suggesting that the character of the LR-TD-B3LYP PES is very different in the region above the S_0 minimum compared to the PES in the region of the S_1 minimum. This result is consistent with the results of the previous section that found substantial change in the LR-TDDFT electron density difference at the S_1 minimum compared to at the S_0 minimum. The vibronic spectrum obtained within the vertical gradient approach is much more narrow due to the small vibronic shoulder peak; this same peak is almost as large as the 0-0 transition for the adiabatic Hessian approach, showing that the S_1 minimum likely undergoes a significant change in geometry given the more intense vibronic peak.

The vibronic spectrum obtained within the vertical gradient approach shows good agreement with the AIMD trajectory based approach that employs second order

truncation of the cumulant expansion. This latter method goes beyond the harmonic approximation to the shape of the PES by sampling nuclear configurations that may occur in anharmonic regions of the PES, which may be responsible for the increased broadening compared to the vertical gradient approach. The good agreement between methods is perhaps not surprising since both methods are sampling the S_1 PES region directly above the S_0 minimum. Interestingly, if the same LR-TDDFT S_1 normal modes and displacements that characterize the vibronic spectrum are used to compute the spectrum within the second or third order truncation to the cumulant expansion of the linear response function within the GBOM, large changes in the spectrum suggest significant change in curvature of the ground and excited state PES and/or a large Duschinsky rotation, leading to non-Gaussian fluctuations of the energy gap (see appendix E). These large differences in curvature or a large rotation of normal modes may be due to the symmetry breaking going from the ground state S_0 minimum to the LR-TD-B3LYP S_1 minimum.

Perhaps the most striking result of this work is the comparison of the spectra computed with the Hessian and normal modes of the ΔSCF PIMOM S_1 minimum to that computed from the LR S_1 minimum. Here we again see a large difference between the intensity of the vibronic shoulder peak, with the spectrum obtained with the PIMOM S_1 minimum normal modes in good agreement with both the vertical gradient and the AIMD trajectory based methods, suggesting that all three of these methods are consistent in their treatment of the character of the S_1 state.

In Fig. 6.2b the same spectra are compared for computation with the CAM-B3LYP functional. Here we see much better agreement with all methods. The adiabatic Hessian LR-TD-CAM-B3LYP and AIMD based spectra computed from the LR-TD-CAM-B3LYP excitation energies are nearly indistinguishable. The CAM-B3LYP functional predicts a larger gap between the S_1 and S_2 states, suggesting that there is much less mixing of these two excited states and as seen from the excitation energies and oscillator strengths, the LR-TD-CAM-B3LYP S_1 state maintains similar character in the region of the vertical transition and at both the LR and PIMOM S_1 minima.

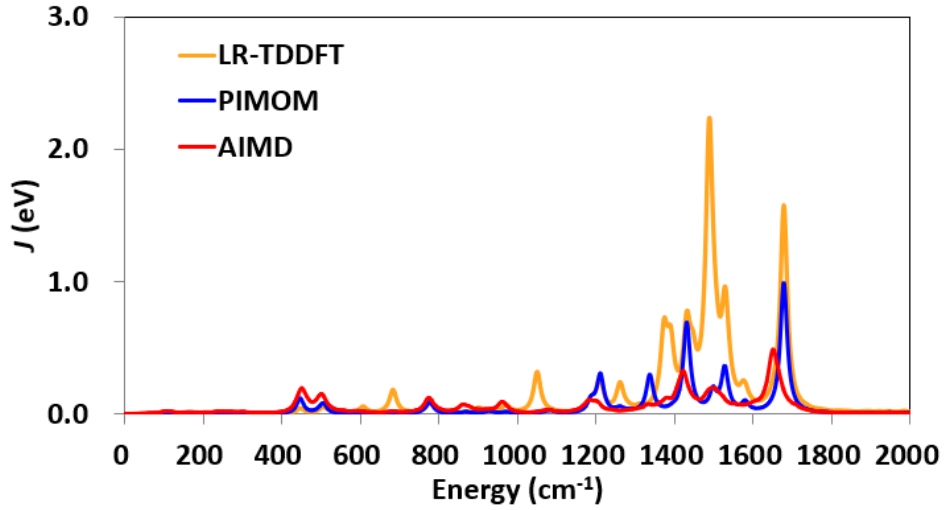

Figure 6.3: B3LYP S_0/S_1 spectral density computed using parameters from the LR-TDDFT and PIMOM normal modes from S_0 and S_1 optimized geometries, and that computed from the S_0 to S_1 energy gap time correlation function along the ground state AIMD trajectory.

Plotting the spectral density allows us to compare how the different methods treat the modes that couple the S_0 and S_1 transition. The spectral densities in Fig. 6.3 computed from LR-TDDFT and PIMOM are both obtained from a GBOM parametrized with the ground and excited state normal modes. We also show the spectral density computed from the energy gap time correlation function obtained from the AIMD trajectory. The spectral density based on the AIMD trajectory shows 10∼20 cm^{-1} red-shift of the peaks compared with the normal mode parametrization due to the inclusion of anharmonicity of the PES in the vibrations of the chromophore. The spectral densities in Fig. 6.3 show that there is a high intensity peak at around 1500 cm^{-1} in the LR-TDDFT spectral density, whereas the same region of the PIMOM and AIMD trajectory spectral density shows very little intensity. This large peak of B_2 symmetry corresponds to the normal mode responsible for a significant amount of the large vibronic shoulder present in the adiabatic Hessian LR-TDDFT spectrum. This normal mode involves antisymmetric C-C stretches of the center ring coupled to the motion of the dimethyl amine groups. Because the LR-TD-B3LYP S_1 minimum is not of C_{2v} symmetry, con-

trary to other methods, this symmetry breaking leads to enhanced coupling with the anti-symmetric stretch, giving rise to the large peak in spectral density. We further analyze this normal mode in the following section.

6.3.3 Normal mode analysis

To analyze the nature of the S_1 and S_2 PESs along the B_2 anti-symmetric stretch normal mode motion, we performed a scan along this ground state normal mode, computing both the LR-TDDFT and PIMOM energy gaps, shown in Fig. 6.4. The inset of Fig. 6.4(a) shows the normal mode vectors corresponding to the atomic displacements. The PES scan presents well-separated surfaces of the S_1 and S_2 states with PIMOM along the full normal mode displacement coordinate, unlike LR-TDDFT, where the surfaces are in close proximity at the minimum. Additionally, the shape of both the S_1 and S_2 LR-TDDFT PES along this mode clearly deviates from harmonic behavior, unlike the PIMOM PESs.

The LR-TDDFT oscillator strengths plotted in Fig. 6.4(b) show that at the S_0 minimum, S_1 is a bright state with oscillator strength $f \approx 0.8$, whereas the S_2 state is dark. As the atoms are displaced along this normal mode, the LR-TDDFT S_1 state loses oscillator strength and the LR-TDDFT S_2 state gains oscillator strength, showing that these two states mix together along this coordinate. At displacements of $\pm$ 0.2 au, the two states have nearly identical oscillator strengths of $f \approx 0.4$.

Overall, this normal mode analysis supports our finding above that the character of the S_1 state is treated quite differently by adiabatic LR-TDDFT compared to PIMOM. The LR-TDDFT method leads to S_1 and S_2 state mixing in some regions of the PES, both along this normal mode and at the S_1 minimum, whereas PIMOM maintains consistent S_1 character.

6.4 Conclusions

Calculating accurate optical spectra from first principles is essential for connecting spectroscopic experiments to the electronic characterization and dynamics of chromophores. The accuracy of the simulated spectra relies heavily on the quality of

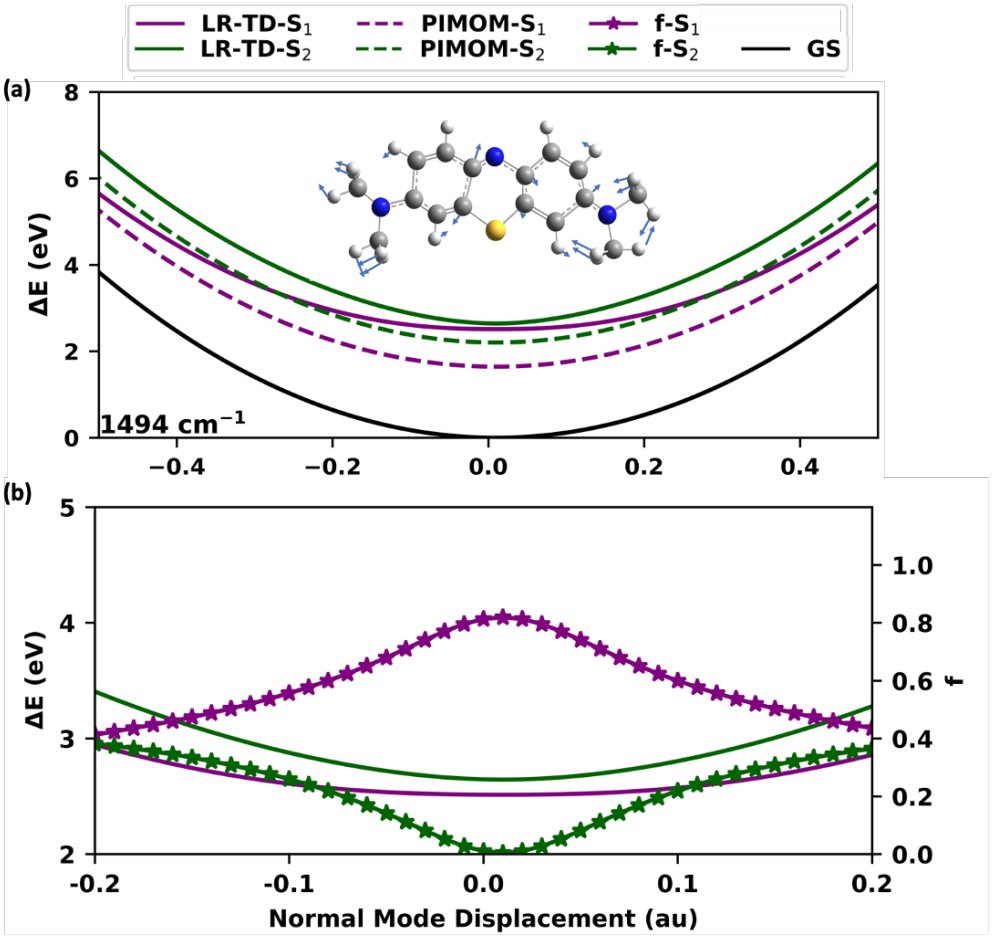

Figure 6.4: B3LYP potential surface scans of S_1 and S_2 states with respect to the ground state. (a) LR-TDDFT PESs are shown in solid lines, PIMOM PESs are shown in dashed lines, and ground state (GS) PES is drawn in black. The inset shows the displacement vectors for the ground state normal mode, a B_2 asymmetric stretch. (b) For LR-TDDFT, the oscillator strengths are plotted with the energies along the normal mode displacement.

the excited state calculation and the method chosen for computing the spectra. In this chapter, we compared the behavior of the widely used LR-TDDFT approach with PIMOM for computing the excited states of methylene blue, then applied a number of approaches for simulating the vibronic spectra.

We find that the adiabatic LR-TD-B3LYP approach yields S_1 and S_2 states that mix together near the S_1 minimum. Although the S_1 state is bright and the S_2 state is dark at the ground state minimum, analysis of a key normal mode that strongly couples to the $S_0 \rightarrow S_1$ transition shows that the S_2 state borrows intensity from S_1 along this normal mode displacement, with S_1 and S_2 having nearly identical oscillator strengths at the S_1 minimum. In contrast, the PIMOM method produces diabatic states of consistent character across the PES, with a larger energy gap between S_1 and S_2. PIMOM also yields consistent character for both B3LYP and CAM-B3LYP S_1 PESs and electron densities, showing that it is less susceptible to density functional differences than the LR-TDDFT approach.

When applying these two excited state methods to the computation of vibronic spectra using a Hessian computed at the S_1 minimum, they yield very different results for methylene blue. The standard adiabatic Hessian LR-TD-B3LYP approach produces a very large vibronic shoulder in the spectrum due to a change of character of the PES at the S_1 minimum because of the adiabatic treatment of the excited states. The spectra generated from LR-TD-B3LYP with a vertical gradient or an AIMD trajectory based approach differs significantly from the adiabatic Hessian LR-TD3LYP approach, with no large vibronic shoulder. Large changes in the spectra with second and third order truncation of the cumulant expansion using the LR-TD-B3LYP S_1 parametrized GBOM suggest substantial changes in PES curvature or a large Duschinsky rotation matrix, with large mixing of normal mode coordinates possibly caused by the decrease in symmetry going from the S_0 C_{2v} to the LR-TD-B3LYP S_1 C_s minimum. In contrast, if the PIMOM method is used to compute S_1 minimum and corresponding Hessian and normal modes, the resulting vibronic spectrum is in very good agreement with the vertical gradient and AIMD trajectory based approaches, showing that all of these methods have a consistent treatment of the S_1 state in the region of the vertical excitation and

at the PIMOM S_1 minimum. Switching from the B3LYP to the CAM-B3LYP functional increases the gap between the S_1 and S_2 states, with adiabatic Hessian LR-TDDFT, PIMOM, and AIMD trajectory based approaches all producing spectra in good agreement.

The large differences between the TD-B3LYP adiabatic Hessian and vertical gradient methods suggest the breakdown of the Born-Oppenheimer or harmonic approximation in the region of the LR-TD-B3LYP S_1 minimum. Indeed, the need for including non-adiabatic effects is supported by a recent study by some of the authors of solvated methylene blue that showed that there is significant population transfer from the S_1 state to the S_2 state upon photoexcitation, which is strongly coupled to the intensity of the vibronic shoulder.[453] Inclusion of this population transfer increases the vibronic shoulder, bringing the predicted spectrum more in line with experimental spectrum of aqueously solvated methylene blue.

Our results here point to the challenge of using an adiabatic excited state approach for the computation of some excited state properties, including the Hessian computed at an adiabatic excited state minimum. Because adiabatic surfaces can change in character, the character of the state at the minimum may not accurately describe the system in the region of the vertical excitation. The state mixing seen here, and the resulting inconsistent description of the S_1 states, could happen with other adiabatic excited state approaches. The use of a vertical gradient or AIMD energy gap time correlation function based approach may more accurately describe the vertical excitation. Additionally, a dynamic AIMD energy gap time correlation function based approach can describe the effects of coupling to an explicit environment and samples anharmonic nuclear configurations.

Overall, our study shows that the ΔSCF PIMOM approach produces states that are more aligned with a diabatic model, thus not subject to adiabatic state mixings that may lead to a change in PES character. In this study, the PIMOM Hessian method, vertical gradient LR method, and AIMD trajectory based method all produced vibronic spectra in good agreement with each other. Given that PIMOM, in some cases, will be more computationally affordable than LR-TDDFT at finding an excited state minimum, it offers an appealing alternative to the LR-TDDFT

method for computing vibronic spectra. Additionally, for non-adiabatic methods requiring a diabatic treatment of the excited state PES, PIMOM presents a viable path forward for computing excited state couplings and properties.

Chapter 7

Applying PIMOM to Lanthanides

In an attempt to extend the pool for which the PIMOM is crucial for locating electronic excited states, the lanthanides section of the periodic table was targeted. In this chapter, we test and show that PIMOM successfully located and distinguished between close-lying excited states that more sophisticated, and computationally expensive, methods fail to locate. In collaboration with the Chick Jarrold Group at Indiana University, the PIMOM model was especially vital to study photoelectron spectra of $Gd_2O_2^-$ and Gd_2O^- and to provide a description of strong photoelectron-valence electron interactions. In this chapter I will discuss the work on the photoelectron spectra of Gd_2O^-.[454] For the study on $Gd_2O_2^-$, please refer to reference.[455]

7.1 Introduction

With the ever-increasing need for faster, more efficient computational analysis and data storage, the development of practical quantum computing materials has been a central focus of a number of fields in the scientific community.[456, 457, 458, 459] Of particular interest is the design of bi- or multi- stable magnetic species; these magnetic states, ideally, can be controlled by some external perturbation, like an electric field.[460, 461] To this end, the lanthanides have proven to be enticing candidates because of their intrinsic large magnetic anisotropy and fascinating magnetic properties arising from the partially-filled core-like $4f$ orbitals.[462, 463]

Fundamentally, the lanthanides (Ln) exhibit a rich manifold of nearly identical electronic states in a narrow energy window afforded by the partially occupied $4f$ orbitals and additional close-lying $6s$ and $5d$ orbitals. As an example, CeO ($4f1$ σ_{6s}) has 16 states within a 0.5 eV window of energy.[464, 465, 466]

We recently reported the effects of strong electron-neutral interactions in the photoelectron spectra of Sm_2O^- and $Gd_2O_2^-$.[467, 455] Specifically, the probability of populating excited neutral states via anion detachment increased relative to the ground state neutral with decreasing photon energy and, therefore, decreasing photoelectron kinetic energy (e-KE); this observation is opposite of what would be expected to arise from threshold effects.[468] Pronounced effects were observed in a number of Sm-rich suboxide clusters,[469, 2] but it was not observed in homometallic Ce-homologs, which implicated the greater density of electronic states from Sm's $4f^5$or $4f^6$ subshell occupancy, compared to Ce's lone $4f$ electron. The effects were attributed to shake-up transitions or inelastic scattering resulting from strong photoelectron-valence electron (PEVE) interactions. An enhancement of the effects with decreasing photon energy is explained by the corresponding increase in PEVE interaction time associated with a decrease in the photoelectron velocity.[467]

The exceptionally high density of electronic states in SmxOy- anion and neutral suboxide clusters render them difficult to interrogate experimentally and computationally,[469, 2, 470] and the exact nature of the excited states of Sm_2O being populated due to PEVE interactions could not readily be determined from the broad manifold of unresolved transitions observed in its anion PE spectrum. In order to probe the nuances of the PEVE interactions in more detail, the photoelectron spectra $Gd_2O_2^-$ were similarly examined over a range of photon energies. Relative to Sm_2O^-, $Gd_2O_2^-$ has a simpler electronic structure because the Gd-centers have half-filled $4f^7$ subshells, and therefore zero orbital angular momentum, and the incremental difference in oxidation state results in two fewer electrons in metal-local orbitals. $Gd_2O_2^-$, therefore, provided a canvas for exploring the fundamental physics of this effect. Our studies suggested the impact of two distinct PEVE interactions in which the electric field of the departing photoelectron (i)

resulted in a time-dependent outervalence orbital mixing which, in turn, provides an accessible route to increased population of excited neutral states as well as two-electron transitions observed in the spectra and (ii) affected the ordering of ferromagnetic (FM) and antiferromagnetic (AFM) states of the remnant neutral core. These effects have been observed in comparable physical systems described in the literature.[471, 472, 473, 474, 475]

Features in the PE spectra of $Gd_2O_2^-$ suggested a large axial zero-field splitting parameter (ca. -15 cm^{-1}) compared to typical sub-cm^{-1} coupling between Gd_3^+ centers in gadolinium complexes.[476] The higher coupling in the cluster anion may have a solution-phase analog in Gd2 complexes in which the Gd centers are coupled by radical anion bridging ligands.[477, 478]

Herein, we report another example PEVE interactions which give rise to inverse-threshold law behavior observed in our previous experiments, but which also exhibit photoelectron angular distribution anomalies that point to additional PEVE-driven phenomena.

To lay the groundwork for understanding the electronic structure of Gd_2O/Gd_2O^-, DFT calculations on Gd_2O^- (vide infra) predict isoenergetic bent and linear Gd−O−Gd structures as the lowest energy structures. As depicted in 7.1, which shows the linear structure, the general electronic structure can be described as two Gd centers with $4f^7\ 6s^2$ electronic configurations, with the excess electron in a δ_g molecular orbital (MO) arising from the combination of the $5d_\delta$ orbitals. The occupancy of the $5d_\delta$ orbital introduces non-zero overall orbital angular momentum, and spin-orbit splitting in the anion would favor the linear structure by ca. 1000 cm^{-1} relative to the bent structure.

A $^{16}\Delta_\Omega$ electronic term would result from FM coupled $4f^7$ centers; a $^2\Delta_\Omega$ term would arise from AFM coupled centers. Because the 'outer-valence' δ_{5d} and $\sigma_{6s,u}/\sigma_{6s,g}$ orbitals are close in energy, numerous close-lying photodetachment transitions are anticipated, and are observed, as will be described below. However, a new and exciting finding in the present study is anomalous photoelectron angular distributions observed among the plethora of transitions. We propose that it may be another effect due to strong PEVE driven transitions involving changes in the

spin projection quantum number.

7.2 Computational Details

Calculations were carried out using the Gaussian suite of electronic structure programs[479] and employed the B3LYP/ANO-ECPplusPVTZ model chemistry. The ANO-ECPplusPVTZ incorporates the Stuttgart relativistic small-core atomic natural orbital basis set and effective core potential and corresponding valence basis set for Gd[480] and a Dunning-style correlation consistent basis set for O.[18] All converged Kohn-Sham determinants were characterized using stability calculations. Geometry optimizations were carried out using standard techniques and potential energy surface stationary points were characterized using analytic second-derivative calculations.[140, 245] Reported energies include zero-point energy corrections.

In order to facilitate convergence for challenging electronically excited states, the projected initial maximum overlap method PIMOM was used.[371] More specifically, this method drives self-consistent field convergence toward challenging electronic structures using an initial guess from the ground state molecular orbitals and a projected overlap metric.

For molecules exhibiting complex electronic structure, specifically when energy gaps between electronic states are quite small, multi-determinantal wave functions might be a better representation of the true electronic structure than using Kohn-Sham (KS) DFT. With this in mind, KS DFT results must be used with care. This has been achieved through evaluation of KS determinant stability and spin-squared expectation values. Indeed, evaluating anion-neutral energy gaps and Franck-Condon simulations using such DFT methods yielded results that are in very good agreement with experimental spectra, which in turn facilitated the assignment of spectral peaks and the determination of the molecular and electronic states that are present in the experimental photoelectron spectra.

The simplest points of comparison between the computational and experimental results are theadiabatic EA (EAa), adiabatic detachment energies (ADE), and the

vertical detachment energies (VDE). The calculated EAa is the energy difference between the zero-point level of the neutral and the zero-point level of the anion. The more general ADE is the difference in zero-point corrected energies of the optimized initial ground state of anion and any optimized neutral electronic state, and generally coincides with the onset (in e^-BE) of signal for a particular transition. The VDE is the energy (e^-BE) at which the maximum intensity of a transition is observed. In the Born-Oppenheimer picture of electronic transitions, it is the energy at which the Franck-Condon overlap between the initial and final states is at a maximum. Computationally, it corresponds to the difference in energy between the anion ground state and the neutral state, confined to the geometry of the anion.

A more detailed comparison between the computational and experimental results involves a simulation of the vibrational structure of a transition, based on the structures, vibrational frequencies, and normal coordinates of the anion and neutral. A more detailed description of the home-written simulation code was provided previously.[481]

7.3 Results and Discussion

Along the lanthanide series, the properties of adjacent elements are very similar. The incremental increase in 4f subshell occupancy, which increases nuclear shielding, results in similar effective nuclear charges for neighboring elements, leaving the outer-valence electrons to govern very similar chemical and physical properties.[1] However, as will be shown, there are distinct differences in the electronic structures in several Ln_2O anion and neutral molecules that can be attributed to differences in the spin-orbit coupling associated with different 4f subshell occupancies.

7.3.1 Anion PE Spectrum of Gd_2O^-, and comparison to Ce_2O^- and Sm_2O^-.

7.2 shows the PE spectra of (a) Ce_2O^-, (b) Sm_2O^-, and (c) Gd_2O^- , collected using 3.495 eV (blue) and 2.330 (green) photon energies, with the electric field

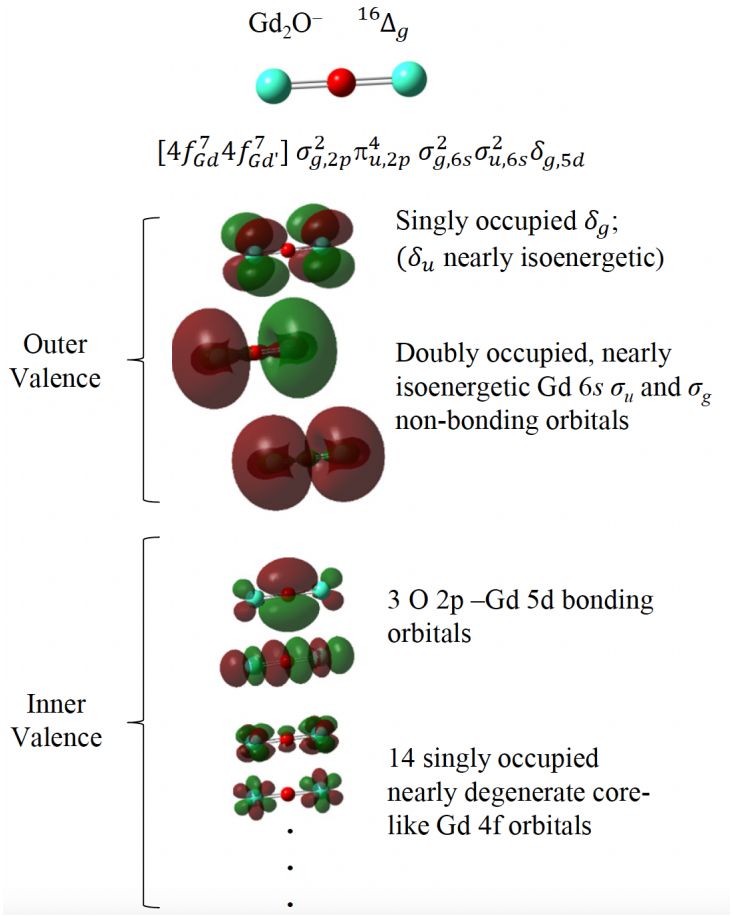

Figure 7.1: 1. Molecular and electronic structure of Gd_2O^- calculated using DFT with a B3LYP hybrid density functional. The energy separation between the inner valence and outer valence orbitals is calculated to be 3.9 eV; detachment transitions observed in this study therefore involve only the outer valence electrons. Additional states found computationally are included in Table 7.1 and in appendix F

.

polarization parallel (dark colors) and perpendicular (light colors) to the electron drift path. The Ce_2O^- and Sm_2O^- spectra were published previously,[467, 469, 482] and are included here for direct comparison. The lowest energy transitions in the Ce_2O^- and Sm_2O^- spectra, labeled X, are intense and have parallel PADs typical of detachment from 6s-based molecular orbitals.[482, 483, 484] The spectra are qualitatively similar in appearance. Band **A** in the Ce_2O^- spectrum is not resolved from band **X** in the 3.495 eV spectrum, but it is resolved in the 2.330 eV spectrum.

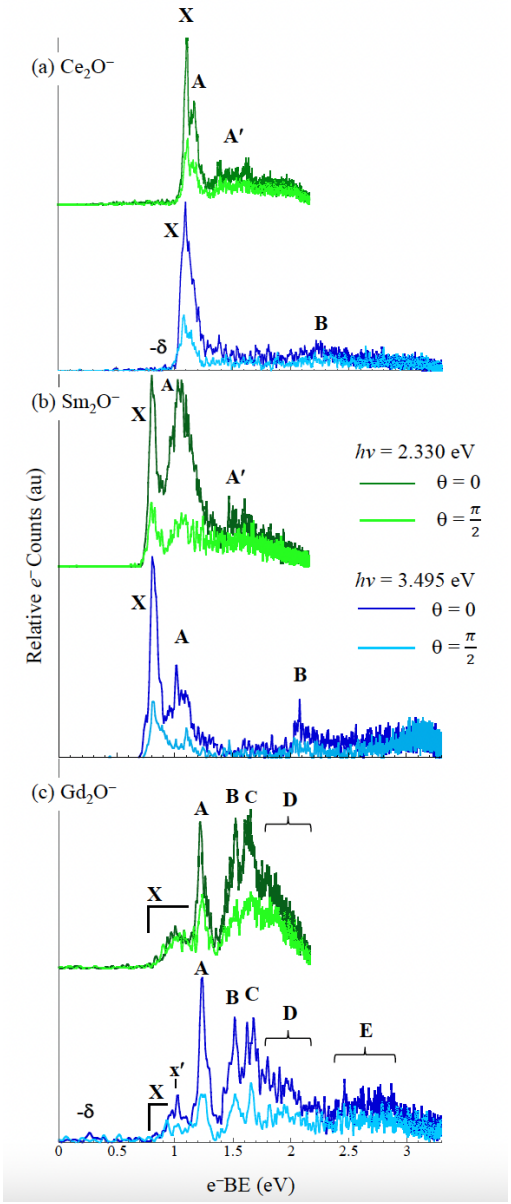

Figure 7.2: Anion PE spectra of (a) Ce_2O^-, (b) Sm_2O^- and (c) Gd_2O^- measured using 2.330 eV (green traces) and 3.495 eV (blue traces) photon energies. Darker colors are spectra measured with the laser polarization parallel the electron drift path, lighter traces represent perpendicular polarization. Part (a) reprinted with permission from ref. 1 Copyright 2016 AIP Publishing. Part (b) reprinted with permission from ref. 2. Copyright 2017 AIP Publishing.

Bands **X**, **A**, and **B** in the Sm_2O^- spectrum are not three individual electronic transitions. Rather, they are manifolds of close-lying transitions associated with a common detachment process (e.g., detachment of an electron from the $\sigma_{6s,g}$ orbital) but differing in terms coupling between the $4f^6$ (^7F) centers on the two Sm atoms. Note that the ratio of the integrated intensities of band **A** to band **X** is significantly higher in the spectrum obtained with 2.330 eV photon energy, an effect attributed to the strong PEVE interactions noted in the Introduction section. The transitions in the spectraof Ce_2O^- and Sm_2O^- can be described in similar terms, with band **X** in both being assigned to states accessed by detaching electrons from the outer-valence MOs with 6s character.

The PE spectrum of Gd_2O^- is strikingly different from the Ce_2O^- and Sm_2O^- spectra. In both the spectra collected with 3.495 eV and 2.330 eV photon energies, numerous transitions lie between 0.7 eV and 2.3 eV, labeled **X**, **A**, **B**, **C** and **D**. Peak positions are summarized in Table 7.1. As with the Sm_2O^- spectrum, these features appear to be manifolds of electronic transitions rather than five individual transitions, and features within each band are partially resolved. Bands **B**, **C** and **D** are more intense relative to bands **X** and **A** in the spectrum collected with 2.330 eV photon energy, which points to PEVE interactions.

Band **X** in the PE spectrum of Gd_2O^- is relatively low-intensity and broadened, while the more intense, parallel feature (**A**) is comparable to band **X** in the Ce_2O^- and Sm_2O^- spectra. Irregular peak spacings within band **A** are discerned in the spectrum obtained with 2.330 eV, and their positions are summarized in Table 7.1. At higher e^-BE, the congested features grouped into portions labeled **B**, **C**, **D**, and **E**, in addition to considerable continuum signal do not readily correlate with features in the two other Ln_2O^- spectra shown. The fact that the spectrum of chGd2O- is more congested with electronic transitions is unexpected. As noted in the Introduction, the 4f 7 (8S) centers on the two Gd centers in Gd_2O^-, in contrast to the $4f^6$ (^7F) centers in Sm_2O^-, do not introduce numerous close-lying spin-orbit states present in $Sm_2OSm_2O^-$.

There are several subtle differences between the spectra of Gd_2O^- obtained with the two photon energies. Band **X** in the spectrum collected with 3.495 eV (blue

trace) is punctuated by a narrow feature labeled **x'** at e^-BE = 1.00 ± 0.01 eV, with parallel PAD. In the spectrum obtained with 2.330 eV, band has overall more isotropic (*vide infra*) PAD. In addition, bands **C** and **D** observed in the spectrum collected with 2.330 eV should be better resolved than the same features in the spectrum collected with 3.495 eV per Equation (1). Instead, these bands appear broadened in the 2.330 eV spectrum relative to the 3.495 eV spectrum.

A reproducible and unusual effect is seen in the different appearances of the spectra obtained with the laser polarization parallel and perpendicular to the direction of electron collection. This effect is observed in spectra collected with both 2.330 and 3.495 eV photon energies, but it is more distinct in the former because the transitions are better resolved [again, Equation (1)]. The 2.330 eV spectrum is shown on an expanded scale in Fig. 7.3(a) with contrasting colors (green and red) used to illustrate the differences. 7.3(b) shows a narrower e^-BE range, with the spectrum collected with perpendicular polarization scaled by a factor of 2 to facilitate comparison. On the low e^-BE edge of bands **X**, **A**, and **B**, distinct peaks are observed in the perpendicular spectrum, labeled with symbols, that coincide with a local intensity minimum in the parallel spectrum. **B** and **C** in the spectrum obtained with 2.330 eV is more congested than the same band in the 3.495 eV spectrum, which shows a distinct maximum intensity in the spectrum measured with perpendicular polarization at a local minimum in the parallel analog, as can be seen in Fig. 7.2(c).

This observation supports the assertion that these bands are manifolds of close-lying, but distinct, electronic transitions, but the striking difference in PAD across these manifolds suggests that transitions within them involve detachment from orbitals of different symmetry. Electronic structure calculations on Gd_2O^- and Gd_2O were therefore conducted to support interpretation of the anomalous PADs observed in the spectra.

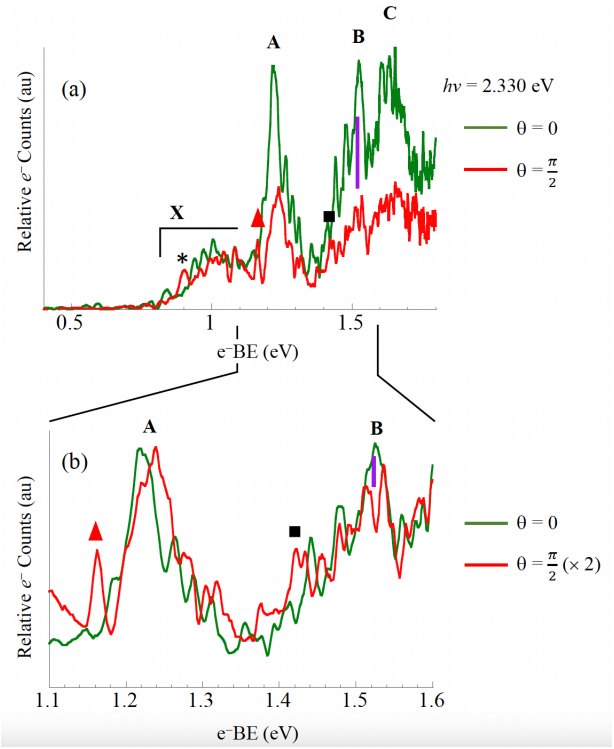

Figure 7.3: (a) Anion PE spectrum of Gd_2O^- measured using 2.330 eV photon energy shown on an expanded scale and with more contrasting colors to distinguish between the parallel (green) and perpendicular (red) polarizations. (b) Close-up of the 1.1 - 1.6 eV range, with the perpendicular spectrum scaled by a factor of 2, demonstrating distinct differences in spectral profiles between the spectra taken with different polarization.

7.3.2 Computed Electronic Structures of Gd_2O^- and Gd_2O and Spectral Assignments.

Results of calculations on the Gd_2O anion and neutral suggest a high density of electronic states, a sampling of which are summarized in Table 7.2. A more comprehensive list of states is included in appendix F. Neutral states that are accessible by 1-electron detachment transitions from any of the anions predicted to be stable with respect to the e^- + neutral detachment continuum are separated from neutral states with orbital occupancies that differ by more than one electron from the bound anions. Several structural parameters and representative vibrational frequencies are included. Linear and bent structures converged for the neutral. In general, the bend mode for all of the structures is low frequency ($\leq$ 100 cm^{-1}). The Gd−O symmetric stretch is not expected to be active in any of the anion to neutral transitions; the Gd−O bond distance changes by approximately 0.03 at most between different electronic states. The symmetric stretch frequency in the linear structures is approximately 200 cm^{-1} in linear molecules, low because it involves motion of the heavy Gd centers, while it is higher frequency in the bent structures (ca. 480 cm^{-1}), as it involves motion of the O-atom relative to the two Gd centers.

7.3.2.1 Ground States of the Anion and Neutral

As noted in the introduction, bent and linear Gd−O−Gd structures were predicted to be isoenergetic (within $<$ 0.001 eV) with the B3LYP/ANO-ECPplusPVTZ method. Both can be described as having the same electronic structures illustrated in 7.1, though the bent structure features some overlap between the two terminal 5d orbitals with a $^{16}A_1$ electronic term. When using Douglas-Kroll-Hess 2nd order relativistic integrals[485] and B3PW91 functional,[486] rather than an effective core potential, the bent structure is predicted to be more stable by about 0.15 eV; however, the combination of greater charge delocalization[467, 469, 482, 483, 487, 488, 3] and spin-orbit coupling in the linear structure suggests it is more stable. For a sense of scale, the spin-orbit components of the $6s$ $5d$ state of Gd^+ span approximately 0.23 eV.[489] While the analogous splitting in Gd_2O^- may be

lower, this splitting exceeds the highest computed difference in bent to linear energy. However, since both the bent and linear structures are local minima, the bend potential could be rather complicated with strong vibronic coupling.

The EA of the neutral is calculated to be 0.28 eV, which is much lower in energy than most of the signal observed in the spectrum. The lowest energy neutral state is a linear $^{15}\Sigma_g$ state, which is one-electron accessible from detachment of the single electron in the $15\Sigma_g$ orbital of the $^{16}\Delta_g$ state. Low-intensity signal is observed in the Gd_2O^- spectrum measured using 3.495 eV photon energy at 0.26 eV, labeled "--δ," which we attribute to the $^{15}\Sigma_g \leftarrow {}^{16}\Delta_g$ transition based on this computational result, as indicated in Table 7.1. This transition is predicted to be at a much lower energy than the analogous transition in the Ce_2O^- spectrum [Fig. 7.2(a)]; In contrast to the calculated relative orbital energies shown in Fig. 7.1, calculations on Ce_2O^- predicted the (singly-occupied) 5d-based MOs to lie below the σ_u orbital.[482] The differences in relative energies of analogous MOs is not unexpected, given the differences in orbital occupancies of the atomic systems. For example, the atomic Ce- orbital occupancy is 4f 5d2 6s2, while the Gd- occupancy is $4f^7\ 5d\ 6s^2\ 6p$.[42]

As noted in earlier studies on lanthanides and lanthanide oxides, the cross section for detachment of electrons from MOs with 4f or 5d character is very small compared to the cross section for detachment from MOs with 6s character.[482, 490, 491] Therefore, the more intense features are associated with detaching electrons from either of the close-lying σ_g and σ_u orbitals (Figure 7.1). Calculations predict these transitions to lie at e^-BE values between 0.95 eV and 2.04 eV, the energy interval in which numerous detachment transitions are observed experimentally. In a simple one-electron picture, there would be only four transitions originating from the $^{16}\Delta_g$ state in this energy range, as there are four electrons occupying theσ_g and σ_u orbitals. The spectrum, on the other hand, is congested with numerous partially-resolved transitions.

7.3.2.2 Excited States of the Anion

Low-lying electronic states of the anion may contribute to the number of observed transitions. Excited anionic states, calculated using PIMOM, were found by promoting an electron from the Δ_g to the Δ_u orbital ($^{16}\Delta_u$ $T_0 = 0.18$ eV), or flipping the spin of the Δ_g electron relative to the high-spin $4f$ cores ($^{14}\Delta_g$; T0 = 0.67 eV, not bound with the calculated detachment continuum). The low excitation energy of the $^{16}\Delta_u$ state reflects the weak coupling between the $5d_\Delta$ atomic orbitals, and the relatively high excitation energy of the $^{14}\Delta_g$ state reflects strong coupling between the sole unpaired outervalence electron with the $4f^7$ centers on the Gd atoms. The AFM coupled $^2\Delta$ state ($T_0 = 0.14$ eV) is the lowest energy bound excited state found for the anion. The structure of this AFM coupled state and the neutral AFM coupled states (vide infra) are calculated to have broken symmetry ($C_{\infty v}$ rather than $D_{\infty v}$ symmetry). Both Gd−O bondlengths are included in Table 7.2. This geometric symmetry breaking is likely an artifact of the single determinant structure of our DFT calculations and due to asymmetric spin polarization. Indeed, with a multi-determinantal wave function one would expect equal Gd–O bond distances.

The two bound excited states predicted for Gd_2O^- could increase congestion in the spectrum of Gd_2O^-. However, the additional irregularly spaced partially resolved features in the various bands, and the change in relative intensities of the numerous transitions with photon energy, again point to PEVE interactions that may result in the appearance of two-electron transitions, or transitions involving a change in the magnetic coupling between the two Gd $4f^7$ centers.

7.3.2.3 Neutral Excited States

Nominally one-electron detachment from the σ_u orbital would result in increased but weak bonding between the Gd centers, and calculations on states resulting from σ_u detachment are predicted to be bent. Neutral structures that converged in a bent geometry are distinguished by their C_{2v} term symbols in Table 7.1 (the optimized energy, as well as the energy of the state confined to a linear structure, are included in Table 7.1). The lowest energy bent neutral ($\angle$Gd−O−Gd = 106°),

a $^{17}B_2$ state, is predicted to lie 0.95 eV above the ground state anion, and we tentatively assign this transition to **X**.

A transition from the linear anion to this bent neutral state would exhibit an extended progression in the bend mode, which has a calculated harmonic frequency of 100 cm^{-1} and would therefore be unresolved in the experimental spectrum. Figure 7.4 shows a simulation based on the ADE and VDE values calculated for the $^{16}B_2 \leftarrow^{16} \Delta_g$ transition (red trace) both with the origin shifted to agree with band **X** transition in the experimental spectrum (green) and at the computed origin [panels (a) and (b), respectively]. The progression would necessarily be anharmonic and perturbed by strong vibronic coupling, given the increase in spin-orbit coupling with the more linear structure sampled at higher bend quanta. The VDE value for the $^{17}B_2 \leftarrow^{16} \Delta_g$ transition is computationally identical to the energy for the analogous neutral linear state (imaginary bend frequency), which is 1.22 eV. The blue trace shows the simulation based on the hypothetical $^{17}\Delta_u \leftarrow^{16} \Delta_g$ transition, which appears similar to band **A**. As a final comparison, a simulation based on the bent structures for both the anion and neutral (black trace) is included; it does not agree with any features in the experimental spectrum, providing further support for the linear anion.

The striking differences in the PE spectra of Gd_2O^- and Ce_2O^- or Sm_2O^- can be attributed to the linear structure of Gd_2O^- and bent structures ofCe_2O^- and Sm_2O^-. Among the three triatomics, only Gd_2O^- has (single) occupancy of every 4f-based molecular orbital, including the least stable $\sigma_{g,4f}$ and $\sigma_{u,4f}$ orbitals in the ligand field of the O-atom. Analogous $a_{1,4f}$ and $b_{1,4f}$ orbitals are unoccupied in $Ce_2O^-$and Sm_2O^-. $Gd_2O^-$is therefore unique in that configuration interaction between these orbitals and their like-symmetry

Continuum signal lies between bands **X** and **A**, raising the question of whether strong vibronic coupling between bent and linear neutral states is in evidence. Again, considering the large spin-orbit splitting expected for any linear structure, the linear $^{17}\Delta_u$ could conceivably be a metastable structure with which the linear anion would be structurally similar (i.e., a near-vertical transition). We therefore tentatively assign band **A**, which is nearly vertical, to the $^{17}\Delta_u \leftarrow^{16} \Delta_g$ transition.

The calculated transition energy (1.22 eV) agrees with the most intense partially resolved feature in this band.

The associated lower-spin 15B2 state accessed by detaching the electron (also bent; ∠ Gd−O−Gd = 105°) is predicted to lie at e^{-1}BE = 1.30 eV, with a 1.66 eV calculated VDE. The coupling between a single electron in the σ_u orbital with the core-like $4f^7$ electrons is significant, given the predicted 0.35 eV $^{17}B_2$ $-^{15}$ B_2 splitting. Again, an electron occupies the 5d outer-valence orbital as well, which also couples to the unpaired electron in the b2 (σ_u)orbital. Unlike the linear $^{16}\Delta_u$ state, which has an imaginary bend frequency, the lower-spin linear $^{15}\Delta_u$ state is a local minimum computed to be 0.36 eV higher in energy than the $^{15}B_2$ structure with the same nominal electronic configuration. The $^{15}B_2 \leftarrow^{16} \Delta_g$ transition would again be broadened by an extended vibrational progression in the bend mode, while the $^{15}\Delta_u \leftarrow^{16} \Delta_g$ would be nearly vertical. The calculated transition energy of the latter (1.66 eV) is in reasonable agreement with band **C**, which we therefore tentatively assign to the $^{15}\Delta_u \leftarrow^{16} \Delta_g$ transition.

The calculated $^{17}\Delta_g$ neutral state, accessed by detaching the σ_g^β electron, increases antibonding between the two Gd centers and therefore results in a stable linear structure, is predicted to be 1.62 eV above the anion ground state, with the lower spin $^{15}\Delta_g$ (from PIMOM) analog at 2.04 eV. Taking into account that the calculated $^{17}\Delta_g \leftarrow {}^{16}\Delta_g$ is lower than the calculated $^{15}\Delta_u \leftarrow {}^{16}\Delta_g$, we tentatively assign band **B** to $^{17}\Delta_g \leftarrow {}^{16}\Delta_g$, and band **D** to $^{15}\Delta_u \leftarrow {}^{16}\Delta_g$. These assignments agree well with the calculated $^{15}\Delta \leftarrow {}^{17}\Delta$ splittings for both the $^{2s+1}\Delta_g$ and $^{2s+1}\Delta_u$ states. However, bands **B**, **C** and **D** have multiple partially resolved features, some of which have opposite PDS, and continuum signal and congestion is more prevalent in the experimental PE spectrum collected with lower photon energy.

7.3.2.4 Two-electron Transitions

We first consider electronic states that might be accessible via shake up (two-electron) transitions that might be prevalent because of PEVE interactions. We conducted a thorough search of electronic states associated with permuting the valence electrons in the states that are one-electron accessible from the $^{16}\Delta_g$

($\sigma_g^2\sigma_u^2$,$\sigma_g^2\sigma_u\delta_g$ and $\sigma_g\sigma_u^2\delta_g$) to the unoccupied 5*d*- (δ,π,σ) and 6*p*- (π,σ) based MOs, which should be low energy based on the electronic structure of GdO.[492] States that converged in a 3.5 eV energy window are included in Table 7.2, and additional higher energy states that converged are included in appendix F. There are numerous states that would be accessed vial detachment from the σ_u or σ_g orbital coupled with $\delta_u \leftarrow \delta_g$ or $\pi_{6p} \leftarrow \delta_g$ promotion in the 1.5 – 2.0 eV range. As suggested in a previous study, these transitions would arise from the polarization of outer-valence orbitals by the electric field from the departing electron.13 For example, an electron ejected along the Gd–O–Gd axis would polarize the electron in theδ_g away from the photoelectron in a way that could be described as $c_1(t)\delta_g + c_2(t)\delta_u$. The final neutral state would therefore have non-zero probability of having a singly occupied δ_u orbital, though the initial state had a singly occupied δ_g orbital. Wang and coworkers observed evidence of a time-independent valence orbital polarization in their anion PE spectra of dipole-bound anionic states.[471]

Several of the states calculated to be in the 1.5 – 2.0 eV e^-BE range are accessible via a one-electron transition from a bound excited state of the anion, which may account for some of the congestion observed in the spectrum. However, the spectra collected with 2.330 eV and 3.495 eV photon energies were collected under identical ion source conditions. The fact that bands **B**, **C** and **D** are more intense when compared to band **A** in the spectrum collected with 2.330 eV photon energy than in the 3.495 eV spectrum shows that the spectral congestion increases with decreasing e^-KE, which result in longer PEVE interaction times. Longer interaction times result in an increased population of final states that are accessed by two-electron transitions.[467]

Excited states involving detachment from the σ_g or σ_u orbitals along with promotion of an electron from either the σ_g or σ_u orbital to the δ_g or δ_u orbital are calculated to lie above 2.8 eV. The manifold of transitions labeled **E** may include some of these transitions, but considering the large number of close-lying states predicted to be in this energy range, any specific assignments would be speculative. Anion PE spectra of other lanthanide suboxides exhibit low-intensity features with similar profiles, but at different energies [e.g., band A′ in the PE spectrum of

Ce_2O^- shown in Fig. 7.2(a)].[469, 2, 482, 483, 492]

7.3.3 Anomalous Photoelectron Angular Distributions

None of the preceding discussion addresses the curious differences in PAD of features within a given manifold. All anion PE spectra of lanthanide suboxides measured with the experimental apparatus described here have shown the hallmarks of detachment transitions from diffuse molecular orbitals with *Ln* 6s character, which are large detachment cross sections and parallel PAD. The PE spectrum of Gd_2O^- obtained using 3.495 eV photon energy [7.2(c)], at first glance, appears to have the same characteristics, but closer inspection of this spectrum, in addition to the better-resolved spectrum obtained with 2.330 eV photon energy [7.3] shows that several partially-resolved features have opposite PAD. Table 7.1 includes an indication of which partially resolved peaks are more intense in spectra obtained with $\theta = 0(\|)$ and $\theta = \frac{\pi}{2} \perp$ laser polarization.

Spin-orbit coupling has been implicated in disparate asymmetry parameters for different final components within a spin-orbit multiplet. Early studies on Cd ($4d^{1}05s^{2}\ ^{1}S_0$) atomic ionization processes[493] showed nearly isotropic PAD for transitions to the excited $4d^{9}5s^{2}\ ^{2}D_{3/2}$ state ($\beta = -0.12$), with more a parallel PAD ($\beta = 1.49$) for transitions to the $4d^{9}5s^{2}\ ^{2}D_{5/2}$ state. Subsequent studies by others suggested the possibility that this effect was due to an autoionizing transition, and that the actual asymmetries plotted against e^-KE, versus photon energy, were similar.[494, 495] Different final states associated with 2p ionization of O-atoms showed disparate asymmetry parameters for the ^{1}D and ^{3}S cationic states, 0.34 and 0.71 respectively.[496] But, again, these values change dramatically with e^-KE, and the different final states are associated with different e^-KE values for any given photon energy.

In contrast, there are transitions with distinct perpendicular polarization dispersed throughout the spectrum of Gd_2O^- . Parallel transitions, such as those observed in most of the PE spectrum, are consistent with detachment from orbitals with strong 6s character. Given a linear Gd_2O^- anion, detachment from the $\sigma_u$or σ_g orbitals will result in no change in orbital angular momentum between the anion and neutral

Band	e- BE/eV		Tentative Assignment
$-\delta$[a]	0.26 ± 0.02 (‖)	Signal at this energy in 2.330 eV spectrum indistinguishable from noise	$^{15}\sum_g - ^{16}\Delta_g$
X[b]	0.84± 0.02 (‖)		
	0.90± 0.02 (⊥)		$^{17}B_2 - ^{16}\Delta_g$
	0.94± 0.02 (‖)		
	0.97 ± 0.02 (‖)		
	1.00 ± 0.01 (‖)		
	1.08 ± 0.03 (isotropic)		
A[b]	1.16± 0.02 (⊥)		
	1.22± 0.02 (‖)		$^{17}\Delta_u - ^{16}\Delta_g$
	1.24± 0.02 (⊥)		
	1.26± 0.02 (‖)		
	1.29± 0.02 (‖)		
	1.31± 0.02 (⊥)		
B[b]	1.43± 0.04 (⊥)		($^{15}B_2 - ^{16}\Delta_g$ contributes to continuum signal
	1.44± 0.02 (‖)		
	1.48± 0.02 (‖)		
	1.53± 0.02 (‖)		$^{17}\Delta_g - ^{16}\Delta_g$
C[a]	1.62± 0.03 (‖)	Features broadened and less resolved in the 2.330 eV spectrum	
	1.66± 0.03 (⊥)		$^{15}\Delta_u - ^{16}\Delta_g$
	1.68± 0.03 (‖)		
D[b]	1.7 – 2.1 (‖)		$^{15}\Delta_g - ^{16}\Delta_g$
E[a]	2.42± 0.03 (‖)		
	2.5 – 3.0 (isotropic)		

[a] Feature better resolved or only observed in the 3.495 eV PE spectrum; position based on this spectrum.

[b] Feature better resolved in the 2.330 eV PE spectrum; position based on this spectrum.

Table 7.1: Positions of bands, or any partially resolved peaks within those bands, along with the angle relative to the laser polarization at which the signal is more intense, observed in the PE spectra of Gd_2O^-. Tentative assignments based on computational results are included.

	Molecular Term	Electronic configuration (O 2p orbitals are omitted)	Relative energy (ev)	Gd–O (A)
Gd_2O $2e^-$ accessible from bound states of anion	$^{15}\Gamma_g$ (5d)	$4f_a^{7\alpha}\ 4f_b^{7\alpha}\ldots\ \sigma_g^{\beta}\sigma_u^{\alpha}\delta_g^2$	3.53	
	$^{17}\sum_u$ (5d)	$4f_a^{7\alpha}\ 4f_b^{7\alpha}\ldots\ \sigma_g^2\sigma_u^{\alpha}\sigma_{g,5d}^{\alpha}$	3.37	
	$^{15}\prod_u$ (5d)	$4f_a^{7\alpha}\ 4f_b^{7\alpha}\ldots\ \sigma_g^{\beta}\sigma_u^2\pi_{u,5d}^{\alpha}$	3.19	
	$^{15}\Gamma_u$ (5d)	$4f_a^{7\alpha}\ 4f_b^{7\alpha}\ldots\ \sigma_g^{\beta}\sigma_u^{\beta}\delta_u^{\alpha}\delta_g^{\alpha}$	2.90	
	$^{17}\phi_u$ (6p)	$4f_a^{7\alpha}\ 4f_b^{7\alpha}\ldots\ \sigma_g^2\delta_u^{\alpha}\pi_{u,6p}^{\alpha}$	2.80	
	$^{17}\sum_g$ (6p)	$4f_a^{7\alpha}\ 4f_b^{7\alpha}\ldots\ \sigma_g^{\alpha}\sigma_u^2\sigma_{g,6p}^{\alpha}$	2.55	
	$^{15}\prod_u$ (6p)	$4f_a^{7\alpha}\ 4f_b^{7\alpha}\ldots\ \sigma_g^{\beta}\sigma_u^2\pi_{u,6p}^{\alpha}$	2.35	
	$^{15}\prod_g$ (5d)	$4f_a^{7\alpha}\ 4f_b^{7\alpha}\ldots\ \sigma_g^2\sigma_u^{\alpha}\pi_{u,5d}^{\alpha}$	2.31	
	$^{17}\Gamma_u$ (5d)	$4f_a^{7\alpha}\ 4f_b^{7\alpha}\ldots\ \sigma_g^2\delta_u^{\alpha}\delta_g^{\alpha}$	2.22	
	$^{17}\sum_u$ (6p)	$4f_a^{7\alpha}\ 4f_b^{7\alpha}\ldots\ \sigma_g^2\sigma_u^{\alpha}\sigma_{g,6p}^{\alpha}$	2.12*	
	$^{17}\prod_u$ (6p)	$4f_a^{7\alpha}\ 4f_b^{7\alpha}\ldots\ \sigma_g^{\alpha}\sigma_u^2\pi_{u,6p}^{\alpha}$	2.02	
	$^{15}\prod_g$ (6p)	$4f_a^{7\alpha}\ 4f_b^{7\alpha}\ldots\ \sigma_g^2\sigma_u^{\beta}\pi_{u,6p}^{\alpha}$	1.98	
	$^{17}\prod_g$ (6p)	$4f_a^{7\alpha}\ 4f_b^{7\alpha}\ldots\ \sigma_g^2\sigma_u^{\alpha}\pi_{u,6p}^{\alpha}$	1.58*	
Gd_2O $1e^-$ accessible from bound states of anion	$^{13}\Delta_g$	$4f_a^{7\alpha}\ 4f_b^{7\alpha}\ldots\ \sigma_g^{\beta}\sigma_u^2\delta_g^{\beta}$	2.53	
	$^{15}\Delta_g$	$4f_a^{7\alpha}\ 4f_b^{7\alpha}\ldots\ \sigma_g^{\alpha}\sigma_u^2\delta_g^{\beta}$	2.50	
	$^{15}\Delta_u$	$4f_a^{7\alpha}\ 4f_b^{7\alpha}\ldots\ \sigma_g^{\beta}\sigma_u^2\delta_u^{\alpha}$	2.20	
	$^{15}\Delta_g$	$4f_a^{7\alpha}\ 4f_b^{7\alpha}\ldots\ \sigma_g^{\beta}\sigma_u^2\delta_g^{\alpha}$	2.04	
	$^{17}\Delta_g$	$4f_a^{7\alpha}\ 4f_b^{7\alpha}\ldots\ \sigma_g^{\alpha}\sigma_u^2\delta_g^{\alpha}$	1.62	
	$^{3}\Delta_g$	$4f_a^{7\alpha}\ 4f_b^{7\beta}\ldots\ \sigma_g^2\sigma_u^{\alpha}\delta_u^{\alpha}$	1.57	
	$^{17}\Delta_g$	$4f_a^{7\alpha}\ 4f_b^{7\alpha}\ldots\ \sigma_g^2\sigma_u^{\alpha}\delta_u^{\alpha}$	1.38	
	$^{15}B_2$; $^{15}\Delta_u$	$4f_a^{7\alpha}\ 4f_b^{7\alpha}\ldots\ \sigma_g^2\sigma_u^{\alpha}\delta_g^{\alpha}$	1.30; 1.66*	
	$^{3}\Delta_g$	$4f_a^{7\alpha}\ 4f_b^{7\beta}\ldots\ \sigma_g^2\sigma_u^{\alpha}\delta_g^{\alpha}$	0.96	2.054;1.957
	$^{15}B_2$; $^{15}\Delta_u$	$4f_a^{7\alpha}\ 4f_b^{7\alpha}\ldots\ \sigma_g^2\sigma_u^{\alpha}\delta_g^{\alpha}$	0.95; 1.22*	2.011;1.988
	$^{1}\sum_g$	$4f_a^{7\alpha}\ 4f_b^{7\beta}\ldots\ \sigma_g^2\sigma_u^2$	0.28	1.989
	$^{15}\sum_g$	$4f_a^{7\alpha}\ 4f_b^{7\alpha}\ldots\ \sigma_g^2\sigma_u^2$	0.28	1.990
Gd_2O^-	$^{14}\Delta_g$	$4f_a^{7\alpha}\ 4f_b^{7\alpha}\ldots\ \sigma_g^2\sigma_u^2\delta_g^{\beta}$	0.67 (not bound)	
	$^{16}\prod_u$	$4f_a^{7\alpha}\ 4f_b^{7\alpha}\ldots\ \sigma_g^2\sigma_u^2\pi_u^{\alpha}$ (6p)	0.35 (not bound)	
	$^{16}\Delta_u$	$4f_a^{7\alpha}\ 4f_b^{7\alpha}\ldots\ \sigma_g^2\sigma_u^2\delta_u^{\alpha}$	0.18*	
	$^{2}\Delta$	$4f_a^{7\alpha}\ 4f_b^{7\beta}\ldots\ \sigma_g^2\sigma_u^2\delta_g^{\alpha}$	0.14	2.140;1.917
	$^{16}A_1$; $^{16}\Delta_g$	$4f_a^{7\alpha}\ 4f_b^{7\alpha}\ldots\ \sigma_g^2\sigma_u^2\delta_g^{\alpha}$	0; 0	2.017;2.008

Table 7.2: Summary of several of the electronic states calculated for Gd_2O^- and Gd_2O. Asterisks (*) indicate energies determined from single-point calculations when structure optimizations failed to converge. The molecular terms for states that are only accessible via shake-up transitions include the AO-basis of the electron excitation accompanying detachment.

electronic states, giving a selection rule of ΔS, $\Delta M_s = \mp 1/2$. The two sets of $^{17}\Delta \leftarrow {}^{16}\Delta$ ($\Delta M_s = +1/2$) and $^{15}\Delta \leftarrow {}^{16}\Delta$ ($\Delta M_s = -1/2$)transitions fall into this category, and the resulting photoelectron would carry away $l = 1$ unit of angular momentum, consistent with the parallel PAD.[497] From the standpoint of orbital angular momentum, there is no explanation for the features with perpendicular PAD, unless the orbital angular momentum of the ejected electron is affected by PEVE interactions in a way that was not observed in previous studies on similar strongly correlated systems.[455]

Considering the strong coupling between unpaired outervalence electrons and the $4f^7$ cores evident from the energy associated with $\alpha \rightarrow \beta$ spin flips in the δ orbitals (ca. 0.8 eV, Table 7.1) it is conceivable that there is similarly strong coupling between the orbital angular momentum of the ejected electron and the projection of the spin angular momentum of the $4f^7$ cores. 7.4 shows a schematic of the energies of the individual M_s levels of the $^{16}\Delta_g$ anion ground state, assuming an axial zero field splitting of -20cm^{-1}, following $E_{M_s} = \left({M_s}^2 - \frac{1}{4}\right)D$ for half integer spins, as well as the levels of the $^{17}\Delta_u$and $^{15}\Delta_u$ states that follow $E_{M_s} = ({M_s}^2)D$ for integer spins. We assume D = -20 cm^{-1}, for the sake of illustration.

From the lowest energy degenerate levels of the anion, $M_s = \pm 15/2$, the detachment of a single electron from the σ_u orbital would access the $M_s = \pm 8$ levels of the $^{17}\sigma_u$ state or the $M_s = \pm 7$ levels of the $^{15}\sigma_u$state, given the selection rule noted above. These transitions are represented by green arrows in 7.4, which also shows transitions from excited M_s levels of the anion. If, however, interaction between the photoelectron with $l = 1$ strongly interacts with the coupled $4f^7$ Gd cores in a way that changes the orbital angular momentum of the outgoing electron to $l = 0$, 2, the resulting PAD would be perpendicular,[497] coupled with $\Delta M_s = \pm 1/2 + 1$ (red dotted arrows) or $\Delta M_s = \pm 1/2 - 1$ (blue dotted arrows) transitions. We note here that neither spin nor orbital angular momentum are good quantum numbers, though we will still frame idea in L–S terms.

The schematic shown if 7.4 is oversimplified in that it assumes equal axial zero-field splitting for the anion and two neutral states, D = -20cm^{-1}, but this scheme would result in differences in energy between the parallel and perpendicular tran-

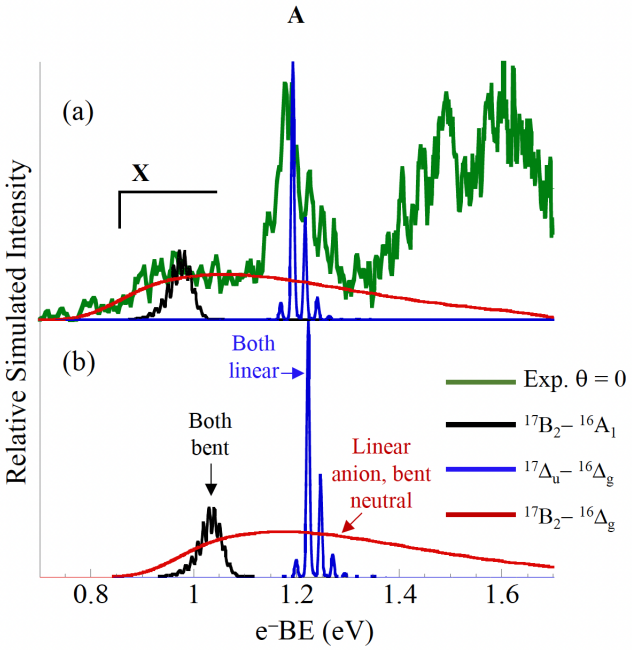

Figure 7.4: (a) Simulations based on calculated anion and neutral structures. The black trace is based on bent structures for both the anion and neutral, the blue trace is based on the linear structures for both the anion and neutral, and the red trace is based on the linear anion and bent neutral. Transition origins have been adjusted to compare with the experimental spectrum (green). (b) Same simulations shown at the calculated transition energies (Table 7.2).

sitions. The simulation shown 7.5(a) assumes D = -20cm^{-1} for anion and two neutral states, equal oscillator strength for all transitions, and thermal population of the four lowest excited M_s levels of the anion (i.e., electronic sequence bands, represented in part by the groupings of green, red, and blue arrows in 7.4). Note that the transitions associated with $\Delta M_s = \pm 1/2 + 1$ (red dotted arrows) can only occur from the excited M_s levels of the anion. The simulation shows that the sequence bands are close in energy and would not be resolved experimentally, but the $l = 0$, 2 perpendicular transitions would appear at lower ($\Delta M_s = \pm 1/2 + 1$, dotted red line) and higher ($\Delta M_s = \pm 1/2 - 1$, dotted blue line) energies relative to the $l = 1$ ($\Delta M_s = \pm 1/2$, green line) parallel transition. The energy interval between the three groups of transitions is dependent on the value of D for the neutral states. Again, note that equal oscillator strength -20cm^{-1} as assumed for all transitions, rather than arbitrarily giving the perpendicular transitions lower oscillator strength. Given these assumptions, the simulation of the $^{17}\Delta_u \leftarrow ^{16}\Delta_g$ transition resembles band **A** in 7.5(c).

If instead we assume D = -20cm^{-1} for the anion and D = $+20\ \text{cm}^{-1}$ for the neutral states and apply the same set of selection rules, the simulated transitions appear very different, as shown in 7.5(b). The electronic sequence bands are well separated, trailing to lower e^-BE, and the perpendicular transitions coincide in energy, appearing at lower e^-BE than the parallel transition. The result is similar in appearance to band **B**.

This rationale raises the question of why this phenomenon hasn't been observed in the spectra of Sm_2O^- or $Gd_2O_2^-$. In both cases, the crowding of electronic transitions made it difficult or impossible to discern features between spectra taken with the different laser polarizations. However, our previously reported PE spectrum of the $MnMoO_3^-$ molecule[3] ($^7A'$ anion ground state) exhibited an anomalous PAD. Figure 6 shows the spectrum near the origin transition obtained using parallel (green) and perpendicular (red) laser polarizations. This relatively narrow electronic transition includes a short vibrational progression, and both the $v' = 0$ and $v' = 1$ members exhibit minima in the perpendicular spectrum where the peaks reach maximum intensity in the parallel spectrum. The S/N in the more intense

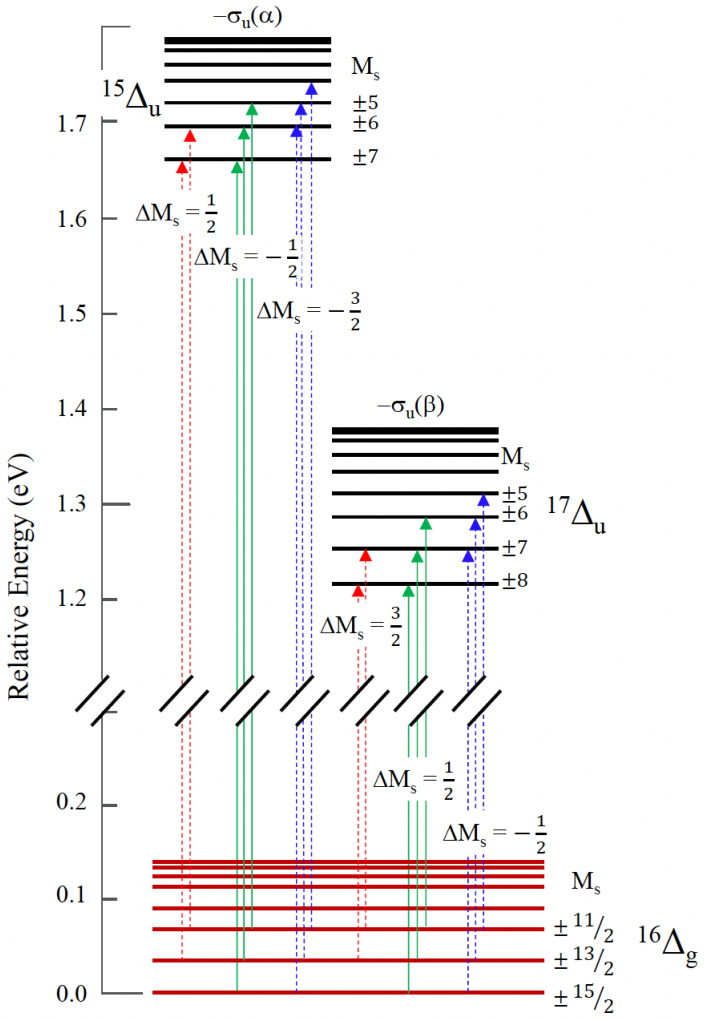

Figure 7.5: Energies of the M_s levels of the $^1 6\Delta_g$ state of Gd_2O^- and the neutral $^1 7\Delta_u$ and $^1 5\Delta_u$ states accessed by detachment of an electron from the σ_u outer valence orbital. The green arrows show transitions that follow the $\Delta S = +1/2$ (accessing $^1 7\Delta_g$) and -1/2 (accessing $^1 5\Delta_g$) selection rule. The blue and red dashed arrows are hypothetically allowed transitions if angular momentum from the $l = 1$ photoelectron generated from detachment from an orbital with zero orbital angular momentum were transferred to change M_s by an additional unit.

$v' = 0$ transition is sufficient to determine a splitting of 0.017 eV (137 cm^{-1}) between the partially resolved features in the perpendicular spectrum, which would be consistent with D = -17 cm^{-1} for neutral $MnMoO_3$.

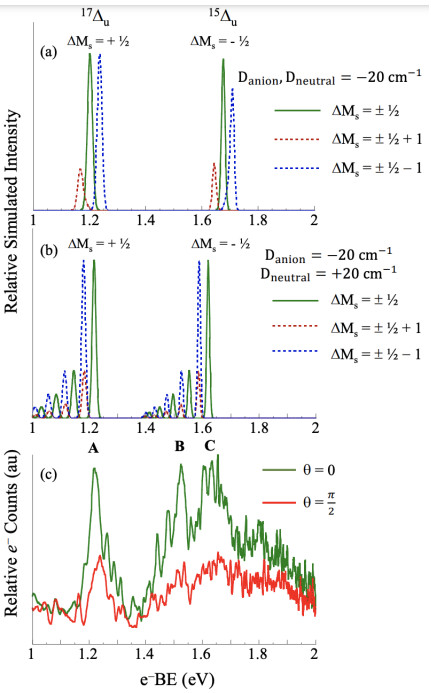

Figure 7.6: (a) Simulation based on the energy levels shown in 7.4, assuming thermal population of the 5 lowest energy Ms levels of the $^{16}\Delta_g$ anion. Color coding of transitions is consistent with the arrows representing the transitions in 7.4. D is assumed to be $-20cm^{-1}$ cm^{-1} for the $^{16}\Delta_g$, $^{17}\Delta_g$, and $^{15}\Delta_g$ states. (b) Simulation of the same transitions assuming D is -20 cm^{-1} for the $^{16}\Delta_g$, state, and $+20$ cm^{-1} for the $^{17}\Delta_g$ and $^{15}\Delta_g$ states. ADEs for the transitions based on computed energies for the (unsplit) states. (c) Experimental PE spectrum of Gd_2O^- in the same energy range, for direct comparison to the simulated profiles

A more sophisticated theoretical treatment to calculate D for the numerous close-lying electronic states of Gd_2O^- and Gd_2O is beyond the scope of this report. However, the simulations based on values of D in line with those reported for di-gadolinium complexes in which the Gd centers are bridged by N_2^{3-} ligands[478, 477] show profiles that are qualitatively similar to what is observed in the PE spectrum of Gd_2O^- , suggesting that anion PE spectra of these strongly correlated systems

could provide another means for modeling potential single molecule magnet properties.

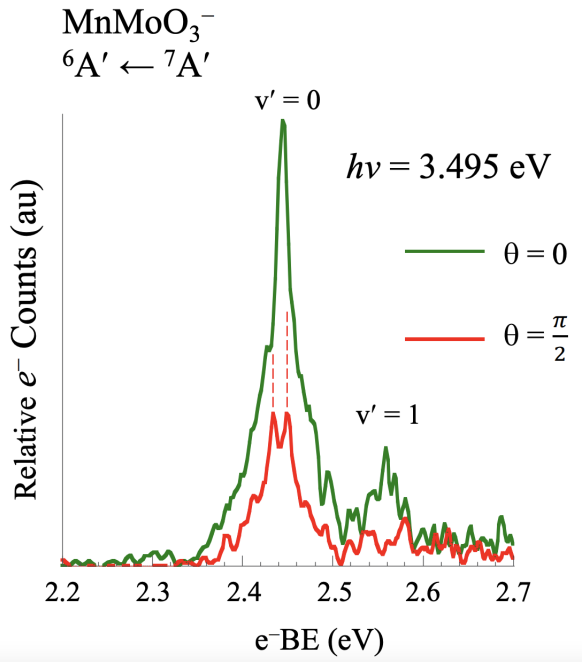

Figure 7.7: (a) Anion PE spectrum previously reported for $MnMoO_3^-$ measured using 3.495 eV photon energy shown on an expanded scale and with contrasting colors to distinguish between the parallel (green) and perpendicular (red) polarizations. The spectrum obtained with perpendicular polarization shows dips at energies where the parallel spectrum peaks. Reprinted with permission from ref. 3. Copyright 2020 AIP Publishing.

7.4 Conclusion

In an extension of our studies on the manifestation of PEVE interactions on the PE spectra of strongly correlated molecular systems, the anion PE spectrum of Gd_2O^- was presented and compared with the Ce_2O^- and Sm_2O^- analogs. The motivation for targeting Gd_2O^- was the expectation of simple electronic structure of the $4f^7$ (^8S) subshell occupancy in Gd atoms, which should reduce the number of close-lying states compared to the numerous spin-orbit components arising from the $4f^6$ (^7F_j) subshell of Sm. Based on the analysis of the spectrum with supporting

calculations, we conclude:

1. The Gd_2O^- PE spectrum exhibits numerous electronic transitions over a wider range of e^-BEs compared to the Ce_2O^- and Sm_2O^- spectra. However, like Sm_2O^- the intensities of transitions to excited states increase relative to the ground state with lower photon energy, which is consistent with the hypothesis that the ejected electron creates a time-dependent perturbation of the electronic structure of the neutral Gd_2O remnant, resulting in observation of two-electron (shake-up) transitions.

2. Calculations predict the linear and bent structures of Gd_2O^- to be nearly identical in energy. However, because of the stability from spin-orbit splitting in the linear $^1 6\sigma_g$ state, we assert that the true ground state is linear.

3. The group of intense spectral features that lie between 0.7 eV and 2.3 eV are assigned to transitions involving detachment of an electron from outervalence σ_u and σ_g orbitals that have large Gd 6s contributions. A very low-intensity transition observed at e^-BE = 0.26 eV in the spectrum measured with 3.495 eV that is assigned to the transition to the ground state via detachment of the δ_g (Gd 5d-based) outervalence electron.

4. The spectra show parallel transition manifolds in general, which is consistent with detachment from σ_u and σ_g orbitals. However, several distinct perpendicular transitions are observed adjacent to several of the vertical transitions. A possible explanation invoking interaction between the ejected electron and the high-spin neutral is proposed. Specifically, the angular momentum of electrons ejected from σ_u or σ_g orbitals, which is $l = 1$, can be switched to $l = 0$, 2 with an associated change in the M_s of the remnant neutral, which would be spin-orbit coupling between a free electron and the spin of a neutral.

Evidence of strong time-dependent electron-neutral coupling continues to challenge how we envision photodetachment and provides interesting directions for theory.

Chapter 8

Summary and Outlook

This dissertation, titled "Improvements in Maximum Overlap Methods for Studying Excited Electronic States and Exotic Ground States and Computational Simulations of Metal Oxide Photodetachment Spectra" discussed twp broadly defined sections. The first section presented and demonstrated a new pair of tools developed for locating excited states at a ground state computational cost, termed the Projection-based Maximum Overlap Method (PMOM) and Projection-based Initial Maximum Overlap Method (PIMOM). The second section presented collaborative work on the hydrolysis of transition metal oxides, specifically TiO_2 and ZrO_2.

The first portion of this Ph. D. work focuses on the development of an efficient method for calculating electronic excited states. Computational studies of electronic excited states impacts all areas of chemistry and a range of related scientific fields including materials science and biology. Many of the available computational models for such calculations involve significant computational expense and some can be quite sensitive to user selected options. Since advancements in excited state studies demand accurate and efficient modeling, it is crucial that new and affordable excited state methodologies be developed and validated.

One approach to excited state calculations is to alter well-developed ground state models in order to effectively turn excited state calculations into ground state problems. These models often suffer from numerical instabilities or require the user to define and impose constraints on the electronic structure. With this in mind, I

have developed the Projected Maximum Overlap Method (PMOM) and the Projected Initial Maximum Overlap Method (PIMOM). In a further study, I have explored the use of this method to specifically study optimized minimum energy structures, adiabatic excitation energies, and vibrational frequencies for electronic excited states. PIMOM demonstrated its ability to reproduce excited state vibrational frequencies obtained by more expensive models, such as time–dependent DFT. This work has shown the efficacy and robustness of these models paired with a spin-purification technique to remedy spin-contamination that is often observed in ground state approximations to excited state electronic structures.

Importantly, PMOM and PIMOM provide at least an order of magnitude decrease in computational cost for frequency calculations and evaluations of other response properties relative to conventional excited state methods.

PMOM and PIMOM have also been used in a number of high-impact collaborative studies. In collaboration with the Chick Jarrold Group at Indiana University, PIMOM has been used to explore exotic electronic states in systems with a high density of states due to f-block elements.[454, 455] PIMOM successfully located and distinguished between close–lying excited states that more sophisticated, and computationally expensive, methods fail to locate. The model was especially crucial to study the photoelectron spectra of $Gd_2O_2^-$ and Gd_2O^- and to provide a description of strong photoelectron-valence electron interactions. This work is fundamental in understanding strongly correlated electronic materials, a prominent grand challenge problem in materials science.

The presented PIMOM formulation employs a simple form for the projector operator. In some cases, the $\mathscr{P}^{\text{target}}$ operator may not be compactly presentable for a system's Hilbert space. In these systems, one may find degenerate sub-spaces corresponding to a single eigenvalue of the operator containing multiple (perhaps infinite) $|i\rangle\langle i|$-like terms.[324, 325, 326, 327, 328] For such cases, two-argument projector operators may be more prudent for the formulation of the PIMOM algorithm.

The second area of work described in the dissertation emphasized the importance of synergistic interactions between experimentalists and theorists. Such collabora-

tive efforts can lead to a holistic understanding of chemical processes yielding an understanding whose whole is greater than the sum of its parts. In collaboration with Daniel Neumark's lab at UC Berkeley, we studied the hydrolysis of TiO_2 and ZrO_2. In the first, $TiO_3H_2^-$ anions were used to probe the simplest titania/water reaction, $TiO_2^{0/-} + H_2O$. The resultant spectra show vibrationally resolved vibrational structure. Calculations were able to clearly assign the spectrum to detachment from the cis-dihydroxide $TiO(OH)_2^-$ This work represented a significant improvement in resolution over previous measurements, yielding an electron affinity of 1.2529(4) eV as well as several vibrational frequencies for neutral TiO(OH)2. The second study used electronic structure calculations and complementary high-resolution anion photoelectron spectra of the $ZrO_3H_2^-$ to investigate the reaction between zirconium dioxide and a single water molecule, $ZrO_0/^- + H_2O$. Simulations clearly showed that both cis– and trans–dihydroxide structures are present in the experiment. Additionally, it was found that water-splitting is stabilized more by ZrO_2 than TiO_2, suggesting Zr-based catalysts are more reactive toward hydrolysis. These two studies demonstrate the value of computational chemistry in predicting and resolving experimental observations to enhance fundamental knowledge and guide the development of catalyst design principles.

Appendix A

Chapter 6 Supplemental Information

A.1 Model Chemistry Benchmarking

Preliminary studies suggested meaningful functional and basis set dependencies in calculations of $TiO(OH)_2$ neutral and anion species. Using both B3LYP and ωB97XD approximate density functionals, three basis/effective core potential (ECP) sets were considered: (1) the all-electron Def2TZVP basis set for all atoms; (2) the Stuttgart/Cologne ECP (designated ECP10MDF) with the corresponding valence electron basis set on Ti and the aug-cc-pVDZ all electron basis set for H and O centers (SC), and (3) the Stuttgart/Cologne ECP (designated ECP10MDF) with a modified form of the corresponding valence electron basis set that includes higher angular momentum functions for Ti and aug-cc-pVTZ to describe orbitals on H and O atoms (SDD+TZ). Tables A.1 and A.1, below, give calculated adiabatic detachment energies (ADEs) and vertical detachment energies (VDEs) for the six functional/basis set combinations considered. For comparison, HF and CCSD results are also included. All CCSD and HF geometry optimization calculations converge to the expected planar C_{2v} geometry (1-1a) for both anion and neutral. However, all geometry optimizations of neutral 1-1a' using ωB97XD converged to non-planar structures. Similarly, the neutral 1-1a' B3LYP/SC and B3LYP/SDD+TZ geometry optimizations converged to non-planar geometries. Optimization of the 1-1a anion converged to the expected planar structure in all cases. Given these results and the good agreement with CCSD for the ADE and VDE predictions, the

B3LYP/Def2TZVP model chemistry was chosen for all calculations and results reported in this chapter.

A.2 Optimized Anion Geometries

1-1a	**SCF= -1076.658415 Eh**		
O	0	1.681205	-0.884975
O	0	0	1.724638
H	0	2.495033	-0.375347
Ti	0	0	0.0506
O	0	-1.681205	-0.884975
H	0	-2.495033	-0.375347

1-1b	**SCF= -1076.655399 Eh**		
O	1.514645	-1.098055	0.00023
O	0.25786	1.734672	-0.000049
H	2.39847	-0.722566	0.000328
Ti	-0.002131	0.081778	-0.000009
O	-1.819521	-0.5802	-0.000179
H	-1.975457	-1.527889	-0.000156

1-1c	**SCF= -1076.574996 Eh**		
Ti	-0.496421	0.351564	0
O	0.386009	0.58243	1.426741
O	0.386009	0.58243	-1.426741
O	0.386009	-1.788347	0
H	0.828529	-1.373255	-0.770533
H	0.828529	-1.373255	0.770533

1-1e	**SCF= -1076.650841 Eh**		
O	-1.70048	-0.812812	0
O	-0.000011	1.77743	0
H	-1.745299	-1.771464	0
Ti	0	0.105836	0
O	1.700492	-0.812803	0
H	1.745296	-1.771455	0

A.3 Neutral Optimized Geometries

1-1a'	**SCF= -1076.614767 Eh**		
O	0	1.614349	-0.832274
O	0	0	1.665003
H	0	2.523117	-0.520464
Ti	0	0	0.04715
O	0	-1.614349	-0.832274
H	0	-2.523117	-0.520464

1-1b'	**SCF= -1076.610776 Eh**		
O	1.542949	-0.935835	0.000239
O	0.135796	1.665754	-0.000085
H	2.475001	-0.702562	0.000328
Ti	0.000264	0.053464	0.000002
O	-1.721628	-0.605333	-0.000177
H	-2.137748	-1.47034	-0.000184

1-1c'	**SCF= -1076.546523 Eh**		
Ti	-0.382121	0.229875	0
O	0.281138	0.845209	1.386187
O	0.281138	0.845209	-1.386187
O	0.281138	-1.825638	0
H	0.82968	-1.98774	-0.780128
H	0.82968	-1.98774	0.780128

A.4 Figures

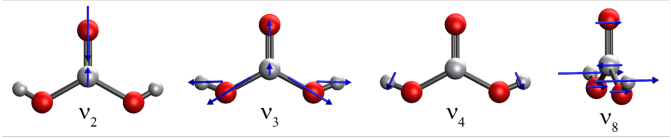

Figure A.1: Vibrational modes of the 1-1a' TiO_3H_2 isomer that are active in the cryo-SEVI spectrum.

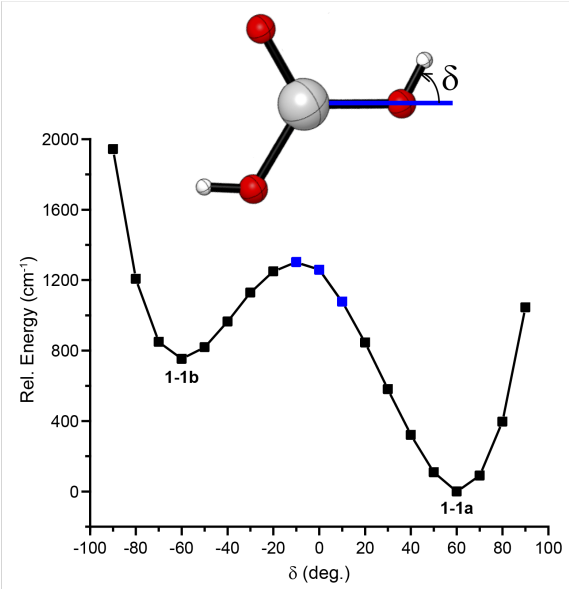

Figure A.2: Scan of the anion potential energy surface along the angular coordinate δ, defined in the top panel, which is used to distinguish between the cis- and trans-OH isomers 1-1a and 1-1b. These calculations were performed in Gaussian3 and carried out at the B3LYP/SDD+TZ level, as use of an ECP reduces computational expense. Points in black correspond to a constrained optimization where the value of δ was fixed and the other geometrical parameters were allowed to relax; for each of the -10° $\leq \delta \leq$ 10° data points, shown in blue, a single point calculation was carried out using the adjacent geometries with the δ-angle fixed at the appropriate value. The resultant barrier height for the trans-to-cis rotation is 549 cm^{-1}, and that of the cis-to¬-trans rotation is 1302 cm^{-1}; these constitute upper bounds for the true barrier heights due to the inability to perform a constrained optimization for the $\delta \approx 0$ geometries.

A.5 Tables

	Absolute Energy (E_h)		
Model Chemistry	**Anion**	**Neutral**	**ADE (eV)**
B3LYP/Def2TZVP	-1076.6312	-1076.5858	1.23
B3LYP/SC	-285.4334	-285.3810	1.42
B3LYP/SDD+TZ	-285.4891	-285.4368	1.42
ωB97XD/Def2TZVP	-1076.5214	-1076.4824	1.06
ωB97XD/SC	-285.3247	-285.2800	1.22
ωB97XD/SDD+TZ	-285.3771	-285.3328	1.21
HF/Def2TZVP	-1074.3943	-1074.3467	1.30
HF/SC	-283.6908	-283.6372	1.46
HF/SDD+TZ	-283.7421	-283.6909	1.39
CCSD/Def2TZVP	-1075.2521	-1075.2104	1.13
CCSD/SC	-284.4526	-284.4032	1.34
CCSD/SDD+TZ	-284.6343	-284.5847	1.35

Table A.1: Absolute energies including ZPE for optimized 1-1a anion and 1-1a' neutral geometries and the calculated ADEs using initial candidate model chemistries.

	Absolute Energy (E_h)		
Model Chemistry	**Anion**	**Neutral**	**VDE (eV)**
B3LYP/Def2TZVP	-1076.6312	-1076.5765	1.49
B3LYP/SC	-285.4334	-285.3720	1.67
B3LYP/SDD+TZ	-285.4891	-285.4278	1.67
4kωB97X-D/Def2TZVP	-1076.5214	-1076.4709	1.37
ωB97X-D/SC	-285.3247	-285.2688	1.52
ωB97X-D/SDD+TZ	-285.3771	-285.3217	1.51
HF/Def2TZVP	-1074.3943	-1074.3207	2.00
HF-SC	-283.6908	-283.6111	2.17
HF/SDD+TZ	-283.7421	-283.6655	2.09
CCSD/Def2TZVP	-1075.2521	-1075.1978	1.48
CCSD/SC	-284.4526	-284.3902	1.70
CCSD/SDD+TZ	-284.6343		

Table A.2: Absolute energies including ZPE for anionic and neutral 1-1a using the anion 1-1a geometry, and the calculated VDEs using initial candidate model chemistries.

	1-1a (C_{2v})				**1-1b** (C_s)			
mode	**sym.**	**anion**	**neutral**	**scale factor**	**sym.**	**anion**	**neutral**	**scale factor**
ν_1	a_1	3855.0	3866.9	1.000	a'	3854.7	3877.6	1.000
ν_2	a_1	941.2	1061.6	0.957	a'	3850.0	3865.2	1.000
ν_3	a_1	552.6	683.0	0.993	a'	945.5	1058.8	0.960
ν_4	a_1	502.4	484.9	0.852	a'	649.9	786.7	1.000
ν_5	a_1	166.3	194.1	1.000	a'	543.9	684.4	0.991
ν_6	a_2	334.6	509.4	1.000	a'	496.6	506.1	1.000
ν_7	b_1	334.7	528.6	1.000	a'	471.9	335.3	1.237
ν_8	b_1	68.2	16.2	3.750	a'	225.5	252.7	1.000
ν_9	b_2	3854.7	3863.8	1.000	a'	155.1	177.3	1.000
ν_{10}	b_2	661.4	790.06	1.000	a''	338.7	522.1	1.000
ν_{11}	b_2	489.4	489.5	1.000	a''	281.7	453.5	1.000
ν_{12}	b_2	205.2	225.9	1.000	a''	102.8	56.4	1.071

Table A.3: Vibrational frequencies in cm^{-1} for the lowest-energy anion and neutral states of 1-1a TiO_3H_2 obtained at the B3LYP/Def2TZVP level. The scaling factors used to adjust neutral 1-1a' frequencies are also provided.

	anion	neutral	% change
terminal Ti=O bond length, Å	1.67	1.62	-3.0
hydroxyl Ti-O bond length, Å	1.92	1.84	-4.2
O-H bond length, Å	0.96	0.96	0.0
O-Ti-O angle, deg.	121.8	122.8	+0.8
H-O-Ti angle, deg.	118.9	132.5	+11.4

Table A.4: Structural parameters for the 1-1a anion and 1-1a' neutral geometries obtained at the B3LYP/Def2TZVP level, as well as the percent changes in these parameters that occur upon detachment.

Neutral	
State	**Energy (eV)**
$\tilde{X}\ ^1A_1$	0.00
$\tilde{a}\ ^3A_1$	3.86
$\tilde{b}\ ^3B_2$	4.02
$\tilde{c}\ ^3B_1$	4.11
$\tilde{A}\ ^1B_2$	4.20
$\tilde{B}\ ^1A_1$	4.36
$\tilde{d}\ ^3B_2$	4.42
$\tilde{C}\ ^1B_1$	4.45
$\tilde{D}\ ^1B_2$	4.55
$\tilde{e}\ ^3B_1$	4.71

Table A.5: Ten lowest-energy electronic states of the 1-1a' neutral specie found using the B3LYP/Def2TZVP model chemistry. Excitation energies were obtained from a TDDFT calculation.

Appendix B

Chapter 7 Supplemental Information

B.1 Tables

Model Chemistry	**Anion**	**Neutral**	**ADE(eV)**
B3LYP/Def2TZVP	274.2558806	274.2143184	1.13
B3LYP/SC	273.7720854	273.7262703	1.25
ωB97XD/Def2TZVP	274.1629665	274.1299711	0.90
ωB97XD/SC	273.68070	273.6434247	1.01
B3PW91/Def2TZVP	274.1829258	274.1435448	1.07
B3PW91/SC	273.7006408	273.6580344	1.16
M06L/Def2TZVP	274.1939821	274.1669927.	0.73
M06L/SC	273.7239104	273.6964000	0.75
DSDPBEP86/Def2TZVP	273.2305063	273.1963100	0.93
DSDPBEP86/SC	272.7459145	272.7065000	1.07
PBE1PBE/Def2TZVP	273.9775000	273.9394262	1.04
PBE1PBE/SC	273.4962528	273.4544886	1.14

Table B.1: Absolute energies without including ZPE for optimized **1-1a** anion and **1-1a'** neutral geometries and the calculated ADEs using initial candidate model chemistries. Energies are presented in Hartree unless otherwise noted.

Model Chemistry	**Anion**	**Neu**	**ADE(eV)**
B3LYP/Def2TZVP	-274.228913	-274.186326	1.16
B3LYP/SC	-273.745086	-273.698169	1.28
ωB97XD/Def2TZVP	-274.135416	-274.101485	0.92
ωB97XD/SC	-273.653117	-273.614931	1.04
B3PW91/Def2TZVP	-274.155631	-274.115309	1.10
B3PW91/SC	-273.673349	-273.62971	1.19
M06L/Def2TZVP	-274.167045	-274.138852	0.77
M06L/SC	-273.696712	-273.668007	0.78
DSDPBEP86/Def2TZVP	-273.631667	-273.596151	0.97
DSDPBEP86/SC	-273.096346	-273.056491	1.08
PBE1PBE/Def2TZVP	-273.95000	-273.911023	1.06
PBE1PBE/SC	-273.468754	-273.425994	1.16

Table B.2: Absolute energies including ZPE for optimized **1-1a** anion and **1-1a'** neutral geometries and the calculated ADEs using initial candidate model chemistries. Energies are presented in Hartree unless otherwise noted.

Model Chemistry	**Anion**	**Neutral**	**ADE(Ev)**
B3LYP/Def2TZVP	-274.2526755	-	-
B3LYP/SC	-273.7692272	-273.722743	1.26
ωB97XD/Def2TZVP	-274.159672	-	-
ωB97XD/SC	-273.6776874	-273.6386888	1.03
B3PW91/Def2TZVP	-274.1796354	-	-
B3PW91/SC	-273.69770	-273.6543431	1.18
M06L/Def2TZVP	-274.1916209	-	-
M06L/SC	-273.7209521	-273.6926436	0.77
DSDPBEP86/Def2TZVP	-273.2272116	-	-
DSDPBEP86/SC	-272.7427958	-272.7036951	1.06
PBE1PBE/Def2TZVP	-273.9742372	-	-
PBE1PBE/SC	-273.4933016	-273.450847	1.16

Table B.3: Absolute energies including ZPE for optimized **1-1b** anion and **1-1b'** neutral geometries and the calculated ADEs using initial candidate model chemistries. Energies are presented in Hartree unless otherwise noted.

Model Chemistry	**Anion**	**Neu**	**ADE(Ev)**
B3LYP/Def2TZVP	-274.22599	-	-
B3LYP/SC	-273.742466	-273.695245	1.28
ωB97XD/Def2TZVP	-274.135416	-	-
ωB97XD/SC	-273.6503	-273.610722	1.04
B3PW91/Def2TZVP	-274.15262	-	-
B3PW91/SC	-273.670616	-273.626476	1.20
M06L/Def2TZVP	-274.164979	-	-
M06L/SC	-273.693786	-273.664728	0.79
DSDPBEP86/Def2TZVP	-273.628824	-	-
DSDPBEP86/SC	-273.093789	-273.05401	1.08
PBE1PBE/Def2TZVP	-273.947001	-	-
PBE1PBE/SC	-273.466038	-273.422846	1.18

Table B.4: Absolute energies including ZPE for optimized **1-1b** anion and **1-1b'** neutral geometries and the calculated ADEs using initial candidate model chemistries. Energies are presented in Hartree unless otherwise noted.

Model Chemistry	**Anion**	**Neutral**	**ADE(eV)**
B3LYP/Def2TZVP	-274.18030207	-274.13788055	1.15
B3LYP/SC	-273.69705894	-273.65431302	1.16
ωB97XD/Def2TZVP	-274.08812593	-274.05096200	1.01
ωB97XD/SC	-273.60488812	-273.56888652	0.98
B3PW91/Def2TZVP	-274.10959592	-274.06841387	1.12
B3PW91/SC	-273.62851630	-273.58746213	1.12
M06L/Def2TZVP	-274.1238743	-274.09444318	0.80
M06L/SC	-273.65201195	-273.62745912	0.67
DSDPBEP86/Def2TZVP	-273.14408280	-273.10332587	1.11
DSDPBEP86/SC	-272.65968617	-272.61817811	1.13
PBE1PBE/Def2TZVP	-273.90436899	-273.86364332	1.11
PBE1PBE/SC	-273.42415240	-273.38340727	1.11

Table B.5: Absolute energies without including ZPE for optimized **1-1c** anion and **1-1c'** neutral geometries and the calculated ADEs using initial candidate model chemistries. Energies are presented in Hartree unless otherwise noted.

Model Chemistry	**Anion**	**Neu**	**ADE(Ev)**
B3LYP/Def2TZVP	-274.150733	-274.108175	1.16
B3LYP/SC	-273.668736	-273.624781	1.20
ωB97XD/Def2TZVP	-274.057899	-274.020648	1.01
ωB97XD/SC	-273.57454	-273.538753	0.97
B3PW91/Def2TZVP	-274.079871	-274.038453	1.13
B3PW91/SC	-273.600535	-273.557588	1.17
M06L/Def2TZVP	-274.094029	-274.064567	0.80
M06L/SC	-273.622262	-273.59754	0.67
DSDPBEP86/Def2TZVP	-273.5593	-273.521209	1.04
DSDPBEP86/SC	-273.025923	-272.98685	1.06
PBE1PBE/Def2TZVP	-273.874383	-273.833515	1.11
PBE1PBE/SC	-273.395825	-273.353275	1.16

Table B.6: Absolute energies including ZPE for optimized **1-1c** anion and **1-1c'** neutral geometries and the calculated ADEs using initial candidate model chemistries. Energies are presented in Hartree unless otherwise noted.

Vibrational Modes	**Anion**	**Neutral**	**change**	**%**
ν_{12} dihedral angle	29.2°	23.00°	6.2°	21%
ν_{11} OZrOH angle	118.6°	114.7°	3.9°	3 %
ν_{10} ZrOH in-plane	123.3°	134.8°	11.5°	9%
ν_{9} ZrOH out-of-plane	123.3°	134.8°	11.5°	9%
ν_{8} sym. ZrO(H) str.	2.05Å	1.99Å	0.06Å	3

Table B.7: Structural parameters for the **1-1a** anion and **1-1a'** neutral geometries obtained at the ωB97XD/SC level, as well as the percent changes in these parameters that occur upon detachment.

Vibrational Modes	**Anion**	**Neutral**	**Change**	**%**
ν_{12} dihedral	29.5°	18.8°	10.7°	36%
ν_{11} OZrOH angle (trans)	123.4°	145.6°	22.2°	18%
ν_{10} (H)OMO(H)	115.4°	123.6°	8.2°	7%
ν_9 Trans OMOH	112.2°	114.6°	2.4°	2%
ν_8 OZrOH angle (trans)	123.4°	145.6°	22.2°	18%
ν_7 OZrOH angle (cis)	123.9°	135.2°	11.3°	9%
ν_5 sym. ZrO(H) str.	2.05Å	1.99Å	0.06Å	3

Table B.8: Structural parameters for the **1-1b** anion and **1-1b'** neutral geometries obtained at the ωB97XD/SC level, as well as the percent changes in these parameters that occur upon detachment.

Vibrational Modes	**Computed Frequency**	**Scaled frequency**	**Scaling factor**
ν_{12}	87.6	66.9	0.76
ν_{11}	170.2	166.0	0.97
ν_{10}	213.1	175.0	0.82
ν_9	428.7	380.3	0.89
ν_8	439.5	393.9	0.90
ν_7	492.7	419.3	0.85
ν_6	513.7	428.3	0.83
ν_5	622.8	597.0	0.96

Table B.9: Vibrational frequencies in cm^{-1} for the lowest energy neutral state of **1-1a** ZrO_3H_2 obtained at the ωB97XD/SC level. The scaling factors used to adjust neutral **1-1a'** frequencies are also provided.

Vibrational Modes	**Computed Frequency**	**Scaled frequency**	**Scaling factor**
ν_{12}	82.4	65.0	0.79
ν_{11}	159.9	155.0	0.97
ν_{10}	196.9	175.0	0.89
ν_{9}	323.8	384.0	1.18
ν_{8}	339.5	393.0	1.16
ν_{7}	385.7	419.0	1.08
ν_{6}	395.2	425.0	1.07
ν_{5}	606.9	597.0	0.98

Table B.10: Vibrational frequencies in cm^{-1} for the lowest energy neutral state of **1-1a** ZrO_3D_2 obtained at the ωB97XD/SC level. The scaling factors used to adjust neutral **1-1a'** frequencies are also provided.

Vibrational Modes	**Computed Frequency**	**Scaled frequency**	**Scaling factor**
ν_{12}	75.0	72.4	0.96
ν_{11}	141.0	113.9	0.81
ν_{10}	191.0	169.0	0.88
ν_{9}	234.6	204.0	0.87
ν_{8}	416.8	350.0	0.84
ν_{7}	468.5	405.0	0.86
ν_{6}	506.2	430.3	0.85
ν_{5}	643.6	547.1	0.85

Table B.11: Vibrational frequencies in cm^{-1} for the lowest energy neutral state of **1-1b** ZrO_3H_2 obtained at the ωB97XD/SC level. The scaling factors used to adjust neutral **1-1b'** frequencies are also provided.

Vibrational Modes	**Computed Frequency**	**Scaled frequency**	**Scaling factor**
ν_{12}	70.9	69.0	0.97
ν_{11}	117.3	110.0	0.94
ν_{10}	181.1	155.0	0.86
ν_{9}	218.6	196.0	0.90
ν_{8}	316.4	347.0	1.10
ν_{7}	361.1	379.0	1.05
ν_{6}	390.0	430.3	1.10
ν_{5}	626.7	548.0	0.88

Table B.12: Vibrational frequencies in cm^{-1} for the lowestenergy neutral state of **1-1b** ZrO_3D_2 obtained at the ωB97XD/SC level. The scaling factors used to adjust neutral **1-1b'** frequencies are also provided.

1-1a	**CryoSEVI**	**ωB97XD/SC**
EA (eV)	1.1636(5)	1.04
ν_{12} (cm^{-1})	67(3)	87.6
ν_{11} (cm^{-1})	167(2)	170.3
ν_{9} (cm^{-1})	388(4)	428.8
ν_{6} (cm^{-1})	429(6)	513.7
ν_{5} (cm^{-1})	597(2)	622.8

Table B.13: Electronic and vibrational energies for neutral **1-1a'** extracted from the $ZrO(OH)_2^-$ cryo-SEVI spectrum, and compared to the (unscaled) results obtained from ωB97XD/SC calculations.

1-1b	**CryoSEVI**	**ωB97XD/SC**
EA (eV)	1.1636(5)	1.04
ν_{12} (cm^{-1})	73(3)	75.0
ν_{11} (cm^{-1})	115(3)	141.0
ν_{10} (cm^{-1})	167(2)	191.0
ν_{9} (cm^{-1})	201(4)	234.6
ν_{8} (cm^{-1})	356(6)	416.9

Table B.14: Electronic and vibrational energies for neutral **1-1b'** extracted from the $ZrO(OH)_2^-$ cryo-SEVI spectrum, and compared to the (unscaled) results obtained from ωB97XD/SC calculations.

Peak	**eBE**	**Shift**	**Assignment**	
			1-1a'	**1-1b'**
A	9385(4)	0	0_0^0	0_0^0
B	9452(4)	67	12_0^1	
C	9458(4)	73		12_0^1
D	9500(4)	115		11_0^1
E	9529(4)	144		12_0^2
F	9552(2)	167	11_0^1	10_0^1
G	9570(4)	185		$11_0^1 12_0^1$
H	9613(4)	228		12_0^3
I	9624(2)	239		$10_0^1 12_0^1$
J	9659(6)	274		$9_0^1 12_0^1$
K	9666(4)	281		12_0^4
L	9705(6)	320		$10_0^1 12_0^2$
M	9712(6)	327		$11_0^1 12_0^3$
N	9743(4)	358		8_0^1
O	9763(4)	378		
P	9773(4)	388	9_0^1	$10_0^1 12_0^3$
Q	9814(12)	429	6_0^1	$8_0^1 12_0^1$
R	9844(6)	459	$9_0^1 12_0^1$	$10_0^1 11_0^1 12_0^1$
S	9887(8)	502	$6_0^1 12_0^1$	$11_0^3 12_0^2$
T	9933(3)	548		$10_0^1 11_0^2 12_0^2$
U	9939(4)	554		
V	9982(1)	597	5_0^1	$7_0^1 11_0^1 12_0^1$

Table B.15: Peak positions, shifts from peak A, and assignments for the detachment transitions in the cryo-SEVI spectrum of $ZrO(OH)_2^-$. Uncertainties in peak positions correspond to one standard deviation obtained from a Gaussian fit to the corresponding feature in the high-resolution scan.

Peak	**eBE**	**Shift**	**Assignment**	
			1-1a'	**1-1b'**
A	9369(6)	0	0_0^0	0_0^0
B	9434(3)	65	12_1^0	
C	9438(3)	69		12_1^0
D	9479(5)	110		11_1^0
E	9504(5)	135		12_2^0
F	9524(3)	155	11_1^0	10_1^0
G	9540(4)	171		$11_0^1 12_0^1$
H	9579(8)	210		12_3^0
I	9593(11)	224	$11_0^1 12_0^1$	$10_0^1 12_0^1$
J	9623(8)	254		$11_0^1 12_0^2$
K	9634(7)	265		$9_0^1 12_0^1$
L	9669(7)	300		$10_0^1 12_0^2$
M	9686(12)	317		$11_0^1 12_0^3$
N	9716(7)	347		8_1^0
O	9729(16)	360		$10_0^1 12_0^3$
P	9753(7)	384	9_1^0	
Q	9767(4)	398		$11_0^3 12_1^0$
R	9778(3)	409		
S	9790(3)	421		$8_0^1 12_1^0$
T	9794(1)	425	6_1^0	

Table B.16: Peak positions, shifts from peak A, and assignments for the detachment transitions in the cryo-SEVI spectrum of $ZrO(OD)_2^-$. Uncertainties in peak positions correspond to one standard deviation obtained from a Gaussian fit to the corresponding feature in the high-resolution scan.

B.2 Figures

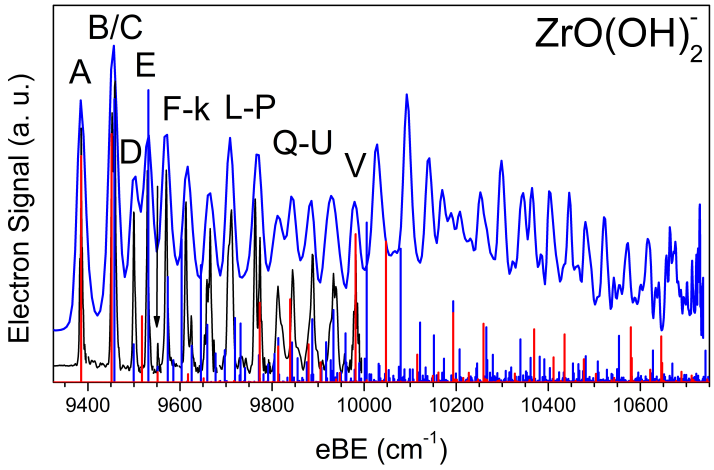

Figure B.1: Cryo-SEVI spectrum of ZrO_3H_2 displaying the full range of the overview spectrum ($h\nu$ = 10,747 cm^{-1}). High resolution spectra were collected only up to ~10,000 cm^{-1}. Red and blue sticks correspond to FC-simulations for detachment from the **1-1a** and **1-1b** isomers of ZrO_3H_2, respectively.

B.2.1 Spectra with FC-simulations (theor. values)

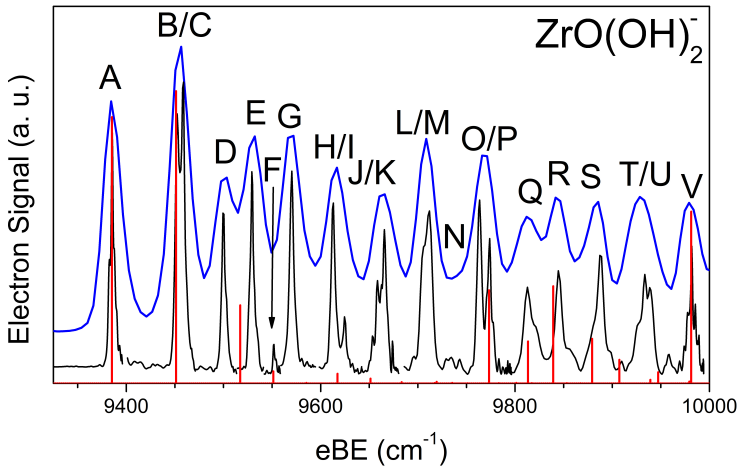

Figure B.2: Cryo-SEVI spectrum of ZrO_3H_2 with Franck-Condon simulations for detachment from the **1-1a** structure of $ZrO(OH)_2^-$ using neutral frequencies that have not been scaled.

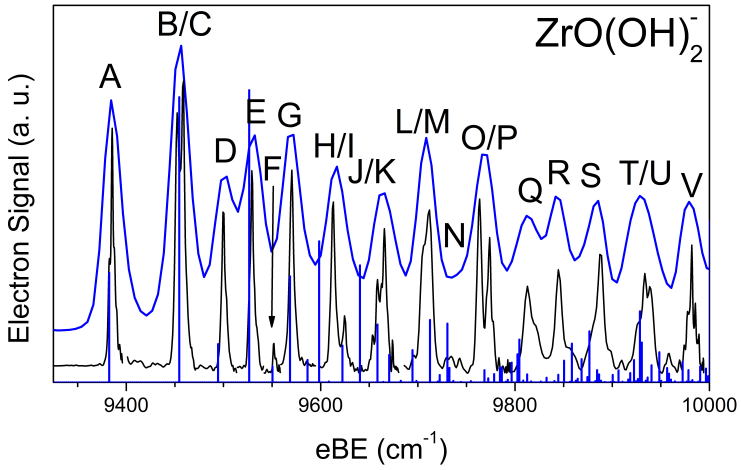

Figure B.3: Cryo-SEVI spectrum of ZrO_3H_2 with Franck-Condon simulations for detachment from the **1-1b** structure of $ZrO(OH)_2^-$ using neutral frequencies that have not been scaled.

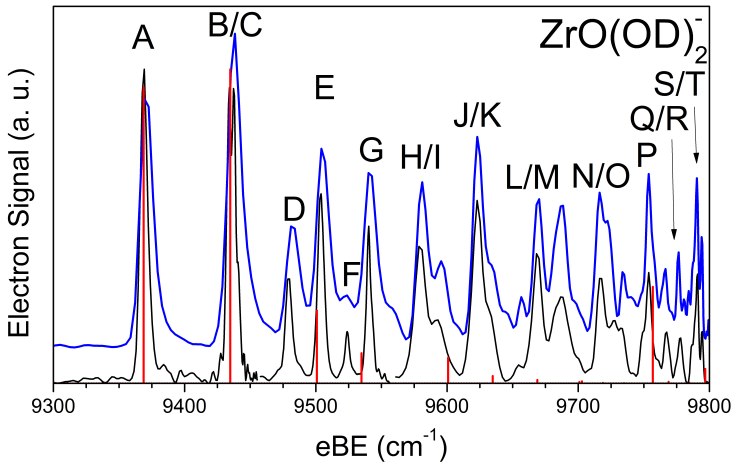

Figure B.4: Cryo-SEVI spectrum of ZrO_3D_2 with Franck-Condon simulations for detachment from the **1-1a** structure of $ZrO(OD)_2^-$ using neutral frequencies that have not been scaled.

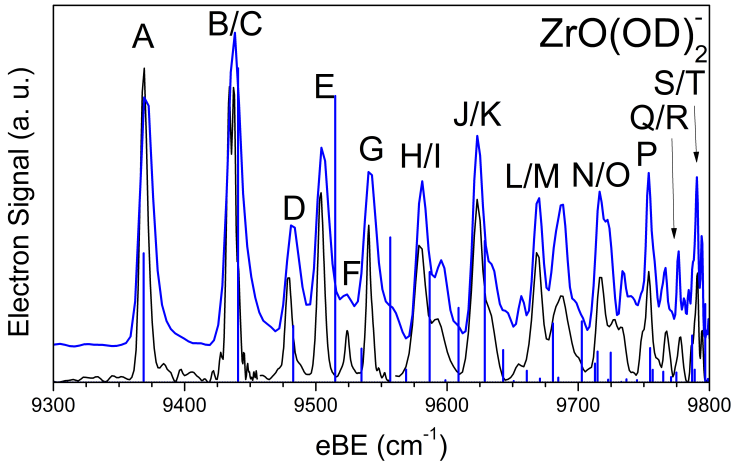

Figure B.5: Cryo-SEVI spectrum of ZrO_2D_2 with Franck-Condon simulations for detachment from the **1-1b** structure of $ZrO(OD)_2^-$ using neutral frequencies that have not been scaled.

B.2.2 Spectra with FC-simulations (scaled values)

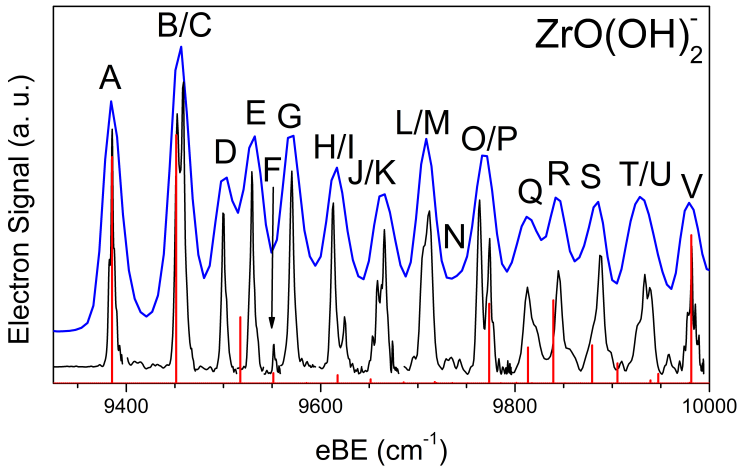

Figure B.6: Cryo-SEVI spectrum of ZrO_3H_2 with Franck-Condon simulations for detachment from the **1-1a** structure of $ZrO(OH)_2^-$ using experimental values where possible.

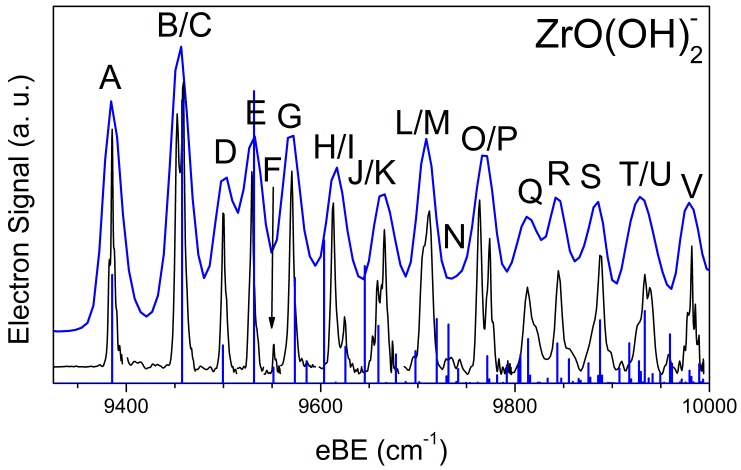

Figure B.7: Cryo-SEVI spectrum of ZrO_3H_2 with Franck-Condon simulations for detachment from the **1-1b** structure of $ZrO(OH)_2^-$ using experimental values where possible.

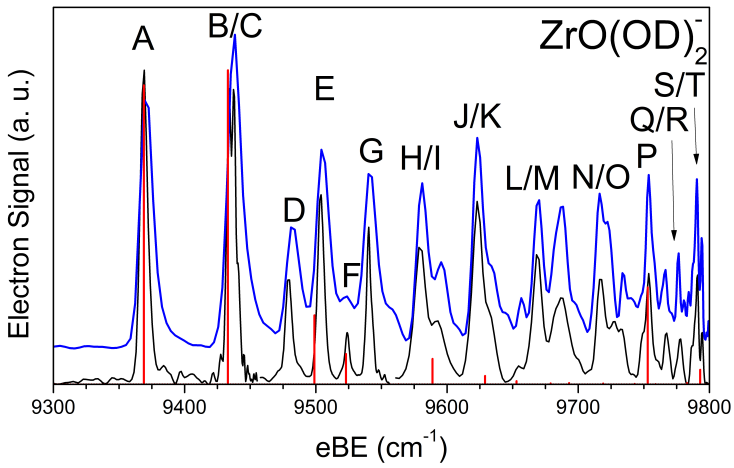

Figure B.8: Cryo-SEVI spectrum of ZrO_3D_2 with Franck-Condon simulations for detachment from the **1-1a** structure of $ZrO(OD)_2^-$ using experimental values where possible.

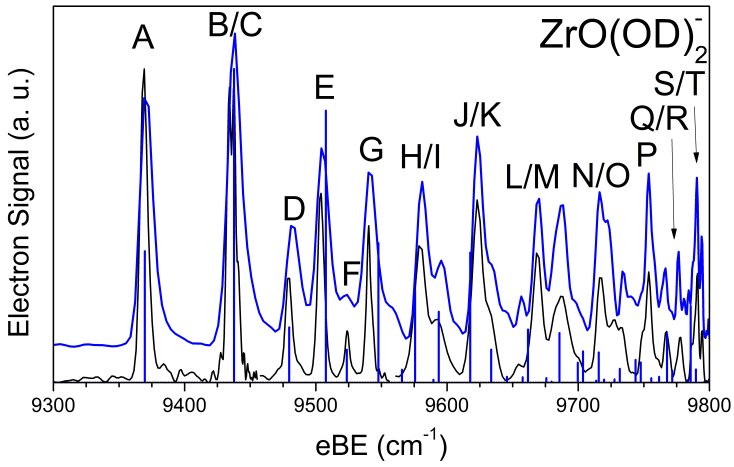

Figure B.9: Cryo-SEVI spectrum of ZrO_3D_2 with Franck-Condon simulations for detachment from the **1-1b** structure of $ZrO(OD)_2^-$ using experimental values where possible.

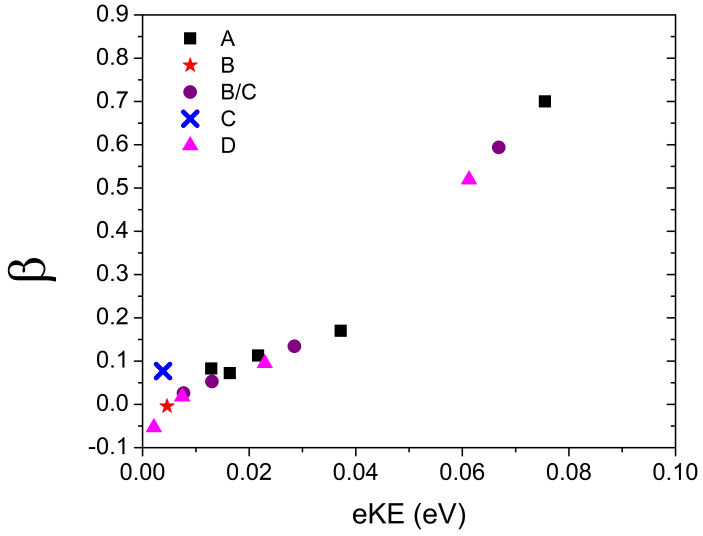

Figure B.10: Photoelectron angular distributions for peaks A, B, C, and D of ZrO_3H_2

B.3 Geometries

B.3.1 Optimized Anion Geometries

The Cartesian coordinates for the optimized geometries of the doublet anion $ZrO_3H_2^-$ species identified by ωB97XD/SC are provided below. The total converged SCF energy is also given for each structure.

1-1a

SCF= -273.680703012 E_h

Zr	-0.17653491	0.14741320	0.00000000
O	-0.17653491	-0.96122535	1.72894132
O	-0.17653491	-0.96122535	-1.72894132
O	1.13307209	1.38221915	0.00000000
H	0.41068900	-0.78733776	-2.46539459
H	0.41068900	-0.78733776	2.46539459

1-1b

SCF= -273.677687402 E_h

Zr	0.00224031	0.07100173	-0.21275434
O	-1.60014474	-1.12838066	0.23540247
O	1.84515558	-0.67677432	0.33093769
O	-0.21961565	1.75174680	0.38631180
H	2.09942250	-1.59299417	0.21211062
H	-2.39219647	-0.381980958	0.67684718

1-1c

SCF= -273.604888118 E_h

Zr	-0.45547340	-0.00001041	0.25604928
O	-0.10951737	1.49537562	-0.74043818
O	-0.10943080	-1.49537720	-0.74044033
O	2.03218352	0.00004343	0.27622859
H	1.85653478	-0.76618443	-0.30238602
H	1.85651829	0.76626591	-0.30238572

B.3.2 Optimized Neutral Geometries

The Cartesian coordinates for the optimized geometries of the singlet neutral ZrO_3H_2 species identified by ωB97XD/SC are provided below. The total converged SCF energy is also given for each structure.

1-1a

SCF= -273.643424650 E_h

Zr	-0.139370	0.102224	0.000000
O	-0.139370	-0.916493	1.716582
O	-0.139370	-0.916493	-1.716582
O	0.899747	1.526420	0.000000
H	0.303360	-0.818216	-2.560212
H	0.303360	-0.818216	2.560212

1-1b

SCF= -273.638688778 E_h

Zr	-0.000033	0.042830	-0.138065
O	-1.677871	-0.994163	0.157195
O	1.827503	-0.697161	0.180508
O	-0.121664	1.760309	0.244604
H	2.336248	-1.477916	0.392220

1-1c

SCF= -273.568886517 E_h

Zr	-0.363473	0.200499	0.000000
O	0.514401	0.741324	1.467455
O	0.514401	0.741324	-1.467455
O	0.514401	-1.980668	0.000000
H	1.096654	-2.017909	-0.770067
H	1.096654	-2.017909	0.770067

Appendix C

Chapter 2 Supplemental Information

C.1 Tables

C.1.1 Single Excitations

Molecule	Model Chemistry	Transition	MOM	IMOM	PMOM	PIMOM	TD / CIS
Propenal	B3LYP/Def2TZVP	$n \rightarrow \pi^*$	f	f	3.27	Conv.	3.61
	HF/Def2TZVP	$n \rightarrow \pi^*$	f	f	2.70	Conv.	4.88
Propanamide	B3LYP/Def2TZVP	$n \rightarrow \pi^*$	f	f	5.38	Conv.	6.10
	HF/Def2TZVP	$n \rightarrow \pi^*$	f	f	4.78	Conv.	6.96
Tetrafluoroethene	B3LYP/Def2TZVP	$\pi \rightarrow 3s$	f	f	7.24	Conv.	7.44
	HF/Def2TZVP	$\pi \rightarrow 3s$	f	18	7.96	Conv.	8.76
Nitrobenzene	B3LYP/Def2TZVP	$\pi \rightarrow \pi^*$	f	f	5.43	Conv.	6.47
	HF/Def2TZVP	$\pi \rightarrow \pi^*$	f	f	v.c	6.30	7.46

Table C.1: Excitation energies in eV. The failure of the SCF procedure to converge to either the target or any solution is indicated with the letter "f," whereas variational collapse is indicated by "v.c."

C.1.2 Double Excitations

Molecule	Model Chemistry	Transition	MOM	IMOM	PMOM	PIMOM	Exp
Vanadium tetrachloride	B3LYP/LANL2DZ	$^4T_2$	f	f	1.47	Conv.	1.30
	HF/LANL2DZ	$^4T_2$	f	f	2.88	Conv.	
Cobalt tetraiodide	B3LYP/LANL2DZ	$^4T_2$	f	f	0.26	Conv.	0.33
	HF/LANL2DZ	$^4T_2$	f	f	0.14	Conv.	

Table C.2: Excitation energies in eV. The failure of the SCF procedure to converge to either the target or any solution is indicated with the letter "f".

Molecule	Model Chemistry	State	MOM	IMOM	PMOM	PIMOM	PG-IMOM
Benzene	BLYP/6-311G*	$5\ ^1A_g$	f	f	10.34	Conv.	10.21
	HF/6-311G*	$5\ ^1A_g$	f	f	14.17	Conv.	-
Napthalene	BLYP/6-311G*	$4\ ^1A_g$	6.86	f	Conv.	Conv.	6.77
	HF/6-311G*	$4\ ^1A_g$	f	f	10.47	Conv.	-
Anthracene	BLYP/6-311G*	$2\ ^1A_g$	f	f	4.67	Conv.	4.62
	HF/6-311G*	$2\ ^1A_g$	f	f	8.13	Conv.	-

Table C.3: Excitation energies in eV. The failure of the SCF procedure to converge to either the target or any solution is indicated with the letter “f”.

C.1.3 IP Excitations

Molecule	Model Chemistry	State	MOM	IMOM	PMOM	PIMOM	Exp
Propanone	B3LYP/6-311G(d,p)	$2b_1$	f	f	12.39	Conv.	12.59
	HF/6-311G(d,p)	$2b_1$	f	f	10.76	Conv.	
Methanol	B3LYP/6-311G(d,p)	$7a'$	f	f	12.43	Conv.	12.68
	Hf/6-311G(d,p)	$7a'$	f	f	11.73	Conv.	
Pyridine	B3LYP/6-311G(d,p)	$9b_2$	f	f	12.45	Conv.	12.61
	Hf/6-311G(d,p)	$9b_2$	f	f	12.90	Conv.	
formaldehyde	B3LYP/6-311G(d,p)	$1b_1$	14.48	Conv.	Conv.	Conv.	14.48
	HF/6-311G(d,p)	$1b_1$	12.30	Conv.	Conv.	Conv.	

Table C.4: Excitation energies in eV. The failure of the SCF procedure to converge to either the target or any solution is indicated with the letter "f".

C.1.4 N_{virt} Calculation Tables

Molecule	Model Chemistry	MOM	IMOM	PMOM	PIMOM
Propenal	B3LYP/Def2TZVP	3.1 | 4.2	3.1 | 8.1	0.1 | 0.1	0.1 | 0.1
	HF/Def2TZVP	4.0 | 6.3	5.1 | 6.1	0.4 | 0.1	0.4 | 0.0
Propanamide	B3LYP/Def2TZVP	6.0 | 1.1	10.5 | 11.1	0.0 | 0.0	0.0 | 0.0
	HF/Def2TZVP	2.8 | 7.1	6.7 | 9.1	0.6 | 0.1	0.6 | 0.1
Tetrachloroethane	B3LYP/Def2TZVP	1.0 | 1.0	2.0 | 1.0	0.0 | 0.0	0.0 | 0.0
	HF/Def2TZVP	7.1 | 7.2	0.0 | 0.0	0.0 | 0.0	0.0 | 0.0
Nitrobenzene	B3LYP/Def2TZVP	6.0 | 4.1	1.0 | 4.0	0.0 | 0.0	0.0 | 0.0
	HF/Def2TZVP	17.5 | 15.7	6.0 | 5.0	1.0 | 0.1	0.0 | 0.0
Vanadium tetrachloride	B3LYP/Def2TZVP	7.8 | 6.8	8.4 | 6.3	0.2 | 0.0	0.2 | 0.0
	HF/Def2TZVP	7.5 | 7.5	8.2 | 7.0	0.6 | 0.1	0.6 | 0.1
Cobalt tetraiodide	B3LYP/Def2TZVP	11.0 | 7.6	11.9 | 11.8	0.0 | 0.3	0.0 | 0.3
	HF/Def2TZVP	7.1 | 6.7	11.0 | 9.1	0.0 | 0.6	0.0 | 0.6

Table C.5: Values of the N_{virt} metric for singly excited states. Values corresponding to the α and β spin–orbital spaces are separated by a vertical pipe.

Molecule	Model Chemistry	MOM	IMOM	PMOM	PIMOM
Benzene	BLYP/6-311G*	4.1	3.3	0.0	0.0
	HF/6-311G*	3.3	4.1	0.0	0.0
Naphthalene	BLYP/6-311G*	0.0	10.5	0.0	0.0
	HF/6-311G*	10.1	15.9	0.0	0.0
Anthracene	BLYP/6-311G*	8.4	14.0	0.0	0.0
	HF/6-311G*	14.8	16.0	0.1	0.1

Table C.6: Values of the N_{virt} metric for the computed doubly excited states.

Molecule	Model Chemistry	MOM	IMOM	PMOM	PIMOM
Propanone	B3LYP/6-311G(d,p)	4.1 | 3.1	2.1 | 3.1	0.0 | 0.1	0.0 | 0.1
	HF/6-311G(d,p)	2.8 | 7.1	6.7 | 6.0	0.6 | 0.1	0.6 | 0.1
Methanol	B3LYP/6-311G(d,p)	1.1 | 3.0	2.0 | 2.0	0.0 | 0.1	0.0 | 0.1
	HF/6-311G(d,p)	1.0 | 2.4	1.0 | 1.3	0.0 | 0.6	0.0 | 0.6
Pyridine	B3LYP/6-311G(d,p)	8.7 | 7.3	6.1 | 5.4	0.0 | 0.0	0.0 | 0.0
	HF/6-311G(d,p)	6.5 | 6.8	11.0 | 7.3	0.1 | 0.2	0.1 | 0.2
formaldehyde	B3LYP/6-311G(d,p)	0.0 | 0.0	0.0 | 0.0	0.0 | 0.0	0.0 | 0.0
	HF/6-311G(d,p)	0.0 | 0.1	0.0 | 0.1	0.0 | 0.1	0.0 | 0.1

Table C.7: Values of the N_{virt} metric for the different ionized excited states computed. Values corresponding to the α and β spin–orbital spaces are separated by a vertical pipe.

Appendix D

Chapter 3 Supplemental Information

D.1 Tables

System	6-311G	6-311++G(d,p)	aug-cc-PVDZ	aug-cc-PVTZ	Exp.
BH	1.67	1.69	1.69	1.68	**2.87**
BF	4.24	4.31	4.29	4.34	**6.34**
SiO	4.12	4.44	3.78	4.39	**5.31**
CO	6.21	6.60	6.56	6.6	**8.07**
N_2	6.97	7.53	7.44	7.57	**8.59**
ScO	1.77	1.72	1.71	1.38	**2.04**
BeH	2.37	2.35	2.36	2.33	**2.48**
AsF	2.96	2.87	2.96	3.37	**3.19**
NH	3.64	3.61	3.61	3.59	**3.70**
CrF	1.44	1.23	1.22	1.23	**1.01**
CuH	2.46	2.70	2.61	2.65	**2.91**
Li_2	1.09	1.07	1.07	1.06	**1.74**
CCl_2	1.36	1.29	1.35	1.27	**2.14**
CH_2S	1.64	1.67	1.64	1.64	**2.03**
Mg_2	2.32	2.26	2.27	2.27	**3.23**
PH_2	2.13	2.24	2.24	2.22	**2.27**
$C_2H_2O_2$	1.93	2.12	2.09	2.11	**2.72**
HCP	3.74	3.60	3.50	3.56	**4.31**
CH_2O	2.79	3.01	2.96	3.00	**3.49**
C_3H_4O	2.64	2.78	2.74	2.77	**3.21**
SiF_2	3.79	3.96	3.94	3.95	**5.34**
HCN	5.7	5.59	5.45	5.57	**6.48**
C_2H_2	4.64	4.38	4.22	4.38	**5.23**
MAE	**0.78**	**0.68**	**0.74**	**0.70**	
RMSE	**0.96**	**0.84**	**0.90**	**0.85**	

Table D.1: Excitation energies obtained using Δ-B3LYP.

System	6-311G	6-311++G(d,p)	aug-cc-PVDZ	aug-cc-PVTZ	Exp.
BH	2.75	2.74	2.67	2.69	**2.87**
BF	6.13	6.09	6.08	6.09	**6.34**
SiO	4.83	5.20	4.54	5.16	**5.31**
CO	7.51	7.95	7.90	7.96	**8.07**
N_2	7.92	8.50	8.41	8.56	**8.59**
ScO	1.35	2.00	1.97	1.98	**2.04**
BeH	2.58	2.56	2.58	2.57	**2.48**
AsF	2.95	2.87	2.96	3.03	**3.19**
NH	3.98	3.90	3.87	3.86	**3.70**
CrF	1.47	1.25	1.22	1.25	**1.01**
CuH	3.35	2.98	2.92	2.96	**2.91**
Li_2	1.93	1.93	1.93	1.93	**1.74**
CCl_2	X	1.99	1.71	1.96	**2.14**
CH_2S	2.04	2.06	2.04	2.07	**2.03**
Mg_2	3.45	3.26	3.32	3.26	**3.23**
PH_2	2.19	2.34	2.33	2.34	**2.27**
$C_2H_2O_2$	2.21	2.42	2.39	2.42	**2.72**
HCP	3.91	3.86	3.74	3.82	**4.31**
CH_2O	3.36	3.59	3.54	3.60	**3.49**
C_3H_4O	2.98	3.15	3.11	3.16	**3.21**
SiF_2	4.85	5.31	5.25	5.31	**5.34**
HCN	6.02	5.95	5.82	5.96	**6.48**
C_2H_2	4.92	4.70	4.55	4.73	**5.23**
MAE	**0.34**	**0.17**	**0.24**	**0.17**	
RMSE	**0.38**	**0.22**	**0.33**	**0.23**	

Table D.2: Excitation energies obtained using TDDFT.

System	6-311G	6-311++G(d,p)	aug-cc-PVDZ	aug-cc-PVTZ	Exp.
BH	1.64	1.5	1.68	1.47	**2.87**
BF	4.39	4.51	4.47	4.55	**6.34**
SiO	2.90	3.74	3.52	3.68	**5.31**
CO	6.36	7.00	6.95	6.99	**8.07**
N_2	7.25	8.06	6.77	8.08	**8.59**
ScO	1.60	2.05	2.02	2.04	**2.04**
BeH	2.64	2.64	2.62	2.61	**2.48**
AsF	3.57	3.44	3.54	3.66	**3.19**
NH	3.79	3.84	3.83	3.80	**3.70**
CrF	0.98	0.60	0.59	0.60	**1.01**
CuH	1.7	1.42	1.38	1.37	**2.91**
Li_2	0.96	0.92	0.92	0.94	**1.74**
CCl_2	0.69	1.07	0.93	1.05	**2.14**
CH_2S	0.58	0.90	0.88	0.77	**2.03**
Mg_2	2.69	2.46	2.47	2.45	**3.23**
PH_2	2.20	2.38	2.35	2.34	**2.27**
$C_2H_2O_2$	3.12	3.30	3.26	3.27	**2.72**
HCP	3.03	2.95	2.72	2.76	**4.31**
CH_2O	1.51	1.66	1.98	2.00	**3.49**
C_3H_4O	1.29	1.67	1.61	1.64	**3.21**
SiF_2	3.97	4.09	4.08	4.07	**5.34**
HCN	4.88	4.78	4.62	4.73	**6.48**
C_2H_2	4.07	3.71	3.53	3.68	**5.23**
MAE	**1.07**	**1.00**	**1.09**	**0.97**	
RMSE	**1.27**	**1.19**	**1.29**	**1.13**	

Table D.3: Excitation energies obtained using Δ-HF.

System	6-311G	6-311++G(d,p)	aug-cc-PVDZ	aug-cc-PVTZ	Exp.
BH	3.03	2.89	2.85	2.86	**2.87**
BF	6.49	6.54	6.51	6.57	**6.34**
SiO	5.23	6.09	4.17	6.09	**5.31**
CO	8.01	8.74	8.69	8.76	**8.07**
N_2	8.56	9.45	9.38	9.53	**8.59**
ScO	2.30	2.07	2.10	2.05	**2.04**
BeH	2.78	2.76	2.74	2.73	**2.48**
AsF	3.83	3.76	3.84	3.95	**3.19**
NH	4.05	4.18	4.18	4.19	**3.70**
CrF	1.15	0.99	0.93	0.99	**1.01**
CuH	3.97	3.93	3.92	3.93	**2.91**
Li_2	2.11	2.10	2.10	2.13	**1.74**
CCl_2	2.08	2.40	2.15	2.39	**2.14**
CH_2S	1.99	2.71	2.70	2.61	**2.03**
Mg_2	3.59	3.34	3.35	3.34	**3.23**
PH_2	2.33	2.68	2.72	2.78	**2.27**
$C_2H_2O_2$	3.24	3.56	3.55	3.59	**2.72**
HCP	3.46	3.59	3.35	4.24	**4.31**
CH_2O	3.99	4.10	4.39	4.44	**3.49**
C_3H_4O	4.36	4.58	4.54	4.58	**3.21**
SiF_2	5.69	5.96	5.93	5.94	**5.34**
HCN	5.54	5.95	5.50	5.65	**6.48**
C_2H_2	4.68	4.49	4.34	4.68	**5.23**
MAE	**0.41**	**0.55**	**0.60**	**0.55**	
RMSE	**0.52**	**0.63**	**0.70**	**0.65**	

Table D.4: Excitation energies obtained using CIS.

System	Exp.	TDDFT	Δ-B3LYP	AP-Δ-B3LYP	CIS	Δ-HF	AP-Δ-HF
BH	**2.48**	2.75	1.67	2.26	3.03	1.64	2.89
BF	**6.34**	6.13	4.24	5.17	6.49	4.39	6.37
SiO	**5.31**	4.83	4.12	4.40	5.23	2.90	3.05
CO	**8.07**	7.51	6.21	6.92	8.01	6.36	-
N_2	**8.59**	7.92	6.97	7.45	8.56	7.25	7.99
CuH	**2.91**	3.35	2.46	2.80	3.97	1.70	2.61
Li_2	**1.74**	1.93	1.09	1.25	2.11	0.96	1.55
CCl_2	**2.14**	x	1.36	1.92	2.08	0.69	1.89
CH_2S	**2.03**	2.04	1.64	1.71	1.99	0.58	0.59
Mg_2	**3.23**	3.45	2.32	2.79	3.59	2.69	4.07
C_2H_2O	**2.72**	2.21	1.93	2.14	3.24	3.12	3.56
HCP	**4.31**	3.91	3.74	3.97	3.46	3.03	3.52
CH_2O	**3.49**	3.36	2.89	2.94	3.99	1.51	1.59
C_3H_4O	**3.21**	2.98	2.54	2.64	4.36	1.29	1.33
SiF_2	**5.34**	4.85	3.79	4.38	5.69	3.97	5.52
HCN	**6.48**	6.02	5.70	6.01	5.54	4.88	5.47
C_2H_2	**5.23**	4.92	4.64	5.92	4.68	4.07	-
MEA		**0.34**	**0.92**	**0.57**	**0.47**	**1.37**	**0.86**
RMSE		**0.38**	**1.04**	**0.65**	**0.59**	**1.47**	**1.10**

Table D.5: Excitation energies obtained using the 6-311G basis set before and after approximate projection.

System	Exp.	TDDFT	Δ-B3LYP	AP-Δ-B3LYP	CIS	Δ-HF	AP-Δ-HF
BH	**2.87**	2.74	1.69	2.30	2.89	1.50	2.68
BF	**6.34**	6.09	4.31	5.26	6.54	4.51	6.54
SiO	**5.31**	5.20	4.44	4.83	6.09	3.74	3.97
CO	**8.07**	7.95	6.60	7.37	8.74	7.00	8.63
N_2	**8.59**	8.50	7.53	8.03	9.45	8.06	8.83
CuH	**2.91**	2.98	2.70	3.00	3.93	1.42	1.93
Li_2	**1.74**	1.93	1.07	1.21	2.10	0.92	1.47
CCl_2	**2.14**	1.99	1.29	1.81	2.40	1.07	2.18
CH_2S	**2.03**	2.06	1.67	1.75	2.71	0.90	0.92
Mg_2	**3.23**	3.26	2.26	2.70	3.34	2.46	3.79
C_2H_2O	**2.72**	2.42	2.12	2.31	3.56	3.30	3.31
HCP	**4.31**	3.86	3.60	3.83	3.59	2.95	3.26
CH_2O	**3.49**	3.59	3.01	3.17	4.10	1.66	1.76
C_3H_4O	**3.21**	3.15	2.78	2.87	4.58	1.67	1.73
SiF_2	**5.34**	5.31	3.96	4.72	5.96	4.09	5.92
HCN	**6.48**	5.96	5.59	5.85	5.95	4.78	5.23
C_2H_2	**5.23**	4.70	4.38	4.61	4.49	3.71	-
MEA		**0.17**	**0.86**	**0.47**	**0.63**	**1.22**	**0.76**
RMSE		**0.22**	**0.97**	**0.52**	**0.70**	**1.29**	**0.91**

Table D.6: Excitation energies obtained using the 6-311++G(d,p) basis set before and after approximate projection.

System	Exp.	TDDFT	Δ-B3LYP	AP-Δ-B3LYP	CIS	Δ-HF	AP-Δ-HF
BH	**2.48**	2.67	1.69	2.22	2.85	1.68	2.62
BF	**6.34**	6.08	4.29	5.25	6.51	4.47	6.51
SiO	**5.31**	4.54	3.78	4.71	4.17	3.52	3.78
CO	**8.07**	7.90	6.56	7.33	8.69	6.95	8.55
N_2	**8.59**	8.41	7.44	7.94	9.38	6.77	8.76
CuH	**2.91**	2.92	2.61	2.90	3.92	1.38	1.89
Li_2	**1.74**	1.93	1.07	1.20	2.10	0.92	1.46
CCl_2	**2.14**	1.71	1.35	1.86	2.15	0.93	2.01
CH_2S	**2.03**	2.04	1.64	1.72	2.70	0.88	0.89
Mg_2	**3.23**	3.32	2.27	2.71	3.35	2.47	3.80
C_2H_2O	**2.72**	2.39	2.09	2.28	3.55	3.26	3.65
HCP	**4.31**	3.74	3.50	3.67	3.35	2.72	2.99
CH_2O	**3.49**	3.54	2.96	3.12	4.39	1.98	2.08
C_3H_4O	**3.21**	3.11	2.74	2.83	4.54	1.61	1.67
SiF_2	**5.34**	5.25	3.94	4.7	5.93	4.08	5.94
HCN	**6.48**	6.44	5.45	5.71	5.50	4.62	5.07
C_2H_2	**5.23**	4.55	4.22	4.44	4.34	3.53	-
MEA		**0.22**	**0.94**	**0.52**	**0.68**	**1.33**	**0.80**
RMSE		**0.30**	**1.05**	**0.57**	**0.77**	**1.39**	**0.96**

Table D.7: Excitation energies obtained using the aug-cc-PVDZ basis set before and after approximate projection.

System	Exp.	TDDFT	Δ-B3LYP	AP-Δ-B3LYP	CIS	Δ-HF	AP-Δ-HF
BH	**2.48**	2.69	1.68	2.21	2.86	1.47	2.62
BF	**6.34**	6.09	4.34	5.28	6.57	4.55	6.58
SiO	**5.31**	5.16	4.39	4.78	6.09	3.68	3.94
CO	**8.07**	7.96	6.60	7.37	8.76	6.99	8.62
N_2	**8.59**	8.56	7.57	8.05	9.53	8.08	8.84
CuH	**2.91**	2.96	2.65	2.95	3.93	1.37	1.90
Li_2	**1.74**	1.93	1.06	1.21	2.13	0.94	1.48
CCl_2	**2.14**	1.96	1.27	1.75	2.39	1.05	2.10
CH_2S	**2.03**	2.07	1.64	1.71	3.34	0.77	0.77
Mg_2	**3.23**	2.34	2.27	2.79	2.78	2.45	3.70
C_2H_2O	**2.72**	2.42	2.11	2.3	3.59	3.27	3.65
HCP	**4.31**	3.82	3.56	3.72	4.24	2.76	2.99
CH_2O	**3.49**	3.60	3.00	3.15	4.44	2.00	2.10
C_3H_4O	**3.21**	3.16	2.77	2.86	4.58	1.64	1.70
SiF_2	**5.34**	5.31	3.95	4.73	5.94	4.07	5.97
HCN	**6.48**	5.95	5.57	5.82	5.65	4.73	5.14
C_2H_2	**5.23**	5.95	4.38	4.59	4.68	3.68	-
MEA		**0.23**	**0.87**	**0.49**	**0.70**	**1.23**	**0.79**
RMSE		**0.32**	**0.97**	**0.53**	**0.79**	**1.29**	**0.94**

Table D.8: Excitation energies obtained using the aug-cc-PVTZ basis set before and after approximate projection.

System	State	Exp.	CIS	Δ-HF	AP-Δ-HF
BH	$1^1\Pi$	2251	2442	2441	2191
BF	$1^1\Pi$	1265	1169	1171	1162
SiO	$1^1\Pi$	853	738	722	710
N_2	$1^1\Pi$g	1694	1774	1770	1736
CuH	$2^1\Sigma^+$	1698	1734	1589	1588
Li_2	$1^1\Sigma_u^+$+	255	273	235	322
Mg_2	$1^1\Sigma_u^+$	191	254	184	120
CH_2S	1^1A_2	799	811	725	672
		820	845	901	897
		1316	1393	1473	1461
		3034	3140	3267	3241
		3081	3275	3418	3389
$C_2H_2O_2$	1^1A_u	233	263	256	240
		379	440	434	429
		509	572	557	556
		720	871	893	885
		735	910	904	936
		952	1086	1067	1054
		1172	1389	1376	1352
		1196	1394	1401	1394
		1281	1577	1580	1576
		1391	1730	1660	1667
		2809	3250	3248	3204
HCP	$1^1A''$	567	509	755	603
		951	975	926	1027
HCN	$1^1A''$	941	975	759	1053
		1496	1559	1579	1738
C_3H_4O	$1^1A''$	250	182	247	255
		333	341	315	313
		488	541	540	535
		582	704	547	544
		644	508	660	677
		909	1118	996	818
		1266	1611	1160	1138
		1133	1321	1406	1390
CH_2O	$1^1A''$	683	275	664	575
		899	1020	1077	1076
		1177	1457	1143	1089
		1321	1592	1522	1507
		2851	3228	3238	3207
		2968	3346	3375	3342
CCl_2	1^1B_1	303	289	273	247
		634	560	540	426
SiF_2	1^1B_1	252	263	247	244
		860	728	704	668
		984	828	803	771
MEA			**145**	**136**	**140**
RMSE			**187**	**176**	**172**

Table D.9: Vibrational frequencies obtained using the 6-311G basis set before and after approximate projection.

System	State	Exp.	TDDFT	Δ-B3LYP	AP-Δ-B3LYP
BH	$1^1\Pi$	2251	2259	2462	2353
BF	$1^1\Pi$	1265	1061	1157	1141
SiO	$1^1\Pi$	853	769	754	709
CO	$1^1\Pi$	1518	1385	1531	1430
N_2	$^1\Pi\_g$	1694	1622	1680	1659
CuH	$2^1\Sigma^+$	1698	1138	1291	1790
Li_2	$1^1\Sigma_u^+$	255	256	200	256
Mg_2	$1^1\Sigma_u^+$	191	116	188	158
CH_2S	1^1A_2	799	811	742	724
		820	845	823	830
		1316	1393	1368	1370
		3034	3140	3121	3111
		3081	3275	3260	3250
C_2H_2	1^1A_u	1048	1108	1114	1111
		1385	1398	1385	1385
$C_2H_2O_2$	1^1A_u	233	260	255	252
		379	386	392	379
		509	533	531	531
		720	823	816	810
		735	828	818	820
		952	1028	1032	1020
		1172	1259	1230	1172
		1196	1302	1287	1282
		1281	1412	1305	1301
		1391	1481	1464	1474
		2809	3032	3060	3035
HCP	$1^1A''$	567	714	705	741
		951	866	949	859
HCN	$1^1A''$	941	1000	1004	1009
		1496	1436	1417	1431
C_3H_4O	$1^1A''$	250	254	241	258
		333	304	298	298
		488	518	507	509
		582	534	532	520
		644	738	663	701
		909	964	969	970
		1266	1114	1090	1080
		1133	1369	1298	1297
CH_2O	$1^1A''$	683	428	564	575
		899	930	924	1076
		1177	1253	1142	1089
		1321	1369	1361	1507
		2851	3050	3020	3207
		2968	3174	3140	3342
CCl_2	1^1B_1	303	241	262	256
		634	458	540	498
SiF_2	1^1B_1	252	192	218	213
		860	542	645	614
		984	554	755	709
MEA			**111**	**85**	**98**
RMSE			**155**	**117**	**130**

Table D.10: Vibrational frequencies obtained using the 6-311G basis set before and after approximate projection.

System	State	Exp.	CIS	Δ-HF	AP-Δ-HF
BH	$1^1\Pi$	2251	2532	2511	2332
BF	$1^1\Pi$	1265	1316	1311	1307
SiO	$1^1\Pi$	853	905	807	883
CO	$1^1\Pi$	1518	1636	1706	1428
N_2	$1^1\Pi$g	1694	1919	1894	1844
CuH	$2^1\Sigma_u^+$+	1698	1810	1718	1588
Li_2	$1^1\Sigma_u^+$+	255	272	245	337
Mg_2	$1^1\Sigma_u^+$	191	157	197	120
CH_2S	1^1A_2	799	862	827	816
		820	1068	894	895
		1316	1491	1491	1485
		3034	3262	3256	3239
		3081	3367	3382	3366
$C_2H_2O_2$	1^1A_u	233	254	248	233
		379	439	431	424
		509	547	523	525
		720	834	823	823
		735	851	840	871
		952	1015	976	969
		1172	1301	1286	1279
		1196	1326	1309	1286
		1281	1703	1680	1673
		1391	1813	1790	1805
		2809	3172	3172	3169
HCP	$1^1A''$	567	593	625	894
		951	1045	1004	1190
HCN	$1^1A''$	941	976	917	1034
		1496	1633	1555	1786
C_3H_4O	$1^1A''$	250	164	251	265
		333	332	313	312
		488	519	535	531
		582	676	543	543
		644	427	641	665
		909	1089	984	988
		1266	1535	1170	1153
		1133	1260	1402	1391
CH_2O	$1^1A''$	683	437	796	733
		899	948	1089	1109
		1177	1386	1235	1208
		1321	1632	1520	1513
		2851	3132	3211	3195
		2968	3219	3329	3310
CCl_2	$^1B_1$	303	312	313	316
		634	678	671	636
SiF_2	1^1B_1	252	290	284	279
		860	831	836	816
		984	947	951	946
MEA			**140**	**116**	**126**
RMSE			**182**	**173**	**175**

Table D.11: Vibrational frequencies obtained using the 6-311++G(d,p) basis set before and after approximate projection.

System	State	Exp.	TDDFT	Δ-B3LYP	AP-Δ-B3LYP
BH	$1^1\Pi$	2089	2363	2510	2421
BF	$1^1\Pi$	1265	1224	1262	1256
SiO	$1^1\Pi$	853	884	881	809
CO	$1^1\Pi$	1518	1539	1693	1596
N_2	$1^1\Pi g$	1694	1737	1791	1765
CuH	$2^1\Sigma^+$	1698	1650	1637	1623
Li_2	$1^1\Sigma_u^+$	255	261	208	267
Mg_2	$1^1\Sigma_u^+$	191	156	191	162
CH_2S	1^1A_2	799	801	782	795
		820	896	836	822
		1316	1372	1351	1355
		3034	3127	3112	3101
		3081	3240	3228	3217
C_2H_2	1^1A_u	1048	1092	1103	1100
		1385	1433	1420	1419
$C_2H_2O_2$	1^1A_u	233	251	243	241
		379	386	400	392
		509	519	516	517
		720	779	758	762
		735	780	772	767
		952	971	974	965
		1172	1197	1224	1211
		1196	1239	1242	1238
		1281	1528	1426	1404
		1391	1572	1556	1564
		2809	2966	3003	2979
HCP	$1^1A''$	567	694	716	712
		951	957	947	947
HCN	$1^1A''$	941	983	985	991
		1496	1531	1509	1528
C_3H_4O	$1^1A''$	250	261	240	258
		333	295	292	292
		488	504	498	501
		582	508	514	502
		644	709	625	679
		909	934	941	950
		1266	1094	1087	1080
		1133	1376	1313	1307
CH_2O	$1^1A''$	683	575	698	634
		899	891	894	914
		1177	1300	1247	1215
		1321	1358	1301	1314
		2851	2987	2954	2973
		2968	3085	3048	3070
CCl_2	1^1B_1	303	192	300	301
		634	590	638	620
SiF_2	1^1B_1	252	233	242	240
		860	672	748	723
		984	768	861	835
MEA			**77**	**66**	**63**
RMSE			**105**	**101**	**92**

Table D.12: Vibrational frequencies obtained using the 6-311++G(d,p) basis set before and after approximate projection.

System	State	Exp.	CIS	Δ-HF	AP-Δ-HF
BH	$1^1\Pi$	2251	2538	2506	2319
BF	$1^1\Pi$	1265	1272	1265	1265
SiO	$1^1\Pi$	853	859	773	767
CO	$1^1\Pi$	1518	1615	1645	1277
N_2	$1^1\Pi$g	1694	1914	1843	1842
CuH	$2^1\Sigma_u^+$+	1698	1814	1722	1581
Li_2	$1^1\Sigma_u^+$+	255	272	245	336
Mg_2	$1^1\Sigma_u^+$	191	158	199	125
CH_2S	1^1A_2	799	849	826	817
		820	1068	880	889
		1316	1475	1474	1473
		3034	3273	3264	3241
		3081	3384	3394	3372
$C_2H_2O_2$	1^1A_u	233	255	247	234
		379	436	428	422
		509	542	519	523
		720	831	826	821
		735	850	838	872
		952	1025	990	989
		1172	1284	1273	1268
		1196	1309	1291	1268
		1281	1700	1664	1655
		1391	1800	1772	1783
		2809	3180	3179	3118
HCP	$1^1A''$	567	593	583	759
		951	1045	950	1082
HCN	$1^1A''$	941	965	905	1008
		1496	1625	1536	1768
C_3H_4O	$1^1A''$	250	160	250	264
		333	331	312	312
		488	516	531	529
		582	671	541	541
		644	413	627	651
		909	1076	978	982
		1266	1527	1165	1148
		1133	1245	1391	1380
CH_2O	$1^1A''$	683	449	798	729
		899	934	1075	1096
		1177	1368	1226	1198
		1321	1627	1496	1490
		2851	3143	3218	3201
		2968	3238	3343	3322
CCl_2	$^1B_1$	303	309	307	309
		634	683	669	635
SiF_2	1^1B_1	252	280	274	266
		860	819	823	808
		984	932	934	935
MEA			**136**	**109**	**119**
RMSE			**183**	**168**	**166**

Table D.13: Vibrational frequencies obtained using the aug-cc-PVDZ basis set before and after approximate projection.

System	State	Exp.	TDDFT	Δ-B3LYP	AP-Δ-B3LYP
BH	$1^1\Pi$	2089	1754	2492	2397
BF	$1^1\Pi$	1265	1190	1231	1224
SiO	$1^1\Pi$	853	884	881	766
CO	$1^1\Pi$	1518	1522	1673	1574
N_2	$1^1\Pi$g	1694	1741	1793	1767
CuH	$2^1\Sigma^+$	1698	1647	1650	1780
Li_2	$1^1\Sigma_u^+$	255	261	261	268
Mg_2	$1^1\Sigma_u^+$	191	80	191	163
CH_2S	1^1A_2	799	789	770	784
		820	898	840	827
		1316	1356	1336	1341
		3034	3132	3117	3105
		3081	3254	3240	3228
C_2H_2	1^1A_u	1048	1090	1101	1099
		1385	1432	1419	1419
$C_2H_2O_2$	1^1A_u	233	250	242	239
		379	382	395	387
		509	515	512	513
		720	780	763	763
		735	782	773	772
		952	984	989	977
		1172	1181	1209	1198
		1196	1227	1231	1226
		1281	1521	1418	1400
		1391	1566	1550	1561
		2809	2974	3012	2979
HCP	$1^1A''$	567	700	711	714
		951	943	933	935
HCN	$1^1A''$	941	975	973	979
		1496	1524	1501	1522
C_3H_4O	$1^1A''$	250	262	241	258
		333	295	292	291
		488	505	496	499
		582	508	517	505
		644	721	625	680
		909	931	940	950
		1266	1088	1082	1076
		1133	1369	1313	1308
CH_2O	$1^1A''$	683	544	682	619
		899	874	878	898
		1177	1279	1248	1218
		1321	1355	1273	1288
		2851	2995	2955	2975
		2968	3100	3056	3078
CCl_2	1^1B_1	303	192	294	295
		634	590	645	627
SiF_2	1^1B_1	252	223	237	233
		860	662	737	712
		984	758	846	822
MEA			**81**	**66**	**65**
RMSE			**111**	**100**	**92**

Table D.14: Vibrational frequencies obtained using the aug-cc-PVDZ basis set before and after approximate projection.

System	State	Exp.	CIS	Δ-HF	AP-Δ-HF
BH	$1^1\Pi$	2251	2545	2522	2430
BF	$1^1\Pi$	1265	1366	1363	1358
SiO	$1^1\Pi$	853	937	823	818
CO	$1^1\Pi$	1518	1632	1676	1323
N_2	$1^1\Pi$g	1694	1899	1873	1817
CuH	$2^1\Sigma_u^+$+	1698	1814	1570	1586
Li_2	$1^1\Sigma_u^+$+	255	273	243	334
Mg_2	$1^1\Sigma_u^+$	191	156	194	107
CH_2S	1^1A_2	799	847	830	823
		820	1070	882	889
		1316	1487	1490	1487
		3034	3262	3261	3243
		3081	3362	3383	3366
$C_2H_2O_2$	1^1A_u	233	257	251	237
		379	439	431	425
		509	544	520	525
		720	839	833	826
		735	859	845	876
		952	1009	972	974
		1172	1296	1281	1276
		1196	1327	1307	1285
		1281	1709	1674	1665
		1391	1805	1787	1800
		2809	3162	3162	3116
HCP	$1^1A''$	567	509	593	791
		951	975	985	1080
HCN	$1^1A''$	941	976	861	1033
		1496	1633	1671	1765
C_3H_4O	$1^1A''$	250	166	253	268
		333	333	314	314
		488	519	535	532
		582	679	546	546
		644	437	654	676
		909	1089	989	994
		1266	1638	1169	1152
		1133	1257	1405	1395
CH_2O	$1^1A''$	683	437	796	733
		899	948	1089	1109
		1177	1386	1235	1208
		1321	1632	1520	1513
		2851	3132	3211	3195
		2968	3132	3329	3310
CCl_2	$^1B_1$	303	311	311	316
		634	676	666	635
SiF_2	1^1B_1	252	464	291	282
		860	831	867	850
		984	899	986	987
MEA			**144**	**119**	**124**
RMSE			**182**	**177**	**169**

Table D.15: Vibrational frequencies obtained using the aug-cc-PVTZ basis set before and after approximate projection.

System	State	Exp.	TDDFT	Δ-B3LYP	AP-Δ-B3LYP
BH	$1^1\Pi$	2089	2395	2520	2348
BF	$1^1\Pi$	1265	1274	1301	1295
SiO	$1^1\Pi$	853	896	896	817
CO	$1^1\Pi$	1518	1547	1687	1582
N_2	$1^1\Pi g$	1694	1730	1873	1751
CuH	$2^1\Sigma^+$	1698	1664	1656	1793
Li_2	$1^1\Sigma_u^+$	255	260	209	267
Mg_2	$1^1\Sigma_u^+$	191	157	191	161
CH_2S	1^1A_2	799	787	770	784
		820	902	845	830
		1316	1368	1349	1353
		3034	3130	3118	3109
		3081	3237	3227	3219
C_2H_2	1^1A_u	1048	1093	1102	1099
		1385	1436	1424	1424
$C_2H_2O_2$	1^1A_u	233	250	244	243
		379	382	401	393
		509	515	516	518
		720	780	769	765
		735	782	776	776
		952	984	977	969
		1172	1181	1227	1215
		1196	1227	1243	1239
		1281	1521	1422	1401
		1391	1566	1551	1560
		2809	2974	3003	2975
HCP	$1^1A''$	567	691	705	700
		951	958	949	950
HCN	$1^1A''$	941	990	988	991
		1496	1528	1507	1525
C_3H_4O	$1^1A''$	250	264	242	259
		333	296	293	293
		488	509	500	503
		582	510	519	507
		644	721	635	686
		909	939	951	958
		1266	1092	1088	1081
		1133	1380	1315	1310
CH_2O	$1^1A''$	683	567	689	635
		899	885	891	912
		1177	1300	1251	1217
		1321	1358	1300	1313
		2851	2991	2960	2979
		2968	3085	3050	3072
CCl_2	1^1B_1	303	270	299	300
		634	628	639	623
SiF_2	1^1B_1	252	243	253	249
		860	710	772	750
		984	823	886	866
MEA			**73**	**68**	**62**
RMSE			**102**	**103**	**85**

Table D.16: Vibrational frequencies obtained using the aug-cc-PVTZ basis set before and after approximate projection.

Appendix E

Chapter 4 Supplemental Information

E.1 CAM-B3LYP electron density differences

The CAM-B3LYP density differences, see Fig. E.1, are in excellent agreement for both PIMOM and LR-TDDFT for the S_0, LR-TD-CAM-B3LYP S_1, and PIMOM S_1 optimized geometries. The CAM-B3LYP PIMOM density differences are very similar to the B3LYP PIMOM density differences, again showing that the PIMOM method is not as subject to the functional dependencies of the LR-TDDFT procedure.

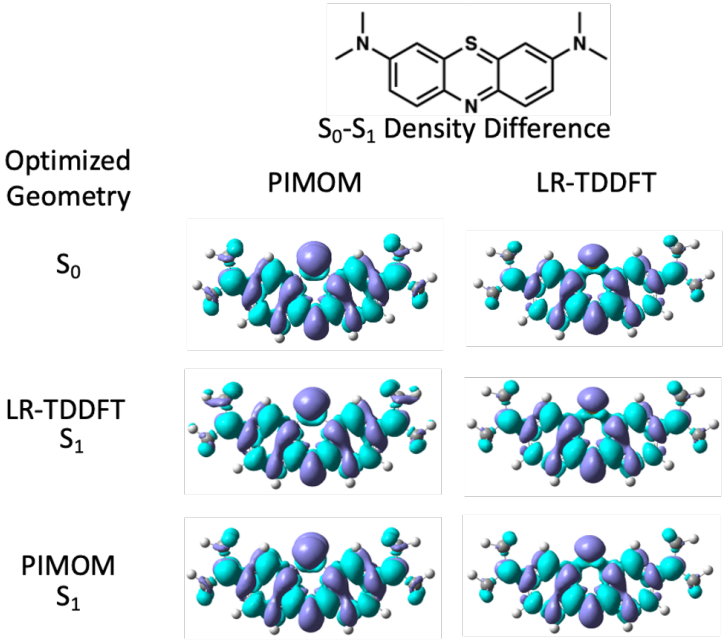

Figure E.1: The structure of the methylene blue chromophore and the CAM-B3LYP density difference between the ground and S_1 excited state at the ground state S_0, LR-TDDFT S_1, and PIMOM S_1 optimized geometries.

E.2 Tables

The electronic excitation energies in eV for S_1 and S_2 obtained using B3LYP and CAM-B3LYP functionals using PIMOM and LR-TDDFT are summarized below in Tables E.1 and E.2.

Electornic State	$\mathbf{E}^{PIMOM}_{Vertical}$	$\mathbf{E}^{PIMOM}_{Adiabatic}$	$\mathbf{E}^{LR-TDDFT}_{Vertical}$	$\mathbf{E}^{LR-TDDFT}_{Adiabatic}$
$\mathbf{S}_1$	1.62	1.58	2.48	2.39
$\mathbf{S}_2$	2.16	2.01	2.61	-[a]

[a] Optimizing the S_2 state from different starting points repeatedly led to the S_1 state.

Table E.1: B3LYP S_1 and S_2 vertical and adiabatic excitation energies in eV obtained using PIMOM and LR-TDDFT approaches.

Electornic State	$\mathbf{E}^{PIMOM}_{Vertical}$	$\mathbf{E}^{PIMOM}_{Adiabatic}$	$\mathbf{E}^{LR-TDDFT}_{Vertical}$	$\mathbf{E}^{LR-TDDFT}_{Adiabatic}$
$\mathbf{S}_1$	1.90	1.84	2.62	2.59
$\mathbf{S}_2$	2.39	2.20	3.00	2.83

Table E.2: CAM-B3LYP S_1 and S_2 vertical and adiabatic excitation energies in eV obtained using PIMOM and LR-TDDFT approaches.

E.3 Optimized Geometries

Ground State CAM-B3LYP/6-31G*

SCF=-1182.32200279E_h

1 1

H	0.89120	4.751684	2.433144
H	0.00000	6.261148	2.205119
H	0.89120	4.751684	2.433144
H	0.00000	7.087077	0.299734
H	0.89122	6.227235	0.960052
H	0.89122	6.227235	0.960052
H	0.00000	7.087077	0.299734
H	0.89122	6.227235	0.960052
H	0.89122	6.227235	0.960052
H	0.00000	6.261148	2.205119
H	0.89120	4.751684	2.433144
H	0.89120	4.751684	2.433144
H	0.00000	4.451592	2.078282
H	0.00000	4.451592	2.078282
H	0.00000	2.195415	3.030460
H	0.00000	2.195415	3.030460
H	0.00000	2.731716	1.903001
H	0.00000	2.731716	1.903001
C	0.00000	5.196966	1.979127
C	0.00000	6.197028	0.325947
C	0.00000	6.197028	0.325947
C	0.00000	5.196966	1.979127
C	0.00000	3.592793	1.421727
C	0.00000	3.592793	1.421727
C	0.00000	2.346574	1.956890
C	0.00000	2.346574	1.956890
C	0.00000	2.627807	0.826086
C	0.00000	2.627807	0.826086
C	0.00000	3.778985	0.002038
C	0.00000	3.778985	0.002038
C	0.00000	1.172389	1.144619
C	0.00000	1.172389	1.144619
C	0.00000	1.364357	0.275364
C	0.00000	1.364357	0.275364
N	0.00000	0.000000	1.768399
N	0.00000	5.015293	0.532319
N	0.00000	5.015293	0.532319
S	0.00000	0.000000	1.352160

Ground State B3LYP/6-31G*
SCF=-1182.77678750E$_h$

1 1

H	0.89221	4.783111	2.441572
H	0.00000	6.294299	2.209406
H	0.89221	4.783111	2.441572
H	0.00000	7.119983	0.298272
H	0.89217	6.258097	0.963361
H	0.89217	6.258097	0.963361
H	0.00000	7.119983	0.298272
H	0.89217	6.258097	0.963361
H	0.89217	6.258097	0.963361
H	0.00000	6.294299	2.209406
H	0.89221	4.783111	2.441572
H	0.89221	4.783111	2.441572
H	0.00000	4.465572	2.085866
H	0.00000	4.465572	2.085866
H	0.00000	2.204905	3.037830
H	0.00000	2.204905	3.037830
H	0.00000	2.747041	1.905664
H	0.00000	2.747041	1.905664
C	0.00000	5.228471	1.986384
C	0.00000	6.229265	0.328190
C	0.00000	6.229265	0.328190
C	0.00000	5.228471	1.986384
C	0.00000	3.608236	1.425854
C	0.00000	3.608236	1.425854
C	0.00000	2.354488	1.963229
C	0.00000	2.354488	1.963229
C	0.00000	2.642056	0.827877
C	0.00000	2.642056	0.827877
C	0.00000	3.798246	0.000237
C	0.00000	3.798246	0.000237
C	0.00000	1.177196	1.150179
C	0.00000	1.177196	1.150179
C	0.00000	1.373614	0.276506
C	0.00000	1.373614	0.276506
N	0.00000	0.000000	1.779984
N	0.00000	5.042486	0.533711
N	0.00000	5.042486	0.533711
S	0.00000	0.000000	1.363323

LR-TD-S_1-CAM-B3LYP/6-31G*
E= -1181.910361 E_h

1 1

H	0.89070	4.733462	2.445155
H	0.00000	6.247990	2.233201
H	0.89070	4.733462	2.445155
H	0.00000	7.092278	0.335206
H	0.89066	6.239307	0.932947
H	0.89066	6.239307	0.932947
H	0.00000	7.092278	0.335206
H	0.89066	6.239307	0.932947
H	0.89066	6.239307	0.932947
H	0.00000	6.247990	2.233201
H	0.89070	4.733462	2.445155
H	0.89070	4.733462	2.445155
H	0.00000	4.466472	2.075012
H	0.00000	4.466472	2.075012
H	0.00000	2.214144	3.037376
H	0.00000	2.214144	3.037376
H	0.00000	2.714809	1.891444
H	0.00000	2.714809	1.891444
C	0.00000	5.186372	1.995391
C	0.00000	6.206523	0.296569
C	0.00000	6.206523	0.296569
C	0.00000	5.186372	1.995391
C	0.00000	3.605672	1.420476
C	0.00000	3.605672	1.420476
C	0.00000	2.357907	1.962788
C	0.00000	2.357907	1.962788
C	0.00000	2.621635	0.813044
C	0.00000	2.621635	0.813044
C	0.00000	3.781921	0.002222
C	0.00000	3.781921	0.002222
C	0.00000	1.172920	1.164285
C	0.00000	1.172920	1.164285
C	0.00000	1.356729	0.254080
C	0.00000	1.356729	0.254080
N	0.00000	0.000000	1.826558
N	0.00000	5.019121	0.549281
N	0.00000	5.019121	0.549281
S	0.00000	0.000000	1.356550

LR-TD-S_1 B3LYP/6-31G*
E= -1182.376500 E_h

1 1

H	4.77589	2.422273	0.891647
H	6.29042	2.201788	0.000000
H	4.77589	2.422273	0.891647
H	7.12749	0.291204	0.000000
H	6.27222	0.974638	0.892012
H	6.27222	0.974638	0.892012
H	7.12465	0.449626	0.000000
H	6.27669	0.834046	0.889322
H	6.27669	0.834046	0.889322
H	6.23582	2.347323	0.000000
H	4.71807	2.533039	0.892143
H	4.71807	2.533039	0.892143
H	4.47318	2.102921	0.000000
H	4.52020	2.030167	0.000000
H	2.23186	3.079537	0.000000
H	2.27590	3.019467	0.000000
H	2.73450	1.871760	0.000000
H	2.69222	1.905217	0.000000
C	5.22652	1.968801	0.000000
C	6.23870	0.338386	0.000000
C	6.24379	0.190556	0.000000
C	5.17796	2.088815	0.000000
C	3.61149	1.447253	0.000000
C	3.65647	1.379538	0.000000
C	2.36434	2.002964	0.000000
C	2.39231	1.940063	0.000000
C	2.63997	0.792451	0.000000
C	2.62997	0.823752	0.000000
C	3.80060	0.018647	0.000000
C	3.80995	0.029640	0.000000
C	1.16222	1.212640	0.000000
C	1.20111	1.174253	0.000000
C	1.37186	0.232997	0.000000
C	1.34698	0.215603	0.000000
N	0.01263	1.862341	0.000000
N	5.05125	0.518405	0.000000
N	5.04364	0.635481	0.000000
S	0.00000	1.321534	0.000000

PIMOM-S_1-CAM-B3LYP/6-31G*
E= -1181.938075 E_h

1 1

H	0.89072	4.739399	2.441615
H	0.00000	6.254125	2.230489
H	0.89072	4.739399	2.441615
H	0.00000	7.097357	0.332279
H	0.89058	6.240921	0.934324
H	0.89058	6.240921	0.934324
H	0.00000	7.097357	0.332279
H	0.89058	6.240921	0.934324
H	0.89058	6.240921	0.934324
H	0.00000	6.254125	2.230489
H	0.89072	4.739399	2.441615
H	0.89072	4.739399	2.441615
H	0.00000	4.468218	2.077716
H	0.00000	4.468218	2.077716
H	0.00000	2.210733	3.033980
H	0.00000	2.210733	3.033980
H	0.00000	2.718988	1.888384
H	0.00000	2.718988	1.888384
C	0.00000	5.192452	1.993810
C	0.00000	6.211251	0.298621
C	0.00000	6.211251	0.298621
C	0.00000	5.192452	1.993810
C	0.00000	3.609423	1.420571
C	0.00000	3.609423	1.420571
C	0.00000	2.356335	1.959934
C	0.00000	2.356335	1.959934
C	0.00000	2.624531	0.810091
C	0.00000	2.624531	0.810091
C	0.00000	3.784185	0.002648
C	0.00000	3.784185	0.002648
C	0.00000	1.177989	1.160173
C	0.00000	1.177989	1.160173
C	0.00000	1.359558	0.253437
C	0.00000	1.359558	0.253437
N	0.00000	0.000000	1.829982
N	0.00000	5.023833	0.547372
N	0.00000	5.023833	0.547372
S	0.00000	0.000000	1.365869

PIMOM-S_1 B3LYP/6-31G*
E= -1182.406008 E_h

1 1

H	0.89157	4.772054	2.449406
H	0.00000	6.288722	2.234005
H	0.89157	4.772054	2.449406
H	0.00000	7.130790	0.327902
H	0.89135	6.270414	0.939506
H	0.89135	6.270414	0.939506
H	0.00000	7.130790	0.327902
H	0.89135	6.270414	0.939506
H	0.89135	6.270414	0.939506
H	0.00000	6.288722	2.234005
H	0.89157	4.772054	2.449406
H	0.89157	4.772054	2.449406
H	0.00000	4.481309	2.084472
H	0.00000	4.481309	2.084472
H	0.00000	2.220048	3.041047
H	0.00000	2.220048	3.041047
H	0.00000	2.735978	1.892631
H	0.00000	2.735978	1.892631
C	0.00000	5.225373	2.000192
C	0.00000	6.242974	0.302334
C	0.00000	6.242974	0.302334
C	0.00000	5.225373	2.000192
C	0.00000	3.623856	1.424136
C	0.00000	3.623856	1.424136
C	0.00000	2.363677	1.965886
C	0.00000	2.363677	1.965886
C	0.00000	2.639788	0.813618
C	0.00000	2.639788	0.813618
C	0.00000	3.801953	0.004244
C	0.00000	3.801953	0.004244
C	0.00000	1.182113	1.164540
C	0.00000	1.182113	1.164540
C	0.00000	1.369710	0.255913
C	0.00000	1.369710	0.255913
N	0.00000	0.000000	1.833022
N	0.00000	5.052080	0.548463
N	0.00000	5.052080	0.548463
S	0.00000	0.000000	1.372003

Appendix F

Chapter 5 Supplemental Information

F.1 Tables

Electronic Configuration	Elec. State	Rel. Energy (eV)	Single Point Energies (eV)	Optimized Gd-O-Gd Angle (°)
$4fa^7 4fb^7 \sigma_g^2 \sigma_u^1 \delta_g^1$	$^{17}\Delta_u$	1.22	1.22	180
$4fa^7 4fb^7 \sigma_g^1 \sigma_u^2 \delta_g^1$	$^{17}\Delta_g$	1.62	1.62	180
$4fa^7 4fb^7 \sigma_g^2 \sigma_u^1 \delta_u^1$	$^{17}\Delta_g$	1.38	1.39	180
$4fa^7 4fb^7 \sigma_g^2 \sigma_u^1 \pi_u^1$	$^{17}\Pi_g$ (6p)	.	1.58	180
$4fa^7 4fb^7 \sigma_g^1 \sigma_u^2 \delta_u^1$	$^{17}\Delta_u$	1.79	1.81	180
$4fa^7 4fb^7 \sigma_g^1 \sigma_u^2 \pi_u^1$	$^{17}\Pi_u$ (6p)	2.02	2.04	180
$4fa^7 4fb^7 \sigma_g^2 \sigma_u^1 \sigma_g^1$	$^{17}\Sigma_u$ (6p)	.	2.12	.
$4fa^7 4fb^7 \sigma_g^2 \delta_g^1 \sigma_g^1$	$^{17}\Delta_g$ (6p)	2.12	3.63	180
$4fa^7 4fb^7 \sigma_g^2 \delta_g^1 \delta_u^1$	$^{17}\Gamma_u$	2.22	2.49	110
$4fa^7 4fb^7 \sigma_g^2 \sigma_u^1 \pi_u^1$	$^{17}\Pi_g$ (5d)	2.31	2.36	126
$4fa^7 4fb^7 \sigma_g^1 \sigma_u^2 \sigma_g^1$	$^{17}\Sigma_g$ (6p)	2.55	2.62	180
$4fa^7 4fb^7 \sigma_g^2 \delta_g^1 \pi_u^1$	$^{17}\Phi_u$ (6p)	2.80	3.27	111
$4fa^7 4fb^7 \sigma_g^1 \sigma_u^2 \pi_u^1$	$^{17}\Pi_u$ (5d)	.	2.84	.
$4fa^7 4fb^7 \sigma_g^1 \sigma_{u(\beta)}^1 \delta_g^1 \delta_u^1$	$^{17}\Gamma_g$	2.85	2.87	180
$4fa^7 4fb^7 \sigma_g^1 \sigma_u^2 \sigma_g^1$	$^{17}\Sigma_g$ (5d)	.	2.99	.
$4fa^7 4fb^7 \sigma_g^2 \sigma_u^1 \sigma_g^1$	$^{17}\Sigma_u$ (5d)	3.37	3.46	137
$4fa^7 4fb^7 \sigma_{g(\beta)}^1 \sigma_u^1 \delta_g^1 \pi_u^1$	$^{17}\Phi_g$ (6p)	3.62	3.63	180
$4fa^7 4fb^7 \sigma_g^1 \sigma_{u(\beta)}^1 \delta_g^1 \pi_u^1$	$^{17}\Phi_g$ (6p)	3.68	3.70	180
$4fa^7 4fb^7 \sigma_g^2 \delta_g^1 \pi_u^1$	$^{17}\Phi_u$ (5d)	.	3.95	.
$4fa^7 4fb^7 \sigma_{g(\beta)}^1 \sigma_u^1 \delta_g^1 \sigma_g^1$	$^{17}\Delta_u$ (6p)	.	4.04	.
$4fa^7 4fb^7 \sigma_u^2 \delta_g^1 \pi_u^1$	$^{17}\Phi_u$ (6p)	4.05	4.09	180
$4fa^7 4fb^7 \sigma_g^1 \sigma_{u(\beta)}^1 \delta_g^1 \sigma_g^1$	$^{17}\Delta_u$ (6p)	.	4.10	.
$4fa^7 4fb^7 \sigma_g^1 \sigma_u^1 \delta_g^1 \sigma_g^1$	$^{17}\Delta_u$ (6p)	.	4.13	.
$4fa^7 4fb^7 \sigma_{g(\beta)}^1 \sigma_u^1 \delta_g^1 \pi_u^1$	$^{17}\Phi_g$ (5d)	.	4.33	.
$4fa^7 4fb^7 \sigma_g^1 \sigma_{u(\beta)}^1 \delta_g^1 \pi_u^1$	$^{17}\Phi_g$ (5d)	.	4.39	.
$4fa^7 4fb^7 \sigma_g^2 \delta_g^1 \sigma_g^1$	$^{17}\Delta_g$ (5d)	.	4.47	.
$4fa^7 4fb^7 \sigma_u^2 \delta_g^1 \sigma_g^1$	$^{17}\Delta_g$ (6p)	.	4.54	.
$4fa^7 4fb^7 \sigma_u^2 \delta_g^1 \pi_u^1$	$^{17}\Phi_u$ (5d)	4.73	4.80	180
$4fa^7 4fb^7 \sigma_{g(\beta)}^1 \sigma_u^1 \delta_g^1 \sigma_g^1$	$^{17}\Delta_u$ (5d)	4.73	4.83	126
$4fa^7 4fb^7 \sigma_g^1 \sigma_{u(\beta)}^1 \delta_g^1 \sigma_g^1$	$^{17}\Delta_u$ (5d)	.	4.90	.
$4fa^7 4fb^7 \sigma_u^2 \delta_g^1 \sigma_g^1$	$^{17}\Delta_g$ (5d)	5.18	5.30	180

Table F.1: DFT predicted relative energies of 17-tet electronic excitations of Gd_2O using PIMOM. States for which only single point energies are listed did not converge upon optimization.

Electronic Configuration	Elec. State	Rel. Energy (eV)	Single Point Energies (eV)	Optimized Gd-O-Gd Angle (°)
$4fa^7 4fb^7 \sigma_g^2 \sigma_u^2$	$^{15}\Sigma_g$	0.28	.	180
$4fa^7 4fb^7 \sigma_g^2 \sigma_{u(\beta)}^1 \delta_g^1$	$^{15}\Delta_u$	1.30	1.66	105
$4fa^7 4fb^7 \sigma_{g(\beta)}^1 \sigma_u^2 \delta_g^1$	$^{15}\Delta_g$	2.04	2.05	180
$4fa^7 4fb^7 \sigma_g^2 \sigma_u^1 \delta_{g(\beta)}^1$	$^{15}\Delta_u$	1.67	2.08	109
$4fa^7 4fb^7 \sigma_g^2 \sigma_{u(\beta)}^1 \delta_u^1$	$^{15}\Delta_g$	1.84	1.84	180
$4fa^7 4fb^7 \sigma_g^2 \sigma_{u(\beta)}^1 \pi_u^1$	$^{15}\Pi_g$ (6p)	1.98	1.98	180
$4fa^7 4fb^7 \sigma_{g(\beta)}^1 \sigma_u^1 \delta_g^2$	$^{15}\Gamma_g$	3.53	4.14	180
$4fa^7 4fb^7 \sigma_{g(\beta)}^1 \sigma_u^2 \delta_u^1$	$^{15}\Delta_u$	2.20	2.23	180
$4fa^7 4fb^7 \sigma_{g(\beta)}^1 \sigma_u^2 \pi_u^1$	$^{15}\Pi_u$ (6p)	2.35	2.37	180
$4fa^7 4fb^7 \sigma_g^1 \sigma_u^2 \delta_{g(\beta)}^1$	$^{15}\Delta_g$	2.50	2.50	180
$4fa^7 4fb^7 \sigma_g^2 \sigma_{u(\beta)}^1 \sigma_g^1$	$^{15}\Sigma_u$ (5d)	.	2.54	.
$4fa^7 4fb^7 \sigma_g^2 \sigma_{u(\beta)}^1 \pi_u^1$	$^{15}\Pi_g$ (5d)	.	2.85	.
$4fa^7 4fb^7 \sigma_{g(\beta)}^1 \sigma_{u(\beta)}^1 \delta_g^1 \delta_u^1$	$^{15}\Gamma_u$	2.90	2.93	180
$4fa^7 4fb^7 \sigma_{g(\beta)}^1 \sigma_u^2 \sigma_g^1$	$^{15}\Sigma_g$ (5d)	.	2.97	.
$4fa^7 4fb^7 \sigma_{g(\beta)}^1 \sigma_u^2 \pi_u^1$	$^{15}\Pi_u$ (5d)	3.19	3.24	180
$4fa^7 4fb^7 \sigma_g^2 \sigma_{u(\beta)}^1 \sigma_g^1$	$^{15}\Sigma_u$ (6p)	.	3.46	.
$4fa^7 4fb^7 \sigma_{g(\beta)}^1 \sigma_{u(\beta)}^1 \delta_g^1 \pi_u^1$	$^{15}\Phi_g$ (6p)	.	3.70	.
$4fa^7 4fb^7 \sigma_g^2 \delta_g^2$	$^{15}\Gamma_g$	.	3.78	.
$4fa^7 4fb^7 \sigma_u^2 \delta_g^2$	$^{15}\Gamma_g$	4.53	4.55	180

Table F.2: DFT predicted relative energies of 15-tet electronic excitations of Gd_2O using PIMOM. States for which only single point energies are listed did not converge upon optimization.

Electronic Configuration	Elec. State	Rel. Energy (eV)	Single Point Energies (eV)	Optimized Gd-O-Gd Angle (°)
$4fa^7 4fb^7 \sigma_g^2 \sigma_{u(\beta)}^1 \delta_{g(\beta)}^1$	$^{13}\Delta_u$	.	2.15	.
$4fa^7 4fb^7 \sigma_{g(\beta)}^1 \sigma_u^2 \delta_{g(\beta)}^1$	$^{13}\Delta_g$	2.53	2.53	180

Table F.3: DFT predicted relative energies of 13-tet electronic excitations of Gd_2O using PIMOM. States for which only single point energies are listed did not converge upon optimization.

Electronic Configuration	Elec. State	Rel. Energy (eV)	Single Point Energies (eV)	Optimized Gd-O-Gd Angle (°)
$4fa^7 4fb^7 \sigma_g^2 \sigma_u^2 \delta_g^1$	$^{16}\Delta_g$	0.00	0.00	180
$4fa^7 4fb^7 \sigma_g^2 \sigma_u^2 \delta_u^1$	$^{16}\Delta_u$	.	0.18	.
$4fa^7 4fb^7 \sigma_g^2 \sigma_u^2 \pi_u^1$	$^{16}\Pi_u$ (6p)	0.35	0.35	180
$4fa^7 4fb^7 \sigma_u^2 \sigma_g^2 \delta_{g(\beta)}^1$	$^{14}\Delta_g$	.	0.67	.
$4fa^7 4fb^7 \sigma_g^2 \sigma_u^2 \sigma_g^1$	$^{16}\Sigma_u$ (6p)	.	0.70	.
$4fa^7 4fb^7 \sigma_g^2 \sigma_u^2 \pi_u^1$	$^{16}\Pi_u$ (5d)	.	0.97	.
$4fa^7 4fb^7 \sigma_g^2 \sigma_u^2 \sigma_g^1$	$^{16}\Sigma_u$ (5d)	1.20	1.21	180
$4fa^7 4fb^7 \sigma_g^2 \sigma_u^1 \delta_g^1 \pi_u^1$	$^{16}\Phi_g$ (6p)	.	2.28	.
$4fa^7 4fb^7 \sigma_g^2 \sigma_u^1 \delta_g^1 \sigma_g^1$	$^{16}\Delta_u$ (6p)	1.55	2.49	92
$4fa^7 4fb^7 \sigma_g^1 \sigma_u^2 \delta_g^1 \pi_u^1$	$^{16}\Phi_u$ (6p)	.	2.64	.
$4fa^7 4fb^7 \sigma_g^2 \sigma_u^1 \delta_g^1 \pi_u^1$	$^{16}\Phi_g$ (5d)	2.80	2.80	107
$4fa^7 4fb^7 \sigma_g^1 \sigma_u^2 \delta_g^1 \sigma_g^1$	$^{16}\Delta_g$ (6p)	.	2.89	.
$4fa^7 4fb^7 \sigma_g^2 \sigma_u^1 \delta_g^1 \sigma_g^1$	$^{16}\Delta_u$ (5d)	2.92	2.92	180
$4fa^7 4fb^7 \sigma_g^1 \sigma_u^2 \delta_g^1 \pi_u^1$	$^{16}\Phi_u$ (5d)	3.17	3.18	180
$4fa^7 4fb^7 \sigma_g^1 \sigma_u^2 \delta_g^1 \sigma_g^1$	$^{16}\Delta_g$ (5d)	3.25	3.27	180

Table F.4: DFT predicted relative energies of electronic states of Gd_2O^- using PIMOM. States for which only single point energies are listed did not converge upon optimization.

Bibliography

[1] Simon Cotton. *Lanthanide and actinide chemistry*. John Wiley & Sons, 2013.

[2] Josey E Topolski, Jared O Kafader, Vicmarie Marrero-Colon, Srinivasan S Iyengar, Hrant P Hratchian, and Caroline Chick Jarrold. Exotic electronic structures of $SmxCe_3^-$ xoy (x= 0-3; y= 2-4) clusters and the effect of high neutral density of low-lying states on photodetachment transition intensities. *J. Chem. Phys.*, 149(5):054305, 2018.

[3] Jarrett L Mason, Ankur K Gupta, Abbey J McMahon, Carley N Folluo, Krishnan Raghavachari, and Caroline Chick Jarrold. The striking influence of oxophilicity differences in heterometallic Mo−−Mn oxide cluster reactions with water. *J. Chem. Phys.*, 152(5):054301, 2020.

[4] Klaus-Peter Huber and Gerhard Herzberg. *Molecular spectra and molecular structure: IV. Constants of diatomic molecules*. Springer Science & Business Media, 1979.

[5] Gerhard Herzberg. Molecular spectra and molecular structure. vol. III: Electronic spectra and electronic structure of polyatomic molecules. *New York: Van Nostrand, Reinhold, 1966*, 1966.

[6] Max Born and Robert Oppenheimer. Zur quantentheorie der molekeln. *Ann. Phys. (Berl.)*, 389(20):457–484, 1927.

[7] DR Hartree. The wave mechanics of an atom with a non-coulomb central field. part i. theory and methods. In *Mathematical Proceedings of the Cam-*

bridge Philosophical Society, volume 24, pages 89–110. Cambridge University Press, 1928.

[8] Wolfgang Pauli. Über den zusammenhang des abschlusses der elektronengruppen im atom mit der komplexstruktur der spektren. *Z. Phys.*, 31(1):765–783, 1925.

[9] John C Slater. The theory of complex spectra. *Phys. Rev.*, 34(10):1293, 1929.

[10] John C Slater. Atomic shielding constants. *Phys. Rev.*, 36(1):57, 1930.

[11] S Francis Boys. Electronic wave functions-i. a general method of calculation for the stationary states of any molecular system. *Proc. Math. Phys.*, 200(1063):542–554, 1950.

[12] H Bernhard Schlegel and Michael J Frisch. Transformation between cartesian and pure spherical harmonic gaussians. *Int. J. Quantum Chem.*, 54(2):83–87, 1995.

[13] Wim Klopper and Werner Kutzelnigg. Gaussian basis sets and the nuclear cusp problem. *J. Mol. Struct.: THEOCHEM* , 135:339–356, 1986.

[14] Peter MW Gill. Molecular integrals over gaussian basis functions. *Adv. Quantum Chem.*, 25:141–205, 1994.

[15] Warren J Hehre, Robert F Stewart, and John A Pople. self-consistent molecular-orbital methods. I. use of gaussian expansions of slater-type atomic orbitals. *J. Chem. Phys.*, 51(6):2657–2664, 1969.

[16] WJ Hehre and JA Pople. Self-consistent molecular orbital methods. XIII. an extended gaussian-type basis for boron. *J. Chem. Phys.*, 56(8):4233–4234, 1972.

[17] RBJS Krishnan, J Stephen Binkley, Rolf Seeger, and John A Pople. Self-consistent molecular orbital methods. XX. a basis set for correlated wave functions. *J. Chem. Phys.*, 72(1):650–654, 1980.

[18] Thom H Dunning Jr. Gaussian basis sets for use in correlated molecular calculations. I. the atoms boron through neon and hydrogen. *J. Chem. Phys.*, 90(2):1007–1023, 1989.

[19] David E Woon and Thom H Dunning Jr. Calculation of the electron affinities of the second row atoms: Al−−Cl. *J. Chem. Phys.*, 99(5):3730–3737, 1993.

[20] David E Woon and Thom H Dunning Jr. Gaussian basis sets for use in correlated molecular calculations. IV. calculation of static electrical response properties. *J. Chem. Phys.*, 100(4):2975–2988, 1994.

[21] David E Woon and Thom H Dunning Jr. Gaussian basis sets for use in correlated molecular calculations. V. core-valence basis sets for boron through neon. *J. Chem. Phys.*, 103(11):4572–4585, 1995.

[22] Clemens Carel Johannes Roothaan. New developments in molecular orbital theory. *Rev. Mod. Phys.*, 23(2):69, 1951.

[23] GG Hall. The molecular orbital theory of chemical valency VIII. a method of calculating ionization potentials. *Proc. Math. Phys.*, 205(1083):541–552, 1951.

[24] JA Pople and R_K Nesbet. Self-consistent orbitals for radicals. *J. Chem. Phys.*, 22(3):571–572, 1954.

[25] Per-Olov Löwdin. Correlation problem in many-electron quantum mechanics I. review of different approaches and discussion of some current ideas. *Adv. Chem. Phys.*, pages 207–322, 1958.

[26] JA Pople, R Seeger, and R Krishnan. Variational configuration interaction methods and comparison with perturbation theory. *Int. J. Quantum Chem.*, 12(S11):149–163, 1977.

[27] Rodney J Bartlett and George D Purvis. Many-body perturbation theory, coupled-pair many-electron theory, and the importance of quadruple excitations for the correlation problem. *Int. J. Quantum Chem.*, 14(5):561–581, 1978.

[28] Rodney J Bartlett. Many-body perturbation theory and coupled cluster theory for electron correlation in molecules. *Ann. Rev. Phys. Chem.*, 32(1):359–401, 1981.

[29] Carlos F Bunge. Cracking electron correlation. *Phys. Scr.*, 2005(T120):78, 2005.

[30] Laimutis Bytautas and Klaus Ruedenberg. A priori identification of configurational deadwood. *Chem. Phys.*, 356(1-3):64–75, 2009.

[31] Jiří Čížek. On the correlation problem in atomic and molecular systems. calculation of wavefunction components in ursell-type expansion using quantum-field theoretical methods. *J. Chem. Phys.*, 45(11):4256–4266, 1966.

[32] Jiří Čížek. On the use of the cluster expansion and the technique of diagrams in calculations of correlation effects in atoms and molecules. *Adv. Chem. Phys.*, pages 35–89, 1969.

[33] J Čížek and J Paldus. Correlation problems in atomic and molecular systems iii. rederivation of the coupled-pair many-electron theory using the traditional quantum chemical methodst. *Int. J. Quantum Chem.*, 5(4):359–379, 1971.

[34] George D Purvis III and Rodney J Bartlett. A full coupled-cluster singles and doubles model: The inclusion of disconnected triples. *J. Chem. Phys.*, 76(4):1910–1918, 1982.

[35] Jozef Noga and Rodney J Bartlett. The full CCSDT model for molecular electronic structure. *J. Chem. Phys.*, 86(12):7041–7050, 1987.

[36] Krishnan Raghavachari, Gary W. Trucks, John A. Pople, and Martin Head-Gordon. A fifth-order perturbation comparison of electron correlation theories. *Chemical Physics Letters*, 157(6):479 – 483, 1989.

[37] Jürgen Gauss and John F Stanton. Perturbative treatment of triple excitations in coupled-cluster calculations of nuclear magnetic shielding constants. *J. Chem. Phys.*, 104(7):2574–2583, 1996.

[38] Trygve Helgaker, Jürgen Gauss, Poul Jo/rgensen, and Jeppe Olsen. The prediction of molecular equilibrium structures by the standard electronic wave functions. *J. Chem. Phys.*, 106(15):6430–6440, 1997.

[39] Chr Møller and Milton S Plesset. Note on an approximation treatment for many-electron systems. *Phys. Rev.*, 46(7):618, 1934.

[40] P Hohenberg and WJPR Kohn. Density functional theory (DFT). *Phys. Rev.*, 136:B864, 1964.

[41] Walter Kohn and Lu Jeu Sham. Self-consistent equations including exchange and correlation effects. *Phys. Rev.*, 140(4A):A1133, 1965.

[42] Wolfram Koch and Max C Holthausen. *A chemist's guide to density functional theory*. John Wiley & Sons, 2015.

[43] John P Perdew. Accurate density functional for the energy: Real-space cutoff of the gradient expansion for the exchange hole. *Phys. Rev. Lett.*, 55(16):1665, 1985.

[44] Swapan K Ghosh and Robert G Parr. Phase-space approach to the exchange-energy functional of density-functional theory. *Phys. Rev. A*, 34(2):785, 1986.

[45] Axel D Becke and Marc R Roussel. Exchange holes in inhomogeneous systems: A coordinate-space model. *Phys. Rev. A*, 39(8):3761, 1989.

[46] Axel D Becke. A new mixing of hartree–fock and local density-functional theories. *J. Chem. Phys.*, 98(2):1372–1377, 1993.

[47] James B Foresman, Martin Head-Gordon, John A Pople, and Michael J Frisch. Toward a systematic molecular orbital theory for excited states. *J. Phys. Chem.*, 96(1):135–149, 1992.

[48] EKU Gross and Walter Kohn. Local density-functional theory of frequency-dependent linear response. *Phys. Rev. Lett.*, 55(26):2850, 1985.

[49] Rüdiger Bauernschmitt and Reinhart Ahlrichs. Treatment of electronic excitations within the adiabatic approximation of time dependent density functional theory. *Chem. Phys. Lett.*, 256(4-5):454–464, 1996.

[50] Monika Musiał and Rodney J Bartlett. Charge-transfer separability and size-extensivity in the equation-of-motion coupled cluster method: Eom-ccx. *J. Chem. Phys.*, 134(3):034106, 2011.

[51] Hideo Sekino and Rodney J Bartlett. A linear response, coupled-cluster theory for excitation energy. *Int. J. Quantum Chem.*, 26(S18):255–265, 1984.

[52] H Nakatsuji and K Hirao. Cluster expansion of the wavefunction. symmetry-adapted-cluster expansion, its variational determination, and extension of open-shell orbital theory. *J. Chem. Phys.*, 68(5):2053–2065, 1978.

[53] Henrik Koch, Rika Kobayashi, Alfredo Sanchez de Merás, and Poul Jo/rgensen. Calculation of size-intensive transition moments from the coupled cluster singles and doubles linear response function. *J. Chem. Phys.*, 100(6):4393–4400, 1994.

[54] Benjamin Kaduk, Tim Kowalczyk, and Troy Van Voorhis. Constrained density functional theory. *Chem. Rev.*, 112(1):321–370, 2012.

[55] Antoine Georges, Gabriel Kotliar, Werner Krauth, and Marcelo J Rozenberg. Dynamical mean-field theory of strongly correlated fermion systems and the limit of infinite dimensions. *Rev. Mod. Phys.*, 68(1):13, 1996.

[56] John F Stanton, Jürgen Gauss, Naoto Ishikawa, and Martin Head-Gordon. A comparison of single reference methods for characterizing stationary points of excited state potential energy surfaces. *J. Chem. Phys.*, 103(10):4160–4174, 1995.

[57] So Hirata, Martin Head-Gordon, and Rodney J Bartlett. Configuration interaction singles, time-dependent hartree–fock, and time-dependent density functional theory for the electronic excited states of extended systems. *J. Chem. Phys.*, 111(24):10774–10786, 1999.

[58] Fritz Reiche and Willy Thomas. Über die zahl der dispersionselektronen, die einem stationären zustand zugeordnet sind. *Z. Phys.*, 34(1):510–525, 1925.

[59] Erich Runge and Eberhard KU Gross. Density-functional theory for time-dependent systems. *Phys. Rev. Lett.*, 52(12):997, 1984.

[60] Ig Tamm. Relativistic interaction of elementary particles. In *Selected Papers*, pages 157–174. Springer, 1991.

[61] SM Dancoff. Non-adiabatic meson theory of nuclear forces. *Phys. Rev.*, 78(4):382, 1950.

[62] Andreas Dreuw and Martin Head-Gordon. Single-reference ab initio methods for the calculation of excited states of large molecules. *Chem. Rev.*, 105(11):4009–4037, 2005.

[63] Chi Y Cheng, Matthew S Ryley, Michael JG Peach, David J Tozer, Trygve Helgaker, and Andrew M Teale. Molecular properties in the tamm–dancoff approximation: indirect nuclear spin–spin coupling constants. *Mol. Phys.*, 113(13-14):1937–1951, 2015.

[64] Christine Jamorski, Mark E Casida, and Dennis R Salahub. Dynamic polarizabilities and excitation spectra from a molecular implementation of time-dependent density-functional response theory: N_2 as a case study. *J. Chem. Phys.*, 104(13):5134–5147, 1996.

[65] Rüdiger Bauernschmitt, Marco Häser, Oliver Treutler, and Reinhart Ahlrichs. Calculation of excitation energies within time-dependent density functional theory using auxiliary basis set expansions. *Chem. Phys. Lett.*, 264(6):573–578, 1997.

[66] Maja Parac and Stefan Grimme. Comparison of multireference møller- plesset theory and time-dependent methods for the calculation of vertical excitation energies of molecules. *J. Phys. Chem. A*, 106(29):6844–6850, 2002.

[67] Thomas M Halasinski, Douglas M Hudgins, Farid Salama, Louis J Allamandola, and Thomas Bally. Electronic absorption spectra of neutral pentacene ($C_{22}H_{14}$) and its positive and negative ions in ne, ar, and kr matrices. *J. Phys. Chem. A*, 104(32):7484–7491, 2000.

[68] So Hirata, Timothy J Lee, and Martin Head-Gordon. Time-dependent density functional study on the electronic excitation energies of polycyclic aromatic hydrocarbon radical cations of naphthalene, anthracene, pyrene, and perylene. *J. Chem. Phys.*, 111(19):8904–8912, 1999.

[69] Liang Shen, Hong-Yu Zhang, and Hong-Fang Ji. Successful application of td-dft in transient absorption spectra assignment. *Org. Lett.*, 7(2):243–246, 2005.

[70] Xavier Blase, Ivan Duchemin, and Denis Jacquemin. The bethe–salpeter equation in chemistry: relations with td-dft, applications and challenges. *Chem. Soc. Rev.*, 47(3):1022–1043, 2018.

[71] Yasumitsu Suzuki and Kazuyuki Watanabe. Excitons in two-dimensional atomic layer materials from time-dependent density functional theory: monolayer and bi-layer hexagonal boron nitride and transition-metal dichalcogenides. *Phys. Chem. Chem. Phys.*, 22(5):2908–2916, 2020.

[72] Daniel J Cole and Nicholas DM Hine. Applications of large-scale density functional theory in biology. *J. Phys.: Condens. Matter*, 28(39):393001, 2016.

[73] Zheng-Li Cai, Karina Sendt, and Jeffrey R Reimers. Failure of density-functional theory and time-dependent density-functional theory for large extended π systems. *J. Chem. Phys.*, 117(12):5543–5549, 2002.

[74] Stefan Grimme and Maja Parac. Substantial errors from time-dependent density functional theory for the calculation of excited states of large π systems. *ChemPhysChem*, 4(3):292–295, 2003.

[75] David J Tozer, Roger D Amos, Nicholas C Handy, Bjorn O Roos, and Luis Serrano-Andres. Does density functional theory contribute to the under-

standing of excited states of unsaturated organic compounds? *Mol. Phys.*, 97(7):859–868, 1999.

[76] Andreas Dreuw and Martin Head-Gordon. Failure of time-dependent density functional theory for long-range charge-transfer excited states: the zincbacteriochlorin- bacteriochlorin and bacteriochlorophyll- spheroidene complexes. *J. Am. Chem. Soc.*, 126(12):4007–4016, 2004.

[77] David J Tozer and Nicholas C Handy. Improving virtual Kohn–Sham orbitals and eigenvalues: Application to excitation energies and static polarizabilities. *J. Chem. Phys.*, 109(23):10180–10189, 1998.

[78] Björn O Roos, Peter R Taylor, and Per EM Sigbahn. A complete active space scf method (CASSCF) using a density matrix formulated super-ci approach. *Chem. Phys.*, 48(2):157–173, 1980.

[79] Geerd HF Diercksen, Björn O Roos, and Andrzej J Sadlej. Electron correlation and properties of many-electron systems. *Int. J. Quantum Chem.*, 24(S17):265–288, 1983.

[80] Jeppe Olsen, Björn O Roos, Poul Jo/rgensen, and Hans Jo/rgen Aa Jensen. Determinant based configuration interaction algorithms for complete and restricted configuration interaction spaces. *J. Chem. Phys.*, 89(4):2185–2192, 1988.

[81] Kerstin Andersson, Per Aake Malmqvist, Björn O Roos, Andrzej J Sadlej, and Krzysztof Wolinski. Second-order perturbation theory with a casscf reference function. *J. Phys. Chem.*, 94(14):5483–5488, 1990.

[82] Kerstin Andersson, Per-Åke Malmqvist, and Björn O Roos. Second-order perturbation theory with a complete active space self-consistent field reference function. *J. Chem. Phys.*, 96(2):1218–1226, 1992.

[83] Allen J Bard. Photoelectrochemistry and heterogeneous photo-catalysis at semiconductors. *J. Photochem.*, 10(1):59–75, 1979.

[84] M. Gratzel. Photoelectrochemical cells. *Nature*, 414(6861):338–44, 2001.

[85] George Phani, Gavin Tulloch, David Vittorio, and Igor. Skryabin. Titania solar cells: new photovoltaic technology. *Renewable Energy*, 22(1-3):303–309, 2000.

[86] Michael. Gratzel. Photoelectrochemical cells. *Nature (London, U. K.)*, 414(6861):338–344, 2001.

[87] Kazuko Satake, Ai Katayama, Hideki Ohkoshi, Takeshi Nakahara, and Takashi Takeuchi. Titania NO_x sensors for exhaust monitoring. *Sens. Actuators B Chem.*, 20(2-3):111–117, 1994.

[88] G. K. Mor, Oomman K. Varghese, Maggie Paulose, and Craig A. Grimes. A self-cleaning, room-temperature titania-nanotube hydrogen gas sensor. *Sens. Lett.*, 1(1):42–46, 2003.

[89] Amy L Linsebigler, Guangquan Lu, and John T Yates Jr. Photocatalysis on TiO_2 surfaces: principles, mechanisms, and selected results. *Chem. Rev.*, 95(3):735–758, 1995.

[90] Kazuhito Hashimoto, Hiroshi Irie, and Akira. Fujishima. TiO_2 photocatalysis: A historical overview and future prospects. *Jpn. J. Appl. Phys., Part 1*, 44(12):8269–8285, 2005.

[91] Severin N. Habisreutinger, Lukas Schmidt-Mende, and Jacek K. Stolarczyk. Photocatalytic reduction of CO_2 on TiO_2 and other semiconductors. *Angew. Chem. Int. Ed.*, 52(29):7372–7408, 2013.

[92] Akira Fujishima and Kenichi Honda. Electrochemical photolysis of water at a semiconductor electrode. *Nature*, 238(5358):37–38, 1972.

[93] Allen J Bard. Design of semiconductor photoelectrochemical systems for solar energy conversion. *J. Phys. Chem.*, 86(2):172–177, 1982.

[94] Meng Ni, Michael K. H. Leung, Dennis Y. C. Leung, and K. Sumathy. A review and recent developments in photocatalytic water-splitting using TiO_2

for hydrogen production. *Renewable Sustainable Energy Rev.*, 11(3):401–425, 2006.

[95] Jenny Schneider, Masaya Matsuoka, Masato Takeuchi, Jinlong Zhang, Yu Horiuchi, Masakazu Anpo, and Detlef W. Bahnemann. Understanding TiO_2 photocatalysis: Mechanisms and materials. *Chem. Rev.*, 114(19):9919–9986, 2014.

[96] Michael A. Henderson. The interaction of water with solid surfaces: fundamental aspects revisited. *Surf. Sci. Rep.*, 46(1-8):1–308, 2002.

[97] Ulrike. Diebold. Perspective: A controversial benchmark system for water-oxide interfaces: $H_2O/TiO_2(110)$. *J. Chem. Phys.*, 147(4):040901/1–040901/3, 2017.

[98] Rentao Mu, Zhi-jian Zhao, Zdenek Dohnalek, and Jinlong. Gong. Structural motifs of water on metal oxide surfaces. *Chem. Soc. Rev.*, 46(7):1785–1806, 2017.

[99] Michael A Henderson. The influence of oxide surface structure on adsorbate chemistry: desorption of water from the smooth, the microfaceted and the ion sputtered surfaces of TiO_2 (100). *Surf. Sci.*, 319(3):315–328, 1994.

[100] Thomas Bredow and Karl Jug. Theoretical investigation of water adsorption at rutile and anatase surfaces. *Surf. Sci.*, 327(3):398–408, 1995.

[101] Michael A Henderson. Structural sensitivity in the dissociation of water on TiO_2 single-crystal surfaces. *Langmuir*, 12(21):5093–5098, 1996.

[102] David Brinkley, Michelle Dietrich, Thomas Engel, Paul Farrall, Gerhard Gantner, Adam Schafer, and Amy Szuchmacher. A modulated molecular beam study of the extent of H_2O dissociation on TiO_2 (110). *Surf. Sci.*, 395(2-3):292–306, 1998.

[103] G. S. Herman, Z. Dohnalek, N. Ruzycki, and U. Diebold. Experimental investigation of the interaction of water and methanol with anatase-TiO_2(101). *J. Phys. Chem. B*, 107(12):2788–2795, 2003.

[104] Masato Takeuchi, Gianmario Martra, Salvatore Coluccia, and Masakazu. Anpo. Investigations of the structure of h2o clusters adsorbed on TiO_2 surfaces by near-infrared absorption spectroscopy. *J. Phys. Chem. B*, 109(15):7387–7391, 2005.

[105] Shijing Tan, Hao Feng, Yongfei Ji, Yang Wang, Jin Zhao, Aidi Zhao, Bing Wang, Yi Luo, Jinlong Yang, and J. G. Hou. Observation of photocatalytic dissociation of water on terminal Ti sites of TiO_2^-(110) $\times$ 1 surface. *J. Am. Chem. Soc.*, 134(24):9978–9985, 2012.

[106] L. E. Walle, A. Borg, E. M. J. Johansson, S. Plogmaker, H. Rensmo, P. Uvdal, and A. Sandell. Mixed dissociative and molecular water adsorption on anatase TiO_2(101). *J. Phys. Chem. C*, 115(19):9545–9550, 2011.

[107] Zhenhua Geng, Xiao Chen, Wenshao Yang, Qing Guo, Chenbiao Xu, Dongxu Dai, and Xueming. Yang. Highly efficient water dissociation on anatase TiO_2(101). *J. Phys. Chem. C*, 120(47):26807–26813, 2016.

[108] HH Kristoffersen, JØ Hansen, U Martinez, YY Wei, J Matthiesen, R Streber, Ralf Bechstein, E Lægsgaard, F Besenbacher, B Hammer, et al. Role of steps in the dissociative adsorption of water on rutile TiO_2 (110). *Phys. Rev. Lett.*, 110(14):146101, 2013.

[109] P. C. Redfern, P. Zapol, L. A. Curtiss, T. Rajh, and M. C. Thurnauer. Computational studies of catechol and water interactions with titanium oxide nanoparticles. *J. Phys. Chem. B*, 107(41):11419–11427, 2003.

[110] Ting Zheng, Chunya Wu, Mingjun Chen, Yu Zhang, and Peter T. Cummings. DFT study of water adsorption on rutile TiO_2 (110) surface: Effects of surface steps. *J. Chem. Phys.*, 145(4):044702/1–044702/8, 2016.

[111] Richard L Kurtz, Roger Stock-Bauer, Theodore E Msdey, Elisa Román, and JoséL De Segovia. Synchrotron radiation studies of h2o adsorption on TiO_2 (110). *Surf. Sci.*, 218(1):178–200, 1989.

[112] Markus B Hugenschmidt, Lara Gamble, and Charles T Campbell. The interaction of H_2O with a TiO_2 (110) surface. *Surf. Sci.*, 302(3):329–340, 1994.

[113] L-Q Wang, Kim F Ferris, PX Skiba, Ashley N Shultz, Donald R Baer, and Mark H Engelhard. Interactions of liquid and vapor water with stoichiometric and defective TiO_2(100) surfaces. *Surf. Sci.*, 440(1-2):60–68, 1999.

[114] Renald Schaub, Peter Thostrup, Nuria Lopez, Erik Lægsgaard, Ivan Stensgaard, Jens Kehlet Nørskov, and Flemming Besenbacher. Oxygen vacancies as active sites for water dissociation on rutile TiO_2 (110). *Phys. Rev. Lett.*, 87(26):266104, 2001.

[115] S. Wendt, R. Schaub, J. Matthiesen, E. K. Vestergaard, E. Wahlstroem, M. D. Rasmussen, P. Thostrup, L. M. Molina, E. Laegsgaard, I. Stensgaard, B. Hammer, and F. Besenbacher. Oxygen vacancies on TiO_2(110) and their interaction with H_2O and O_2: A combined high-resolution STM and DFT study. *Surf. Sci.*, 598(1-3):226–245, 2005.

[116] Oier Bikondoa, Chi L. Pang, Roslinda Ithnin, Christopher A. Muryn, Hiroshi Onishi, and Geoff. Thornton. Direct visualization of defect-mediated dissociation of water on TiO_2(110). *Nat. Mater.*, 5(3):189–192, 2006.

[117] Z. Zhang, O. Bondarchuk, Bruce D. Kay, J. M. White, and Z. Dohnalek. Imaging water dissociation on TiO_2(110): Evidence for inequivalent geminate oh groups. *J. Phys. Chem. B*, 110(43):21840–21845, 2006.

[118] Masakazu Anpo, Takahito Shima, Sukeya Kodama, and Yutaka Kubokawa. Photocatalytic hydrogenation of propyne with water on small-particle titania: size quantization effects and reaction intermediates. *J. Phys. Chem.*, 91(16):4305–4310, 1987.

[119] Hua-Jin Zhai and Lai-Sheng. Wang. Probing the electronic structure of early transition metal oxide clusters: Molecular models towards mechanistic insights into oxide surfaces and catalysis. *Chem. Phys. Lett.*, 500(4-6):185–195, 2010.

[120] A. W. Castleman Jr. Cluster structure and reactions: Gaining insights into catalytic processes. *Catal. Lett.*, 141(9):1243–1253, 2011.

[121] Sandra M. Lang and Thorsten M. Bernhardt. Gas phase metal cluster model systems for heterogeneous catalysis. *Phys. Chem. Chem. Phys.*, 14(26):9255–9269, 2012.

[122] Enrico Berardo and Martijn A. Zwijnenburg. Modeling the water splitting activity of a TiO_2 rutile nanoparticle. *J. Phys. Chem. C*, 119(24):13384–13393, 2015.

[123] ME Geusic, MD Morse, SC O'brien, and RE Smalley. Surface reactions of metal clusters i: The fast flow cluster reactor. *Rev. Sci. Instrum.*, 56(11):2123–2130, 1985.

[124] Raghunath O. Ramabhadran, Jennifer E. Mann, Sarah E. Waller, David W. Rothgeb, Caroline C. Jarrold, and Krishnan. Raghavachari. New insights on photocatalytic H_2 liberation from water using transition-metal oxides: Lessons from cluster models of molybdenum and tungsten oxides. *J. Am. Chem. Soc.*, 135(45):17039–17051, 2013.

[125] Matias R. Fagiani, Xiaowei Song, Sreekanta Debnath, Sandy Gewinner, Wieland Schoellkopf, Knut R. Asmis, Florian A. Bischoff, Fabian Mueller, and Joachim. Sauer. Dissociative water adsorption by $Al_3O_4^+$ in the gas phase. *J. Phys. Chem. Lett.*, 8(6):1272–1277, 2017.

[126] Hongbin Wu and Lai-Sheng Wang. Electronic structure of titanium oxide clusters: TiOy (y= 1- 3) and (TiO_2)n (n= 1- 4). *J. Chem. Phys.*, 107(20):8221–8228, 1997.

[127] Hua-Jin Zhai and Lai-Sheng. Wang. Probing the electronic structure and band gap evolution of titanium oxide clusters $(TiO_2)n^-$ (n = 1-10) using photoelectron spectroscopy. *J. Am. Chem. Soc.*, 129(10):3022–3026, 2007.

[128] Jongjin B. Kim, Marissa L. Weichman, and Daniel M. Neumark. High-resolution anion photoelectron spectra of TiO_2^-, ZrO_2^-, and HfO_2^- ob-

tained by slow electron velocity-map imaging. *Phys. Chem. Chem. Phys.*, 15(48):20973–20981, 2013.

[129] Jongjin B. Kim, Marissa L. Weichman, and Daniel M. Neumark. Structural isomers of Ti_2O_4 and Zr_2O_4 anions identified by slow photoelectron velocity-map imaging spectroscopy. *J. Am. Chem. Soc.*, 136(19):7159–7168, 2014.

[130] Gustavo E Scuseria, Curtis L Janssen, and Henry F Schaefer Iii. An efficient reformulation of the closed-shell coupled cluster single and double excitation (CCSD) equations. *J. Chem. Phys.*, 89(12):7382–7387, 1988.

[131] Seymour H Vosko, Leslie Wilk, and Marwan Nusair. Accurate spin-dependent electron liquid correlation energies for local spin density calculations: a critical analysis. *Can. J. Phys.*, 58(8):1200–1211, 1980.

[132] Chengteh Lee, Weitao Yang, and Robert G Parr. Development of the colle-salvetti correlation-energy formula into a functional of the electron density. *Phys. Rev. B*, 37(2):785, 1988.

[133] Axel D Becke. Becke's three parameter hybrid method using the LYP correlation functional. *J. Chem. Phys.*, 98(492):5648–5652, 1993.

[134] Philip J Stephens, Frank J Devlin, Cary F Chabalowski, and Michael J Frisch. Ab initio calculation of vibrational absorption and circular dichroism spectra using density functional force fields. *J. Phys. Chem.*, 98(45):11623–11627, 1994.

[135] Florian Weigend and Reinhart. Ahlrichs. Balanced basis sets of split valence, triple zeta valence and quadruple zeta valence quality for h to rn: Design and assessment of accuracy. *Phys. Chem. Chem. Phys.*, 7(18):3297–3305, 2005.

[136] Mark E Casida, Christine Jamorski, Kim C Casida, and Dennis R Salahub. Molecular excitation energies to high-lying bound states from time-dependent density-functional response theory: Characterization and correction of the time-dependent local density approximation ionization threshold. *J. Chem. Phys.*, 108(11):4439–4449, 1998.

[137] R Eric Stratmann, Gustavo E Scuseria, and Michael J Frisch. An efficient implementation of time-dependent density-functional theory for the calculation of excitation energies of large molecules. *J. Chem. Phys.*, 109(19):8218–8224, 1998.

[138] Richard L. Martin. Natural transition orbitals. *J. Chem. Phys.*, 118(11):4775–4777, 2003.

[139] M. J. Frisch, G. W. Trucks, H. B. Schlegel, G. E. Scuseria, M. A. Robb, J. R. Cheeseman, G. Scalmani, V. Barone, G. A. Petersson, H. Nakatsuji, X. Li, M. Caricato, A. Marenich, J. Bloino, B. G. Janesko, R. Gomperts, B. Mennucci, H. P. Hratchian, J. V. Ortiz, A. F. Izmaylov, J. L. Sonnenberg, D. Williams-Young, F. Ding, F. Lipparini, F. Egidi, J. Goings, B. Peng, A. Petrone, T. Henderson, D. Ranasinghe, V. G. Zakrzewski, J. Gao, N. Rega, G. Zheng, W. Liang, M. Hada, M. Ehara, K. Toyota, R. Fukuda, J. Hasegawa, M. Ishida, T. Nakajima, Y. Honda, O. Kitao, H. Nakai, T. Vreven, K. Throssell, J. A. Montgomery, Jr., J. E. Peralta, F. Ogliaro, M. Bearpark, J. J. Heyd, E. Brothers, K. N. Kudin, V. N. Staroverov, T. Keith, R. Kobayashi, J. Normand, K. Raghavachari, A. Rendell, J. C. Burant, S. S. Iyengar, J. Tomasi, M. Cossi, J. M. Millam, M. Klene, C. Adamo, R. Cammi, J. W. Ochterski, R. L. Martin, K. Morokuma, O. Farkas, J. B. Foresman, , and D. J. Fox. Gaussian development version Revision I.09, 2016.

[140] Rolf Seeger and John A Pople. Self-consistent molecular orbital methods. XVIII. constraints and stability in hartree–fock theory. *J. Chem. Phys.*, 66(7):3045–3050, 1977.

[141] HP Hratchian and HB Schlegel. Theory and applications of computational chemistry: The first 40 years. *Dykstra, CE*, 195, 2005.

[142] Fabrizio Santoro, Alessandro Lami, Roberto Improta, and Vincenzo. Barone. Effective method to compute vibrationally resolved optical spectra of

large molecules at finite temperature in the gas phase and in solution. *J. Chem. Phys.*, 126(18):184102/1–184102/11, 2007.

[143] Yuan Liu and Chuangang. Ning. Calculation of photodetachment cross sections and photoelectron angular distributions of negative ions using density functional theory. *J. Chem. Phys.*, 143(14):144310/1–144310/9, 2015.

[144] Michael A. Duncan. Invited review article: Laser vaporization cluster sources. *Rev. Sci. Instrum.*, 83(4):041101/1–041101/19, 2012.

[145] Jongjin B. Kim, Christian Hock, Tara I. Yacovitch, and Daniel M. Neumark. Slow photoelectron velocity-map imaging spectroscopy of cold thiozonide (S_3^-). *J. Phys. Chem. A*, 117(34):8126–8131, 2013.

[146] Nikhil Avinash Patil and Balasubramanian Kandasubramanian. Biological and mechanical enhancement of zirconium dioxide for medical applications. *Ceram. Int.*, 2019.

[147] Lukas Hingsammer, Markus Grillenberger, Martin Schagerl, Michael Malek, and Stefan Hunger. Biomechanical testing of zirconium dioxide osteosynthesis system for Le fort i advancement osteotomy fixation. *J. Mech. Behav. Biomed. Mater.*, 77:34–39, 2018.

[148] Tse-Wei Chen, Airathevar Sivasamy Vasantha, Shen-Ming Chen, Dunia A Al Farraj, Mohamed Soliman Elshikh, Roua M Alkufeidy, and Manal M Al Khulaifi. Sonochemical synthesis and fabrication of honeycomb like zirconium dioxide with chitosan modified electrode for sensitive electrochemical determination of anti-tuberculosis (tb) drug. *Ultrason. Sonochem.*, 59:104718, 2019.

[149] Petri Sjoholm, Derek b Ingham, Matti Lehtimaki, Leena Perttu-Roiha, Howard Goodfellow, and Heikki Torvela. Gas-cleaning technology. In *Industrial Ventilation Design Guidebook*, pages 1197–1316. Elsevier, 2001.

[150] Steffen Dudczig, Dániel Veres, Christos G Aneziris, Erik Skiera, and Rolf W Steinbrech. Nano-and micrometre additions of SiO_2, ZrO_2 and TiO_2 in

fine grained alumina refractory ceramics for improved thermal shock performance. *Ceram. Int.*, 38(3):2011–2019, 2012.

[151] Christos G Aneziris, Steffen Dudczig, Nora Gerlach, Harry Berek, and Daniel Veres. Thermal shock performance of fine grained al2o3 ceramics with TiO_2 and ZrO_2 additions for refractory applications. *Adv. Eng. Mater.*, 12(6):478–485, 2010.

[152] Victor E Henrich and Paul Anthony Cox. *The surface science of metal oxides*. Cambridge university press, 1996.

[153] I Shishkovsky, I Yadroitsev, Ph Bertrand, and I Smurov. Alumina–zirconium ceramics synthesis by selective laser sintering/melting. *Appl. Surf. Sci.*, 254(4):966–970, 2007.

[154] Larry L Fehrenbacher. Stabilized zirconium dioxide and hafnium dioxide compositions, January 11 1972.

[155] Georgy A Gogotsi. Deformational behaviour of ceramics. *J. Eur. Ceram. Soc.*, 7(2):87–92, 1991.

[156] Hans-Günther Lintz and Costas Georgios Vayenas. Solid ion conductors in heterogeneous catalysis. *Angew. Chem. Int. Ed. Engl.*, 28(6):708–715, 1989.

[157] Edward F Sverdrup, Albert D Glasser, and David H Archer. Fuel cell comprising a stabilized zirconium oxide electrolyte and a doped indium or tin oxide cathode, 1971.

[158] Charlotte Froese Fischer. *Hartree–Fock method for atoms. A numerical approach*. John Wiley and Sons, Inc., New York, 1977.

[159] A Boudghene Stambouli and E Traversa. Solid oxide fuel cells (SOFCs): a review of an environmentally clean and efficient source of energy. *Renewable Sustainable Energy Rev.*, 6(5):433–455, 2002.

[160] Alessandro Iannaci, Tommy Pepè Sciarria, Barbara Mecheri, Fabrizio Adani, Silvia Licoccia, and Alessandra D'Epifanio. Power generation using a low-cost sulfated zirconium oxide based cathode in single chamber microbial fuel cells. *J. Alloys Compd.*, 693:170–176, 2017.

[161] K Sayama and H Arakawa. Photocatalytic decomposition of water and photocatalytic reduction of carbon dioxide over zirconia catalyst. *J. Phys. Chem.*, 97(3):531–533, 1993.

[162] Lingling Yang, Han Zhou, Tongxiang Fan, and Di Zhang. *Semiconductor photocatalysts for water oxidation: current status and challenges*, volume 16. Royal Society of Chemistry, 2014.

[163] Martin Muhler, Robert Schlögl, and Gerhard Ertl. The nature of the iron oxide-based catalyst for dehydrogenation of ethylbenzene to styrene 2. surface chemistry of the active phase. *J. Catal.*, 138(2):413–444, 1992.

[164] Nicola H Perry and Tatsumi Ishihara. Roles of bulk and surface chemistry in the oxygen exchange kinetics and related properties of mixed conducting perovskite oxide electrodes. *Materials*, 9(10):858, 2016.

[165] Fazila Seker, Kathleen Meeker, Thomas F Kuech, and Arthur B Ellis. Surface chemistry of prototypical bulk II- VI and III- V semiconductors and implications for chemical sensing. *Chem. Rev.*, 100(7):2505–2536, 2000.

[166] H Darmstadt, L Sümmchen, J-M Ting, U Roland, S Kaliaguine, and C Roy. Effects of surface treatment on the bulk chemistry and structure of vapor grown carbon fibers. *Carbon*, 35(10-11):1581–1585, 1997.

[167] Hind A Al-Abadleh. Review of the bulk and surface chemistry of iron in atmospherically relevant systems containing humic-like substances. *RSC Adv.*, 5(57):45785–45811, 2015.

[168] JA Marcos, RH Buitrago, and EA Lombardo. Surface chemistry and catalytic activity of La_1−y $MyCoO_3$ perovskite (m= Sr or Th): 1. bulk and surface reduction studies. *J. Catal.*, 105(1):95–106, 1987.

[169] W Prellier, MP Singh, and P Murugavel. The single-phase multiferroic oxides: from bulk to thin film. *J. Phys.: Condens. Matter*, 17(30):R803, 2005.

[170] Zhongnan Xu and John R Kitchin. Relationships between the surface electronic and chemical properties of doped 4d and 5d late transition metal dioxides. *J. Chem. Phys.*, 142(10):104703, 2015.

[171] Jean Horkans and MW Shafer. An investigation of the electrochemistry of a series of metal dioxides with rutile-type structure: MoO_2, WO_2, ReO_2, RuO_2, OsO_2, and IrO_2. *J. Electrochem. Soc.*, 124(8):1202–1207, 1977.

[172] Yan Tang, Shu Zhao, Bo Long, Jin-Cheng Liu, and Jun Li. On the nature of support effects of metal dioxides MO_2 (m= Ti, Zr, Hf, Ce, Th) in single-atom gold catalysts: Importance of quantum primogenic effect. *J. Phys. Chem. C*, 120(31):17514–17526, 2016.

[173] Harold H Kung. *Transition metal oxides: surface chemistry and catalysis*, volume 45. Elsevier, 1989.

[174] G Busca and V Lorenzelli. Infrared spectroscopic identification of species arising from reactive adsorption of carbon oxides on metal oxide surfaces. *Mater. Chem.*, 7(1):89–126, 1982.

[175] Victor E Henrich and PA Cox. Fundamentals of gas-surface interactions on metal oxides. *Appl. Surf. Sci.*, 72(4):277–284, 1993.

[176] M Calatayud, A Markovits, M Menetrey, B Mguig, and C Minot. Adsorption on perfect and reduced surfaces of metal oxides. *Catal. Today*, 85(2-4):125–143, 2003.

[177] Marco Daturi, Claude Binet, Serafin Bernal, José A Pérez Omil, and Jean Claude Lavalley. FTIR study of defects produced in ZrO_2 samples by thermal treatment residual species into cavities and surface defects. *J. Chem. Soc., Faraday Trans.*, 94(8):1143–1147, 1998.

[178] GK Chuah and S Jaenicke. The preparation of high surface area zirconia—influence of precipitating agent and digestion. *Appl. Catal., A*, 163(1-2):261–273, 1997.

[179] Xin Xia, Richard Oldman, and Richard Catlow. Computational modeling study of bulk and surface of yttria-stabilized cubic zirconia. *Chem. Mater.*, 21(15):3576–3585, 2009.

[180] G Haas, A Menck, H Brune, JV Barth, JA Venables, and K Kern. Nucleation and growth of supported clusters at defect sites: Pd/MgO (001). *Phys. Rev. B*, 61(16):11105, 2000.

[181] KR Heim, ST Coyle, GG Hembree, JA Venables, and MR Scheinfein. Growth of nanometer-size metallic particles on CaF_2 (111). *J. Appl. Phys.*, 80(2):1161–1170, 1996.

[182] John A Venables. Nucleation growth and pattern formation in heteroepitaxy. *Phys. A (Amsterdam, Neth.)*, 239(1-3):35–46, 1997.

[183] G Fahsold, A Pucci, and K-H Rieder. Growth of fe on MgO (001) studied by He-atom scattering. *Phys. Rev. B*, 61(12):8475, 2000.

[184] Edward I Solomon, Paul M Jones, and Jennifer A May. Electronic structures of active sites on metal oxide surfaces: definition of the copper-zinc oxide methanol synthesis catalyst by photoelectron spectroscopy. *Chem. Rev.*, 93(8):2623–2644, 1993.

[185] Hiroyoshi Yamamoto, Nobuyuki Watanabe, Akihide Wada, Kazunari Domen, and Chiaki Hirose. Adsorption and decomposition of formic acid on MgO (001) surface as investigated by temperature programmed desorption and sum-frequency generation spectroscopy: Recurrence induced defect sites. *J. Chem. Phys.*, 106(11):4734–4744, 1997.

[186] Zili Wu, Meijun Li, Jane Howe, Harry M Meyer III, and Steven H Overbury. Probing defect sites on CeO_2 nanocrystals with well-defined surface planes

by raman spectroscopy and o2 adsorption. *Langmuir*, 26(21):16595–16606, 2010.

[187] Michael J Borda, Alicia R Elsetinow, Daniel R Strongin, and Martin A Schoonen. A mechanism for the production of hydroxyl radical at surface defect sites on pyrite. *Geochim. Cosmochim. Acta*, 67(5):935–939, 2003.

[188] Jérôme Joubert, Alain Salameh, Vincent Krakoviack, Françoise Delbecq, Philippe Sautet, Christophe Copéret, and Jean Marie Basset. Heterolytic splitting of H_2 and CH_4 on γ-alumina as a structural probe for defect sites. *J. Phys. Chem. B*, 110(47):23944–23950, 2006.

[189] Hua-Jin Zhai and Lai-Sheng Wang. Probing the electronic structure of early transition metal oxide clusters: Molecular models towards mechanistic insights into oxide surfaces and catalysis. *Chem. Phys. Lett.*, 500(4):185 – 195, 2010.

[190] A.W. Castleman. Cluster structure and reactions: Gaining insights into catalytic processes. *Catal. Lett.*, 141(1243):1243, 2011.

[191] Raghunath O Ramabhadran, Jennifer E Mann, Sarah E Waller, David W Rothgeb, Caroline C Jarrold, and Krishnan Raghavachari. New insights on photocatalytic H_2 liberation from water using transition-metal oxides: lessons from cluster models of molybdenum and tungsten oxides. *J. Am. Chem. Soc.*, 135(45):17039–17051, 2013.

[192] Matias R Fagiani, Xiaowei Song, Sreekanta Debnath, Sandy Gewinner, Wieland Schöllkopf, Knut R Asmis, Florian A Bischoff, Fabian Müller, and Joachim Sauer. Dissociative water adsorption by $Al_3O_4^+$ in the gas phase. *J. Phys. Chem. Lett.*, 8(6):1272–1277, 2017.

[193] Krishnan Raghavachari and Mathew D Halls. Quantum chemical studies of semiconductor surface chemistry using cluster models. *Mol. Phys.*, 102(4):381–393, 2004.

[194] Jennifer E Mann, Nicholas J Mayhall, and Caroline Chick Jarrold. Properties of metal oxide clusters in non-traditional oxidation states. *Chem. Phys. Lett.*, 525:1–12, 2012.

[195] Jarrett L Mason, Hassan Harb, Josey E Topolski, Hrant P Hratchian, and Caroline Chick Jarrold. Exceptionally complex electronic structures of lanthanide oxides and small molecules. *Acc. Chem. Res.*, 52(11):3265–3273, 2019.

[196] Geng Zhang, Hideshi Hattori, and Kozo Tanabe. Aldol addition of acetone, catalyzed by solid base catalysts: magnesium oxide, calcium oxide, strontium oxide, barium oxide, lanthanum (III) oxide and zirconium oxide. *Appl. Catal.*, 36:189–197, 1988.

[197] Saadet Saglam Atsu, Mehmet A Kilicarslan, H Cenker Kucukesmen, and P Sema Aka. Effect of zirconium-oxide ceramic surface treatments on the bond strength to adhesive resin. *J. Prosthet. Dent.*, 95(6):430–436, 2006.

[198] Yasuko Nakano, Tokio Iizuka, Hideshi Hattori, and Kozo Tanabe. Surface properties of zirconium oxide and its catalytic activity for isomerization of 1-butene. *J. Catal.*, 57(1):1–10, 1979.

[199] Dennis M Hausmann and Roy G Gordon. Surface morphology and crystallinity control in the atomic layer deposition (ALD) of hafnium and zirconium oxide thin films. *J. Cryst. Growth*, 249(1-2):251–261, 2003.

[200] B Bachiller-Baeza, I Rodriguez-Ramos, and A Guerrero-Ruiz. Interaction of carbon dioxide with the surface of zirconia polymorphs. *Langmuir*, 14(13):3556–3564, 1998.

[201] A Hess and E Kemnitz. Surface acidity and catalytic behavior of modified zirconium and titanium dioxides. *Appl. Catal., A*, 149(2):373–389, 1997.

[202] Ren-Zhong Li, Hong-Guang Xu, Guo-Jin Cao, Xi-Ling Xu, and Wei-Jun Zheng. Interaction of TiO_2^- with water: Photoelectron spectroscopy and density functional calculations. *J. Chem. Phys.*, 139(18):184303, 2013.

[203] Hong-Guang Xu, Xiao-Na Li, Xiang-Yu Kong, Sheng-Gui He, and Wei-Jun Zheng. Interaction of TiO^+ with water: infrared photodissociation spectroscopy and density functional calculations. *Phys. Chem. Chem. Phys.*, 15(40):17126–17133, 2013.

[204] Marissa L Weichman, Sreekanta Debnath, John T Kelly, Sandy Gewinner, Wieland Schöllkopf, Daniel M Neumark, and Knut R Asmis. Dissociative water adsorption on gas-phase titanium dioxide cluster anions probed with infrared photodissociation spectroscopy. *Top. Catal.*, 61(1-2):92–105, 2018.

[205] Jessalyn A DeVine, Ali Abou Taka, Mark C Babin, Marissa L Weichman, Hrant P Hratchian, and Daniel M Neumark. High-resolution photoelectron spectroscopy of $TiO_3H_2^-$: Probing the TiO_2^-+ H_2O dissociative adduct. *J. Chem. Phys.*, 148(22):222810, 2018.

[206] Xiao-Nan Wu, Jia-Bi Ma, Bo Xu, Yan-Xia Zhao, Xun-Lei Ding, and Sheng-Gui He. Collision-induced dissociation and density functional theory studies of CO adsorption over zirconium oxide cluster ions: Oxidative and nonoxidative adsorption. *J. Phys. Chem. A*, 115(21):5238–5246, 2011.

[207] Yan-Xia Zhao, Xun-Lei Ding, Yan-Ping Ma, Zhe-Chen Wang, and Sheng-Gui He. Transition metal oxide clusters with character of oxygen-centered radical: a DFT study. *Theor. Chem. Acc.*, 127(5-6):449–465, 2010.

[208] Jia-bi Ma, Xiao-nan Wu, Yan-xia Zhao, Xun-lei Ding, and Sheng-gui He. Experimental and theoretical study of hydrogen atom abstraction from C_2H_6 and C_4H_{10} by zirconium oxide clusters anions. *Chin. J. Chem. Phys.*, 23(2):133, 2013.

[209] Jia-Bi Ma, Bo Xu, Jing-Heng Meng, Xiao-Nan Wu, Xun-Lei Ding, Xiao-Na Li, and Sheng-Gui He. Reactivity of atomic oxygen radical anions bound to titania and zirconia nanoparticles in the gas phase: low-temperature oxidation of carbon monoxide. *J. Am. Chem. Soc.*, 135(8):2991–2998, 2013.

[210] Xiao-nan Wu, Yan-xia Zhao, Sheng-gui He, and Xun-lei Ding. Experimental and theoretical study of hydrogen atom abstraction from ethylene by stoichiometric zirconium oxide clusters. *Chin. J. Chem. Phys.*, 22(6):635, 2013.

[211] Johannes Kreutzer, Peter Blaha, and Ulrich Schubert. Assessment of different basis sets and dft functionals for the calculation of structural parameters, vibrational modes and ligand binding energies of Zr_4O_2 (carboxylate) 12 clusters. *Comput. Theor. Chem.*, 1084:162–168, 2016.

[212] Kazuhiro Sayama and Hironori Arakawa. Effect of carbonate addition on the photocatalytic decomposition of liquid water over a ZrO_2 catalyst. *J. Photochem. Photobiol., A*, 94(1):67–76, 1996.

[213] Juan Li, Junli Chen, Wei Song, Junlong Liu, and Wenjie Shen. Influence of zirconia crystal phase on the catalytic performance of Au/ZrO_2 catalysts for low-temperature water gas shift reaction. *Appl. Catal., A*, 334(1-2):321–329, 2008.

[214] Sahar Zinatloo-Ajabshir and Masoud Salavati-Niasari. Facile route to synthesize zirconium dioxide (ZrO_2) nanostructures: structural, optical and photocatalytic studies. *J. Mol. Liq.*, 216:545–551, 2016.

[215] Hadi Fallah Moafi, Abdollah Fallah Shojaie, and Mohammad Ali Zanjanchi. The comparison of photocatalytic activity of synthesized TiO_2 and ZrO_2 nanosize onto wool fibers. *Appl. Surf. Sci.*, 256(13):4310–4316, 2010.

[216] PA Agron, EL Fuller Jr, and HF Holmes. IR studies of water sorption on ZrO_2 polymorphs. I. *J. Colloid Interface Sci.*, 52(3):553–561, 1975.

[217] Witold Piskorz, Joanna Gryboś, Filip Zasada, Piotr Zapała, Sylvain Cristol, Jean-Françios Paul, and Zbigniew Sojka. Periodic dft study of the tetragonal ZrO_2 nanocrystals: equilibrium morphology modeling and atomistic surface hydration thermodynamics. *J. Phys. Chem. C*, 116(36):19307–19320, 2012.

[218] Mekhrdod Subhoni, Kholmirzo Kholmurodov, Aleksandr Doroshkevich, Elmar Asgerov, Tomoyuki Yamamoto, Andrei Lyubchyk, Valer Almasan, and Afag Madadzada. Density functional theory calculations of the water interactions with ZrO_2 nanoparticles Y_2O_3 doped. In *Journal of Physics: Conference Series*, volume 994, page 012013. IOP Publishing, 2018.

[219] Claudio M Lousada, Adam Johannes Johansson, Tore Brinck, and Mats Jonsson. Reactivity of metal oxide clusters with hydrogen peroxide and water–a DFT study evaluating the performance of different exchange–correlation functionals. *Phys. Chem. Chem. Phys.*, 15(15):5539–5552, 2013.

[220] Sergey V Ushakov and Alexandra Navrotsky. Direct measurements of water adsorption enthalpy on hafnia and zirconia. *Appl. Phys. Lett.*, 87(16):164103, 2005.

[221] Weijun Zheng, Kit H Bowen, Jun Li, Iwona Dabkowska, and Maciej Gutowski. Electronic structure differences in ZrO_2 vs HfO_2. *J. Phys. Chem. A*, 109(50):11521–11525, 2005.

[222] Jongjin B Kim, Marissa L Weichman, and Daniel M Neumark. Structural isomers of Ti_2O_4 and Zr_2O_4 anions identified by slow photoelectron velocity-map imaging spectroscopy. *J. Am. Chem. Soc.*, 136(19):7159–7168, 2014.

[223] Jongjin B Kim, Marissa L Weichman, and Daniel M Neumark. High-resolution anion photoelectron spectra of TiO_2^-, ZrO_2^-, and HfO_2^- obtained by slow electron velocity-map imaging. *Phys. Chem. Chem. Phys.*, 15(48):20973–20981, 2013.

[224] George V. Chertihin and Lester Andrews. Reactions of laser ablated titanium, zirconium, and hafnium atoms with oxygen molecules in condensing argon. *J. Phys. Chem. C*, 99(17):6356–6366, 1995.

[225] Dale J. Brugh, Richard D. Suenram, and Walter J. Stevens. Fourier transform microwave spectroscopy of jet-cooled ZrO_2 produced by laser vaporization. *J. Chem. Phys.*, 111(8):3526–3535, 1999.

[226] Anh Le, Timothy C. Steimle, Varun Gupta, Corey A. Rice, John P. Maier, Sheng H. Lin, and Chih-Kai Lin. The visible spectrum of zirconium dioxide, zro2. *J. Chem. Phys.*, 135(10):104303, 2011.

[227] Shenggang Li and David A Dixon. Molecular structures and energetics of the (ZrO_2)n and (HfO_2)n (n= 1- 4) clusters and their anions. *J. Phys. Chem. A*, 114(7):2665–2683, 2010.

[228] S. M. Woodley, S. Hamad, J. A. Mejías, and C. R. A. Catlow. Properties of small tio2, zro2 and hfo2 nanoparticles. *J. Mater. Chem.*, 16:1927–1933, 2006.

[229] Martin Kaupp. On the relation between π bonding, electronegativity, and bond angles in high-valent transition metal complexes. *Chem. Eur. J.*, 5(12):3631–3643, 1999.

[230] Daniel K. W. Mok, Foo-tim Chau, John M. Dyke, and Edmond P. F. Lee. A combined ab initio and franck–condon simulation study of the photodetachment spectrum of zro2-. *Chem. Phys. Lett.*, 458(1):11 – 14, 2008.

[231] Zongtang Fang, Matthew D Outlaw, Kyle K Smith, Natalie W Gist, Shenggang Li, David A Dixon, and James L Gole. Computational study of the hydrolysis reactions of small MO_2 (m= Zr and Hf) nanoclusters with water. *J. Phys. Chem. C*, 116(15):8475–8492, 2012.

[232] Mingyang Chen, Tjerk P. Straatsma, and David A. Dixon. Molecular and dissociative adsorption of water on (TiO_2)n clusters, n = 1–4. *J. Phys. Chem. A*, 119(46):11406–11421, 2015.

[233] Chengteh Lee, Weitao Yang, and Robert G Parr. Development of the colle-salvetti correlation-energy formula into a functional of the electron density. *Phys. Rev. B*, 37(2):785, 1988.

[234] Carlo Adamo and Vincenzo Barone. Toward reliable density functional methods without adjustable parameters: The PBE0 model. *J. Chem. Phys.*, 110(13):6158–6170, 1999.

[235] Jeng-Da Chai and Martin Head-Gordon. Long-range corrected hybrid density functionals with damped atom–atom dispersion corrections. *Phys. Chem. Chem. Phys.*, 10(44):6615–6620, 2008.

[236] Yan Zhao and Donald G Truhlar. The m06 suite of density functionals for main group thermochemistry, thermochemical kinetics, noncovalent interactions, excited states, and transition elements: two new functionals and systematic testing of four M06-class functionals and 12 other functionals. *Theor. Chem. Acc.*, 120(1-3):215–241, 2008.

[237] Yan Zhao and Donald G Truhlar. A new local density functional for main-group thermochemistry, transition metal bonding, thermochemical kinetics, and noncovalent interactions. *J. Chem. Phys.*, 125(19):194101, 2006.

[238] D Andrae, U Haeussermann, M Dolg, H Stoll, and H Preuss. Energy-adjustedab initio pseudopotentials for the second and third row transition elements. *Theor. Chim. Acta*, 77(2):123–141, 1990.

[239] Jan ML Martin and Andreas Sundermann. Correlation consistent valence basis sets for use with the stuttgart–dresden–bonn relativistic effective core potentials: The atoms Ga−−Kr and In−−Xe. *J. Chem. Phys.*, 114(8):3408–3420, 2001.

[240] Benjamin P Pritchard, Doaa Altarawy, Brett Didier, Tara D Gibson, and Theresa L Windus. New basis set exchange: An open, up-to-date resource for the molecular sciences community. *J. Chem. Inf. Model.*, 59(11):4814–4820, 2019.

[241] John P Perdew, Kieron Burke, and Matthias Ernzerhof. Generalized gradient approximation made simple. *Phys. Rev. Lett.*, 77(18):3865, 1996.

[242] Florian Weigend and Reinhart Ahlrichs. Balanced basis sets of split valence, triple zeta valence and quadruple zeta valence quality for H to Rn: Design and assessment of accuracy. *Phys. Chem. Chem. Phys.*, 7(18):3297–3305, 2005.

[243] MJ Frisch, GW Trucks, HB Schlegel, GE Scuseria, MA Robb, JR Cheeseman, G Scalmani, V Barone, B Mennucci, GA Petersson, et al. Gaussian development version revision h. j04+. *Gaussian Inc., Wallingford CT*, 2011.

[244] Rüdiger Bauernschmitt and Reinhart Ahlrichs. Stability analysis for solutions of the closed shell Kohn–Sham equation. *J. Chem. Phys.*, 104(22):9047–9052, 1996.

[245] Rüdiger Bauernschmitt and Reinhart Ahlrichs. Stability analysis for solutions of the closed shell Kohn–Sham equation. *J. Chem. Phys.*, 104(22):9047–9052, 1996.

[246] HP Hratchian and HB Schlegel. Theory and applications of computational chemistry: The first 40 years. *Dykstra, CE*, pages 195–249, 2005.

[247] Henry F Schaefer III and Yukio Yamaguchi. A new dimension to quantum chemistry: Theoretical methods for the analytic evaluation of first, second, and third derivatives of the molecular electronic energy with respect to nuclear coordinates. *J. Mol. Struct.: THEOCHEM* , 135:369–390, 1986.

[248] R Eric Stratmann, John C Burant, Gustavo E Scuseria, and Michael J Frisch. Improving harmonic vibrational frequencies calculations in density functional theory. *J. Chem. Phys.*, 106(24):10175–10183, 1997.

[249] Fabrizio Santoro, Roberto Improta, Alessandro Lami, Julien Bloino, and Vincenzo Barone. Effective method to compute franck-condon integrals for optical spectra of large molecules in solution. *J. Chem. Phys.*, 126(8):084509, 2007.

[250] Fabrizio Santoro, Alessandro Lami, Roberto Improta, and Vincenzo Barone. Effective method to compute vibrationally resolved optical spectra of large molecules at finite temperature in the gas phase and in solution. *J. Chem. Phys.*, 126(18):184102, 2007.

[251] Lee M Thompson, Hassan Harb, and Hrant P Hratchian. Natural ionization

orbitals for interpreting electron detachment processes. *J. Chem. Phys.*, 144(20):204117, 2016.

[252] Lee M Thompson, Caroline C Jarrold, and Hrant P Hratchian. Explaining the $MoVO_4^-$ photoelectron spectrum: Rationalization of geometric and electronic structure. *J. Chem. Phys.*, 146(10):104301, 2017.

[253] Jessalyn A. DeVine, Marissa L. Weichman, Benjamin Laws, Jing Chang, Mark C. Babin, Garikoitz Balerdi, Changjian Xie, Christopher L. Malbon, W. Carl Lineberger, David R. Yarkony, Robert W. Field, Stephen T. Gibson, Jianyi Ma, Hua Guo, and Daniel M. Neumark. Encoding of vinylidene isomerization in its anion photoelectron spectrum. *Science*, 358(6361):336–339, 2017.

[254] Mark C. Babin, Jessalyn A. DeVine, Martin DeWitt, John F. Stanton, and Daniel M. Neumark. High-resolution photoelectron spectroscopy of cryogenically cooled NO_3^-. *J. Phys. Chem. C*, 11(2):395–400, 2020.

[255] Jia Zhou, Etienne Garand, and Daniel M. Neumark. Slow electron velocity-map imaging spectroscopy of the C_4H^- and C_4D^- anions. *J. Chem. Phys.*, 127(15):154320, 2007.

[256] Marissa L. Weichman, Lan Cheng, Jongjin B. Kim, John F. Stanton, and Daniel M. Neumark. Low-lying vibronic level structure of the ground state of the methoxy radical: Slow electron velocity-map imaging (sevi) spectra and köppel-domcke-cederbaum (kdc) vibronic hamiltonian calculations. *J. Chem. Phys.*, 146(22):224309, 2017.

[257] Yeon Jae Ko, Haopeng Wang, Rui Cao, Dunja Radisic, Soren N. Eustis, Sarah T. Stokes, Svetlana Lyapustina, Shan Xi Tian, and Kit H. Bowen. Photoelectron spectroscopy of homogeneous nucleic acid base dimer anions. *Phys. Chem. Chem. Phys.*, 12:3535–3541, 2010.

[258] Steven J. Kregel, Glen K. Thurston, and Etienne Garand. Photoelectron

spectroscopy of anthracene and fluoranthene radical anions. *J. Chem. Phys.*, 148(23):234306, 2018.

[259] Christopher G. Bailey, Caroline E. H. Dessent, Mark A. Johnson, and Kit H. Bowen. Vibronic effects in the photon energy-dependent photoelectron spectra of the CH_3CN^- dipole-bound anion. *J. Chem. Phys.*, 104(18):6976–6983, 1996.

[260] Kent M. Ervin and W. C. Lineberger. Photoelectron spectra of dicarbon(1-) and ethynyl(1-). *J. Phys. Chem. C*, 95(3):1167–1177, 1991.

[261] Christian Hock, Jongjin B. Kim, Marissa L. Weichman, Tara I. Yacovitch, and Daniel M. Neumark. Slow photoelectron velocity-map imaging spectroscopy of cold negative ions. *J. Chem. Phys.*, 137(24):244201, 2012.

[262] Jongjin B. Kim, Christian Hock, Tara I. Yacovitch, and Daniel M. Neumark. Slow photoelectron velocity-map imaging spectroscopy of cold thiozonide (s3–). *J. Phys. Chem. A*, 117(34):8126–8131, 2013.

[263] C. E. Cleeton and N. H. Williams. Electromagnetic waves of 1.1 cm wavelength and the absorption spectrum of ammonia. *Phys. Rev.*, 45:234–237, Feb 1934.

[264] Allan M. Oliveira, Yu-Ju Lu, Julia H. Lehman, P. Bryan Changala, Joshua H. Baraban, John F. Stanton, and W. Carl Lineberger. Photoelectron spectroscopy of the methide anion: Electron affinities of •ch3 and •cd3 and inversion splittings of ch3– and cd3–. *J. Am. Chem. Soc.*, 137(40):12939–12945, 2015.

[265] Marissa L. Weichman, Jongjin B. Kim, and Daniel M. Neumark. Rovibronic structure in slow photoelectron velocity-map imaging spectroscopy of CH_2CN^- and CD_2CN^-. *J. Chem. Phys.*, 140(10):104305, 2014.

[266] Michael A. Duncan. Invited review article: Laser vaporization cluster sources. *Rev. Sci. Instrum.*, 83(4):041101, 2012.

[267] U. Even, J. Jortner, D. Noy, N. Lavie, and C. Cossart-Magos. Cooling of large molecules below 1 k and he clusters formation. *J. Chem. Phys.*, 2000.

[268] Christopher P. Harrilal, Andrew F. DeBlase, Joshua L. Fischer, John T. Lawler, Scott A. McLuckey, and Timothy S. Zwier. Infrared population transfer spectroscopy of cryo-cooled ions: Quantitative tests of the effects of collisional cooling on the room temperature conformer populations. *J. Phys. Chem. A*, 122(8):2096–2107, 2018.

[269] Liudmila Voronina and Thomas R. Rizzo. Spectroscopic studies of kinetically trapped conformations in the gas phase: the case of triply protonated bradykinin. *Phys. Chem. Chem. Phys.*, 17:25828–25836, 2015.

[270] Jessalyn A. DeVine, Mark C. Babin, and Daniel M. Neumark. Photoelectron spectra of $Al_2O_2^-$ and $Al_3O_3^-$ via slow electron velocity-map imaging. *Faraday Discuss.*, 217:235–255, 2019.

[271] Mark C. Babin, Martin DeWitt, Marissa L. Weichman, Jessalyn A. DeVine, and Daniel M. Neumark. High-resolution anion photoelectron spectroscopy of cryogenically cooled 4-atom silicon carbides. *Mol. Phys.*, 0(0):1–11, 2020.

[272] Masakazu Anpo, Norikazu Aikawa, Yutaka Kubokawa, Michel Che, Catherine Louis, and Elio Giamello. Photoformation and structure of oxygen anion radicals (O_2^-) and nitrogen-containing anion radicals adsorbed on highly dispersed titanium oxide anchored onto porous vycor glass. *J. Phys. Chem. C*, 89(26):5689–5694, 1985.

[273] Jenny Schneider, Masaya Matsuoka, Masato Takeuchi, Jinlong Zhang, Yu Horiuchi, Masakazu Anpo, and Detlef W. Bahnemann. Understanding TiO_2 photocatalysis: Mechanisms and materials. *Chem. Rev.*, 114(19):9919–9986, 2014.

[274] David J Tozer and Nicholas C Handy. On the determination of excitation energies using density functional theory. *Phys. Chem. Chem. Phys.*, 2(10):2117–2121, 2000.

[275] Trygve Helgaker, Poul Jorgensen, and Jeppe Olsen. *Molecular electronic-structure theory*. John Wiley & Sons, 2014.

[276] Ove Christiansen, Pekka Manninen, Poul Jørgensen, and Jeppe Olsen. Coupled-cluster theory in a projected atomic orbital basis. *J. Chem. Phys.*, 124(8):084103, 2006.

[277] Rodney J Bartlett. Coupled-cluster theory: An overview of recent developments. In *Modern Electronic Structure Theory: Part II*, pages 1047–1131. World Scientific, 1995.

[278] Jan Almöf, Björn Roos, and Per Siegbahn. An MC-SCF computation scheme for large scale calculations on polyatomic systems. *Computers & Chemistry*, 2(2):89–94, 1978.

[279] Piotr Piecuch and Ludwik Adamowicz. State-selective multi-reference coupled-cluster theory using multi-configuration self-consistent-field orbitals. a model study on H_8. *Chem. Phys. Lett.*, 221(1-2):121–128, 1994.

[280] Kurt V Mikkelsen, Hans Ågren, Hans Jo/rgen Aa Jensen, and Trygve Helgaker. A multiconfigurational self-consistent reaction-field method. *J. Chem. Phys.*, 89(5):3086–3095, 1988.

[281] Kimihiko Hirao. *Recent advances in multireference methods*, volume 4. World Scientific, 1999.

[282] Isaiah Shavitt and Rodney J Bartlett. *Many-body methods in chemistry and physics: MBPT and coupled-cluster theory*. Cambridge university press, 2009.

[283] SA Goudsmit and Paul I Richards. The order of electron shells in ionized atoms. *Proc. Natl. Acad. Sci. U. S. A.*, 51(4):664, 1964.

[284] Eric R Scerri. Lowdin's remarks on the aufbau principle and a philosopher's view of ab initio quantum chemistry. *Fundam. World Quantum Chem.*, 2:675–694, 2003.

[285] Sadegh Salehzadeh and Farahnaz Maleki. The 4s and 3d subshells: Which one fills first in progressing through the periodic table and which one fills first in any particular atom? *Found. Chem.*, 18(1):57–65, 2016.

[286] Kevin Carter-Fenk and John M Herbert. State-targeted energy projection: A simple and robust approach to orbital relaxation of non-aufbau self-consistent field solutions. *J. Chem. Theory Comput.*, 16(8):5067–5082, 2020.

[287] LE Dardenne, N Makiuchi, LAC Malbouisson, and JDM Vianna. Multiplicity, instability, and SCF convergence problems in hartree–fock solutions. *Int. J. Quantum Chem.*, 76(5):600–610, 2000.

[288] Haoqing Guo, Qiming Peng, Xian-Kai Chen, Qinying Gu, Shengzhi Dong, Emrys W Evans, Alexander J Gillett, Xin Ai, Ming Zhang, Dan Credgington, et al. High stability and luminescence efficiency in donor–acceptor neutral radicals not following the aufbau principle. *Nat. Mater.*, 18(9):977–984, 2019.

[289] Andreas Dreuw and Michael Wormit. The algebraic diagrammatic construction scheme for the polarization propagator for the calculation of excited states. *Wiley Interdiscip. Rev.: Comput. Mol. Sci.*, 5(1):82–95, 2015.

[290] Michael Filatov. Spin-restricted ensemble-referenced Kohn–Sham method: basic principles and application to strongly correlated ground and excited states of molecules. *Wiley Interdiscip. Rev.: Comput. Mol. Sci.*, 5(1):146–167, 2015.

[291] Kristian Sneskov and Ove Christiansen. Excited state coupled cluster methods. *Wiley Interdiscip. Rev.: Comput. Mol. Sci.*, 2(4):566–584, 2012.

[292] Christel M Marian, Adrian Heil, and Martin Kleinschmidt. The DFT/MRCI method. *Wiley Interdiscip. Rev.: Comput. Mol. Sci.*, 9(2):e1394, 2019.

[293] Michael A Robb. *Theoretical chemistry for electronic excited states*, volume 12. Royal Society of Chemistry, 2018.

[294] Giuseppe MJ Barca, Andrew TB Gilbert, and Peter MW Gill. Simple models for difficult electronic excitations. *J. Chem. Theory Comput.*, 14(3):1501–1509, 2018.

[295] Andrew TB Gilbert, Nicholas A Besley, and Peter MW Gill. Self-consistent field calculations of excited states using the maximum overlap method (MOM). *J. Phys. Chem. A*, 112(50):13164–13171, 2008.

[296] Diptarka Hait and Martin Head-Gordon. Excited state orbital optimization via minimizing the square of the gradient: General approach and application to singly and doubly excited states via density functional theory. *J. Chem. Theory Comput.*, 16(3):1699–1710, 2020.

[297] P Corrêa De Mello, M Hehenberger, and MC Zernert. Converging scf calculations on excited states. *Int. J. Quantum Chem.*, 21(1):251–258, 1982.

[298] Yuncai Mei and Weitao Yang. Charge transfer excitation energies from ground state density functional theory calculations. *J. Chem. Phys.*, 150(14):144109, 2019.

[299] Bo Peng, Benjamin E Van Kuiken, Feizhi Ding, and Xiaosong Li. A guided self-consistent-field method for excited-state wave function optimization: Applications to ligand-field transitions in transition-metal complexes. *J. Chem. Theory Comput.*, 9(9):3933–3938, 2013.

[300] Rodney J Bartlett and Yngve Öhrn. How quantitative is the concept of maximum overlap? *Theor. Chim. Acta*, 21(3):215–234, 1971.

[301] Junzi Liu, Yong Zhang, Peng Bao, and Yuanping Yi. Evaluating electronic couplings for excited state charge transfer based on maximum occupation method δSCF quasi-adiabatic states. *J. Chem. Theory Comput.*, 13(2):843–851, 2017.

[302] Roberto Flores-Moreno, VG Zakrzewski, and JV Ortiz. Assessment of transition operator reference states in electron propagator calculations. *J. Chem. Phys.*, 127(13):134106, 2007.

[303] Oktay Sinanoglu and D Fu-tai Tuan. Quantum theory of atoms and molecules. *Ann. Rev. Phys. Chem.*, 15(1):251–280, 1964.

[304] Peter G Lykos and Howard N Schmeising. Maximum overlap atomic and molecular orbitals. *J. Chem. Phys.*, 35(1):288–293, 1961.

[305] Elvira R Sayfutyarova, Qiming Sun, Garnet Kin-Lic Chan, and Gerald Knizia. Automated construction of molecular active spaces from atomic valence orbitals. *J. Chem. Theory Comput.*, 13(9):4063–4078, 2017.

[306] Chang-Guo Zhan. Maximum overlap method and the bond strength. *Int. J. Quantum Chem.*, 32(1):1–11, 1987.

[307] ZB Maksić, M Eckert-Maksić, and M Randić. Correlation between CH and CC spin-spin coupling constants and s character of hybrids calculated by the maximum overlap method. *Theor. Chim. Acta*, 22(1):70–79, 1971.

[308] Donald H Kobe. Maximum-overlap orbitals, an energy variational principle, and perturbation theory. *Phys. Rev. C*, 3(2):417, 1971.

[309] F Weinhold and TK Brunck. The principle of maximum overlap. *J. Am. Chem. Soc.*, 98(13):3745–3749, 1976.

[310] HW Meldner and JD Perez. Maximum-ovelap orbitals. *Phys. Rev. C*, 7(5):2158, 1973.

[311] Jerzy Cioslowski and Matt Challacombe. Maximum similarity orbitals for analysis of the electronic excited states. *Int. J. Quantum Chem.*, 40(S25):81–93, 1991.

[312] Ernest R Davidson and Larilyn Zeller Stenkamp. SCF methods for excited states. *Int. J. Quantum Chem.*, 10(S10):21–31, 1976.

[313] Nicholas A Besley, Andrew TB Gilbert, and Peter MW Gill. Self-consistent-field calculations of core excited states. *J. Chem. Phys.*, 130(12):124308, 2009.

[314] A Baiardi, L Paoloni, V Barone, VG Zakrzewski, and JV Ortiz. Assessment of electron propagator methods for the simulation of vibrationally resolved valence and core photoionization spectra. *J. Chem. Theory Comput.*, 13(7):3120–3135, 2017.

[315] Warren J. Hehre, Leo Radom, Paul von R. Schleyer, and John Pople. *AB INITIO Molecular Orbital Theory*. John Wiley, 1 edition, 1986.

[316] Giuseppe MJ Barca, Andrew TB Gilbert, and Peter MW Gill. Excitation number: Characterizing multiply excited states. *J. Chem. Theory Comput.*, 14(1):9–13, 2018.

[317] Martin Head-Gordon, Ana M Grana, David Maurice, and Christopher A White. Analysis of electronic transitions as the difference of electron attachment and detachment densities. *J. Phys. Chem.*, 99(39):14261–14270, 1995.

[318] M. J. Frisch, G. W. Trucks, H. B. Schlegel, G. E. Scuseria, M. A. Robb, J. R. Cheeseman, G. Scalmani, V. Barone, G. A. Petersson, H. Nakatsuji, X. Li, M. Caricato, A. V. Marenich, J. Bloino, B. G. Janesko, R. Gomperts, B. Mennucci, H. P. Hratchian, J. V. Ortiz, A. F. Izmaylov, J. L. Sonnenberg, D. Williams-Young, F. Ding, F. Lipparini, F. Egidi, J. Goings, B. Peng, A. Petrone, T. Henderson, D. Ranasinghe, V. G. Zakrzewski, J. Gao, N. Rega, G. Zheng, W. Liang, M. Hada, M. Ehara, K. Toyota, R. Fukuda, J. Hasegawa, M. Ishida, T. Nakajima, Y. Honda, O. Kitao, H. Nakai, T. Vreven, K. Throssell, J. A. Montgomery, Jr., J. E. Peralta, F. Ogliaro, M. J. Bearpark, J. J. Heyd, E. N. Brothers, K. N. Kudin, V. N. Staroverov, T. A. Keith, R. Kobayashi, J. Normand, K. Raghavachari, A. P. Rendell, J. C. Burant, S. S. Iyengar, J. Tomasi, M. Cossi, J. M. Millam, M. Klene, C. Adamo, R. Cammi, J. W. Ochterski, R. L. Martin, K. Morokuma, O. Farkas, J. B. Foresman, and D. J. Fox. Gaussian Development Version, Revision J.05, 2020.

[319] Lee M Thompson, Hassan Harb, and Hrant P Hratchian. Natural ionization

orbitals for interpreting electron detachment processes. *J. Chem. Phys.*, 144(20):204117, 2016.

[320] Hassan Harb and Hrant P Hratchian. δscf dyson orbitals and pole strengths from natural ionization orbitals. *J. Chem. Phys.*, 154(8):084104, 2021.

[321] H. Harb and H. P. Hratchian. Natural ionization orbitals, 2020.

[322] Pablo Ramos and Michele Pavanello. Low-lying excited states by constrained DFT. *J. Chem. Phys.*, 148(14):144103, 2018.

[323] HH Corzo, Annia Galano, O Dolgounitcheva, VG Zakrzewski, and JV Ortiz. NR2 and P3+: accurate, efficient electron-propagator methods for calculating valence, vertical ionization energies of closed-shell molecules. *J. Phys. Chem. A*, 119(33):8813–8821, 2015.

[324] Hyojoon Kim, Ali Nassimi, and Raymond Kapral. Quantum-classical liouville dynamics in the mapping basis. *J. Chem. Phys.*, 129(8):084102, 2008.

[325] Aaron Kelly, Ramses van Zon, Jeremy Schofield, and Raymond Kapral. Mapping quantum-classical liouville equation: Projectors and trajectories. *J. Chem. Phys.*, 136(8):084101, 2012.

[326] Gustavo E Scuseria, Carlos A Jiménez-Hoyos, Thomas M Henderson, Kousik Samanta, and Jason K Ellis. Projected quasiparticle theory for molecular electronic structure. *J. Chem. Phys.*, 135(12):124108, 2011.

[327] Ilya G Ryabinkin, Scott N Genin, and Artur F Izmaylov. Constrained variational quantum eigensolver: Quantum computer search engine in the fock space. *J. Chem. Theory Comput.*, 15(1):249–255, 2018.

[328] Artur F Izmaylov. On construction of projection operators. *J. Phys. Chem. A*, 123(15):3429–3433, 2019.

[329] C. Jouvet, M. Boivineau, M. C. Duval, and B. Soep. Photochemistry in excited states of van der waals complexes. *J. Phys. Chem.*, 91(21):5416–22, 1987.

[330] Hideki Hashimoto, Kazuhiro Yanagi, Masayuki Yoshizawa, Dario Polli, Giulio Cerullo, Guglielmo Lanzani, Sandro De Silvestri, Alastair T. Gardiner, and Richard J. Cogdell. The very early events following photoexcitation of carotenoids. *Arch. Biochem. Biophys.*, 430(1):61–69, 2004.

[331] D. J. Stufkens, M. P. Aarnts, J. Nijhoff, B. D. Rossenaar, and A. Jr Vlcek. Excited states of metal-metal bonded diimine complexes vary from extremely long lived to very reactive with formation of radicals or zwitterions. *Coord. Chem. Rev.*, 171:93–105, 1998.

[332] Giuseppe Cilento and Waldemar Adam. Photochemistry and photobiology without light. *Photochem. Photobiol.*, 48(3):361–8, 1988.

[333] Jai P. Mittal. Excited states and electron transfer reactions of fullerenes. *Pure Appl. Chem.*, 67(1):103–10, 1995.

[334] Deniz Tuna, Andrzej L. Sobolewski, and Wolfgang Domcke. Electronically excited states and photochemical reaction mechanisms of b-glucose. *Phys. Chem. Chem. Phys.*, 16(1):38–47, 2014.

[335] John F. Endicott. The photophysics and photochemistry of coordination compounds. In *Inorg. Electron. Struct. Spectrosc.*, volume 2, pages 291–341. John Wiley & Sons, Inc., 1999.

[336] A. E. Obukhov. Excited states, generation of light and photoprocesses in series of complex N, O, S polyatomic molecules. *Proc. SPIE - Int. Soc. Opt. Eng.*, 2370:268–73, 1995.

[337] M. Klessinger, J. Michl, and Editors. *Excited States and Photochemistry of Organic Molecules.* VCH, 1995.

[338] Michael Scott Herman. *Studies on excited states and reactive intermediates: enthalpies, kinetics and reaction volume changes.* University of Rochester, 1992.

[339] Hans D. Scharf and Joerg Fleischhauer. Nature, multiplicity, and properties of excited states in photoreactions of organic molecules. In *Method. Chim.*, volume 1, Pt. B, pages 650–66. Academic, 1974.

[340] Wai-Pong To, Kaai Tung Chan, Glenna So Ming Tong, Chensheng Ma, Wai-Ming Kwok, Xiangguo Guan, Kam-Hung Low, and Chi-Ming Che. Strongly luminescent gold (III) complexes with long-lived excited states: High emission quantum yields, energy up-conversion, and nonlinear optical properties. *Angew. Chem. Int. Ed.*, 52(26):6648–6652, 2013.

[341] DeLyle Eastwood and Martin Gouterman. Porphyrins: XVIII. luminescence of (CO),(Ni), Pd, Pt complexes. *J. Mol. Spectrosc.*, 35(3):359–375, 1970.

[342] Antonín Vlček Jr and Stanislav Záliš. Modeling of charge-transfer transitions and excited states in d6 transition metal complexes by DFT techniques. *Coord. Chem. Rev.*, 251(3-4):258–287, 2007.

[343] Marc Dierksen and Stefan Grimme. Density functional calculations of the vibronic structure of electronic absorption spectra. *J. Chem. Phys.*, 120(8):3544–3554, 2004.

[344] E Holøien. Radial configurational interaction in helium and similar atomic systems. *Phys. Rev.*, 104(5):1301, 1956.

[345] Henrik Koch, Ove Christiansen, Poul Jørgensen, and Jeppe Olsen. Excitation energies of BH, CH_2 and Ne in full configuration interaction and the hierarchy CCS, CC2, CCSD and CC3 of coupled cluster models. *Chem. Phys. Lett.*, 244(1-2):75–82, 1995.

[346] Joseph JW McDouall, Kathryn Peasley, and Michael A Robb. A simple MC SCF perturbation theory: Orthogonal valence bond møller-plesset 2 (OVB MP2). *Chem. Phys. Lett.*, 148(2-3):183–189, 1988.

[347] Robert J Buenker, Sigrid D Peyerimhoff, and Werner Butscher. Applicability of the multi-reference double-excitation CI (MRD-CI) method to the calcu-

lation of electronic wavefunctions and comparison with related techniques. *Mol. Phys.*, 35(3):771–791, 1978.

[348] Attila Szabo and Neil S Ostlund. *Modern quantum chemistry: introduction to advanced electronic structure theory*. Courier Corporation, 2012.

[349] EKU Gross, JF Dobson, and M Petersilka. Density functional theory of time-dependent phenomena. In *Density functional theory II*, pages 81–172. Springer, 1996.

[350] Benjamin J Coe, Josephine L Harries, Madeleine Helliwell, Lathe A Jones, Inge Asselberghs, Koen Clays, Bruce S Brunschwig, James A Harris, Javier Garín, and Jesús Orduna. Pentacyanoiron (II) as an electron donor group for nonlinear optics: Medium-responsive properties and comparisons with related pentaammineruthenium (II) complexes. *J. Am. Chem. Soc.*, 128(37):12192–12204, 2006.

[351] Stanislav R Stoyanov, John M Villegas, Arvin J Cruz, Loranelle L Lockyear, Joseph H Reibenspies, and D Paul Rillema. Computational and spectroscopic studies of Re (I) bipyridyl complexes containing 2, 6-dimethylphenylisocyanide (CNx) ligand. *J. Chem. Theory Comput.*, 1(1):95–106, 2005.

[352] Giovanna Fronzoni, Mauro Stener, A Reduce, and Pietro Decleva. Time-dependent density functional theory calculations of ligand K edge and metal L edge X-ray absorption of a series of oxomolybdenum complexes. *J. Phys. Chem. A*, 108(40):8467–8477, 2004.

[353] C Lapouge and JP Cornard. Time dependent density functional theory study of electronic absorption properties of lead (II) complexes with a series of hydroxyflavones. *J. Phys. Chem. A*, 109(30):6752–6761, 2005.

[354] Lavanya M Ramaniah and Mauro Boero. Structural, electronic, and optical properties of the diindenoperylene molecule from first-principles density-functional theory. *Phys. Rev. A*, 74(4):042505, 2006.

[355] AG Marinopoulos, Ludger Wirtz, Andrea Marini, Valerio Olevano, Angel Rubio, and Lucia Reining. Optical absorption and electron energy loss spectra of carbon and boron nitride nanotubes: a first-principles approach. *Appl. Phys. A*, 78(8):1157–1167, 2004.

[356] Angelo Domenico Quartarolo, Nino Russo, and Emilia Sicilia. Structures and electronic absorption spectra of a recently synthesised class of photodynamic therapy agents. *Chem. Eur. J.*, 12(26):6797–6803, 2006.

[357] Daniele Varsano, Rosa Di Felice, Miguel AL Marques, and Angel Rubio. A TDDFT study of the excited states of dna bases and their assemblies. *J. Phys. Chem. B*, 110(14):7129–7138, 2006.

[358] Miguel AL Marques, Xabier López, Daniele Varsano, Alberto Castro, and Angel Rubio. Time-dependent density-functional approach for biological chromophores: the case of the green fluorescent protein. *Phys. Rev. Lett.*, 90(25):258101, 2003.

[359] Benjamin J Coe, James A Harris, Bruce S Brunschwig, Inge Asselberghs, Koen Clays, Javier Garín, and Jesús Orduna. Three-dimensional nonlinear optical chromophores based on metal-to-ligand charge-transfer from ruthenium (II) or iron (II) centers. *J. Am. Chem. Soc.*, 127(38):13399–13410, 2005.

[360] Robert J Cave, Kieron Burke, and Edward W Castner. Theoretical investigation of the ground and excited states of coumarin 151 and coumarin 120. *J. Phys. Chem. A*, 106(40):9294–9305, 2002.

[361] Denis Jacquemin, Eric A Perpète, Giovanni Scalmani, Michael J Frisch, Xavier Assfeld, Ilaria Ciofini, and Carlo Adamo. Time-dependent density functional theory investigation of the absorption, fluorescence, and phosphorescence spectra of solvated coumarins. *J. Chem. Phys.*, 125(16):164324, 2006.

[362] Christine Jödicke Jamorski and Mark E Casida. Time-dependent density-functional theory investigation of the fluorescence behavior as a function of alkyl chain size for the 4-(N,N-dimethylamino) benzonitrile-like donor- acceptor systems 4-(N, N-diethylamino) benzonitrile and 4-(N, N-diisopropylamino) benzonitrile. *J. Phys. Chem. B*, 108(22):7132–7141, 2004.

[363] Dmitrij Rappoport and Filipp Furche. Photoinduced intramolecular charge transfer in 4-(dimethyl) aminobenzonitrile- a theoretical perspective. *J. Am. Chem. Soc.*, 126(4):1277–1284, 2004.

[364] David J Tozer. Relationship between long-range charge-transfer excitation energy error and integer discontinuity in Kohn–Sham theory. *J. Chem. Phys.*, 119(24):12697–12699, 2003.

[365] Christine Jamorski Jödicke and Hans Peter Lüthi. Time-dependent density functional theory (TDDFT) study of the excited charge-transfer state formation of a series of aromatic donor- acceptor systems. *J. Am. Chem. Soc.*, 125(1):252–264, 2003.

[366] Andrzej L Sobolewski and Wolfgang Domcke. Ab initio study of the excited-state coupled electron–proton-transfer process in the 2-aminopyridine dimer. *Chem. Phys.*, 294(1):73–83, 2003.

[367] Andreas Dreuw, Graham R Fleming, and Martin Head-Gordon. Charge-transfer state as a possible signature of a zeaxanthin- chlorophyll dimer in the non-photochemical quenching process in green plants. *J. Phys. Chem. B*, 107(27):6500–6503, 2003.

[368] G Herzberg and KK Innes. Ultraviolet absorption spectra of HCN and DCN: I. the α—X and β—X systems. *Can. J. Phys.*, 35(8):842–879, 1957.

[369] Bengt Kleman. The near-ultraviolet absorption spectrum of CS_2. *Can. J. Phys.*, 41(12):2034–2063, 1963.

[370] Giuseppe MJ Barca, Andrew TB Gilbert, and Peter MW Gill. Simple models

for difficult electronic excitations. *J. Chem. Theory Comput.*, 14(3):1501–1509, 2018.

[371] Hector H. Corzo, Ali Abou Taka, Pribram-Jones Aurora, and Hrant P. Hratchian. Using projection operators with maximum overlap methods to simplify challenging self-consistent field optimization. Manuscript submitted for publication, 2021.

[372] K Yamaguchi, Frank Jensen, A Dorigo, and KN Houk. A spin correction procedure for unrestricted hartree-fock and møller-plesset wavefunctions for singlet diradicals and polyradicals. *Chem. Phys. Lett.*, 149(5-6):537–542, 1988.

[373] T Saito, S Nishihara, Y Kataoka, Y Nakanishi, T Matsui, Y Kitagawa, T Kawakami, M Okumura, and K Yamaguchi. Transition state optimization based on approximate spin-projection (ap) method. *Chem. Phys. Lett.*, 483(1-3):168–171, 2009.

[374] Toru Saito, Akira Ito, Tomohiro Watanabe, Takashi Kawakami, Mitsutaka Okumura, and Kizashi Yamaguchi. Performance of the coupled cluster and DFT methods for through-space magnetic interactions of nitroxide dimer. *Chem. Phys. Lett.*, 542:19–25, 2012.

[375] Nicolas Ferré, Nathalie Guihéry, and Jean-Paul Malrieu. Spin decontamination of broken-symmetry density functional theory calculations: deeper insight and new formulations. *Phys. Chem. Chem. Phys.*, 17(22):14375–14382, 2015.

[376] Lee M Thompson and Hrant P Hratchian. Modeling the photoelectron spectra of $MoNbO_2$–accounting for spin contamination in density functional theory. *J. Phys. Chem. A*, 119(32):8744–8751, 2015.

[377] Xianghai Sheng, Lee M Thompson, and Hrant P Hratchian. Assessing the calculation of exchange coupling constants and spin crossover gaps using the

approximate projection model to improve density functional calculations. *J. Chem. Theory Comput.*, 16(1):154–163, 2019.

[378] Ernest R Davidson. Spin-restricted open-shell self-consistent-field theory. *Chem. Phys. Lett.*, 21(3):565–567, 1973.

[379] VR Saunders and IH Hillier. A "level–shifting" method for converging closed shell hartree–fock wave functions. *Int. J. Quantum Chem.*, 7(4):699–705, 1973.

[380] M.F. Guest and V. R. Saunders. On methods for converging open-shell hartree-fock wave-functions. *Mol. Phys.*, 28(3):819–828, 1974.

[381] R McWeeny. SCF theory for excited states: I. optimal orbitals for the states of a configuration. *Mol. Phys.*, 28(5):1273–1282, 1974.

[382] L Brillouin. Actualités sci. et ind. *Nos*, 71(159):1933–1934, 1934.

[383] Carlos F Bunge, Rocio Jauregui, and Eugenio Ley-Koo. Relativistic self-consistent-field atomic calculations using a generalization of brillouin's theorem. *Can. J. Phys.*, 76:421–444, 1998.

[384] CA Coulson. Brillouin's theorem and the hellmann-feynman theorem for hartree-fock wave functions. *Mol. Phys.*, 20(4):687–694, 1971.

[385] Hrant P Hratchian. Communication: An efficient analytic gradient theory for approximate spin projection methods, 2013.

[386] Lee M Thompson and Hrant P Hratchian. Second derivatives for approximate spin projection methods. *J. Chem. Phys.*, 142(5):054106, 2015.

[387] Lee M Thompson and Hrant P Hratchian. Spin projection with double hybrid density functional theory. *J. Chem. Phys.*, 141(3):034108, 2014.

[388] Lee M Thompson and Hrant P Hratchian. On approximate projection models. *Mol. Phys.*, 117(9-12):1421–1429, 2019.

[389] Axel Becke. *The quantum theory of atoms in molecules: from solid state to DNA and drug design.* John Wiley & Sons, 2007.

[390] John C Slater. A simplification of the hartree-fock method. *Phys. Rev.*, 81(3):385, 1951.

[391] Michael J Frisch, John A Pople, and J Stephen Binkley. Self-consistent molecular orbital methods 25. supplementary functions for gaussian basis sets. *J. Chem. Phys.*, 80(7):3265–3269, 1984.

[392] Krishnan Raghavachari and Gary W Trucks. Highly correlated systems. excitation energies of first row transition metals Sc–Cu. *J. Chem. Phys.*, 91(2):1062–1065, 1989.

[393] AD McLean and GS Chandler. Contracted gaussian basis sets for molecular calculations. i. second row atoms, Z= 11–18. *J. Chem. Phys.*, 72(10):5639–5648, 1980.

[394] RC Binning Jr and LA Curtiss. Compact contracted basis sets for third-row atoms: Ga–Kr. *J. Comput. Chem.*, 11(10):1206–1216, 1990.

[395] Timothy Clark, Jayaraman Chandrasekhar, Günther W Spitznagel, and Paul Von Ragué Schleyer. Efficient diffuse function-augmented basis sets for anion calculations. III. the 3-21+ g basis set for first-row elements, Li–F. *J. Comput. Chem.*, 4(3):294–301, 1983.

[396] Nikolai B. Balabanov and Kirk A. Peterson. Systematically convergent basis sets for transition metals. i. all-electron correlation consistent basis sets for the 3d elements Sc-Zn. *J. Chem. Phys.*, 123, 2005.

[397] Rick A. Kendall, Thom H. Dunning, and Robert J. Harrison. Electron affinities of the first-row atoms revisited. systematic basis sets and wave functions. *J. Chem. Phys.*, 96, 1992.

[398] Brian P. Prascher, David E. Woon, Kirk A. Peterson, Thom H. Dunning, and Angela K. Wilson. Gaussian basis sets for use in correlated molecular

calculations. VII. valence, core-valence, and scalar relativistic basis sets for Li, Be, Na, and Mg. *Theor. Chem. Acc.*, 128, 2011.

[399] Angela K. Wilson, David E. Woon, Kirk A. Peterson, and Thom H. Dunning. Gaussian basis sets for use in correlated molecular calculations. IX. the atoms gallium through krypton. *J. Chem. Phys.*, 110, 1999.

[400] David E. Woon and Thom H. Dunning. Gaussian basis sets for use in correlated molecular calculations. III. the atoms aluminum through argon. *J. Chem. Phys.*, 98, 1993.

[401] Benjamin P. Pritchard, Doaa Altarawy, Brett Didier, Tara D. Gibsom, and Theresa L. Windus. A new basis set exchange: An open, up-to-date resource for the molecular sciences community. *J. Chem. Inf. Model.*, 59, 2019.

[402] David Feller. The role of databases in support of computational chemistry calculations. *J. Comput. Chem.*, 17, 1996.

[403] Karen L. Schuchardt, Brett T. Didier, Todd Elsethagen, Lisong Sun, Vidhya Gurumoorthi, Jared Chase, Jun Li, and Theresa L. Windus. Basis set exchange: A community database for computational sciences. *J. Chem. Inf. Model.*, 47, 2007.

[404] M Bencheikh, R Koivisto, O Launila, and JP Flament. The low-lying electronic states of CrF and CrCl: Analysis of the A 6 $\sigma+\rightarrow$ X 6 $\sigma+$ system of CrCl. *J. Chem. Phys.*, 106(15):6231–6239, 1997.

[405] DJ Clouthier and DA Ramsay. The spectroscopy of formaldehyde and thioformaldehyde. *Ann. Rev. Phys. Chem.*, 34(1):31–58, 1983.

[406] RY Dong, R Nanes, and DA Ramsay. Rotational analyses of bands of the system of cis-glyoxal. *Can. J. Chem.*, 71(10):1595–1597, 1993.

[407] J Co D Brand and DG Williamson. Near-ultra-violet spectrum of propenal. *Discuss. Faraday Soc.*, 35:184–191, 1963.

[408] Robert R Birge, Wallace C Pringle, and Peter A Leermakers. Excited-state geometries of the singly substituted methylpropenals. i. vibrational-electronic analysis of s1 (n,. π^*). *J. Am. Chem. Soc.*, 93(25):6715–6726, 1971.

[409] Christopher M Hadad, James B Foresman, and Kenneth B Wiberg. Excited states of carbonyl compounds. 1. formaldehyde and acetaldehyde. *J. Phys. Chem.*, 97(17):4293–4312, 1993.

[410] Dennis J Clouthier and Jerzy Karolczak. A pyrolysis jet spectroscopic study of the rotationally resolved electronic spectrum of dichlorocarbene. *J. Chem. Phys.*, 94(1):1–10, 1991.

[411] Z-L Cai and J-L Bai. Theoretical studies of the electronic spectrum of SiF_2. *Chem. Phys.*, 178(1-3):215–221, 1993.

[412] P. S. Bagus. Self-consistent-field wave functions for hole states of some ne-like and ar-like ions. *Phys. Rev.*, 139:A619–A634, Aug 1965.

[413] Paul S Bagus and Francesc Illas. Orbitals permit the interpretation of core-level spectroscopies in terms of chemistry. *Catal. Lett.*, pages 1–7, 2020.

[414] JIA Deng, Andrew TB Gilbert, and Peter MW Gill. Rydberg states of the helium atom. *Int. J. Quantum Chem.*, 109(9):1915–1919, 2009.

[415] Pierre-François Loos, Anthony Scemama, Aymeric Blondel, Yann Garniron, Michel Caffarel, and Denis Jacquemin. A mountaineering strategy to excited states: Highly accurate reference energies and benchmarks. *J. Chem. Theory Comput.*, 14(8):4360–4379, 2018.

[416] HH Corzo, AM Velasco, C Lavín, and JV Ortiz. MgH rydberg series: Transition energies from electron propagator theory and oscillator strengths from the molecular quantum defect orbital method. *J. Quant. Spectrosc. Radiat. Transfer*, 206:323–327, 2018.

[417] Dennis L Ashford, Melissa K Gish, Aaron K Vannucci, M Kyle Brennaman, Joseph L Templeton, John M Papanikolas, and Thomas J Meyer. Molecular

chromophore–catalyst assemblies for solar fuel applications. *Chem. Rev.*, 115(23):13006–13049, 2015.

[418] Krishanu Sarkar, Koushik Dhara, Mahasweta Nandi, Partha Roy, Asim Bhaumik, and Pradyot Banerjee. Selective zinc (II)-ion fluorescence sensing by a functionalized mesoporous material covalently grafted with a fluorescent chromophore and consequent biological applications. *Adv. Funct. Mater.*, 19(2):223–234, 2009.

[419] Kazuhiro J Fujimoto. Electronic couplings and electrostatic interactions behind the light absorption of retinal proteins. *Front. Mol. Biosci.*, page 898, 2021.

[420] Chase S Linsley, Viola Y Quach, Gaurav Agrawal, Elyse Hartnett, and Benjamin M Wu. Visible light and near-infrared-responsive chromophores for drug delivery-on-demand applications. *Drug Deliv. Transl. Res.*, 5(6):611–624, 2015.

[421] David R Kanis, Mark A Ratner, and Tobin J Marks. Design and construction of molecular assemblies with large second-order optical nonlinearities. quantum chemical aspects. *Chem. Rev.*, 94(1):195–242, 1994.

[422] LarryáR Dalton, WilliamáH Steier, BruceáH Robinson, et al. From molecules to opto-chips: organic electro-optic materials. *J. Mater. Chem.*, 9(9):1905–1920, 1999.

[423] Mark E. Casida. *Time-Dependent Density Functional Response Theory for Molecules*, pages 155–192. World Scientific, 1995.

[424] Rodiger Bauernschmitt and Reinhart Ahlrichs. Treatment of electronic excitations within the adiabatic approximation of time dependent density functional theory. *Chem. Phys. Lett.*, 256(4):454–464, 1996.

[425] Filipp Furche and Reinhart Ahlrichs. Adiabatic time-dependent density functional methods for excited state properties. *J. Chem. Phys.*, 117(16):7433–7447, 2002.

[426] Shane M. Parker and Filipp Furche. *Response Theory and Molecular Properties*, pages 69–86. Springer Singapore, Singapore, 2018.

[427] Adele D. Laurent and Denis Jacquemin. TD-DFT benchmarks: A review. *Int. J. Quantum Chem.*, 113(17):2019–2039, 2013.

[428] Neepa T. Maitra, Fan Zhang, Robert J. Cave, and Kieron Burke. Double excitations within time-dependent density functional theory linear response. *J. Chem. Phys.*, 120(13):5932–5937, 2004.

[429] Robert J. Cave, Fan Zhang, Neepa T. Maitra, and Kieron Burke. A dressed TDDFT treatment of the $^{21}a_g$ states of butadiene and hexatriene. *Chem. Phys. Lett.*, 389(1):39–42, 2004.

[430] Benjamin G. Levine, Chaehyuk Ko, Jason Quenneville, and Todd J. Martinez. Conical intersections and double excitations in time-dependent density functional theory. *Mol. Phys.*, 104(5-7):1039–1051, 2006.

[431] Peter Elliott, Sharma Goldson, Chris Canahui, and Neepa T. Maitra. Perspectives on double-excitations in TDDFT. *Chem. Phys.*, 391(1):110–119, 2011.

[432] Chang-Guo Zhan. Maximum overlap method and the bond strength. *Int. J. Quantum Chem.*, 32(1):1–11, 1987.

[433] ZB Maksić, M Eckert-Maksić, and M Randić. Correlation between ch and cc spin-spin coupling constants and s character of hybrids calculated by the maximum overlap method. *Theor. Chim. Acta*, 22(1):70–79, 1971.

[434] Jerzy Cioslowski and Matt Challacombe. Maximum similarity orbitals for analysis of the electronic excited states. *Int. J. Quantum Chem.*, 40(S25):81–93, 1991.

[435] Hector H. Corzo, Ali Abou Taka, Pribram-Jones Aurora, and Hrant P. Hratchian. Good vibrations: Calculating excited state frequencies using ground state self-consistent field models. Manuscript submitted for publication, 2021.

[436] Malgorzata Biczysko, Julien Bloino, Fabrizio Santoro, and Vincenzo Barone. *Time-Independent Approaches to Simulate Electronic Spectra Lineshapes: From Small Molecules to Macrosystems*, chapter 8, pages 361–443. John Wiley & Sons, Ltd, 2011.

[437] F. Duschinsky. . *Acta Physicochim. URSS.*, 7(7):411, 1937.

[438] Fabrizio Santoro, Alessandro Lami, Roberto Improta, Julien Bloino, and Vincenzo Barone. Effective method for the computation of optical spectra of large molecules at finite temperature including the duschinsky and herzberg–teller effect: The q x band of porphyrin as a case study. *J. Chem. Phys.*, 128(22):224311, 2008.

[439] Peter Macak, Yi Luo, and Hans Ågren. Simulations of vibronic profiles in two-photon absorption. *Chem. Phys. Lett.*, 330(3-4):447–456, 2000.

[440] Aliya Mukazhanova, Kasidet Jing Trerayapiwat, Amir Mazaheripour, Austin G Wardrip, Nathan C Frey, Hung Nguyen, Alon A Gorodetsky, and Sahar Sharifzadeh. Accurate first-principles calculation of the vibronic spectrum of stacked perylene tetracarboxylic acid diimides. *J. Phys. Chem. A*, 124(16):3055–3063, 2020.

[441] Anirban Hazra, Hannah H. Chang, and Marcel Nooijen. First principles simulation of the uv absorption spectrum of ethylene using the vertical franck-condon approach. *J. Chem. Phys.*, 121(5):2125–2136, 2004.

[442] Anirban Hazra and Marcel Nooijen. Vibronic coupling in the excited cationic states of ethylene: Simulation of the photoelectron spectrum between 12 and 18 ev. *J. Chem. Phys.*, 122(20):204327, 2005.

[443] Francisco Jose Avila Ferrer and Fabrizio Santoro. Comparison of vertical and adiabatic harmonic approaches for the calculation of the vibrational structure of electronic spectra. *Phys. Chem. Chem. Phys.*, 14:13549–13563, 2012.

[444] Shaul Mukamel. *Principles of Nonlinear Optical Spectroscopy*. Oxford University Press, New York, 1995.

[445] T. J. Zuehlsdorff, A. Montoya-Castillo, J. A. Napoli, T. E. Markland, and C. M. Isborn. Optical spectra in the condensed phase: Capturing anharmonic and vibronic features using dynamic and static approaches. *J. Chem. Phys.*, 151(7):074111, 2019.

[446] Tim J. Zuehlsdorff, Sapana V. Shedge, Shao-Yu Lu, Hanbo Hong, Vincent P. Aguirre, Liang Shi, and Christine M. Isborn. Vibronic and environmental effects in simulations of optical spectroscopy. *Ann. Rev. Phys. Chem.*, 72(1):165–188, 2021. PMID: 33395546.

[447] Joel S Bader and B J Berne. Quantum and classical relaxation rates from classical simulations. *J. Chem. Phys.*, 100(11):8359, 6 1994.

[448] S. A. Egorov, K. F. Everitt, and J. L. Skinner. Quantum Dynamics and Vibrational Relaxation. *J. Phys. Chem. A*, 103:9494–9499, 1999.

[449] Hyojoon Kim and Peter J. Rossky. Evaluation of Quantum Correlation Functions from Classical Data. *J. Phys. Chem. B*, 106:8240, 2002.

[450] S. Valleau, A. Eisfeld, and A. Aspuru-Guzik. On the alternatives for bath correlators and spectral densities from mixed quantum-classical simulations. *J. Chem. Phys.*, 137(22):224103, 2012.

[451] Tim Zuehlsdorff, Hanbo Hong, Liang Shi, and Christine Isborn. Nonlinear spectroscopy in the condensed phase: The role of duschinsky rotations and third order cumulant contributions. *J. Chem. Phys.*, 153:044127–16, 5 2020.

[452] Thiago B. de Queiroz, Erick R. de Figueroa, Mauricio D. Coutinho-Neto, Cleiton D. Maciel, Enrico Tapavicza, Zohreh Hashemi, and Linn Leppert. First principles theoretical spectroscopy of methylene blue: Between limitations of time-dependent density functional theory approximations and its realistic description in the solvent. *J. Chem. Phys.*, 154(4):044106, 2021.

[453] Angus J Dunnett, Duncan Gowland, Christine M Isborn, Alex W Chin, and Tim J Zuehlsdorff. Influence of non-adiabatic effects on linear ab-

sorption spectra in the condensed phase: Methylene blue. *J. Chem. Phys.*, 155(14):144112, 2021.

[454] Jarrett L Mason, Hassan Harb, Ali Abou Taka, Caleb D Huizenga, Hector H Corzo, Hrant P Hratchian, and Caroline Chick Jarrold. New photoelectron–valence electron interactions evident in the photoelectron spectrum of Gd_2O^-. *J. Phys. Chem. A*, 2021.

[455] Jarrett L. Mason, Hassan Harb, Ali Abou Taka, Abbey J. McMahon, Caleb D. Huizenga, Hector Corzo, Hrant P. Hratchian, and Caroline Chick Jarrold. Photoelectron spectra of Gd_2O_2– and nonmonotonic photon-energy-dependent variations in populations of close-lying neutral states. *J. Phys. Chem. A*, 125(3):857–866, 2021.

[456] Guillem Aromí, David Aguila, Patrick Gamez, Fernando Luis, and Olivier Roubeau. Design of magnetic coordination complexes for quantum computing. *Chem. Soc. Rev.*, 41(2):537–546, 2012.

[457] Juan M Clemente-Juan, Eugenio Coronado, and Alejandro Gaita-Ariño. Magnetic polyoxometalates: from molecular magnetism to molecular spintronics and quantum computing. *Chem. Soc. Rev.*, 41(22):7464–7478, 2012.

[458] David Aguilà, Leoní A Barrios, Verónica Velasco, Olivier Roubeau, Ana Repollés, Pablo J Alonso, Javier Sesé, Simon J Teat, Fernando Luis, and Guillem Aromí. Heterodimetallic

$$lnln'$$

lanthanide complexes: toward a chemical design of two-qubit molecular spin quantum gates. *J. Am. Chem. Soc.*, 136(40):14215–14222, 2014.

[459] Andreas Trabesinger. Quantum leaps, bit by bit. *Nature*, 543(7646):S2–S3, 2017.

[460] Stewart E Barnes, Jun'ichi Ieda, and Sadamichi Maekawa. Rashba spin-orbit anisotropy and the electric field control of magnetism. *Sci. Rep.*, 4(1):1–5, 2014.

[461] Ziyao Zhou, Morgan Trassin, Ya Gao, Yuan Gao, Diana Qiu, Khalid Ashraf, Tianxiang Nan, Xi Yang, Samuel R Bowden, Daniel T Pierce, et al. Probing electric field control of magnetism using ferromagnetic resonance. *Nat. Commun.*, 6(1):1–7, 2015.

[462] Colin A Gould, K Randall McClain, Jason M Yu, Thomas J Groshens, Filipp Furche, Benjamin G Harvey, and Jeffrey R Long. Synthesis and magnetism of neutral, linear metallocene complexes of terbium (II) and dysprosium (II). *J. Am. Chem. Soc.*, 141(33):12967–12973, 2019.

[463] Andrey M Tokmachev, Dmitry V Averyanov, Alexander N Taldenkov, Oleg E Parfenov, Igor A Karateev, Ivan S Sokolov, and Vyacheslav G Storchak. Lanthanide f 7 metalloxenes–a class of intrinsic 2d ferromagnets. *Mater. Horiz.*, 6(7):1488–1496, 2019.

[464] Robert W Field. Diatomic molecule electronic structure beyond simple molecular constants. *Berichte der Bunsengesellschaft für physikalische Chemie*, 86(9):771–779, 1982.

[465] LEONID A Kaledin, JE McCord, and MICHAEL C Heaven. Laser spectroscopy of CeO: Characterization and assignment of states in the 0-3 ev range. *J. Mol. Spectrosc.*, 158(1):40–61, 1993.

[466] Leonid A Kaledin, JoHN E McCoRD, and MICHAEL C HEAvEN. Rotation-electronic deperturbation analysis of the 4f 6s configurational states of CeO. *J. Mol. Spectrosc.*, 170(1):166–171, 1995.

[467] Jarrett L Mason, Josey E Topolski, Joshua Ewigleben, Srinivasan S Iyengar, and Caroline Chick Jarrold. Photoelectrons are not always quite free. *J. Phys. Chem. Lett.*, 10(2):144–149, 2018.

[468] Eugene P Wigner. On the behavior of cross sections near thresholds. *Phys. Rev.*, 73(9):1002, 1948.

[469] Jared O Kafader, Josey E Topolski, Vicmarie Marrero-Colon, Srinivasan S Iyengar, and Caroline Chick Jarrold. The electron shuffle: Cerium influences

samarium 4 f orbital occupancy in heteronuclear Ce−−Sm oxide clusters. *J. Chem. Phys.*, 146(19):194310, 2017.

[470] Marissa L Weichman, Bess Vlaisavljevich, Jessalyn A DeVine, Nicholas S Shuman, Shaun G Ard, Toru Shiozaki, Daniel M Neumark, and Albert A Viggiano. Electronic structure of SmO and SmO^- via slow photoelectron velocity-map imaging spectroscopy and spin-orbit CASPT2 calculations. *J. Chem. Phys.*, 147(23):234311, 2017.

[471] Dao-Fu Yuan, Yuan Liu, Chen-Hui Qian, G Stephen Kocheril, Yue-Rou Zhang, Brenda M Rubenstein, and Lai-Sheng Wang. Polarization of valence orbitals by the intramolecular electric field from a diffuse dipole-bound electron. *J. Phys. Chem. Lett.*, 11(18):7914–7919, 2020.

[472] Michael Fechner, Peter Zahn, Sergey Ostanin, Manuel Bibes, and Ingrid Mertig. Switching magnetization by 180 with an electric field. *Phys. Rev. Lett.*, 108(19):197206, 2012.

[473] Kyung-Han Yun, Minho Lee, and Yong-Chae Chung. Electric field as a novel switch for magnetization of fe/graphene system. *J. Magn. Magn. Mater.*, 362:93–96, 2014.

[474] Wei-Gang Wang, Mingen Li, Stephen Hageman, and CL Chien. Electric-field-assisted switching in magnetic tunnel junctions. *Nat. Mater.*, 11(1):64–68, 2012.

[475] NN Negulyaev, VS Stepanyuk, W Hergert, and J Kirschner. Electric field as a switching tool for magnetic states in atomic-scale nanostructures. *Phys. Rev. Lett.*, 106(3):037202, 2011.

[476] Jean-Pierre Costes, Francoise Dahan, and Franck Nicodeme. A trinuclear gadolinium complex: structure and magnetic properties. *Inorg. Chem.*, 40(20):5285–5287, 2001.

[477] Katie R Meihaus, Jordan F Corbey, Ming Fang, Joseph W Ziller, Jeffrey R Long, and William J Evans. Influence of an inner-sphere k+ ion on the

magnetic behavior of n23–radical-bridged dilanthanide complexes isolated using an external magnetic field. *Inorg. Chem.*, 53(6):3099–3107, 2014.

[478] Jeffrey D Rinehart, Ming Fang, William J Evans, and Jeffrey R Long. Strong exchange and magnetic blocking in N_2 3–radical-bridged lanthanide complexes. *Nat. Chem.*, 3(7):538–542, 2011.

[479] MJ Frisch, GW Trucks, HB Schlegel, GE Scuseria, MA Robb, JR Cheeseman, G Scalmani, V Barone, GA Petersson, H Nakatsuji, et al. Gaussian 16 revision a. 03. 2016; gaussian inc. *Wallingford CT*, 2(4), 2016.

[480] Xiaoyan Cao and Michael Dolg. Valence basis sets for relativistic energy-consistent small-core lanthanide pseudopotentials. *J. Chem. Phys.*, 115(16):7348–7355, 2001.

[481] Richard N Schaugaard, Josey E Topolski, Manisha Ray, Krishnan Raghavachari, and Caroline Chick Jarrold. Insight into ethylene interactions with molybdenum suboxide cluster anions from photoelectron spectra of chemifragments. *J. Chem. Phys.*, 148(5):054308, 2018.

[482] Jared O Kafader, Josey E Topolski, and Caroline Chick Jarrold. Molecular and electronic structures of cerium and cerium suboxide clusters. *J. Chem. Phys.*, 145(15):154306, 2016.

[483] Manisha Ray, Jeremy A Felton, Jared O Kafader, Josey E Topolski, and Caroline Chick Jarrold. Photoelectron spectra of CeO^- and $Ce(OH)_2^-$. *J. Chem. Phys.*, 142(6):064305, 2015.

[484] J.O. Kafader, M. Ray, and C.C. Jarrold. Photoelectron spectrum of pro-. *J. Chem. Phys.*, 143(6):064305 1–6, 2015.

[485] Takahito Nakajima and Kimihiko Hirao. The douglas–kroll–hess approach. *Chem. Rev.*, 112(1):385–402, 2012.

[486] Axel D Becke. Density-functional thermochemistry. iv. a new dynamical correlation functional and implications for exact-exchange mixing. *J. Chem. Phys.*, 104(3):1040–1046, 1996.

[487] JE Topolski, JO Kafader, Manisha Ray, and CC Jarrold. Elucidating cerium+ H_2O reactivity through electronic structure: A combined PES and DFT study. *J. Mol. Spectrosc.*, 336:1–11, 2017.

[488] Josey E Topolski, Jared O Kafader, and Caroline Chick Jarrold. Ce in the +4 oxidation state: Anion photoelectron spectroscopy and photodissociation of small $Ce_xO_yH_z^-$ molecules. *J. Chem. Phys.*, 147(10):104303, 2017.

[489] Yuri Ralchenko. NIST atomic spectra database. *Memorie della Societa Astronomica*, 8:96, 2005.

[490] Steven M O'Malley and Donald R Beck. Calculation of Ce^- binding energies by analysis of photodetachment partial cross sections. *Phys. Rev. A*, 74(4):042509, 2006.

[491] Manisha Ray, Jeremy A Felton, Jared O Kafader, Josey E Topolski, and Caroline Chick Jarrold. Photoelectron spectra of CeO^- and $Ce(OH)_2^-$. *J. Chem. Phys.*, 142(6):064305, 2015.

[492] E. Klingeler, N. Pontius, G. Luttgens, P.S. Bechthold, M. Neeb, and W Eberhardt. Photoelectron spectroscopy of GdO^-. *Phys. Rev. A*, 65:032502 1–3, 2002.

[493] Halstead Harrison. Angular distribution of photoelectrons. i. cadmium and zinc atoms at 584 and 1048 å. *J. Chem. Phys.*, 52(2):901–905, 1970.

[494] TEH Walker and JT Waber. Spin-orbit coupling photoionization. *J. Phys. B: At. Mol. Phys.*, 7(6):674, 1974.

[495] G Schönhense, F Schäfers, Ulrich Heinzmann, and J Kessler. Angle- and spin-resolved photoelectron spectroscopy of the Hg 5d 10 subshell. *Z. Phys. A: Atoms Nucl.*, 304(1):31–40, 1982.

[496] James AR Samson and WH Hancock. Angular distribution of photoelectrons from atomic oxygen at 736 å and 584 å. *Phys. Lett. A*, 61(6):380–382, 1977.

[497] Andrei Sanov. Laboratory-frame photoelectron angular distributions in anion photodetachment: insight into electronic structure and intermolecular interactions. *Ann. Rev. Phys. Chem.*, 65:341–363, 2014.